Novel microbial rhodopsins for optogenetics

Engineering, optimization and application ofmicroscopes, software, screening pipelines, and genetically encoded voltage indicators towards imaging neural dynamics

Meng, X.

DOI
10.4233/uuid:5b2aafbf-4f09-4c4e-9286-4d1a5cb7586e

Publication date
2024

Document Version
Final published version

Citation (APA)
Meng, X. (2024). *Novel microbial rhodopsins for optogenetics: Engineering, optimization and application ofmicroscopes, software, screening pipelines, and genetically encoded voltage indicators towards imaging neural dynamics*. [Dissertation (TU Delft), Delft University of Technology]. https://doi.org/10.4233/uuid:5b2aafbf-4f09-4c4e-9286-4d1a5cb7586e

NOVEL MICROBIAL RHODOPSINS FOR OPTOGENETICS

ENGINEERING, OPTIMIZATION AND APPLICATION OF MICROSCOPES, SOFTWARE, SCREENING PIPELINES, AND GENETICALLY ENCODED VOLTAGE INDICATORS TOWARDS IMAGING NEURAL DYNAMICS

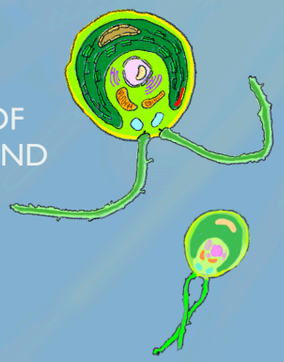

Xin Meng

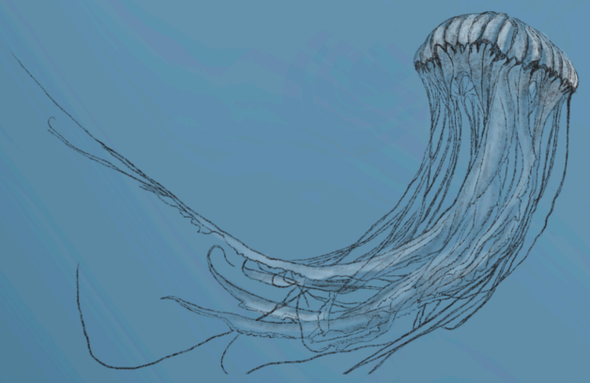

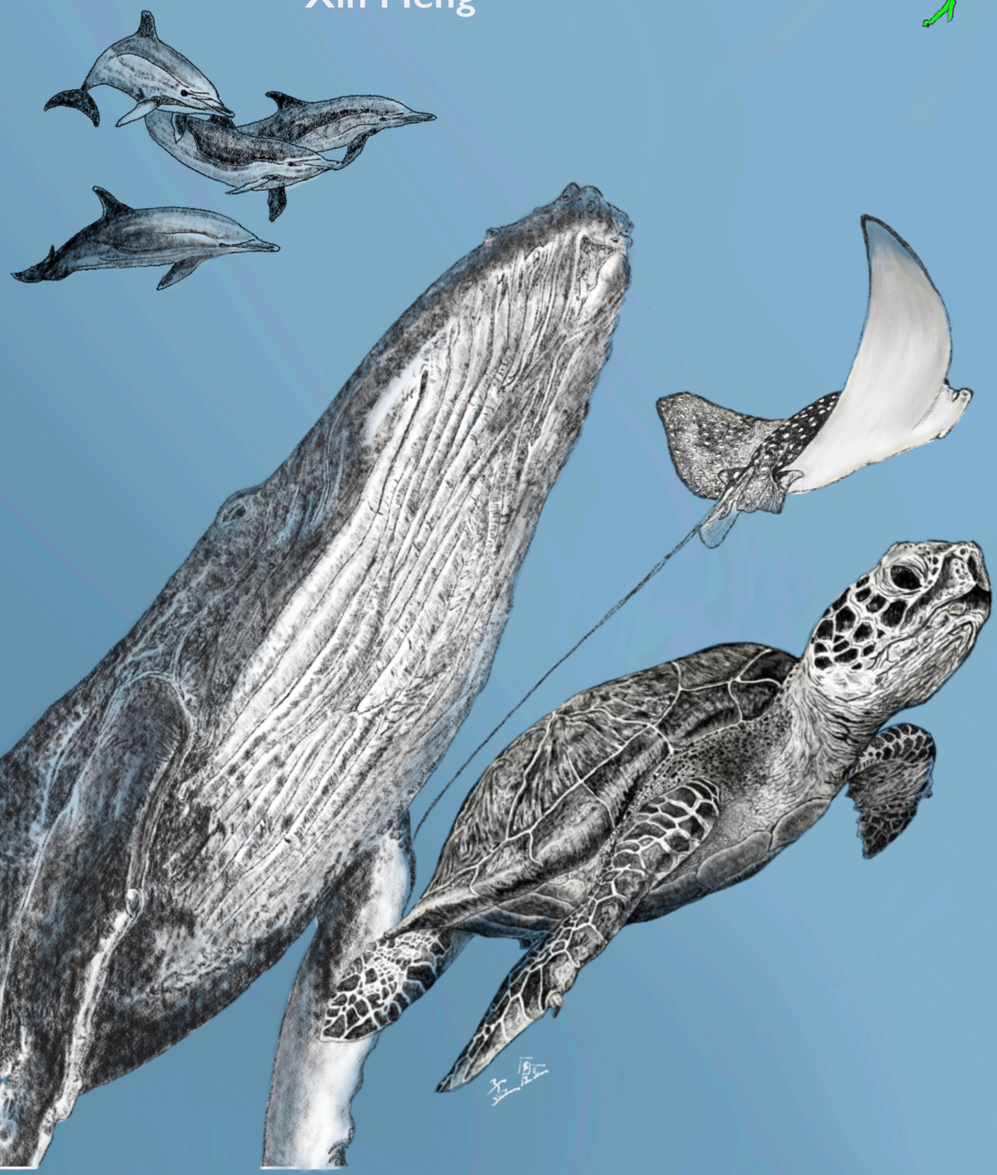

NOVEL MICROBIAL RHODOPSINS FOR OPTOGENETICS Xin Meng

NOVEL MICROBIAL RHODOPSINS FOR OPTOGENETICS

ENGINEERING, OPTIMIZATION AND APPLICATION OF MICROSCOPES, SOFTWARE, SCREENING PIPELINES, AND GENETICALLY ENCODED VOLTAGE INDICATORS TOWARDS IMAGING NEURAL DYNAMICS

Propositions

accompanying the dissertation

Novel microbial rhodopsins for optogenetics

by

Xin Meng

1. A combination of rational design and high throughput screening is the most efficient way to develop new protein sensors for neuroscience. *This proposition pertains to this dissertation.*

2. Machine learning will only greatly help big data interpretation in neuroscience if a proper validation pipeline is established across labs. *This proposition pertains to this dissertation.*

3. Natural machinery such as rhodopsins are underexplored: their use is the future of nano- and bioengineering. *This proposition pertains to this dissertation.*

4. Combining machine learning and QM/MM (quantum mechanics/molecular mechanics) simulation to computationally evolve the protein towards a desired direction is the most thorough way to develop novel biological tools.

5. Understanding the 2P excitation pathway of light-absorbing biosensors is necessary to advance 2P sensor development and create optimized imaging hardware.

6. The further the cultural and genetic homogenization develops globally, the closer we are towards space migration.

7. The ocean will be the greatest contributor to finding a sustainable green energy source.

8. Natural sciences and social sciences can benefit from each other and should work more closely together.

9. Training on scientific writing tools, such as Latex, should be compulsory for both PhD students and PIs to facilitate the thesis writing and revision process.

10. Attending international high-quality training programs at the early stage of the PhD is enormously helpful to the scientific career.

These propositions are regarded as opposable and defendable, and have been approved as such by the Prof. dr. ir. J.P. Hoogenboom and the copromotor Dr. ir. D. Brinks.

Stellingen

behorende bij het proefschrift

Novel microbial rhodopsins for optogenetics

door

Xin Meng

1. Een combinatie van rationeel design en screening met hoge verwerkingscapaciteit is de meest efficiënte manier om nieuwe proteïne sensors voor neurowetenschap te ontwikkelen. *Deze stelling heeft betrekking op dit proefschrift.*

2. Machine learning zal alleen aanzienlijk kunnen helpen bij de interpretatie van big data wanneer er een correcte validatiepijplijn is opgesteld tussen laboratoria. *Deze stelling heeft betrekking op dit proefschrift.*

3. Natuurlijke mechanismen zoals rhodopsines zijn niet genoeg onderzocht: hun gebruik vormt de toekomst van nano- en bioengineering. *Deze stelling heeft betrekking op dit proefschrift.*

4. Het combineren van machine learning en QM/MM (quantum mechanics/molecular mechanics) simulatie om proteïnen computergestuurd te evolueren in een gewenste richting is de meest grondige manier om nieuwe biologische instrumenten te ontwikkelen.

5. Het begrijpen van de 2P excitatie-route van licht-absorberende biosensoren is noodzakelijk om de ontwikkeling van 2P sensoren te bevorderen en geoptimaliseerde imaging hardware te creëren.

6. Des te meer culturele en genetische homogenisatie globaal ontwikkelen, des te dichter we bij ruimtemigratie komen.

7. De oceaan zal de grootste bijdrage leveren in het vinden van een duurzame, groene energiebron.

8. Natuurwetenschappen en sociale wetenschappen kunnen van elkaar profiteren en zouden nauwer moeten samenwerken.

9. Training in wetenschappelijke schrijfinstrumenten, zoals Latex, zou verplicht moeten zijn voor zowel PhD studenten als PIs om het schrijven en reviseren van de thesis te vergemakkelijken.

10. Het bijwonen van internationale, kwalitatief hoogstaande trainingsprogramma's in de beginfase van de PhD is zeer nuttig voor de wetenschappelijke carrière.

Deze stellingen worden opponeerbaar en verdedigbaar geacht en zijn als zodanig goedgekeurd door de promotor Prof. dr. ir. J.P. Hoogenboom
en de copromotor Dr. ir. D. Brinks.

NOVEL MICROBIAL RHODOPSINS FOR OPTOGENETICS

ENGINEERING, OPTIMIZATION AND APPLICATION OF MICROSCOPES, SOFTWARE, SCREENING PIPELINES, AND GENETICALLY ENCODED VOLTAGE INDICATORS TOWARDS IMAGING NEURAL DYNAMICS

Proefschrift

ter verkrijging van de graad van doctor

aan de Technische Universiteit Delft,

op gezag van de Rector Magnificus prof. dr. ir. T.H.J.J. van der Hagen,

voorzitter van het College voor Promoties,

in het openbaar te verdedigen op vrijdag 29 november 2024 om 10:00 uur

door

Xin MENG

Master of Engineering in Optical Engineering, Jiangnan University, China,

geboren te An Hui, China.

Dit proefschrift is goedgekeurd door de

promotor: Prof. dr. ir. J. P. Hoogenboom
copromotor: Dr. ir. D. Brinks

Samenstelling promotiecommissie:

Rector Magnificus,	voorzitter
Prof. dr. ir. J. P. Hoogenboom	Technische Universiteit Delft
Dr. ir. D. Brinks	Technische Universiteit Delft
Onafhankelijke leden:	
Dr. N. Bhattacharya	Technische Universiteit Delft
Prof. dr. T. W. J. Gadella	Universiteit van Amsterdam
Dr. M. Orger	Champalimaud Centre for the Unknown, Portugal
Prof. dr. B. Rieger	Technische Universiteit Delft
Prof. dr. ir. M. H. G. Verhaegen	Technische Universiteit Delft

Keywords: Optogenetics, microbial rhodopsin, voltage imaging, optical engineering, software engineering, protein engineering.
Printed by: Gildeprint
Front & Back: An ocean view, with the algae *Chlamydomanas* chasing the light. Illustrated using a digital pencil.

ISBN 978-94-6496-265-9

An electronic version of this dissertation is available at http://repository.tudelft.nl/. This dissertation was completed without the use of ChatGPT.

CONTENTS

SUMMARY

Optogenetics has revolutionized neuroscience in the last decade. In contrast to traditional electrode-based electrophysiology, optogenetics increases the throughput of targeted neurons by orders of magnitude. Genetically targeted populational neuron activities can thus be monitored and manipulated with high temporal and spatial resolution, thanks to joint efforts from both biological and optical sides. Optogenetics has become an attractive and reliable method for studying neuroscience problems.

In optogenetics, the most widely used protein to report action potentials (AP) is genetically encoded calcium indicators (GECI), which change the green fluorescence level when there is a calcium influx in the neuron. However, it is not a direct measure of membrane potential, which makes them incapable of reporting sub-threshold events. Moreover, they have slow kinetics that can not distinguish a single AP.

To truly report membrane voltage dynamics, genetically encoded voltage indicators (GEVIs) were developed. GEVIs use either voltage-sensing domains (VSD) or microbial rhodopsins to detect the change in membrane potential. This change is reflected through the fluorescence emission difference from the linked fluorescent proteins or the microbial rhodopsins themselves. GEVIs based on different scaffolds have evolved through several iterations to make them brighter and faster, and voltage imaging using GEVIs has provided insights into neuroscience problems *in vivo*. However, the performance is still quite limited: although the VSD-based GEVIs are bright, they require blue laser excitation for the fluorescent proteins. Because of this, they suffer more from scattering in deep tissue, and their transduction time from VSD to fluorescence emission limits the speed; The microbial rhodopsin based GEVIs show a sub-millisecond response. On the other side, the biggest issue is their orders of magnitude lower fluorescence. These drawbacks would result in a poor signal-to-noise ratio (SNR) of measured signals, which is discussed in Chapter 1.

The goal of my PhD is to develop better tools to increase the SNR of voltage imaging. This dissertation achieves this goal from different disciplinary perspectives: optical engineering, software development, and protein engineering through rational design and directed evolution.

Building a versatile multimodel microscope that minimizes noise is essential to all the development and different experiments down the line, and is, therefore, the first topic of this dissertation. There are several unique features in the design of this setup: It can transform between inverted and upright microscope configurations within a minute,

that accommodates both *in vitro* and *in vivo* experiments; It utilizes both continuous-wave (CW) lasers and tunable non-linear pulse laser as excitation source, which covers most of the application needs from in petri dish to deep in tissue; It employs both a point detecting device (photomultiplier tubes (PMT)) and an array detecting device (sCMOS camera), to select from; It integrates spatial and temporal patterning devices to achieve sub-millisecond and sub-micrometer patterning resolution. We named the final product Octoscope. In Chapter 2, we explain the concept and design of Octoscope and demonstrate its unique capabilities, namely multimodal imaging, automated objective reorientation, large-scale screening, and patterned illumination.

Good software is as important as a good piece of hardware. With this in mind, we developed the first advanced open-source software for voltage imaging, named gevidaq, to bring the Octoscope platform to a new level. It aims at smooth and efficient user interaction and provides comprehensive real-time feedback during experiments to facilitate quick parameter adjustment, which is an important aspect of electrophysiology. This software includes both the backend to interact with all kinds of devices as well as a user-friendly frontend. Because of its modular design, a user can assemble a task-specific panel with the recruited device modules with ease. gevidaq contains a data analysis module that includes a trained machine learning network to provide on-the-fly analysis to facilitate a close-loop optogenetics experiment. The design and implementation principles, together with various application examples, are shown in Chapter 3.

With this state-of-the-art infrastructure, we aim to advance voltage imaging from the other side of optogenetics: engineering proteins with better performance. We chose the microbial rhodopsin family as the template because of its ultra-fast kinetics suitable for neuron dynamics, huge protein engineering potentials, and, currently, a minimal amount of exploration. We started the discovery based on a novel rhodopsin family member, heliorhodopsin (HR), whose exact function is unknown. HR is so unique that it does not belong to the two existing rhodopsin families: type I and type II rhodopsins. The main feature is its inverted insertion direction in the membrane, meaning the N-terminal is at the cytoplasmic side. The organization around its retinal protonated Schiff-base (RPSB) cavity is larger and more complex than other rhodopsins, including those engineered as GEVIs. By performing voltage clamp on Octoscope under 532 nm illumination, we found that the wild-type (WT) is voltage sensitive and exhibits fast kinetics. As introduced in Chapter 1, the RPSB vicinity is crucial to the voltage sensing and spectra tuning; thus, we targeted its counterion and other color tuning sites in the retinal binding pocket and characterized their performance in Chapter 4. One retinal binding pocket mutant, S237A, shows increased fluorescence and much improved SNR in reporting voltage steps. We demonstrated that HR has the potential to serve as a GEVI and to be improved under future evolution.

Next, in Chapter 5, we move on to a proton pumping rhodopsin, *Gloeobacter violaceus* rhodopsin (GR). Both of the two major rhodopsins serving as GEVIs, Archaerhodopsin (Arch) and *Acetabularia acetabulum* (Ace), are proton pumping rhodopsins as well. In previous studies, GR shows higher fluorescence than Arch, and its mutant shows a wide range of spectra tuning, which makes it a promising template for GEVI engineering. The

wild-type characterization shows intriguing features: It exhibits large voltage sensitivity and fast kinetics, comparable to the latest Arch-based GEVI QuasAr6; It emits a significant amount of near-infrared fluorescence under red illumination; A large amplitude of photocurrent is present. Towards engineering a brighter and more sensitive GEVI, we performed a rational design approach based on our understanding of the mechanism and characterized around 40 mutants whose mutation sites spread along the whole protein. Three functional regions important for proton transfer were targeted: the retinal binding pocket, the proton donor, and the proton release complex. We found potential GEVI candidates with distinguishing features. One counterion mutant shows brighter fluorescence than QuasAr6 and fast kinetics. Combining it with a mutation in the proton release complex increases its voltage sensitivity several folds, making it more sensitive than QuasAr6 at the cost of slowed-down response. This property makes the mutant potential to become a generic GEVI. Mutations at the proton release sites result in mutants that exhibit the highest voltage sensitivity ever seen, reaching a $\Delta F/F_0$ of more than 170% per 100 mV. Due to the low baseline fluorescence and high sensitivity, the proton release mutant scores the highest SNR in the SNR comparison. One red-shift triple mutant shows strong near-infrared emissions around five times higher than QuasAr6. This might be useful when the proton budget in detection is the bottleneck. Besides these GEVI candidates, we also found another proton release mutant that shows exceptionally high photocurrent, making it a strong candidate for a red-shifted silencer. These results demonstrate that GR is an excellent protein engineering scaffold with a huge optogenetics application potential.

Optogenetics has moved towards a nonlinear two-photon (2P) excitation regime to look into the deeper depth of the brain. However, the one-photon performance of rhodopsin-based GEVIs does not translate to 2P, and little is known about the mechanism. To overcome the fact that rhodopsin-based GEVIs are not developed under 2P excitation and therefore perform poorly, we applied the directed evolution method to improve the brightness of an Arch-based GEVI. An automated cell screening and analysis pipeline was set up based on Octoscope, including the screening software and automated focusing algorithm. In a typical evolution round, a mutant library is generated through error-prone PCR, and HEK cells expressing this library are screened on Octoscope in both the 900 nm tag protein channel and 1200 nm Arch channel. The expression normalized brightness of each cell is ranked afterward through the algorithm powered by a machine learning segmentation network. When revisiting the top outliers, we picked them up through micropipettes and performed single-cell PCR to identify the mutations. We performed two rounds of evolution and increased the 2P brightness of QuasAr1 by 133% in total, as discussed in Chapter 6.

The conclusion of this dissertation is written in Chapter 7. The multi-disciplinary work in this dissertation yields novel tools for optogenetics: a multimodal microscope for *in vitro* and *in vivo* optogenetics, an advanced, open-source software for voltage imaging named gevidaq, several distinguishing GEVI and silencer candidates from HR and GR, and an Arch-based mutant with improved 2P brightness. An outlook on potential improvements and projects is written in section 7.2.

SAMENVATTING

Optogenetica heeft de neurowetenschap in het afgelopen decennium gerevolutioneerd. In tegenstelling tot traditionele op electrode-gebaseerde electrofysiologie wordt door middel van optogenetica de verwerkingssnelheid van geselecteerde neuronen sterk verhoogd. Genetisch geselecteerde neuron activiteiten kunnen hierdoor worden gecontroleerd en gemanipuleerd met een hoge temporele en ruimtelijke resolutie, dankzij gezamenlijke inspanningen vanuit zowel biologische als optische zijden. Optogenetica is een aantrekkelijke en betrouwbare methode geworden voor het bestuderen van neurowetenschappelijke dilemma's.

In optogenetica is het meest gebruikte proteïne om actiepotentialen (AP) te rapporteren genetisch gecodeerde calcium indicatoren (GECI), die het groene fluorescentieniveau veranderen wanneer er een calciuminflux in de neuron plaatsvindt. Het is echter geen directe meting van het membraanpotentieel, waardoor ze niet in staat zijn om gebeurtenissen te rapporteren die onder de grenswaarde liggen. Daarnaast beschikken ze over trage kinetiek die geen onderscheid kan maken tussen afzonderlijke AP's.

Om de dynamiek van membraanspanning echt nauwkeurig te rapporteren, zijn genetisch gecodeerde spanningsindicatoren (GEVI's) ontwikkeld. GEVI's maken gebruik van voltage-gevoelige domeinen (VSD) of microbe rhodopsines om de verandering in membraanpotentieel te detecteren. Deze verandering wordt weerspiegeld in het verschil in de fluorescerende emissie van de gekoppelde fluorescentieproteïnen of in de microbe rhodopsines zelf. GEVI's gebaseerd op verschillende structuren zijn door meerdere iteraties verder ontwikkeld om ze helderder en sneller te maken, en voltage-imaging met behulp van GEVI's heeft inzichten geboden in neurowetenschappelijke problemen *in vivo*. De prestaties zijn echter nog steeds vrij beperkt: hoewel VSD-gebaseerde GEVI's helder zijn, vereisen ze blauwe laserexcitatie voor de fluorescerende proteïnen. Hierdoor hebben ze meer last van verstrooiing in diep weefsel en wordt hun snelheid beperkt door hun transductietijd van VSD naar fluorescerende emissie; De op microbe rhodopsine gebaseerde GEVI's tonen een reactie van minder dan een milliseconde. Tegelijkertijd is het grootste probleem hun extreem lage fluorescentie. Deze nadelen zouden leiden tot een slechte signaal-ruisverhouding (SNR) van de gemeten signalen, en worden besproken in Hoofdstuk 1.

Het doel van mijn PhD is om betere instrumenten te ontwikkelen om de SNR van voltage-imaging te verhogen. Dit proefschrift bereikt dit doel vanuit verschillende disciplinaire perspectieven, namelijk optische engineering, softwareontwikkeling en proteïne engineering, door middel van rationeel ontwerp en gerichte evolutie.

Aangezien de ontwikkeling van een veelzijdig multimodelmicroscoop die ruis minimaliseert essentieel is voor alle ontwikkelingen en verscheidene experimenten in de toekomst, is dit het eerste onderwerp van dit proefschrift. Er zijn verschillende unieke kenmerken in het ontwerp van deze opstelling: het kan binnen een minuut veranderen tussen omgekeerde en rechtopstaande microscoop configuraties, wat zowel *in vitro* als *in vivo* experimenten mogelijk maakt; het maakt gebruik van zowel continue golflasers als instelbare niet-lineaire pulslasers als excitatiebron, die de meeste toepassingsbehoeften van petrischaal tot diep in het weefsel kan dekken; het maakt gebruik van zowel een punt detecterend apparaat (fotomultiplicatorbuizen (PMT)) als een array detecterend apparaat (sCMOS-camera) waaruit geselecteerd kan worden; het integreert ruimtelijke en temporele patroonapparaten om sub-milliseconde en sub-micrometer patroonresolutie te bereiken. Het eindproduct hebben we Octoscope genoemd. In Hoofdstuk 2 lichten we het concept en ontwerp van Octoscope toe en demonstreren we diens unieke mogelijkheden, namelijk multimodaal beeldvormen, geautomatiseerde heroriëntatie van het objectief, grootschalig screenen en gepatroneerde verlichting.

Goede software is net zo belangrijk als een goed stuk hardware. Met dit in gedachten hebben we de eerste geavanceerde open-source software voor voltage-imaging ontwikkeld, genaamd gevidaq, om het Octoscope-platform naar een nieuw niveau te tillen. Het richt zich op soepele en efficiënte gebruikersinteractie en biedt uitgebreide real-time feedback tijdens experimenten om snelle parameteraanpassing te vergemakkelijken, wat een belangrijk aspect is in elektrofysiologie. Deze software omvat zowel de backend om met verschillende soorten apparaten te communiceren als een gebruiksvriendelijke frontend. Door het modulaire ontwerp kan een gebruiker met gemak een taakspecifiek paneel samenstellen met de aangehaalde apparaatmodules. Gevidaq bevat een module voor gegevensanalyse met een getraind machine learning netwerk om on-the-fly analyses te bieden en een close-loop optogenetisch experiment te vergemakkelijken. De principes van het ontwerp en de implementatie worden samen met verschillende toepassingsvoorbeelden toegelicht in Hoofdstuk 3.

Met deze zeer vooruitstrevende infrastructuur streven we ernaar om voltage-imaging verder te ontwikkelen vanuit een ander perspectief dan optogenetica: het ontwikkelen van proteïnen met betere prestaties. We hebben gekozen voor de microbe rodopsinefamilie als sjabloon, vanwege hun ultrasnelle kinetiek die geschikt is voor neuronale dynamiek, de enorme mogelijkheden voor proteïne engineering en omdat dit gebied momenteel nog minimaal onderzocht is. We begonnen de ontdekking gebaseerd op een nieuw rodopsine familielid, heliorhodopsin (HR), waarvan de exacte functie onbekend is. HR is zo uniek dat het niet behoort tot de twee bestaande rhodopsinefamilies: type I en type II rhodopsinen. Het belangrijkste kenmerk is de omgekeerde inbrengrichting in het membraan, wat betekent dat de N-terminaal zich aan de cytoplasmatische zijde bevindt. De organisatie rondom de retinale geprotoneerde Schiff-basis (RPSB) holte is groter en complexer dan bij andere rodopsines, inclusief die ontworpen als GEVI's. Door een (voltage clamp) uit te voeren op Octoscope onder 532 nm verlichting, hebben we ontdekt dat de wild type (WT) gevoelig is voor spanning en snelle kinetiek vertoont. Zoals geïntroduceerd in Hoofdstuk 1 is de nabijheid van RPSB cruciaal voor de spanningswaarneming en spectra-afstemming. Om deze reden hebben we ons gericht op de

tegenion en andere kleurafstellingsplaatsen in de retinale bindingszak en hun prestaties gekarakteriseerd in Hoofdstuk 4. Een mutant van de retinale bindingszak, S237A, vertoont verhoogde fluorescentie en aanzienlijk verbeterde SNR bij het rapporteren van voltage stappen. We hebben aangetoond dat HR de potentie heeft om als GEVI te dienen en te verbeteren onder toekomstige evolutie.

In Hoofdstuk 5 gaan we verder met een proton pompende rhodopsine: *Gloeobacter violaceus* rhodopsine (GR). Beide belangrijke rhodopsines die dienen als GEVI's, Archaerhodopsine (Arch) en *Acetabularia acetabulum* (Ace), zijn eveneens proton pompende rhodopsines. In eerdere studies vertoont GR een hogere fluorescentie dan Arch en vertoont zijn mutant een breed scala aan spectrale afstemming, wat het tot een veelbelovend sjabloon maakt voor GEVI-engineering. De karakterisering van het wildtype demonstreert intrigerende kenmerken: het toont een grote gevoeligheid voor spanning en snelle kinetiek die vergelijkbaar is met de nieuwste Arch-gebaseerde GEVI QuasAr6; het geeft een aanzienlijke hoeveelheid nabij-infrarode fluorescentie af onder rood licht; er is een grote amplitude van fotostroom aanwezig. Om een helderdere en gevoeligere GEVI te ontwikkelen, voerden we een rational design approach uit op basis van ons begrip van het mechanisme. Ook karakteriseerden we ongeveer 40 mutanten waarvan de mutatiesites zich over het hele proteïne verspreidden. Drie functionele regio's die belangrijk zijn voor protonoverdracht zijn behandeld: de retinale bindingszak, de protondonor en het protonafgiftecomplex. Hierbij hebben we potentiële GEVI-kandidaten met onderscheidende kenmerken gevonden. Een tegenion mutant vertoont helderdere fluorescentie dan QuasAr6 en snelle kinetiek. Gecombineerd met een mutatie in het protonafgiftecomplex neemt de spanningsgevoeligheid ervan verschillende malen toe, waardoor het gevoeliger wordt dan QuasAr6, ten koste gaande van een vertraagde reactie. Deze eigenschap maakt de mutant potentieel tot een algemene GEVI. Mutaties op de protonafgifteplaatsen leiden tot mutanten die de hoogste gevoeligheid voor spanning ooit laten zien, met een ΔF / F_0 van meer dan 170% per 100 mV. Vanwege de lage basale fluorescentie en hoge gevoeligheid behaalt de protonafgiftmutant de hoogste SNR in de SNR-vergelijking. Een roodverschuivende drievoudige mutant vertoont sterke nabijinfrarode emissies die ongeveer vijf keer hoger zijn dan QuasAr6. Dit kan nuttig zijn wanneer het protonbudget in detectie de knelpunt is. Naast deze GEVI-kandidaten vonden we ook een andere protonafgiftmutant die uitzonderlijk hoge fotostroom vertoont, waardoor deze een sterke kandidaat is voor een roodverschoven silencer. Deze resultaten tonen aan dat GR een uitstekend proteïne engineering-raamwerk is met een enorm potentieel voor toepassingen in de optogenetica.

Optogenetica heeft zich verplaatst naar een niet-lineair tweefotonen (2P) excitatieregime om dieper in de hersenen te kunnen kijken. De eenfoton-prestaties van op rhodopsine gebaseerde GEVI's vertalen zich echter niet naar 2P en er is weinig bekend over het mechanisme. Om het feit te overwinnen dat op rhodopsine gebaseerde GEVI's niet zijn ontwikkeld onder 2P-excitatie en daarom slecht presteren, pasten we de methode van gerichte evolutie toe om de helderheid van een op Arch gebaseerde GEVI te verbeteren. Een geautomatiseerde cel screening- en analyse-pijplijn werd opgezet op basis van Octoscope, inclusief de screeningssoftware en geautomatiseerd scherpstelalgoritme. In een standaard evolutieronde wordt een mutantbibliotheek gegenereerd via

foutgevoelige PCR. Daarnaast worden HEK-cellen die deze bibliotheek tot expressie brengen gescreend op Octoscope in zowel het 900 nm tag proteïnekanaal als het 1200 nm Arch-kanaal. De genormaliseerde helderheid van elke cel wordt achteraf gerangschikt door het algoritme, aangedreven door een machine learning-segmentatienetwerk. Bij het opnieuw bestuderen van de topuitschieters, hebben we deze opgepikt met micropipetten en vervolgens single-cell PCR uitgevoerd om de mutaties te identificeren. We hebben in totaal twee evolutierondes uitgevoerd en de 2P-helderheid van QuasAr1 in totaal met 133% verhoogd, zoals besproken in Hoofdstuk 6.

De conclusie van dit proefschrift is geschreven in Hoofdstuk 7. Het multidisciplinaire werk in dit proefschrift levert nieuwe tools op voor optogenetica: een multimodale microscoop voor *in vitro* en *in vivo* optogenetica, geavanceerde open-source software voor voltage imaging genaamd gevidaq, verschillende onderscheidende GEVI- en silencerkandidaten van HR en GR, en een op Arch gebaseerde mutant met verbeterde 2P-helderheid. Een vooruitblik op mogelijke verbeteringen en projecten is geschreven in sectie 7.2.

1

INTRODUCTION

Voltage imaging using genetically encoded voltage indicators (GEVIs) has taken the field of neuroscience by storm in the past decade. Its ability to create subcellular and network level readouts of electrical dynamics depends critically on the response kinetics to the voltage of the indicator used. Engineered microbial rhodopsins form a GEVI subclass known for their high voltage sensitivity and fast response kinetics. In this chapter, we review the essential aspects of microbial rhodopsin photocycles that are critical to understanding the mechanisms of voltage sensitivity in these proteins and link them to insights from efforts to create faster, brighter, and more sensitive microbial rhodopsin-based GEVIs. The motivation and outline of this dissertation are introduced at the end of this chapter.

1

1.1. FROM GREEN ALGAE TO RHODOPSIN-BASED VOLTAGE INDICATORS

WHERE there is light, there are green algae (on earth). Green algae are one of the most vital producers of food and diverse bioactive compounds for marine life[1]. Their photosynthesis ability makes them indispensable for the biological chain everywhere on Earth.

Many organisms, including green algae, have developed photoreceptor proteins to help them adapt to the environment. These light-sensing proteins utilize different chromophores (including retinal, bilin, and flavin) to transduce incoming photons into mechanical energy[2, 3]. Rhodopsins are one such superfamily of retinal binding proteins, which are ubiquitous to all domains of life[4]. These proteins covalently bind a molecule of retinal, which is an aldehyde of vitamin-A derived from β-carotene[4, 5]. The retinal chromophore absorbs a photon and undergoes isomerization in the protein environment[5]. This primary phototransduction event triggers distinct protein conformational changes leading to diverse functions ranging from ion transport to signal transduction.

Rhodopsins are divided into two distinct families based on phylogeny: type I (microbial rhodopsins) and type II (animal rhodopsins)[5, 6]. Type I or microbial rhodopsins use all-*trans* retinal as a chromophore to drive ion translocation or photosensory functions in several microbial species spanning Eukaryotes, Bacteria, and Archaea. Type II or animal rhodopsins form a specialized class of G-protein coupled receptors using 11-*cis* retinal as a chromophore and are responsible for visual and non-visual phototransduction in vertebrates and invertebrates. Despite having almost no sequence homology, both animal and microbial rhodopsins share the same overall protein architecture of seven transmembrane α-helices (called the "opsin"), which binds retinal[4, 5]. The emergence of myriad functions and an expansive phylogeny from this common and relatively simple protein scaffold is nothing short of a spectacular feat of evolution. This is particularly stark for microbial rhodopsins, whose functions range from light-driven ion pumps or channels, and phototaxis receptors to photoactivatable enzymes in several terrestrial and aquatic ecosystems. They play a key role in the survival and adaptation of their host microbes and can even exhibit spectral tuning to light availability in local microenvironments[7]. This supports the notion that microbial rhodopsins are essential to maintaining phototrophic energy balance in several biomes[8]. Recent advances in metagenomics have led to an explosion of discoveries of microbial rhodopsins in previously unexplored ecological niches. Their phylogenetic tree is continuously being expanded, with novel members with unknown functions being reported with some regularity[9].

The incredible versatility of microbial rhodopsins has made them a tantalizing bioengineering platform. One of the greatest scientific revolutions of the last twenty years is

Part of this Chapter has been published as: Xin Meng*, Srividya Ganapathy*, Lars van Roemburg, Marco Post, and Daan Brinks. "Voltage Imaging with Engineered Proton-Pumping Rhodopsins: Insights from the Proton Transfer Pathway." *ACS Physical Chemistry Au* (2023). *ACS editor's choice* and front cover of the issue.

the birth of optogenetics[10]. A microbial rhodopsin termed Channelrhodopsin, a cation channel responsible for the phototaxis of green algae, was successfully applied as a light-gated actuator upon transgenic expression in mammalian neurons in 2005[11]. From this point onwards, the application of microbial rhodopsins has revolutionized neuroscience and influenced how we perturb, visualize, engineer, experiment on, and think about the brain. Besides being used as actuators, proton-pumping microbial rhodo psins were engineered to report changes in membrane potential through their voltage-modulated fluorescence[12]. This led to major advances in Voltage Imaging: visualizing cellular electrical dynamics in 3D and 4D fluorescence movies. The ability to directly transduce electrical dynamics into fluorescence sets genetically encoded voltage indicators (GEVIs) apart from genetically encoded calcium indicators (GECIs), which indirectly monitor neuron activity only through calcium influx[13, 14]. Within the broader palette of GEVIs, different protein configurations have been used to convert changes in voltage into changes in fluorescence. These include voltage and pH-sensitive ion channels or pumps containing a native chromophore or voltage-sensing domains (VSDs) from voltage-gated ion channels fused to fluorescent proteins (FPs). Despite their generally low fluorescence quantum yield, GEVIs based on proton-pumping microbial rhodopsins show faster response kinetics and the highest sensitivity to voltage changes, offsetting the higher brightness of VSD-FP sensors[15–20]. Efforts to create the next generation of GEVIs with improved brightness, faster kinetics, and higher voltage sensitivity have spawned a vibrant community of molecular biologists, protein engineers, physicists, and neuroscientists working on engineering microbial rhodopsins.

The native function of microbial rhodopsins is typically described in terms of a photocycle: absorption of a photon starts a process converting the absorbed energy into a sequence of mechanical actions, typically isomerization of the retinal chromophore and subsequent conformational changes of the embedding protein, which for instance leads to transport of an ion through the protein. Each of these changes can be described as a transition out of and into an intermediate state of the protein: the structural features of each intermediate state are intimately linked to the lifetime of the state, its spectral properties (absorption spectrum, fluorescence, and quantum yield) and the kind of perturbations it is sensitive to (for instance, application of a voltage across the protein), which can lead to modification of the photocycle. Linking the mechanics and electromagnetic properties of the intermediate states is, therefore, necessary to understand the intrinsic ion translocation mechanism, the origin of the voltage-sensitive fluorescence, and the influence of protein and electrostatic modifications on both properties in microbial rhodopsins. This knowledge, in turn, informs our ability to improve the properties of microbial rhodopsin-based GEVIs. The first mutations in very early rhodopsin-based GEVIs, namely the bacterial Proteorhodopsin and the archaeal Archaerhodopsin3, were meant to break the proton transfer pathway[12]; subsequent mutations were added to improve kinetics and state transitions towards more fluorescent states.

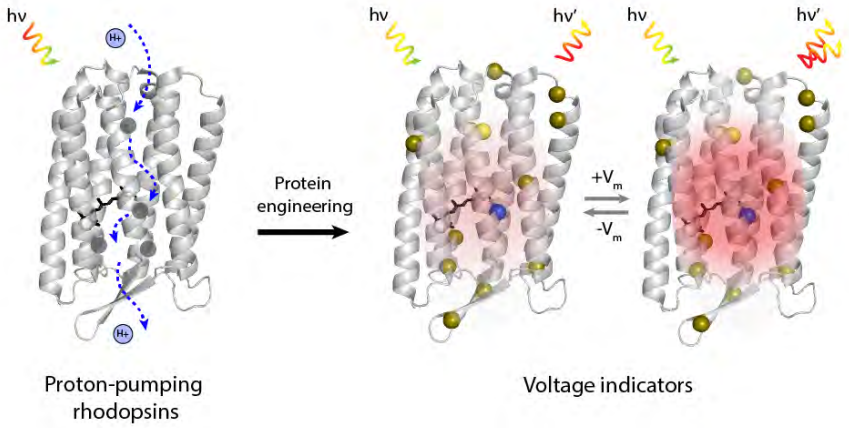

Figure 1.1: Through protein engineering, microbial rhodopsins can function as a membrane voltage indicator. Microbial rhodopsin has more than 7000 photochemically reactive family members with a great diversity in functions, including proton pumps[21]. Through protein engineering approaches, like rational design and directed evolution, they can serve as voltage indicators that change the emitted fluorescence intensity at different membrane potentials in neurons.

Engineering rhodopsins to function as optimized GEVIs is the main goal of my PhD. To provide a piece of comprehensive background knowledge for this thesis, the ion translocation mechanism (with proton transfer in Bacteriorhodopsin as an example), its impact on fluorescence, how it can be engineered, and how it influences GEVI voltage sensitivity will be introduced in the following sections.

1.2. PROTON TRANSFER IN BACTERIORHODOPSIN

For a detailed discussion of the mechanism of proton transport in microbial rhodopsins, we use the well-characterized bacteriorhodopsin (BR) as a model system. BR was discovered in the purple membrane of the halophilic archaea Halobacterium salinarum in 1970 and has since been extensively characterized, making it the best understood of all microbial rhodopsins[4].

All-*trans* retinal is covalently bound to a lysine residue (Lys 216 in BR) on the helix G through a Schiff Base linkage, and this Retinylidene Schiff Base (RSB) is normally protonated (RSBH+)[4]. In the dark, the all-*trans* RSBH+ usually exists in equilibrium with the 13-*cis* isomer (50:50 for BR), where steady-state illumination leads to a uniform all-*trans* population[6, 22]. In the ground state, BR displays a maximum absorbance λ_{max} of ~570

nm. After absorbing a photon, the RSBH+ enters the Franck-Condon S_1 state (H), from which several pathways are open to it: another absorption event can excite it into the Franck-Condon S_n state[23, 24]; it can decay into the excited state intermediate I_{460} and from there decay back to the ground S_0 state through spontaneous emission (see next section) and non-radiative relaxation without further reaction; it can enter the reactive state from I_{460} characterized by photoisomerization at the C13=C14 double bond[4, 25]. A general potential energy diagram of these reactions is shown in Figure 1.2. The all-*trans* to 13-*cis* isomerization triggers a photochemical cycle containing a sequence of intermediate states, ultimately resulting in proton transfer(Figure 1.3)[21, 26–28]. These photointermediates can be distinguished and characterized by time-resolved spectroscopic and structure-based crystallographic methods[26–31].

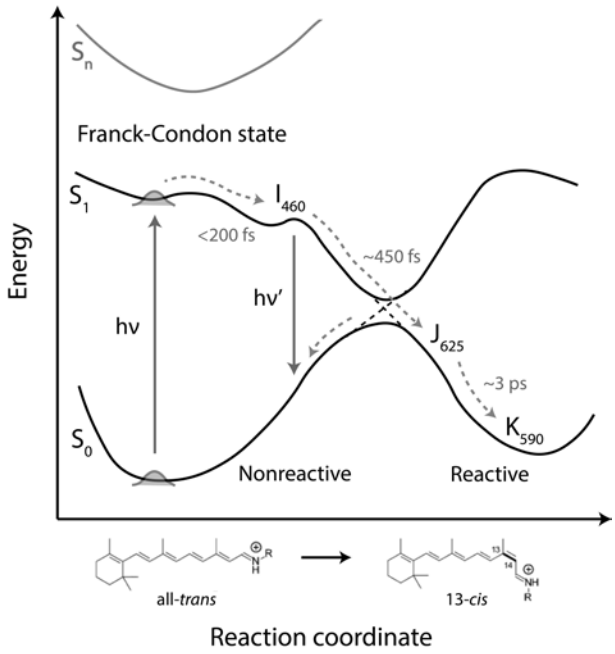

Figure 1.2: Potential energy diagram of the isomerization reaction of retinal in BR. Light absorption brings retinal into the Franck-Condon state from the ground state S_0. From the excited state S_1, the higher excited state S_n can be reached through a multiphoton process. After several hundred femtoseconds, a fraction of the molecules will decay back to the S_0 through nonreactive fluorescence emission; the others will go through the photocycle resulting in the translocation of a proton.

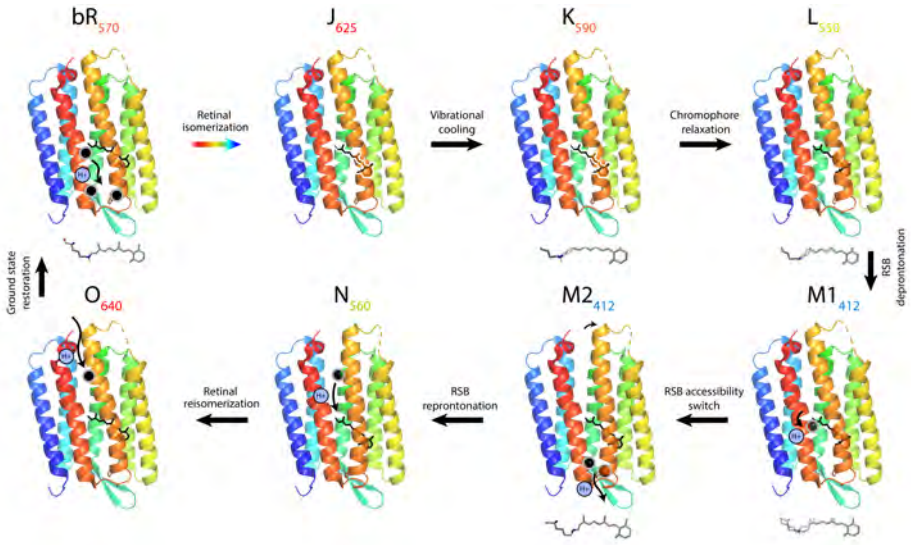

Figure 1.3: Illustration of the bacteriorhodopsin photocycle (PDB ID: 1C3W). L to M_1: proton transfer from RSBH+ to Asp85; M_1 to M_2: proton release from the proton release complex involving Glu194 and Glu204; M_2 to N: reprotonation of RSB from Asp96; N to O: reprotonation of Asp96 from the cytoplastic medium; O to bR: proton transfer from Asp85 to the proton release group. The maximum absorbance wavelength of each intermediate is labeled in numbers. The key residues involved in the transition are marked in black.

The transitions involved in photoisomerization (I ⇒ J ⇒ K) occur in the sub-ps to the ps regime and have been mapped using ultrafast spectroscopy and, more recently, in detail by time-resolved serial femtosecond crystallography[32]. Relaxation of the Franck-Condon to the reactive S_1 state occurs within 100 to 200 fs (reported values vary depending on measurements performed and their conditions), forming the blue-shifted electronically excited I_{460} intermediate, where the retinal is still all-*trans*[33, 34]. This state decays via the conical intersection and forms a vibrationally hot J intermediate in ~450 fs, resulting in the all-*trans* to 13-*cis* isomerization (Figure 1.2)[35, 36]. The J state is characterized by a twisted 13-*cis* RSBH+ geometry with a λ_{max} of 625 nm[33, 37]. The transition to the K intermediate occurs in 3 ps along with a spectral shift from 625 nm to 590 nm [38–40] due to vibrational cooling and conformational relaxation of the chromophore (Figure 1.3)[41, 42]. The Raman spectrum of the K-state has a strong 13-*cis* chromophore fingerprint, indicating that the all-*trans* to 13-*cis* isomerization is complete[42, 43]. Compared to the highly twisted J intermediate, the K intermediate is characterized by a more planar retinal chromophore[42]. After ~70 ps, the protein-retinal complex undergoes further relaxation identified by Raman spectroscopy and renewed hydrogen out-of-plane (HOOP) intensity[29, 42]. This state, termed the KL intermediate, leads to a stronger hydrogen bond association between the RSBH+ and the proton

acceptor Asp85[21, 42].

The L intermediate forms within ~1.5 μs and is spectrally close to the K intermediate[44]. FTIR spectroscopy indicates that the KL to L transition involves structural relaxation of the Schiff base and the β-ionone region of retinal with different kinetics[29, 44]. During the transition from K to KL to L, the distorted chromophore relaxes, and the energy this release is utilized for rearrangement of the protein environmente[44–46]. These perturbations help overturn the proton affinity between RSBH+ (high) and Asp85 (low), facilitating the proton transfer to Asp85 during the subsequent transition from L to M intermediate[4, 29, 47, 48]. Rearrangement of the hydrogen bonding network involving the three water molecules in the cavity facilitates deprotonation of the RSBH+[49–51]. Water402, in particular, plays an important role here since it interacts directly with RSBH+, and the counterions Asp85 and Asp212 (Figure 1.4)[50, 51]. In the L intermediate, the hydrogen bonds between Water402 and Asp85, and between Water402 and the N-H group from RSBH+, are strengthened[26, 50]. This lowers the pK_a of RSBH+, destabilizes the RSB proton and maintains the negative charge at Asp85, which facilitates the deprotonation process[44, 50, 51].

This transfer happens in around 10-40 µs as confirmed by FTIR[26, 52]. Water402 potentially switches its hydrogen bond from Asp85 to Asp212 during the L to M transition and improves the deprotonation efficiency[51].

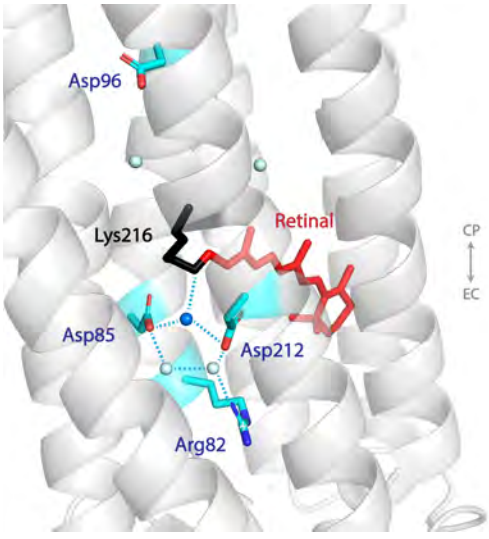

Figure 1.4: The structure of the RSB region in BR (PDB: 1C3W). The retinal chromophore is linked to the helix through Lys216. Three water molecules (water402 in blue, water401, and water406) are found between the RSB and the proton acceptor Asp85. Potential hydrogen bonds are shown in dashed lines. Cytoplasmic side (CP) and extracellular side (EC) directions are marked in light grey in Figure 1.4 to 1.7.

The proton transition to Asp85 marks the formation of the M intermediate, which is characterized by the deprotonated chromophore with a blue-shifted λ_{max} at ~400 nm (Figure 1.3)[53]. Upon decay of the M intermediate, the RSB is reprotonated by the proton donor Asp96 situated 10 Å away on the cytoplasmic side[4, 26, 29]. The defining feature of the M state is a switch in the accessibility of the RSB from the extracellular to the cytoplasmic part of the protein, breaking extracellular access and ensuring vectorial proton pumping. This switch is facilitated by a structural change in the RSB and movement of the protein helices F, and G[54–59]. Proton transfer from the RSB to Asp85 breaks its electrostatic interactions with the extracellular facing residues leading to a distortion in the chromophore. From X-ray crystallography, it was shown that deprotonation leads to an unbending of retinal due to a decrease in its intrinsic curvature[58, 60]. A complementary view has been provided by magnetic resonance studies, where breaking the 'electrostatic yoke' holding the RSB, Asp85, and the surrounding hydrogen-bonded network leads to a release in torsion of the RSB[59, 60]. Concomitantly, an outward tilt of the helix F and movement in the cytoplasmic end of helix G together shape a cytoplasmically open state that facilitates efficient reprotonation of the SB[59, 61–65]. It is likely that these changes occur in a sequential way, i.e. that the distortions in the RSB trigger its rearrangement towards the cytoplasm[58, 66].

This accessibility switch was discovered in the late 90s and has since been incorporated in the photocycle as the transition event from the M_1 to the M_2 intermediate (Figure 1.3)[55]. The M_2 to M_1 back reaction rate was found to increase with increasing proton concentration[55]. The M_2 intermediate accumulates at higher hydration levels than M_1, and the associated conformational change is reversed at the end of the photocycle[66].

A putative proton release group is responsible for releasing the proton into the extracellular medium during the M state, as Asp85 stays protonated until the end of the photocycle[4, 26, 55, 67]. The exact identity of this proton release group is unknown, though it likely involves a water cluster containing one proton, five water molecules and several residues, including Glu204, Glu194, and Arg82 (Figure 1.5)[26, 67, 68]. The protonation status of this group was found to be coupled to that of the counterion Asp85[69–71]. When the counterion is protonated, the pK_a of the proton release group is low (~5) resembling dissociation; when the counterion is anionic, the pK_a of the release group is high (~9.2) indicating that Asp85 protonation leads to extracellular proton release[26, 67]. During the transition from M_1 to the M_2, protonation of Asp85 displaces the Arg82 side-chain towards Glu194 and Glu204, which stabilizes a fluctuating excess proton in the release site[72, 73]. The approaching Arg82 breaks this balance, thereby releasing the proton extracellularly[68]. This early extracellular proton release is a key event in proton transfer, as the coupled rise in pK_a of Asp85 prevents back-transfer to the RSB, ensuring the M_1 to the M_2 directionality[67].

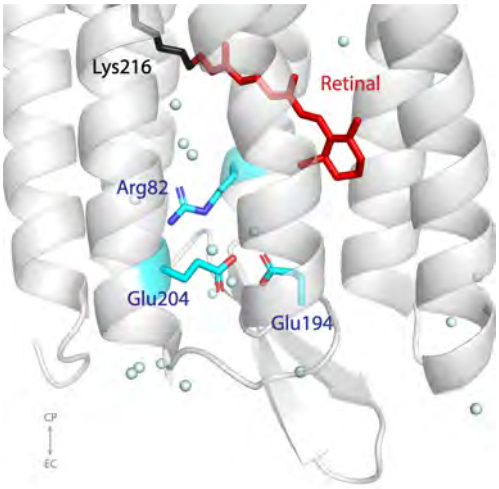

Figure 1.5: The structure of the proton release region in BR. Multiple side chains and water molecules are involved in the proton release process. The key residues, Glu194, Glu204, and Arg82, are illustrated here.

The formation of the subsequent N intermediate occurs in around ~5 ms[4, 64], and is accompanied by proton transfer from the donor Asp96 to the RSB. The structural changes involved in the transition from M_1 to the M_2 to N (e.g. the outward tilt of helix F) allows water to enter the RSB vicinity forming the cytoplasmic proton transfer water cluster[26, 30, 74, 75]. The crystal structure of the accumulated N state displayed a continuous chain of single-file hydrogen-bonded water molecules connecting Asp96 and RSB, serving as the proton conducting pathway[74, 76, 77]. The actual time required to complete this movement (ms) is six orders of magnitude longer than in theory (ns) because of the slow kinetics of prerequisite conformational changes and deprotonation of Asp96[26, 76, 78, 79].

The reprotonation of Asp96 is accompanied by thermal reisomerization of retinal back to all-*trans* upon the decay of the N intermediate and start of the O intermediate[26, 80]. Protons are taken up from the cytoplasmic surface to protonate Asp96 during this transition[27]. The reisomerization of retinal and reprotonation of Asp96 is thought to be coupled by turning off the RSB N–H bond, which collapses the water chain connecting RSB and Asp96, leading to an increased proton affinity of Asp96[27, 81]. The exact mechanism of Asp96 reprotonation is unknown, though it is hypothesized that a group of cytoplasmic residues (Asp36, Asp38, Asp102, Asp104 and Glu166) attract protons through the narrow tunnel towards Asp96, which becomes wider, during the movement of helix F (Figure 1.6)[82–85].

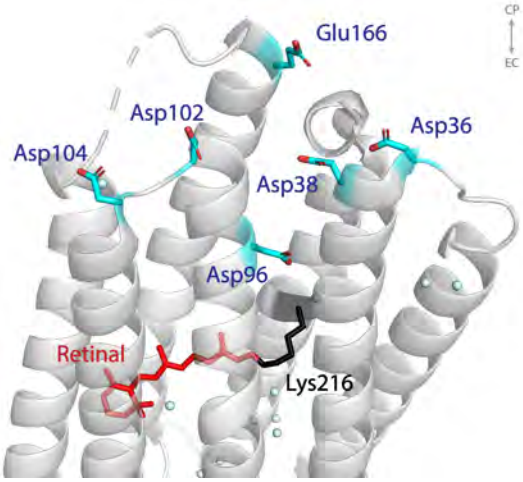

Figure 1.6: The structure of the proton uptake region in BR. Multiple residues, including Asp36, Asp38, Asp102, Asp104, and Glu166, are likely to be involved in the reprotonation process of the proton donor Asp96 during the photocycle.

Resonance Raman spectra of the O intermediate display intense HOOP vibrations arising from distortions in the all-*trans* chromophore relative to its ground state (Figure 1.3)[80]. The decay of O to ground state is the last step of the photocycle, which is characterized by reprotonation of the extracellular proton release group by Asp85[26, 86]. Due to the difficulty in resolving the structure and kinetics of the O intermediate, the mechanism of this long-distance transfer is still unknown[87, 88]. The driving force is thought to be the difference in pK_a between Asp85 and the proton release group in the initial state[26, 89]. It is suggested that Asp212 belongs to the Asp85-to-proton-release-group proton transfer pathway and that Arg82, Glu194 and Glu204 participate in this transfer (Figure 1.5)[67, 89–91]. At the end of the O intermediate, the protein and the retinal are restored to the initial ground state completing the photocycle.

1.3. THE ORIGIN OF FLUORESCENCE

Microbial rhodopsins are weakly fluorescent in their dark state due to spontaneous emission of the RPSB. After photoexcitation and relaxation from the Franck-Condon state, the RPSB can enter the non-reactive S_1 state, emitting a photon relaxing back to the ground S_0. The quantum yield (QY) of fluorescence is low (in the order of 1×10^{-4} to 1×10^{-5} for BR) since the RPSB is optimized to favor the photochemical reaction cycle, thereby leading to a high QY of photoisomerization (0.64 for BR)[92–96]. This is consistent with a short excited state lifetime of ~0.5 ps[35, 39]. Early experiments on BR showed near infra-red fluorescence extending from 600-900 nm with a maximum at ~740 nm and strong pH dependence[92]. Its emission band was found to be composite with contribu-

tions from photointermediate fluorescent states, in addition to spontaneous emission (BR568). These were determined to be the O intermediate and another highly fluorescent intermediate termed "Q", which arise from the sequential absorption of 2 or 3 photons. Both O and Q have distinct decay kinetics (9 and 62 ps, respectively), and their relative contribution towards fluorescence was shown to be dependent on the excitation power and pH[97, 98].

The red-shifted O intermediate is characterized by an all-*trans* chromophore and protonated counterion. Fluorescence from O was found to be pH dependent with the fluorescence lifetime and QY decreasing with an increase in pH[97, 99]. On the other hand, the Q inter-mediate is formed upon photoexcitation of the non-fluorescent N- intermediate, which is stabilized under alkaline conditions[97]. The quantum yield of Q is ~100 times more than BR568[99]. It has a red-shifted absorption like O, and its fluorescence lifetime is relatively insensitive to pH[99]. In fact, pH shifts the equilibrium between the N (branching to Q) and the O states, and, therefore, the emerging fluorescence[99]. The isomerization state of Q is likely to be all-*trans* since it is formed by photoexcitation of the 13-*cis* N state[98, 100]. The accumulation of prefluorescent N can also be influenced in the preceding transition from M to N, which are both still within the 13-*cis* manifold. Optoelectric studies in BR showed that the ratio of M_1/M_2 intermediates and M_2 decay were also found to be influenced by the electrochemical gradient[101, 102]. Here, the membrane potential is likely to impact the reprotonation of the RSB by D96, as the D96N mutant shows a slowing down of M decay[78]. Interestingly, in BR(D96N), illumination with blue/violet light leads to isomerization from the 13-*cis* M to an all-*trans* O-like state short-circuiting the photocyle[103, 104]. This type of optical switching between photostable all-*trans* and 13-*cis* intermediates has been reported in several other rhodopsins and is discussed in further detail in the next section with respect to voltage-sensitive fluorescence[105–107].

The above studies in BR indicate that higher fluorescence is a property of the RPSB with a protonated counterion. This is supported by the longer excited state lifetimes of the BR upon acidification or neutralization of the counterion in the mutant D85N[108, 109]. Recently, a highly fluorescent rhodopsin termed Neorhodopsin (NeoR) was identified with a long excited state lifetime resulting in higher fluorescence Q[107]. NeoR has three Asp/Glu residues, the neutralization of which leads to a sequential increase in QY and red-shifted absorbance band. Extrusion of water molecules from the active site is likely to contribute towards this process. NeoR was also found to cycle between a blue-shifted M-like state and a red-shifted state with a deprotonated chromophore similar to BR[107].

The photointermediate fluorescence of BR was recapitulated in several studies done on variants of Archaerhodopsin-3 (Arch3) from Halorubrum sodomense, which is widely used as a GEVI[19]. The studies on highly fluorescent Arch3 variants indicate that the protein modifications may favor an all-*trans* O-like ground state (which is distinct from the ground state generated during protein biosynthesis) with a protonated RSB and a neutral Schiff base counterion. These studies are further explored in the next section.

1

1.4. THE ORIGIN OF VOLTAGE SENSITIVITY

Investigations of the mechanism of Arch3 voltage sensitivity were carried out shortly after its application as GEVI[110]. Arch3 fluorescence was also thought to arise from a photointermediate, since the high illumination intensities typically used to image Arch3 fluorescence should deplete the ground state. Using pump-probe spectroscopy, Arch3 fluorescence was found to arise from a three-photon process (similar to BR): the first photon initializes the photocycle, the second blue-shifted photon is absorbed by the N-state branching the photocycle to Q, and the third photon excites fluorescence from the Q-state[110]. Through concurrent patch clamp and fluorescence experiments, it was confirmed that the voltage-sensitive fluorescence likely comes from a photointermediate with a long lifetime[110]. It was hypothesized that the membrane potential tunes the equilibrium between the M and N state by affecting the RSB reprotonation efficiency from the proton donor D106 (Figure 1.7[110]; equivalent to Asp96 in BR).

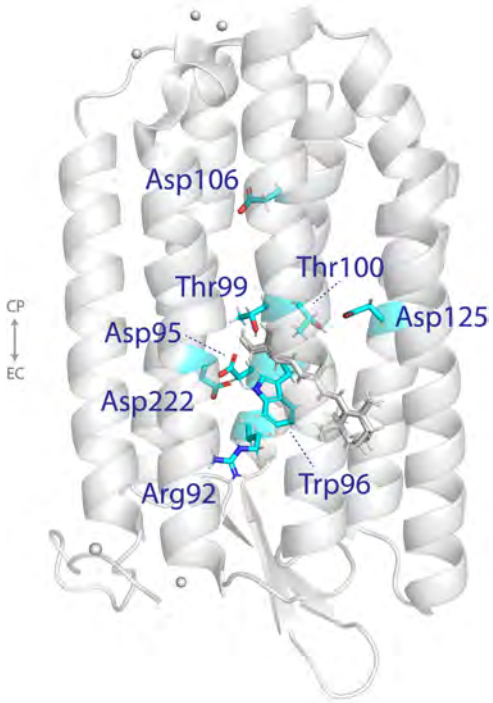

Figure 1.7: Key residues identified for the voltage sensing in Arch3 and Archon1 (PDB: 6GUZ).

Near-IR resonance Raman confocal microscopy studies on Arch3 (D95N) (Figure 1.7; Asp95 is equivalent to the proton acceptor Asp85 in BR) demonstrated that an all-*trans* O-like intermediate predominates at neutral pH. At pH higher than 7, an N-like species

is formed upon excitation of the O-like intermediate[111]. Arch3(D95N) accumulates 13-*cis* N-like species under red illumination, and voltage possibly influences the RSB protonation and, therefore, the equilibrium between M and N[111]. Combining ultraviolet–visible (UV-Vis) absorption, fluorescence, and FT-Raman spectroscopy, two Arch3 derivatives, QuasAr2 and NovArch, were found to be able to cycle between O-like and M-like states using 660 nm and 405 nm illumination[112]. The proton donor mutation D106H was thought to be responsible for the accumulation of the M-like state under red light, as lacking a proton donor to RSB inhibits the M to N transition[112].

Recently a detailed characterization combining experiments and molecular dynamics (MD) simulations on Arch3 and its derivatives QuasAr1, QuasAr2, and Archon1 (described in further detail below) showed different mechanisms of generating voltage-sensitive fluorescence[113]. Steady-state UV–Vis and time-resolved pump-probe spectroscopy on QuasAr1 and QuasAr2 showed that they have orders of magnitude extended excited state lifetimes (4~40 ps) compared to Arch3 and that only a small fraction of the chromophores (4% for QuasAr2 and 1% for QuasAr1) undergo heterogeneous isomerization[113]. In another Arch3 derivative, Archon1, the excited-state lifetime is even longer (around 70 ps) with 0.1% isomerization efficiency. These observations further strengthened the conclusion that neutralizing the counterion prolongs the excited-state lifetime and increases the fluorescence[113]. To further investigate the origin of voltage sensitivity, atomistic MD simulations were carried out based on a homology model of Arch3. From the simulations, the application of a voltage across Arch3 triggers a reorientation of R92 (equivalent to R82 in BR), which in turn leads to a reorganization of the hydrogen-bonded network[113]. Thus, at higher voltage, water molecules were prohibited from entering the RSBH+ vicinity, and a new hydrogen bond involving Asp95 was established. Both the lack of water molecules near RSBH+ and the formation of a separate hydrogen bond involving D95 disfavor the RSBH+ deprotonation[113]. In contrast, in Archon1, the crucial voltage-induced reorientation was found to be the intracellular residue D125. Movement of the protein scaffold at positive voltage removes the D125-T100 hydrogen bond and forms Q95-T99 and T100-W96 hydrogen bonds (Figure 1.7). This rearrangement creates a more rigid chromophore environment and strengthens the RSBH+ D222 hydrogen bond. Although the exact mechanism of voltage sensitivity is still unclear, the studies in Arch3 indicate that the membrane potential tunes the equilibrium in the protonation status of RSB and its counterion via reorganization of the hydrogen bonding network[113].

1.5. ENGINEERING OPSIN-BASED GENETICALLY ENCODED VOLTAGE INDICATORS

In the last decade, microbial rhodopsin-based GEVIs have evolved remarkably, in parallel with efforts to understand their mechanisms of voltage sensitivity. Both evolutionary approaches and targeted mutagenesis approaches have led to significant results, which we review in the next section.

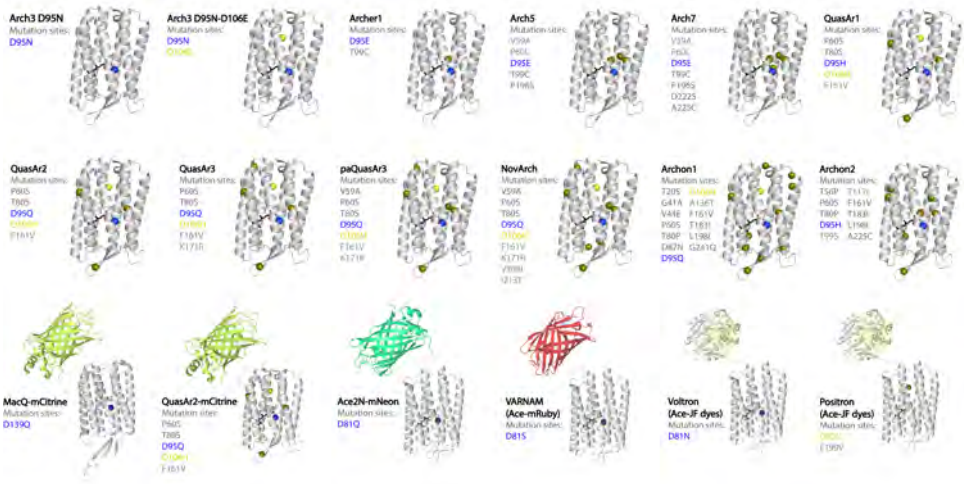

Figure 1.8: Illustration of mutation sites of rhodopsin-based GEVIs compared to the wild-types. Mutations at the counterion are highlighted in blue, and mutations at the proton donor are highlighted in light yellow; mutations at the other sites are shown as dark yellow spheres in the structure illustration.

The first microbial rhodopsin-based GEVI, termed PROPS, was based on the bacterial proteorhodopsin (GPR) as a starting scaffold. GPR was mutated at the counterion Asp97 for pH-modulated fluorescence, and the mutant revealed electrical spiking in E. coli[12, 114]. Despite the decent voltage sensitivity (ΔF / F_0 = 150% per 100mV) and speed, PROPS shows poor membrane expression in mammalian cells[12, 19]. Further screening of microbial rhodopsins that localize well to the eukaryotic membrane led to the application of Arch3[19, 115]. Arch3 was first introduced as an optical silencer allowing significant firing rate suppression within milliseconds[115].

It was later discovered that Arch3 showed fast fluorescence changes modulated by membrane potential upon expression in HEK293 cells[19]. To eliminate the photocurrent measured under standard neural imaging illumination (10 pA, I = 1800 W cm^{-2}), the Arch3 counterion D95 was mutated to an uncharged Asn, analogous to studies on BR (Figure 1.8)[19, 116]. The resulting mutant, Arch3(D95N) has no photocurrent, shows lower RSB pK_a and displays 50% greater sensitivity (ΔF / F_0 = 60% per 100 mV) at the cost of slower kinetics (41 ms)[19].

Through rational site-directed mutagenesis based on Arch3(D95N), the double-mutants Arch3(D95N/D106E) and Arch3(D95Q/D106E) were found to exhibit an improved response speed[117]. The extra mutation on the proton donor D106 was thought to alter the RSB protonation and deprotonation kinetics[117].

A major drawback of the Arch3 sensors is their extremely low quantum yield. Although

the red-shifted excitation wavelength is favorable for deep tissue imaging, it requires high illumination intensities, which is not suitable for in vivo applications[118]. The main goal in the evolution of Arch3 was therefore improving its brightness. The red-shifted Arch3(D95E/T99C) was used as a template for directed evolution[119]. As a powerful way to engineer protein properties, directed evolution uses random mutagenesis to generate a pool of mutant libraries and iterative selection is applied to direct the library performance. Through evolutionary screens, three individual mutations (V59A, P60L, and P196S) were found to improve the brightness[120]. Combining with site-saturation mutagenesis, two mutants, termed Arch5 (V59A/P60L/D95E/T99C/P196S) and Arch7 (V59A/P60L/D95E/T99C/P196S/D222S/A225C) exhibit around 20-fold increase in brightness compared to Arch3 (Figure 1.8)[120]. This study demonstrated that mutations at other sites besides the counterion could influence the fluorescence quantum yield[108, 120]. Arch3(D95E/T99C) and Arch3(D95E/T99C/A225M) were then characterized in primary neuronal cultures and applied to track sensory neurons in C. elegans, and named Archer1 and Archer2, respectively[118]. Both, however, still show a steady photocurrent of 10 pA under 880 $\mathrm{mW\,mm^{-2}}$ illumination[118].

The first Arch3-based GEVIs that found successful applications in neuroscience were engineered using Arch3(D95N) as a template, where several rounds of directed evolution yielded two non-proton pumping variants. QuasAr1 (mutation sites compared to Arch3 P60S/ T80S/D95H/D106H/F161V) and QuasAr2 (H95Q compared to QuasAr1; Figure 1.8) showed the best performance in terms of brightness, voltage sensitivity and kinetics respectively (15 times and 3.3 times brighter than Arch3, 32% and 90% ΔF / F_0 per 100 mV, 0.053 ms and 1.2 ms response fast time constant)[121]. The first five screening iterations resulted in four extra mutation sites (P60S, T80S, D95N, D106Y, and F161V), with T80 and F161 lying at the periphery of the protein[121]. This was followed by a full investigation focusing on the D95 and D106 to further tune the voltage sensitivity and kinetics, leading to the substitutions N95H and Y106H[121]. Combining QuasAr with a sensitive blue-shifted channelrhodopsin variant CheRiff, all-optical electrophysiology (combined optical stimulation and recording of electrophysiological signaling in neurons) was carried out *in vitro*[121, 122].

Following this, a high-throughput multidimensional directed evolution screen was carried out based on QuasAr2[123]. FACS sorting was performed first to eliminate non-fluorescent mutants, and a second stage microscopy-guided robotic cell picking was applied, which evaluated cells in multiple parameter space[123]. The final two chosen mutants, Archon1 (mutation sites compared to Arch3: T20S/G41A/V44E/P60S/T80P/D86N/D95Q/D106H/A136T/F161V/T183I/L197I/G241Q) and Archon2 (mutation sites compared to Arch3: T56P/P60S/T80P/D95H/T99S/T116I/F161V/T183I/L197I/A225C; Figure 1.8), exhibit 2.4 and 6.8 times increased brightness compared to QuasAr2 while retaining voltage sensitivity (81% and 20% ΔF / F_0 per 100 mV)[123]. In addition to the counterion and proton donor, the remaining mutation sites are spread over the whole protein structure. These constructs were used to detect subthreshold neural activity in acute mouse brain slices and in larval zebrafish *in vivo*[123].

These sensors were further engineered to improve their *in vivo* signal-to-noise (SNR)

for application in behaving mice. QuasAr3 was developed through rational design and hierarchical screening to improve the membrane trafficking in neurons, which is a limiting factor for *in vivo* expression[124]. The construct combines a mutation in an intracellular loop (K171R), optimized fusion protein linker, and soma-localized opsin expression. Further investigation on the effects of previously found mutation sites led to the discovery of paQuasAr3 (mutation sites compared to QuasAr2: K171R and V59A; Figure 1.8), which displays 2-3 fold brightness over QuasAr3 and two times the spike detection SNR under concomitant blue illumination[124]. A simultaneous dual-wavelength patterning microscope was developed to perform cell-targeted illumination, which decreased background noise and increased the SNR by a factor of 3.5 to 11[124]. Populational neuron activities were monitored in different brain regions while the head-fixed mice were walking or anesthetized, and electrical compartmentalization of the dendrites was observed[124].

Continuing the directed evolution on paQuasAr3, a brightness-enhanced variant, NovArch (mutation sites compared to parent: V209I/I213T; Figure 1.8), was found[125]. Under blue illumination ($12\,\mathrm{W\,cm^{-2}}$), it shows a 4.8-fold fluorescence enhancement and is around twice as bright as paQuasAr3[125]. More importantly, it is activatable under two-photon (2P) illumination, displaying a 2.7-fold fluorescence enhancement while maintaining the same voltage sensitivity ($\Delta F/F_0 = 41\%$ per 100 mV)[125]. It was demonstrated in acute brain slices (40 to 70 µm deep) that NovArch exhibited a 3.5-fold enhanced spike amplitude and SNR of 96 under 2P enhancement[125]. *In vivo* experiments in behaving mice showed that the spike SNR increased from 4 to 6.8 with the addition of blue light[125].

In the meantime, a soma localized version of Archon1, SomArchon, was developed, which showed 2-fold greater sensitivity in neurons compared to Archon1 while maintaining comparable kinetics and SNR (about 7 to 16 per action potential)[126]. It was applied to report neuron dynamics in behaving mice across different regions and achieved simultaneous recording from 14 neurons in the hippocampus using a conventional microscope[126]. Later, SomArchon was paired with SomCheRiff to perform all-optical interrogation on synaptic inputs of L1 interneurons in awake mice[127].

Despite all these engineering efforts, the quantum yield of microbial rhodopsin-based GEVIs is still two orders of magnitude lower than conventional fluorescent proteins[113, 120]. As an alternative approach to cope with this drawback, microbial rhodopsins can be paired with fluorescent proteins having an emission spectrum that overlaps with the rhodopsin absorption spectrum and form an eFRET (electrochromic Förster resonance energy transfer) indicator[128]. In this case, the rhodopsin serves as a voltage sensor and FRET acceptor: its membrane-potential-modulated absorption spectrum will affect the quenching of the FRET donor, resulting in a change in the brightness of the fluorescent protein[129]. The resulting GEVI retains part of the voltage sensitivity of the rhodopsin and exhibits the bright fluorescence and high quantum yield of the fluorescent protein.

A blue-shifted proton pump Leptosphaeria maculans (Mac) with a slow photocycle was first paired with mCitrine to form the eFRET sensor, MacQ-mCitrine[130]. Similar to

Arch3, mutations were engineered at the counterion D139 (Figure 1.8) and proton donor D150, though the proton donor mutation introduced slow kinetics[117, 130]. MacQ-mCitrine was applied to report spiking events from dendrites of Purkinje neurons in live mice (illumination intensity 10 mW mm^{-2})[130]. QuasAr2 was also used as an acceptor in several eFRET sensors[129]. The optimal length of the linker between the donor and acceptor was determined through the screening of linker truncation libraries. Different fluorescent proteins were paired with QuasAr2, and mCitrine showed the largest sensitivity (ΔF / F_0 = -13.1% per 100 mV)[129]. The resulting GEVI (QuasAr2-mCitrine) was able to report spikes in cultured neurons with an SNR of 7 to 9 under low excitation power (30 mW mm^{-2})[129]. Both MacQ-mCitrine and QuasAr2-mCitrine show a millisecond range fast time constant (2.8 ms and 4.8 ms, respectively)[129, 130].

To further improve upon the kinetics of eFRET voltage sensors, a mutant of the fast rhodopsin derived from Acetabularia acetabulum (Ace, mutation at the counterion D81, Figure 1.8), was fused with a fluorescent protein, mNeonGreen, to generate the sensor Ace-mNeon[131]. In cultured neurons, Ace2N-mNeon shows a ΔF / F_0 of 12% and sub-millisecond response (fast time constant = 0.37 ms, governs 58% of response)[131]. The fast response time allows Ace-mNeon to detect spikes with high accuracy, with spike-timing errors of 0.24 ± 0.01 ms in mice and 0.19 ± 0.002 ms in flies[131]. Later, Ace2N was fused to the red fluorescent protein mScarlet, and the resulting sensor Ace-mScarlet displays comparable performance while avoiding potential crosstalk when used with blue-shifted optogenetics actuators[132].

In the search for better red-shifted eFRET sensors, Ace fused with the bright red fluorophore mRuby3 was subjected to high-throughput screening optimizing Ace mutations and the linker to improve the sensitivity[133]. The resulting construct, Ace-WR-mRuby3 N81S (VARNAM, Figure 1.8), showed comparable sensitivity to Ace-mNeon when imaged under 565 nm excitation[133]. All-optical electrophysiology experiments were carried out using CheRiff and VARNAM in acute slices. Under these imaging conditions, the optical crosstalk of imaging VARNAM generated a constant photocurrent of around 35 pA from CheRiff-positive neurons, which was, however, reasoned to be negligible[133]. Proof-of-concept dual-color simultaneous imaging of Ace-mNeon and VARNAM expressed in different types of Drosophila neurons was performed under 488 nm and 565 nm illumination[133].

As the quantum yield of the protein is a bottleneck in achieving populational neuron imaging, synthetic fluorescent dyes, which are significantly brighter, are also used as donors in eFRET designs[134]. In a FRET design that utilizes Ace2N as the voltage sensing domain, a dye-capturing protein domain, HaloTag, which irreversibly binds the Janelia Fluor (JF) dyes, is linked as a FRET donor[135]. The combined chemogenetic sensor (Voltron, Figure 1.8), is 3-4 fold brighter and is 8 times more photostable than Ace2N-mNeon. It shows a high sensitivity of -23% ΔF / F_0 per 100 mV[135]. Voltron could be used to monitor the activity of 449 neurons from 12 fields of view at 400 Hz in living mice, under moderate illumination intensity (3 to 20 mW mm^{-2})[135].

A disadvantage of eFRET GEVIs is that they show high fluorescence at cellular resting

potentials and at neutral voltages and that they generally show a negative response to voltage. Thus the background fluorescence from non-membrane trafficked GEVIs, and non-target cells can easily overwhelm the signal of active target cells, leading to low SNR, especially in tissue and *in vivo* recordings. A solution to this problem is to invert the polarity of the fluorescence response to the voltage of the rhodopsin voltage-sensing domain. A general rational approach to flip the voltage sensitivity of rhodopsins was eventually presented based on findings in Ace[136]. Based on the transient inward photocurrent of the Ace (D81N), it was reasoned that the voltage sensitivity stems from the protonation equilibrium between RSB and the cytoplasmic proton transfer network[136]. Blocking the proton donor D92 was hypothesized to switch the accessibility of RSB protonation to the extracellular side. This would result in an opposite protonation equilibrium reversing the polarity of the fluorescence response[136]. Experimentally, Voltron D92N indeed displays a positive voltage sensitivity, albeit with slower kinetics. The kinetics were improved by reverting to the negative counterion (N81D), but a 40% loss in sensitivity was observed[136]. Saturation mutagenesis was performed on E199, which possibly mediates the protonation equilibrium of the RSB[136]. The E199V mutant was found to have two times the sensitivity over Voltron N81D D92N and was named Positron (Figure 1.8). Similar results were obtained upon engineering these mutations in the other Ace sensors Ace2N-mNeon and VARNAM. The analogous mutations in Ace1m, Mac, and Arch3 also resulted in an inverse polarity in the voltage response, albeit all to different extents[136].

1.6. MOTIVATION AND OUTLINE OF THIS THESIS

Rhodopsin-based GEVIs have been used as a powerful tool to provide sub-millisecond monitoring of sub-threshold neuron dynamics in behaving animals[124–127, 131, 135]. However, several pitfalls still exist, hindering a wider application in neuroscience. Although the brightness of the single rhodopsin-based sensors has improved greatly, the *in vivo* applications still require high illumination intensity or specialized microscopy, which is not normally offered by commercial microscopes[124, 127]. Even with optimized sensors, voltage imaging remains a challenge: using it to its full potential requires recording large numbers of cells in parallel, with sufficient spatial resolution to determine subcellular dynamics, sufficient temporal resolution to resolve electrical waveform faithfully, and sufficient dynamic range to resolve subtle subthreshold changes in membrane potential. Engineering skills are essential to driving this field forward, as the parallel development of optogenetics tools, software, and hardware that are optimized for their combined use in targeted neuroscientific, electrophysiological, and diagnostic experiments will define this field for decades to come. In my thesis, I have combined these expertise. I started my PhD by building a multimodal microscope and programming a versatile software for rhodopsin engineering and voltage imaging, which will be introduced in Chapter 2 and Chapter 3. Powered by spatial, temporal patterning optics and machine learning based analysis and feedback, this smart microscope platform is the workhorse setup of this thesis and the lab and can perform a wide range of optogenetics experiments beyond the scope of this thesis.

By targeting key residues involved in proton transfer, it is possible to adapt rhodopsins towards desired characteristics[125, 136]. Analogous changes can be made to other rhodopsin scaffolds to quickly evaluate their potential as GEVIs and understand the generalizability of design rules. Through mutagenesis based on rational design in Chapter 4, we explored the potential of a novel rhodopsin family to serve as a GEVI.

To craft a perfect GEVI from rhodopsin, an improved understanding of the interplay between the structural changes that mutations create, their effect on photon absorption properties, and the dynamics of the photocycle, is crucial. This, in turn, requires a better understanding of, for instance, the influence of amino acids and water molecules involved in the creation of the hydrogen-bond network facilitating the proton transfer process, the states that fluorescence originates from, and the effect of voltage on their equilibrium. Information on the photocycles from a variety of mutants can lead to optimization of the illumination conditions to accumulate bright and voltage-sensitive intermediates for better SNR in one-photon (1P) imaging[125, 137]. By applying the current understanding of the key residues involved in tweaking the voltage-sensitive fluorescence, we extensively investigated the performance of various mutants from proton-pumping cyanobacterium rhodopsin, *Gloeobacter violaceus* rhodopsin, in Chapter 5.

Despite successful 1P applications, the major drawback of rhodopsin-based GEVIs is in the 2P imaging performance[138]. While 2P imaging is widely used with GECIs for deep-tissue calcium imaging, successful *in vivo* 2P imaging using rhodopsin-based GEVIs has remained elusive[139]. Although significant improvements have been made to the 2P imaging performance of VSD-based GEVIs, it is still a challenge to use rhodopsin-based GEVIs in 2P imaging[138, 140].

Single mutations are typically created to positively influence one emergent property of the GEVI protein (brightness, sensitivity, response kinetics, photocurrent) but usually also affect other aspects of GEVI functionality. For example, the counterion is typically the first engineering site to block the proton transfer pathway and eliminate the photocurrent; however, mutating the counterion alone often comes at the expense of voltage sensitivity or response kinetics[12]. To optimize GEVI performance, tweaking multiple groups of mutation sites through screening of random mutant libraries is preferable[121, 123–125]. To improve the 2P brightness of Archaerhodopsin-based GEVI, we conducted directed evolution and resulted in a mutant with improved 2P brightness, as described in Chapter 6.

REFERENCES

[1] A. A. El Gamal. “Biological importance of marine algae”. In: *Saudi pharmaceutical journal* 18.1 (2010), pp. 1–25.

[2] T. Kottke, A. Xie, D. S. Larsen, and W. D. Hoff. “Photoreceptors take charge: Emerging principles for light sensing”. In: *Annual Review of Biophysics* 47 (2018), pp. 291–313.

[3] H. Scheer. “Biliproteins”. In: *Angewandte Chemie International Edition in English* 20.3 (1981), pp. 241–261.

[4] O. P. Ernst, D. T. Lodowski, M. Elstner, P. Hegemann, L. S. Brown, and H. Kandori. “Microbial and animal rhodopsins: structures, functions, and molecular mechanisms”. In: *Chemical reviews* 114.1 (2014), pp. 126–163.

[5] J. L. Spudich, C.-S. Yang, K.-H. Jung, and E. N. Spudich. “Retinylidene proteins: structures and functions from archaea to humans”. In: *Annual review of cell and developmental biology* 16.1 (2000), pp. 365–392.

[6] J. Willem and S. Ganapathy. “Rhodopsins: an excitingly versatile protein species for research, development and creative engineering”. In: *Frontiers in Chemistry* 10 (2022).

[7] D. Man, W. Wang, G. Sabehi, L. Aravind, A. F. Post, R. Massana, E. N. Spudich, J. L. Spudich, and O. Béja. “Diversification and spectral tuning in marine proteorhodopsins”. In: *The EMBO journal* 22.8 (2003), pp. 1725–1731.

[8] L. Gómez-Consarnau, J. A. Raven, N. M. Levine, L. S. Cutter, D. Wang, B. Seegers, J. Arıstegui, J. A. Fuhrman, J. M. Gasol, and S. A. Sañudo-Wilhelmy. “Microbial rhodopsins are major contributors to the solar energy captured in the sea”. In: *Science advances* 5.8 (2019), eaaw8855.

[9] A. Pushkarev, K. Inoue, S. Larom, J. Flores-Uribe, M. Singh, M. Konno, S. Tomida, S. Ito, R. Nakamura, S. P. Tsunoda, *et al.* “A distinct abundant group of microbial rhodopsins discovered using functional metagenomics”. In: *Nature* 558.7711 (2018), pp. 595–599.

[10] E. S. Boyden, F. Zhang, E. Bamberg, G. Nagel, and K. Deisseroth. “Millisecond-timescale, genetically targeted optical control of neural activity”. In: *Nature neuroscience* 8.9 (2005), pp. 1263–1268.

[11] G. Nagel, D. Ollig, M. Fuhrmann, S. Kateriya, A. M. Musti, E. Bamberg, and P. Hegemann. “Channelrhodopsin-1: a light-gated proton channel in green algae”. In: *Science* 296.5577 (2002), pp. 2395–2398.

[12] J. M. Kralj, D. R. Hochbaum, A. D. Douglass, and A. E. Cohen. “Electrical spiking in Escherichia coli probed with a fluorescent voltage-indicating protein”. In: *Science* 333.6040 (2011), pp. 345–348.

[13] J. Nakai, M. Ohkura, and K. Imoto. “A high signal-to-noise Ca2+ probe composed of a single green fluorescent protein”. In: *Nature biotechnology* 19.2 (2001), pp. 137–141.

[14] T.-W. Chen, T. J. Wardill, Y. Sun, S. R. Pulver, S. L. Renninger, A. Baohan, E. R. Schreiter, R. A. Kerr, M. B. Orger, V. Jayaraman, *et al.* “Ultrasensitive fluorescent proteins for imaging neuronal activity”. In: *Nature* 499.7458 (2013), pp. 295–300.

[15] M. S. Siegel and E. Y. Isacoff. “A genetically encoded optical probe of membrane voltage”. In: *Neuron* 19.4 (1997), pp. 735–741.

[16] G. Guerrero, M. S. Siegel, B. Roska, E. Loots, and E. Y. Isacoff. “Tuning FlaSh: redesign of the dynamics, voltage range, and color of the genetically encoded optical sensor of membrane potential”. In: *Biophysical Journal* 83.6 (2002), pp. 3607–3618.

[17] B. J. Baker, L. Jin, Z. Han, L. B. Cohen, M. Popovic, J. Platisa, and V. Pieribone. “Genetically encoded fluorescent voltage sensors using the voltage-sensing domain of Nematostella and Danio phosphatases exhibit fast kinetics”. In: *Journal of neuroscience methods* 208.2 (2012), pp. 190–196.

[18] H. H. Yang, F. St-Pierre, X. Sun, X. Ding, M. Z. Lin, and T. R. Clandinin. “Subcellular imaging of voltage and calcium signals reveals neural processing in vivo”. In: *Cell* 166.1 (2016), pp. 245–257.

[19] J. M. Kralj, A. D. Douglass, D. R. Hochbaum, D. Maclaurin, and A. E. Cohen. “Optical recording of action potentials in mammalian neurons using a microbial rhodopsin”. In: *Nature methods* 9.1 (2012), pp. 90–95.

[20] X. M. Zhang, T. Yokoyama, and M. Sakamoto. “Imaging voltage with microbial rhodopsins”. In: *Frontiers in Molecular Biosciences* 8 (2021), p. 738829.

[21] E. G. Govorunova, O. A. Sineshchekov, H. Li, and J. L. Spudich. “Microbial rhodopsins: diversity, mechanisms, and optogenetic applications”. In: *Annual review of biochemistry* 86 (2017), pp. 845–872.

[22] D.-l. Chen, G.-y. Wang, B. Xu, and K.-s. Hu. “All-trans to 13-cis retinal isomerization in light-adapted bacteriorhodopsin at acidic pH”. In: *Journal of Photochemistry and Photobiology B: Biology* 66.3 (2002), pp. 188–194.

[23] A. C. Florean, D. Cardoza, J. L. White, J. Lanyi, R. J. Sension, and P. H. Bucksbaum. “Control of retinal isomerization in bacteriorhodopsin in the high-intensity regime”. In: *Proceedings of the National Academy of Sciences* 106.27 (2009), pp. 10896–10900.

[24] S. Gozem, H. L. Luk, I. Schapiro, and M. Olivucci. “Theory and simulation of the ultrafast double-bond isomerization of biological chromophores”. In: *Chemical reviews* 117.22 (2017), pp. 13502–13565.

[25] K. Kojima, R. Kurihara, M. Sakamoto, T. Takanashi, H. Kuramochi, X. M. Zhang, H. Bito, T. Tahara, and Y. Sudo. “Comparative studies of the fluorescence properties of microbial rhodopsins: spontaneous emission versus photointermediate fluorescence”. In: *The Journal of Physical Chemistry B* 124.34 (2020), pp. 7361–7367.

[26] J. K. Lanyi. “Proton transfers in the bacteriorhodopsin photocycle”. In: *Biochimica et Biophysica Acta (BBA)-Bioenergetics* 1757.8 (2006), pp. 1012–1018.

[27] R. H. Lozier, R. A. Bogomolni, and W. Stoeckenius. “Bacteriorhodopsin: a light-driven proton pump in Halobacterium Halobium.” In: *Biophysical journal* 15.9 (1975), p. 955.

[28] S. P. Balashov and T. G. Ebrey. “Trapping and Spectroscopic Identification of the Photointermediates of Bacteriorhodopsin at Low Temperatures”. In: *Photochemistry and photobiology* 73.5 (2001), pp. 453–462.

[29] U. Haupts, J. Tittor, and D. Oesterhelt. “Closing in on bacteriorhodopsin: progress in understanding the molecule”. In: *Annual review of biophysics and biomolecular structure* 28.1 (1999), pp. 367–399.

[30] M. Kataoka and H. Kamikubo. “Structures of photointermediates and their implications for the proton pump mechanism”. In: *Biochimica et Biophysica Acta (BBA)-Bioenergetics* 1460.1 (2000), pp. 166–176.

[31] D. Zabelskii, N. Dmitrieva, O. Volkov, V. Shevchenko, K. Kovalev, T. Balandin, D. Soloviov, R. Astashkin, E. Zinovev, A. Alekseev, *et al.* “Structure-based insights into evolution of rhodopsins”. In: *Communications biology* 4.1 (2021), p. 821.

[32] G. Nass Kovacs, J.-P. Colletier, M. L. Grünbein, Y. Yang, T. Stensitzki, A. Batyuk, S. Carbajo, R. B. Doak, D. Ehrenberg, L. Foucar, *et al.* “Three-dimensional view of ultrafast dynamics in photoexcited bacteriorhodopsin”. In: *Nature communications* 10.1 (2019), p. 3177.

[33] A. V. Sharkov, A. V. Pakulev, S. V. Chekalin, and Y. A. Matveetz. “Primary events in bacteriorhodopsin probed by subpicosecond spectroscopy”. In: *Biochimica et Biophysica Acta (BBA)-Bioenergetics* 808.1 (1985), pp. 94–102.

[34] T. Kobayashi, T. Saito, and H. Ohtani. “Real-time spectroscopy of transition states in bacteriorhodopsin during retinal isomerization”. In: *Nature* 414.6863 (2001), pp. 531–534.

[35] R. A. Mathies, C. Brito Cruz, W. T. Pollard, and C. V. Shank. “Direct observation of the femtosecond excited-state cis-trans isomerization in bacteriorhodopsin”. In: *Science* 240.4853 (1988), pp. 777–779.

[36] J. Herbst, K. Heyne, and R. Diller. “Femtosecond infrared spectroscopy of bacteriorhodopsin chromophore isomerization”. In: *Science* 297.5582 (2002), pp. 822–825.

[37] G. Atkinson, L. Ujj, and Y. Zhou. “Vibrational spectrum of the J-625 intermediate in the room temperature bacteriorhodopsin photocycle”. In: *The Journal of Physical Chemistry A* 104.18 (2000), pp. 4130–4139.

[38] W. Stoeckenius and R. H. Lozier. “Light energy conversion in Halobacterium halobium”. In: *Journal of supramolecular structure* 2.5-6 (1974), pp. 769–774.

[39] J. Dobler, W. Zinth, W. Kaiser, and D. Oesterhelt. “Excited-state reaction dynamics of bacteriorhodopsin studied by femtosecond spectroscopy”. In: *Chemical physics letters* 144.2 (1988), pp. 215–220.

[40] R. Diller, S. Maiti, G. C. Walker, B. R. Cowen, R. Pippenger, R. A. Bogomolni, and R. M. Hochstrasser. “Femtosecond time-resolved infrared laser study of the J-K transition of bacteriorhodopsin”. In: *Chemical physics letters* 241.1-2 (1995), pp. 109–115.

[41] T. Brack and G. H. Atkinson. “Vibrationally excited retinal in the bacteriorhodopsin photocycle: picosecond time-resolved anti-Stokes resonance Raman scattering”. In: *The Journal of Physical Chemistry* 95.6 (1991), pp. 2351–2356.

[42] S. J. Doig, P. J. Reid, and R. A. Mathies. “Picosecond time-resolved resonance Raman spectroscopy of bacteriorhodopsin’s J, K, and KL intermediates”. In: *The Journal of Physical Chemistry* 95.16 (1991), pp. 6372–6379.

[43] S. O. Smith, J. A. Pardoen, J. Lugtenburg, and R. A. Mathies. “Vibrational analysis of the 13-cis-retinal chromophore in dark-adapted bacteriorhodopsin”. In: *Journal of Physical Chemistry* 91.4 (1987), pp. 804–819.

[44] W. Hage, M. Kim, H. Frei, and R. A. Mathies. “Protein dynamics in the bacteriorhodopsin photocycle: a nanosecond step-scan FTIR investigation of the KL to L transition”. In: *The Journal of Physical Chemistry* 100.39 (1996), pp. 16026–16033.

[45] J. Sasaki, T. Yuzawa, H. Kandori, A. Maeda, and H.-o. Hamaguchi. “Nanosecond time-resolved infrared spectroscopy distinguishes two K species in the bacteriorhodopsin photocycle”. In: *Biophysical journal* 68.5 (1995), pp. 2073–2080.

[46] M. S. Braiman, T. Mogi, T. Marti, L. J. Stern, H. G. Khorana, and K. J. Rothschild. “Vibrational spectroscopy of bacteriorhodopsin mutants: light-driven proton transport involves protonation changes of aspartic acid residues 85, 96, and 212”. In: *Biochemistry* 27.23 (1988), pp. 8516–8520.

[47] S. Druckmann, M. Ottolenghi, A. Pande, J. Pande, and R. Callender. “Acid-base equilibrium of the Schiff base in bacteriorhodopsin”. In: *Biochemistry* 21.20 (1982), pp. 4953–4959.

[48] C.-H. Chang, J.-G. Chen, R. Govindjee, and T. Ebrey. “Cation binding by bacteriorhodopsin”. In: *Proceedings of the National Academy of Sciences* 82.2 (1985), pp. 396–400.

[49] F. M. Hendrickson, F. Burkard, and R. M. Glaeser. “Structural characterization of the L-to-M transition of the bacteriorhodopsin photocycle”. In: *Biophysical journal* 75.3 (1998), pp. 1446–1454.

[50] H. Kandori, Y. Yamazaki, J. Sasaki, R. Needleman, J. K. Lanyi, and A. Maeda. “Water-mediated proton transfer in proteins: an FTIR study of bacteriorhodopsin”. In: *Journal of the American Chemical Society* 117.7 (1995), pp. 2118–2119.

[51] T. Tanimoto, Y. Furutani, and H. Kandori. “Structural changes of water in the Schiff base region of bacteriorhodopsin: proposal of a hydration switch model”. In: *Biochemistry* 42.8 (2003), pp. 2300–2306.

[52] K. GERwERT, G. Souvignier, and B. Hess. “Simultaneous monitoring of light-induced changes in protein side-group protonation, chromophore isomerization, and backbone motion of bacteriorhodopsin by time-resolved Fourier-transform infrared spectroscopy.” In: *Proceedings of the National Academy of Sciences* 87.24 (1990), pp. 9774–9778.

[53] M. Braiman and R. Mathies. “Resonance Raman evidence for an all-trans to 13-cis isomerization in the proton-pumping cycle of bacteriorhodopsin”. In: *Biochemistry* 19.23 (1980), pp. 5421–5428.

[54] J. K. Lanyi and B. Schobert. “Mechanism of proton transport in bacteriorhodopsin from crystallographic structures of the K, L, M1, M2, and M2 intermediates of the photocycle”. In: *Journal of molecular biology* 328.2 (2003), pp. 439–450.

[55] L. Zimanyi, G. Varo, M. Chang, B. Ni, R. Needleman, and J. K. Lanyi. “Pathways of proton release in the bacteriorhodopsin photocycle”. In: *Biochemistry* 31.36 (1992), pp. 8535–8543.

[56] K. Gerwert and F. Siebert. “Evidence for light-induced 13-cis, 14-s-cis isomerization in bacteriorhodopsin obtained by FTIR difference spectroscopy using isotopically labelled retinals”. In: *The EMBO journal* 5.4 (1986), pp. 805–811.

[57] S. Fodor, W. T. Pollard, R. Gebhard, E. Van den Berg, J. Lugtenburg, and R. A. Mathies. “Bacteriorhodopsin’s L550 intermediate contains a C14-C15 s-trans-retinal chromophore.” In: *Proceedings of the National Academy of Sciences* 85.7 (1988), pp. 2156–2160.

[58] S. Subramaniam and R. Henderson. “Molecular mechanism of vectorial proton translocation by bacteriorhodopsin”. In: *Nature* 406.6796 (2000), pp. 653–657.

[59] J. Herzfeld and J. C. Lansing. “Magnetic resonance studies of the bacteriorhodopsin pump cycle”. In: *Annual review of biophysics and biomolecular structure* 31.1 (2002), pp. 73–95.

[60] J. Herzfeld and B. Tounge. “NMR probes of vectoriality in the proton-motive photocycle of bacteriorhodopsin: evidence for an ‘electrostatic steering’mechanism”. In: *Biochimica et Biophysica Acta (BBA)-Bioenergetics* 1460.1 (2000), pp. 95–105.

[61] S. Subramaniam, M. Gerstein, D. Oesterhelt, and R. Henderson. “Electron diffraction analysis of structural changes in the photocycle of bacteriorhodopsin.” In: *The EMBO journal* 12.1 (1993), pp. 1–8.

[62] B. Schobert and J. K. Lanyi. “Halorhodopsin is a light-driven chloride pump.” In: *Journal of Biological Chemistry* 257.17 (1982), pp. 10306–10313.

[63] L. S. Brown, H. Kamikubo, L. Zimányi, M. Kataoka, F. Tokunaga, P. Verdegem, J. Lugtenburg, and J. K. Lanyi. “A local electrostatic change is the cause of the large-scale protein conformation shift in bacteriorhodopsin”. In: *Proceedings of the National Academy of Sciences* 94.10 (1997), pp. 5040–5044.

[64] J. Heberle. “Proton transfer reactions across bacteriorhodopsin and along the membrane”. In: *Biochimica et Biophysica Acta (BBA)-Bioenergetics* 1458.1 (2000), pp. 135–147.

[65] S. Subramaniam, A. Faruqi, D. Oesterhelt, and R. Henderson. “Electron diffraction studies of light-induced conformational changes in the Leu-93→ Ala bacteriorhodopsin mutant”. In: *Proceedings of the National Academy of Sciences* 94.5 (1997), pp. 1767–1772.

[66] S. Subramaniam and R. Henderson. “Crystallographic analysis of protein conformational changes in the bacteriorhodopsin photocycle”. In: *Biochimica et Biophysica Acta (BBA)-Bioenergetics* 1460.1 (2000), pp. 157–165.

[67] A. K. Dioumaev, H.-T. Richter, L. S. Brown, M. Tanio, S. Tuzi, H. Saitô, Y. Kimura, R. Needleman, and J. K. Lanyi. “Existence of a proton transfer chain in bacteriorhodopsin: participation of Glu-194 in the release of protons to the extracellular surface”. In: *Biochemistry* 37.8 (1998), pp. 2496–2506.

[68] F. Garczarek, L. S. Brown, J. K. Lanyi, and K. Gerwert. “Proton binding within a membrane protein by a protonated water cluster”. In: *Proceedings of the National Academy of Sciences* 102.10 (2005), pp. 3633–3638.

[69] S. P. Balashov, E. S. Imasheva, R. Govindjee, and T. G. Ebrey. “Titration of aspartate-85 in bacteriorhodopsin: what it says about chromophore isomerization and proton release”. In: *Biophysical journal* 70.1 (1996), pp. 473–481.

[70] H.-T. Richter, L. S. Brown, R. Needleman, and J. K. Lanyi. “A linkage of the p K a’s of Asp-85 and Glu-204 forms part of the reprotonation switch of bacteriorhodopsin”. In: *Biochemistry* 35.13 (1996), pp. 4054–4062.

[71] H.-T. Richter, R. Needleman, and J. K. Lanyi. “Perturbed interaction between residues 85 and 204 in Tyr-185–> Phe and Asp-85–> Glu bacteriorhodopsins”. In: *Biophysical journal* 71.6 (1996), pp. 3392–3398.

[72] H. J. Sass, G. Büldt, R. Gessenich, D. Hehn, D. Neff, R. Schlesinger, J. Berendzen, and P. Ormos. “Structural alterations for proton translocation in the M state of wild-type bacteriorhodopsin”. In: *Nature* 406.6796 (2000), pp. 649–653.

[73] H. Luecke, B. Schobert, J.-P. Cartailler, H.-T. Richter, A. Rosengarth, R. Needleman, and J. K. Lanyi. “Coupling photoisomerization of retinal to directional transport in bacteriorhodopsin”. In: *Journal of molecular biology* 300.5 (2000), pp. 1237–1255.

[74] B. Schobert, L. S. Brown, and J. K. Lanyi. “Crystallographic structures of the M and N intermediates of bacteriorhodopsin: assembly of a hydrogen-bonded chain of water molecules between Asp-96 and the retinal Schiff base”. In: *Journal of molecular biology* 330.3 (2003), pp. 553–570.

[75] M. Shibata, H. Yamashita, T. Uchihashi, H. Kandori, and T. Ando. “High-speed atomic force microscopy shows dynamic molecular processes in photoactivated bacteriorhodopsin”. In: *Nature nanotechnology* 5.3 (2010), pp. 208–212.

[76] Y. Cao, G. Varo, M. Chang, B. Ni, R. Needleman, and J. K. Lanyi. “Water is required for proton transfer from aspartate-96 to the bacteriorhodopsin Schiff base”. In: *Biochemistry* 30.45 (1991), pp. 10972–10979.

[77] B. Roux, M. Nina, R. Pomes, and J. C. Smith. “Thermodynamic stability of water molecules in the bacteriorhodopsin proton channel: a molecular dynamics free energy perturbation study”. In: *Biophysical journal* 71.2 (1996), pp. 670–681.

[78] H. Otto, T. Marti, M. Holz, T. Mogi, M. Lindau, H. G. Khorana, and M. P. Heyn. “Aspartic acid-96 is the internal proton donor in the reprotonation of the Schiff base of bacteriorhodopsin.” In: *Proceedings of the National Academy of Sciences* 86.23 (1989), pp. 9228–9232.

[79] K. Gerwert, B. Hess, J. Soppa, and D. Oesterhelt. “Role of aspartate-96 in proton translocation by bacteriorhodopsin.” In: *Proceedings of the National Academy of Sciences* 86.13 (1989), pp. 4943–4947.

[80] S. O. Smith, J. A. Pardoen, P. P. Mulder, B. Curry, J. Lugtenburg, and R. Mathies. “Chromophore structure in bacteriorhodopsin’s O640 photointermediate”. In: *Biochemistry* 22.26 (1983), pp. 6141–6148.

[81] A. K. Dioumaev, L. S. Brown, R. Needleman, and J. K. Lanyi. “Partitioning of free energy gain between the photoisomerized retinal and the protein in bacteriorhodopsin”. In: *Biochemistry* 37.28 (1998), pp. 9889–9893.

[82] L. S. Brown, R. Needleman, and J. K. Lanyi. “Functional roles of aspartic acid residues at the cytoplasmic surface of bacteriorhodopsin”. In: *Biochemistry* 38.21 (1999), pp. 6855–6861.

[83] B. Schätzler, N. A. Dencher, J. Tittor, D. Oesterhelt, S. Yaniv-Checover, E. Nachliel, and M. Gutman. “Subsecond proton-hole propagation in bacteriorhodopsin”. In: *Biophysical journal* 84.1 (2003), pp. 671–686.

[84] C. Kandt, J. Schlitter, and K. Gerwert. “Dynamics of water molecules in the bacteriorhodopsin trimer in explicit lipid/water environment”. In: *Biophysical journal* 86.2 (2004), pp. 705–717.

[85] E. Nachliel, M. Gutman, J. Tittor, and D. Oesterhelt. “Proton transfer dynamics on the surface of the late M state of bacteriorhodopsin”. In: *Biophysical journal* 83.1 (2002), pp. 416–426.

[86] C. Zscherp and J. Heberle. “Infrared difference spectra of the intermediates L, M, N, and O of the bacteriorhodopsin photoreaction obtained by time-resolved attenuated total reflection spectroscopy”. In: *The Journal of Physical Chemistry B* 101.49 (1997), pp. 10542–10547.

[87] K. Gerwert, E. Freier, and S. Wolf. “The role of protein-bound water molecules in microbial rhodopsins”. In: *Biochimica et Biophysica Acta (BBA)-Bioenergetics* 1837.5 (2014), pp. 606–613.

[88] H. Luecke, H.-T. Richter, and J. K. Lanyi. “Proton transfer pathways in bacteriorhodopsin at 2.3 angstrom resolution”. In: *Science* 280.5371 (1998), pp. 1934–1937.

[89] R. Govindjee, S. Misra, S. P. Balashov, T. G. Ebrey, R. K. Crouch, and D. R. Menick. "Arginine-82 regulates the pKa of the group responsible for the light-driven proton release in bacteriorhodopsin". In: *Biophysical journal* 71.2 (1996), pp. 1011–1023.

[90] A. K. Dioumaev, L. S. Brown, R. Needleman, and J. K. Lanyi. "Fourier transform infrared spectra of a late intermediate of the bacteriorhodopsin photocycle suggest transient protonation of Asp-212". In: *Biochemistry* 38.31 (1999), pp. 10070–10078.

[91] S. P. Balashov, E. S. Imasheva, T. G. Ebrey, N. Chen, D. R. Menick, and R. K. Crouch. "Glutamate-194 to cysteine mutation inhibits fast light-induced proton release in bacteriorhodopsin". In: *Biochemistry* 36.29 (1997), pp. 8671–8676.

[92] T. Kouyama, K. Kinosita, and A. Ikegami. "Excited-state dynamics of bacteriorhodopsin". In: *Biophysical journal* 47.1 (1985), pp. 43–54.

[93] R. Govindjee, B. Becher, and T. G. Ebrey. "The fluorescence from the chromophore of the purple membrane protein". In: *Biophysical Journal* 22.1 (1978), pp. 67–77.

[94] M. d. C. Marin, D. Agathangelou, Y. Orozco-Gonzalez, A. Valentini, Y. Kato, R. Abe-Yoshizumi, H. Kandori, A. Choi, K.-H. Jung, S. Haacke, *et al.* "Fluorescence enhancement of a microbial rhodopsin via electronic reprogramming". In: *Journal of the American Chemical Society* 141.1 (2018), pp. 262–271.

[95] J. Tittor and D. Oesterhelt. "The quantum yield of bacteriorhodopsin". In: *FEBS letters* 263.2 (1990), pp. 269–273.

[96] R. Govindjee, S. Balashov, and T. Ebrey. "Quantum efficiency of the photochemical cycle of bacteriorhodopsin". In: *Biophysical journal* 58.3 (1990), pp. 597–608.

[97] H. Ohtani, Y. Tsukamoto, Y. Sakoda, and H.-o. Hamaguchi. "Fluorescence spectra of bacteriorhodopsin and the intermediates O and Q at room temperature". In: *FEBS letters* 359.1 (1995), pp. 65–68.

[98] H. Ohtani, M. Kaneko, M. Ishikawa, N. Kamiya, and N. Yamamoto. "Picosecond-millisecond dual-time-base spectroscopy of fluorescent photointermediates formed in the purple membrane of Halobacterium halobium". In: *Chemical physics letters* 299.6 (1999), pp. 571–575.

[99] N. Kamiya, M. Ishikawa, K. Kasahara, M. Kaneko, N. Yamamoto, and H. Ohtani. "Picosecond fluorescence spectroscopy of the purple membrane of Halobacterium halobium in alkaline suspension". In: *Chemical physics letters* 265.6 (1997), pp. 595–599.

[100] S. P. Fodor, J. B. Ames, R. Gebhard, E. M. Van den Berg, W. Stoeckenius, J. Lugtenburg, and R. A. Mathies. "Chromophore structure in bacteriorhodopsin's N intermediate: implications for the proton-pumping mechanism". In: *Biochemistry* 27.18 (1988), pp. 7097–7101.

[101] G. Nagel, B. Kelety, B. Möckel, G. Büldt, and E. Bamberg. "Voltage dependence of proton pumping by bacteriorhodopsin is regulated by the voltage-sensitive ratio of M1 to M2". In: *Biophysical journal* 74.1 (1998), pp. 403–412.

[102] S. Geibel, T. Friedrich, P. Ormos, P. G. Wood, G. Nagel, and E. Bamberg. “The voltage-dependent proton pumping in bacteriorhodopsin is characterized by optoelectric behavior”. In: *Biophysical journal* 81.4 (2001), pp. 2059–2068.

[103] B. Karvaly and Z. Dancsházy. “Bacteriorhodopsin: A molecular photoelectric regulator Quenching of photovoltaic effect of bimolecular lipid membranes containing bacteriorhodopsin by blue light”. In: *FEBS letters* 76.1 (1977), pp. 36–40.

[104] P. Ormos, Z. Dancsházy, and L. Keszthelyi. “Electric response of a back photoreaction in the bacteriorhodopsin photocycle”. In: *Biophysical Journal* 31.2 (1980), pp. 207–213.

[105] S. P. Tsunoda, D. Ewers, S. Gazzarrini, A. Moroni, D. Gradmann, and P. Hegemann. “H+-pumping rhodopsin from the marine alga Acetabularia”. In: *Biophysical journal* 91.4 (2006), pp. 1471–1479.

[106] A. Kawanabe, Y. Furutani, K.-H. Jung, and H. Kandori. “Photochromism of Anabaena sensory rhodopsin”. In: *Journal of the American Chemical Society* 129.27 (2007), pp. 8644–8649.

[107] M. Broser, A. Spreen, P. E. Konold, E. Peter, S. Adam, V. Borin, I. Schapiro, R. Seifert, J. T. Kennis, Y. A. Bernal Sierra, *et al.* “NeoR, a near-infrared absorbing rhodopsin”. In: *Nature communications* 11.1 (2020), p. 5682.

[108] L. Song, M. El-Sayed, and J. Lanyi. “Protein catalysis of the retinal subpicosecond photoisomerization in the primary process of bacteriorhodopsin photosynthesis”. In: *Science* 261.5123 (1993), pp. 891–894.

[109] S. Logunov, M. El-Sayed, and J. Lanyi. “Catalysis of the retinal subpicosecond photoisomerization process in acid purple bacteriorhodopsin and some bacteriorhodopsin mutants by chloride ions”. In: *Biophysical journal* 71.3 (1996), pp. 1545–1553.

[110] D. Maclaurin, V. Venkatachalam, H. Lee, and A. E. Cohen. “Mechanism of voltage-sensitive fluorescence in a microbial rhodopsin”. In: *Proceedings of the National Academy of Sciences* 110.15 (2013), pp. 5939–5944.

[111] E. C. Saint Clair, J. I. Ogren, S. Mamaev, D. Russano, J. M. Kralj, and K. J. Rothschild. “Near-IR resonance Raman spectroscopy of archaerhodopsin 3: effects of transmembrane potential”. In: *The Journal of Physical Chemistry B* 116.50 (2012), pp. 14592–14601.

[112] G. Mei, C. M. Cavini, N. Mamaeva, P. Wang, W. J. DeGrip, and K. J. Rothschild. “Optical switching between long-lived states of opsin transmembrane voltage sensors”. In: *Photochemistry and Photobiology* 97.5 (2021), pp. 1001–1015.

[113] A. Silapetere, S. Hwang, Y. Hontani, R. G. Fernandez Lahore, J. Balke, F. V. Escobar, M. Tros, P. E. Konold, R. Matis, R. Croce, *et al.* “QuasAr Odyssey: the origin of fluorescence and its voltage sensitivity in microbial rhodopsins”. In: *Nature communications* 13.1 (2022), p. 5501.

[114] A. K. Dioumaev, J. M. Wang, Z. Bálint, G. Váró, and J. K. Lanyi. “Proton transport by proteorhodopsin requires that the retinal Schiff base counterion Asp-97 be anionic”. In: *Biochemistry* 42.21 (2003), pp. 6582–6587.

[115] B. Y. Chow, X. Han, A. S. Dobry, X. Qian, A. S. Chuong, M. Li, M. A. Henninger, G. M. Belfort, Y. Lin, P. E. Monahan, *et al.* "High-performance genetically targetable optical neural silencing by light-driven proton pumps". In: *Nature* 463.7277 (2010), pp. 98–102.

[116] J. Tittor, U. Schweiger, D. Oesterhelt, and E. Bamberg. "Inversion of proton translocation in bacteriorhodopsin mutants D85N, D85T, and D85, 96N". In: *Biophysical journal* 67.4 (1994), pp. 1682–1690.

[117] Y. Gong, J. Z. Li, and M. J. Schnitzer. "Enhanced archaerhodopsin fluorescent protein voltage indicators". In: *PLoS One* 8.6 (2013), e66959.

[118] N. C. Flytzanis, C. N. Bedbrook, H. Chiu, M. K. Engqvist, C. Xiao, K. Y. Chan, P. W. Sternberg, F. H. Arnold, and V. Gradinaru. "Archaerhodopsin variants with enhanced voltage-sensitive fluorescence in mammalian and Caenorhabditis elegans neurons". In: *Nature communications* 5.1 (2014), p. 4894.

[119] M. K. Engqvist, R. S. McIsaac, P. Dollinger, N. C. Flytzanis, M. Abrams, S. Schor, and F. H. Arnold. "Directed evolution of Gloeobacter violaceus rhodopsin spectral properties". In: *Journal of molecular biology* 427.1 (2015), pp. 205–220.

[120] R. S. McIsaac, M. K. Engqvist, T. Wannier, A. Z. Rosenthal, L. Herwig, N. C. Flytzanis, E. S. Imasheva, J. K. Lanyi, S. P. Balashov, V. Gradinaru, *et al.* "Directed evolution of a far-red fluorescent rhodopsin". In: *Proceedings of the National Academy of Sciences* 111.36 (2014), pp. 13034–13039.

[121] D. R. Hochbaum, Y. Zhao, S. L. Farhi, N. Klapoetke, C. A. Werley, V. Kapoor, P. Zou, J. M. Kralj, D. Maclaurin, N. Smedemark-Margulies, *et al.* "All-optical electrophysiology in mammalian neurons using engineered microbial rhodopsins". In: *Nature methods* 11.8 (2014), pp. 825–833.

[122] L. Z. Fan, R. Nehme, Y. Adam, E. S. Jung, H. Wu, K. Eggan, D. B. Arnold, and A. E. Cohen. "All-optical synaptic electrophysiology probes mechanism of ketamine-induced disinhibition". In: *Nature methods* 15.10 (2018), pp. 823–831.

[123] K. D. Piatkevich, E. E. Jung, C. Straub, C. Linghu, D. Park, H.-J. Suk, D. R. Hochbaum, D. Goodwin, E. Pnevmatikakis, N. Pak, *et al.* "A robotic multidimensional directed evolution approach applied to fluorescent voltage reporters". In: *Nature chemical biology* 14.4 (2018), pp. 352–360.

[124] Y. Adam, J. J. Kim, S. Lou, Y. Zhao, M. E. Xie, D. Brinks, H. Wu, M. A. Mostajo-Radji, S. Kheifets, V. Parot, *et al.* "Voltage imaging and optogenetics reveal behaviour-dependent changes in hippocampal dynamics". In: *Nature* 569.7756 (2019), pp. 413–417.

[125] M.-P. Chien, D. Brinks, G. Testa-Silva, H. Tian, F. Phil Brooks III, Y. Adam, B. Bloxham, B. Gmeiner, S. Kheifets, and A. E. Cohen. "Photoactivated voltage imaging in tissue with an archaerhodopsin-derived reporter". In: *Science advances* 7.19 (2021), eabe3216.

[126] K. D. Piatkevich, S. Bensussen, H.-a. Tseng, S. N. Shroff, V. G. Lopez-Huerta, D. Park, E. E. Jung, O. A. Shemesh, C. Straub, H. J. Gritton, *et al.* "Population imaging of neural activity in awake behaving mice". In: *Nature* 574.7778 (2019), pp. 413–417.

[127] L. Z. Fan, S. Kheifets, U. L. Böhm, H. Wu, K. D. Piatkevich, M. E. Xie, V. Parot, Y. Ha, K. E. Evans, E. S. Boyden, *et al.* "All-optical electrophysiology reveals the role of lateral inhibition in sensory processing in cortical layer 1". In: *Cell* 180.3 (2020), pp. 521–535.

[128] H. Bayraktar, A. P. Fields, J. M. Kralj, J. L. Spudich, K. J. Rothschild, and A. E. Cohen. "Ultrasensitive measurements of microbial rhodopsin photocycles using photochromic FRET". In: *Photochemistry and Photobiology* 88.1 (2012), pp. 90–97.

[129] P. Zou, Y. Zhao, A. D. Douglass, D. R. Hochbaum, D. Brinks, C. A. Werley, D. J. Harrison, R. E. Campbell, and A. E. Cohen. "Bright and fast multicoloured voltage reporters via electrochromic FRET". In: *Nature communications* 5.1 (2014), p. 4625.

[130] Y. Gong, M. J. Wagner, J. Zhong Li, and M. J. Schnitzer. "Imaging neural spiking in brain tissue using FRET-opsin protein voltage sensors". In: *Nature communications* 5.1 (2014), p. 3674.

[131] Y. Gong, C. Huang, J. Z. Li, B. F. Grewe, Y. Zhang, S. Eismann, and M. J. Schnitzer. "High-speed recording of neural spikes in awake mice and flies with a fluorescent voltage sensor". In: *Science* 350.6266 (2015), pp. 1361–1366.

[132] C. Beck and Y. Gong. "A high-speed, bright, red fluorescent voltage sensor to detect neural activity". In: *Scientific reports* 9.1 (2019), pp. 1–12.

[133] M. Kannan, G. Vasan, C. Huang, S. Haziza, J. Z. Li, H. Inan, M. J. Schnitzer, and V. A. Pieribone. "Fast, in vivo voltage imaging using a red fluorescent indicator". In: *Nature methods* 15.12 (2018), pp. 1108–1116.

[134] S. Liu, C. Lin, Y. Xu, H. Luo, L. Peng, X. Zeng, H. Zheng, P. R. Chen, and P. Zou. "A far-red hybrid voltage indicator enabled by bioorthogonal engineering of rhodopsin on live neurons". In: *Nature Chemistry* 13.5 (2021), pp. 472–479.

[135] A. S. Abdelfattah, T. Kawashima, A. Singh, O. Novak, H. Liu, Y. Shuai, Y.-C. Huang, L. Campagnola, S. C. Seeman, J. Yu, *et al.* "Bright and photostable chemigenetic indicators for extended in vivo voltage imaging". In: *Science* 365.6454 (2019), pp. 699–704.

[136] A. S. Abdelfattah, R. Valenti, J. Zheng, A. Wong, K. Podgorski, M. Koyama, D. S. Kim, and E. R. Schreiter. "A general approach to engineer positive-going eFRET voltage indicators". In: *Nature Communications* 11.1 (2020), p. 3444.

[137] A. Penzkofer, A. Silapetere, and P. Hegemann. "Photocycle dynamics of the Archaerhodopsin 3 based fluorescent voltage sensor QuasAr1". In: *International Journal of Molecular Sciences* 21.1 (2019), p. 160.

[138] D. Brinks, A. J. Klein, and A. E. Cohen. “Two-photon lifetime imaging of voltage indicating proteins as a probe of absolute membrane voltage”. In: *Biophysical journal* 109.5 (2015), pp. 914–921.

[139] M. A. Mohr, D. Bushey, A. Aggarwal, J. S. Marvin, J. J. Kim, E. J. Marquez, Y. Liang, R. Patel, J. J. Macklin, C.-Y. Lee, *et al.* “jYCaMP: an optimized calcium indicator for two-photon imaging at fiber laser wavelengths”. In: *Nature methods* 17.7 (2020), pp. 694–697.

[140] Z. Liu, X. Lu, V. Villette, Y. Gou, K. L. Colbert, S. Lai, S. Guan, M. A. Land, J. Lee, T. Assefa, *et al.* “Sustained deep-tissue voltage recording using a fast indicator evolved for two-photon microscopy”. In: *Cell* (2022).

2

A Compact Microscope for Voltage Imaging

Voltage imaging and optogenetics offer new routes to optically detect and influence neural dynamics. Optimized hardware is necessary to make the most of these new techniques. Here we present the Octoscope, a versatile, multimodal device for all-optical electrophysiology. We illustrate its concept and design and demonstrate its capability to perform both one-photon and two-photon voltage imaging with spatial and temporal light patterning in both inverted and upright configurations, in vitro and in vivo.

2.1. INTRODUCTION

VOLTAGE imaging is a novel technique to probe neural dynamics, allowing the visualization of cellular electrical dynamics through the transduction of changes in cell membrane voltage into changes in fluorescence of a molecular probe embedded in the cell membrane. These probes can either be small molecules[1] or engineered proteins called Genetically Encoded Voltage Indicators (GEVIs)[2, 3]. Voltage imaging can be combined with optogenetic actuators: light-sensitive ion channels or pumps that, upon expression in cells, allow illumination-based control of cellular electrical activity[4–6]. The combination is referred to as all-optical electrophysiology[7].

While GEVI and voltage imaging assay development have sometimes been done on commercial microscope scaffolds[1, 8, 9], custom-built apparatus has often been deemed necessary to achieve optimal results[7, 10–13]. The potential of all-optical electrophysiology to contribute to the answering of neuroscientific questions relies on the availability of microscopes that make optimal use of the advantages voltage imaging offers: recording voltage dynamics at high temporal resolution (<1 ms), over a large number of cells, in 2D and 3D cellular environments and with the flexibility to accommodate different types of samples and experiments. Patterned illumination is often a necessary strategy for signal-to-background discrimination in voltage imaging[12, 13] or cellular stimulation in all-optical electrophysiology[7, 12, 13]. These needs are intensified by the fact that the protein sensors used in voltage imaging have interesting photophysical properties: combined optical and molecular development leads to novel measurement modalities[12–17] that ideally can be developed on the same setup where they are to be applied as in vivo neuroscientific assays.

Many voltage imaging applications use one-photon (1P) imaging for both GEVI development and voltage imaging assays[18–20], though recent years has seen the advent of two-photon (2P) voltage imaging[16, 21]. Thus, a microscope that has the above flexibility in both 1P and 2P imaging modalities would be an ideal platform for the optimization and application of voltage imaging and all-optical electrophysiological assays. Here we introduce the Octoscope, a compact design for a microscope that features imaging and patterned illumination with 1P or 2P illumination and recording on a widefield camera or photomultiplier tube (PMT). Crucially, the design and its compactness allow a precise and reproducible orientation of the objective throughout a 360-degree angle of rotation, allowing voltage imaging, patterned illumination, optogenetics, and all-optical electrophysiology experiments in upright and inverted configurations and at custom angles of the objective.

This Chapter has been published as: Xin Meng, Lex Huismans, Teun Huijben, Greta Szabo, Ruud Van Tol, Izak De Heer, Srividya Ganapathy, and Daan Brinks. "A compact microscope for voltage imaging." *Journal of Optics*, 24, no. 5 (2022): 054004.

2.2. METHOD

2.2.1. OCTOSCOPE CONCEPT AND CUSTOM DESIGNS

The Octoscope consists of two illumination pathways, two detection pathways, and currently two imaging configurations (upright and inverted) for a total of eight different optical stimulation and imaging modalities. This flexibility is made possible by a custom-designed beam combiner (Figure 2.1(a)) and objective holder, featuring exchangeable dichroic mirrors and filters and motorized objective translation and rotation. (Figure 2.1(b)).

This holder is embedded in a setup featuring a 2P illumination pathway through scanning galvanometric mirrors (6215HR, Cambridge Technology), a 1P illumination pathway via a Digital Micromirror Device (DMD, Vialux V7001, Texas Instruments), and detection on a camera or a PMT pathway with motorized switching between the two (Figure 2.1(c)). The beam combiner and objective holder, made of anodized aluminum, mount the tube lenses for 1P excitation, 2P excitation, and the detection pathways. The configuration used in the experiments in this chapter employs 200 mm tube lenses (TTL200, Thorlabs). The beam combiner and objective holder contain exchangeable holders for the dichroic mirrors that combine the 1P and 2P excitation pathways and separate excitation and emission pathways (Figure 2.1(d)). The objective is mounted on a translation stage (M110-DG, Physik Instrumente) which drives linear translation of the objective for focus adjustment. This translatable objective holder contains a prism reflector mounted on the rotation axis of a rotation motor (RS-40, Physik Instrumente) to allow rotation of the objective.

Scan head and scan lens of the 2P excitation pathway are mounted in a custom aluminum holder (Figure 2.1(e)). The scanning module is fixed on a large-area translation stage (TBB1515/M, Thorlabs) so that the scanning mirrors and the scan lens can move along the optical axis for fine adjustment of the focal plane. A compact lens mount with a reflection mirror on the holder turns the incident laser beam 90 degrees and directs it to the first scanning mirror, allowing adjustment of the scanning module position without changes in the alignment of the excitation beam. The scan lens is fixed to the block in a 3D-printed V-clamp.

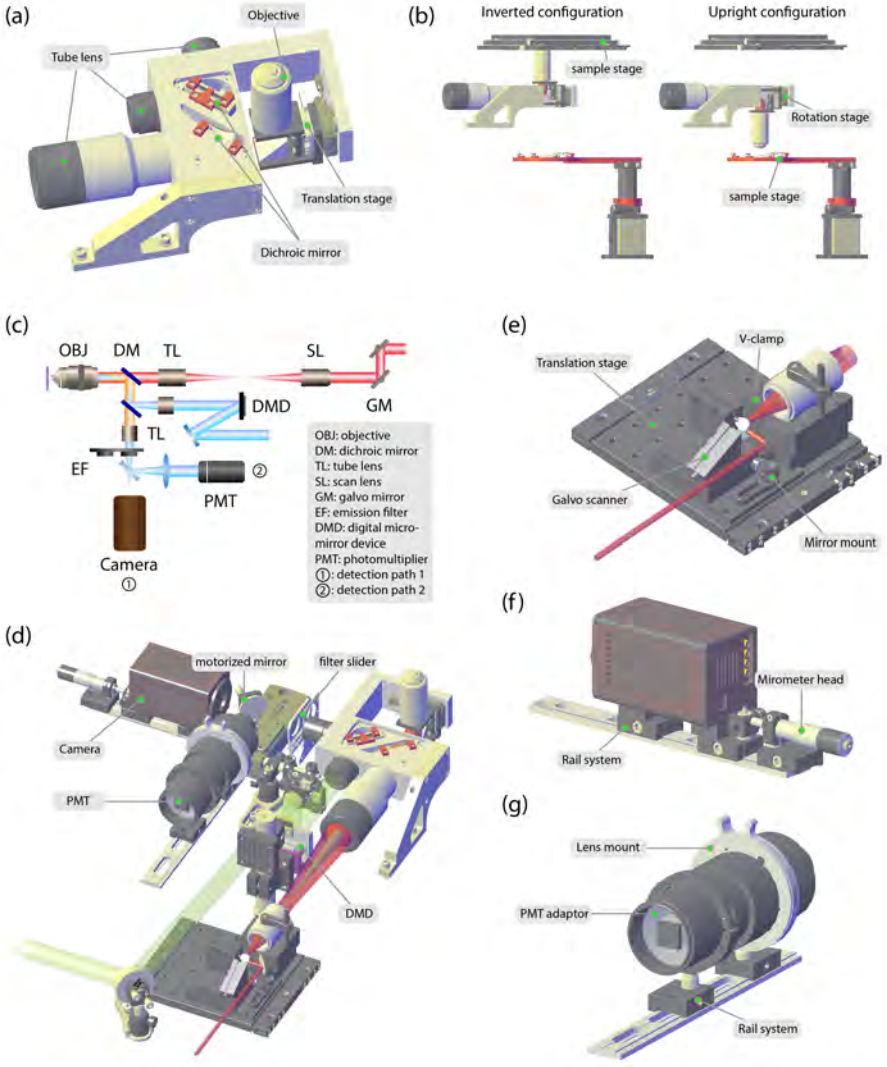

Figure 2.1: Octoscope design. (a) The customized beam combiner block. (b) The beam combiner and objective holder allow automated switching between upright and inverted configurations. (c) Schematic of the 1P and 2P excitation pathways, combined and separated from the emission pathways; (d) the beam combiner and objective holder allow a combination of a 1P and 2P excitation pathway with camera and PMT detection. (e) Mount for the 2P Scan head. (f) Camera translation system. (g) PMT mount.

2.2.2. 1P EXCITATION PATHWAY

In our lab, 1P illumination was provided by three continuous wave lasers (MLL-III-532, CNI; MLL-FN-639, CNI; OBIS 488 LX, Coherent). Their output is made uniform in polarization and beam diameter through zero-order half-wave plates (WPH05M-488, WPH05M-532, WPH05M-633, Thorlabs) and polarizers (CCM5-PBS201/M, Thorlabs) and individual collimators (AC254 mounted achromatic doublets, Thorlabs). The laser beams are then combined using dichroic mirrors (DMLP505, DMLP605, Thorlabs) and lead through an acousto-optic tunable filter (AOTFnC-VI S; AA Optoelectronics) with a modulation rate of 22 kHz to allow fast intensity modulation. The beam diameter is adjusted with a variable telescope (AC254 mounted achromatic doublets, Thorlabs) using flip mounts (TRF90/M, Thorlabs). The beam is guided into the setup over the DMD to allow patterned illumination of the sample. A dichroic mirror (Di03-R405/488/532/635-t3-32x44, Semrock) mounted in the dichroic holder of the beam combiner separates the excitation lines from the fluorescence emission.

2.2.3. 2P EXCITATION PATHWAY

In our lab's incarnation of the Octoscope, we employ 2P excitation using a Spectra-Physics InSight X3 with a tunable range from 680 nm to 1300 nm, 120 fs pulse width, and an average power of 1.4 W at 1200 nm. A high-speed laser shutter (LS2, Uniblitz) is used for binary modulation of the laser beam. ND filters are used for analog modulation of the laser beam intensity. The beam is then magnified by a telescope (AC254-150-B-ML and AC254-500-B-ML, Thorlabs) to 5 mm in diameter, and guided to the galvanometric mirrors. The same input port can be used as a separate 1P excitation pathway for widefield illumination without spatial patterning.

To project the beam to the back aperture of the objective, a scan lens (SL50-2P2, 50 mm focal length, Thorlabs) is combined with the Octoscope tube lens (TTL200MP, Thorlabs) to gain a total magnification factor of 4. The resulting maximum diffraction limited field of view is determined by the scan lens in the scanning system, 14.1 × 14.1 mm after the scan lens at the intermediate plane. A long-pass dichroic mirror (Di03-R785-t3-32x44, Semrock) passes the 2P excitation beam into the objective and reflects the 1P excitation and fluorescence emission.

2.2.4. EMISSION PATHWAYS

The emitted fluorescence is collected by the objective, focused by the imaging tube lens (TTL200, 200 mm focal length, Thorlabs), and then filtered by emission filters placed in a linear translation mount (ELL9, Thorlabs). In the experiments described in this chapter, these are band-pass filters (FF01-560/94-25, FF01-582/64-25, LP02-664RU-25 and FF01-790/SP-25, SemRock). The signal is then passed to detection pathway one, or redirected by a mirror mounted on a motorized translation stage (DDSM50/M, Thorlabs) to

detection pathway two. In our lab, we positioned an sCMOS camera (ORCA Flash4.0 V3, Hamamatsu; 2048 x 2048 pixels, 6.5 µm pixel size) on a rail system (XT34HP/M, Thorlabs) with 3D printed adapter and a micrometer head (150-801ME, Thorlabs) for fine adjustment of the focal position in detection pathway one (Figure 2.1(f)). In pathway two, we used an aspherical lens (LAGC065, Ross Optical) to project the back aperture of the objective onto a PMT. We mounted PMTs (H10721-01, peak sensitivity wavelength at 400 nm; H10721-20, peak sensitivity wavelength at 630 nm; Hamamatsu) in a custom 3D printed adaptor for easy mounting and switching (Figure 2.1(g)) in a Thorlabs SM2 lens tube. In the described configuration, the beam combiner, objective holder, and tube lens holder are all part of a micro-machined whole, which makes the compact geometry of the Octoscope possible; nevertheless, the objective focal plane, 2P excitation plane, and camera image plane can all be independently aligned for perfect overlap with the sample plane using the described custom translation mounts.

2.2.5. ELECTROPHYSIOLOGY SETUP

While not a defining feature of the Octoscope, we describe here the electrophysiology modules used for the experiments described in this chapter. We use a motorized stage for petri dish positioning in the inverted configuration (MAC5000, Ludl), and a home-built sample holder in the upright configuration. In our lab, we added a patch clamp amplifier (Model 2400, A-M Systems) and a micromanipulator (PatchStar system, Scientifica) for patch clamp electrophysiology, which enables fast, faithful recording and control of current through and voltage across the cell membrane, which provides a ground truth measurement for the membrane voltage or current dynamics of an individual cell[22]. We supplemented this with a perfusion system (TC-1-100, TC-E50x30, TC-1-100S, PS-8H, Bioscience tools).

2.2.6. SYNCHRONIZATION AND SOFTWARE

Device triggering, control signals for the Galvanometric mirrors, AOTF, and patch clamp electronics, and detection of signals from the patch clamp amplifier are provided by coupled Input/output devices (USB-6363, National Instruments). The output current from the PMT is amplified by a trans-impedance amplifier (DHPCA-100, FEMTO), and filtered by a programmable electronic filter (USBPGF-S1, Alligator technologies) before being sampled. The camera uses a Camera Link card (FireBird PCI Express Gen II 8×) for data acquisition.

Dedicated instrument control software was written in Python, with hardware control interface backend and user interface frontend. This software package, called "gevidaq", will be explained in detail in Chapter 3.

2.3. RESULTS AND DISCUSSION

2.3.1. IMAGING SPECIFICATIONS

In the experiments described here, a long working distance multiphoton microscopy objective is used (Olympus XLPLN25XWMP2, NA: 1.05, working distance 2 mm), for a total magnification of the imaging system of 27.8. Calibration of the FOV provides, in combination with the used excitation and emission pathways, a 507 × 507 µm FOV for 2P imaging and a diffraction-limited resolution of 500 nm nm at 1200 nm excitation; and a 490 × 490 µm FOV for 1P imaging with an image pixel size of 233 nm (based on the employed camera).

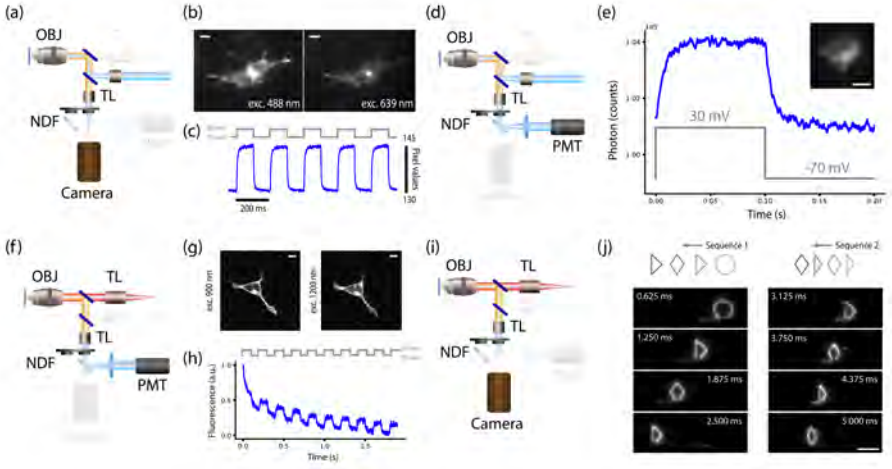

Figure 2.2: Four types of measurements using four different Octoscope configurations. (a) Schematic diagram of camera imaging under 1P excitation. (b) Human embryonic kidney 293T cells (HEK293T cells) expressing Archon1-eGFP[10] under 488 nm excitation (left) and 639 nm excitation (right). (c) Fluorescence trace from camera recording of HEK293T cell expressing Archon1 imaged at 639 nm while membrane potential is changed in steps. (d) schematic of PMT imaging under 1P excitation. (e) Fluorescence recording of a HEK293T cell expressing Archon1 upon altering its membrane potential with a time resolution of 50 μs. (f) Schematic diagram of PMT recording under 2P excitation. (g) 2P image of a HEK293T cell expressing QuasAr1-Citrine[7] under excitation of 900 nm (left) and 1200 nm (right) wavelength. (h) Fluorescence trace from PMT recording under 2P contour scan conditions. (i) Schematic diagram of camera imaging under 2P excitation. (j) Camera recording under 2P patterning (The video is presented as supplementary data on the journal website). Switching laser patterns written into the sample at a switching rate of 1.6 kHz. All scale bars: 10 μm.

2.3.2. MULTIMODAL IMAGING

Fluorescence imaging under widefield 1P excitation (Figure 2.2(a)) provides spatial (Figure 2.2(b)) and temporal (Figure 2.2(c), supplementary video 1) information at resolutions suitable for voltage imaging. For higher time resolution recordings, the PMT can be used for data acquisition (Figure 2.2(d)). In the widefield pathway, patterned illumination using the DMD can be used to specifically illuminate parts of the sample of interest to record e.g. voltage responses of GEVIs with microsecond accuracy (Figure 2.2(e)). Similarly, 2P excitation of the sample and collection of fluorescence on the PMT (Figure 2.2(f)) can be employed for standard raster scanning imaging (Figure 2.2(g)) or patterned illumination where the membrane of a cell can be traced for selective excitation of fluorescence and recording with high time resolution (Figure 2.2(h)). 2P excitation can also be employed with image projection on the camera (Figure 2.2(i),(j), supplementary video 2) for e.g. laser etching[23], local ablation[24] or optogenetic stimulation[25] combined with sample inspection or voltage imaging.

2.3.3. OBJECTIVE ORIENTATION

The rotational motor grants the setup the ability to easily convert between upright and inverted configurations. (Figure 2.3(a)) and effortlessly perform imaging and patterned illumination in both (Figure 2.3(b)). The needed time to convert the configurations only depends on the motor rotating speed, which is currently set to 45 seconds in our setup (Figure 2.3(c), supplementary video 3). In this demonstration experiment, two zebrafish larvae expressing GCaMP6s were positioned onto the two sample stages associated with the inverted and upright configurations. Widefield images of both fish were recorded, after which two DMD illumination patterns were created, one for the top fish and one for the bottom fish. The measurements demonstrate automated, reproducible positioning of the objective and parallel automated switching of illumination patterns, as both fish are illuminated with their appropriate cell selecting DMD patterns. The multimodal capabilities of the Octoscope make it, in the context of voltage imaging, suitable for a range of optogenetic and all-optical electrophysiology experiments, ranging from recordings of protein dynamics[14], single cell and subcellular voltage dynamics[13] to *in vivo* imaging[12].

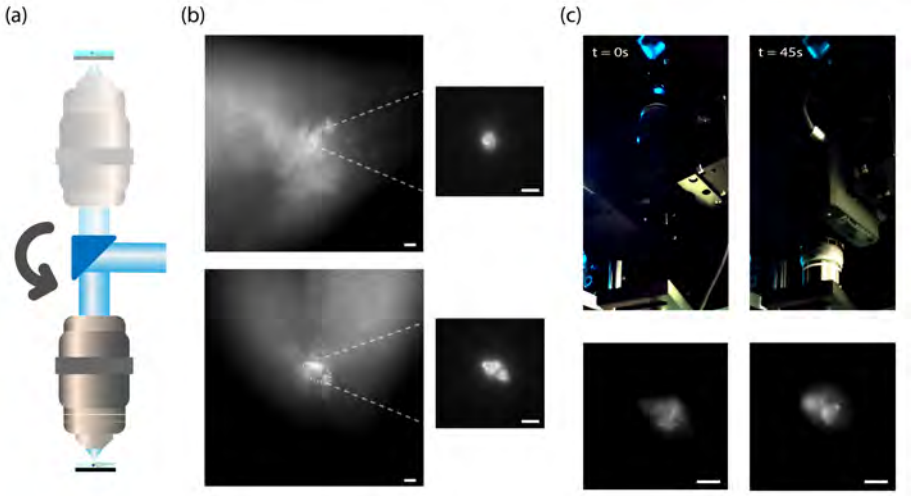

Figure 2.3: Automated inversion of microscope orientation. (a) Sketch of the switching principle. (b) Zebrafish larvae expressing GCaMP6s imaged under widefield excitation with 488 nm, and under DMD projection upon selected cells in dashed line (insert). (c) Two zebrafish larvae expressing GCaMP6s imaged sequentially in inverted (left) and upright configurations (right) in a single automated experiment. Scale bars: 10 µm.

2.3.4. LARGE-SCALE SCREENING IMAGING

The microscope is able to perform large-scale imaging by automated tiling of acquired FOVs with both 1P and 2Pexcitation. Figure 2.4(a) shows the image from a single FOV acquisition with 2P excitation, tuned to 340 µm × 340 µm of sample of cultured HEK293T cells expressing QuasAr1. A zoom-in inspection is shown in Figure 2.4(b), with a pixel resolution of 680 nm. To sample over cells across the petri-dish, 18 × 18 FOVs were automatically imaged and stitched (Figure 2.4(c)). The total area is 6.12 × 6.12 mm, with the diagonal being 8.45 mm. This type of large-scale tiled imaging is useful for, e.g. screens of protein or drug libraries.

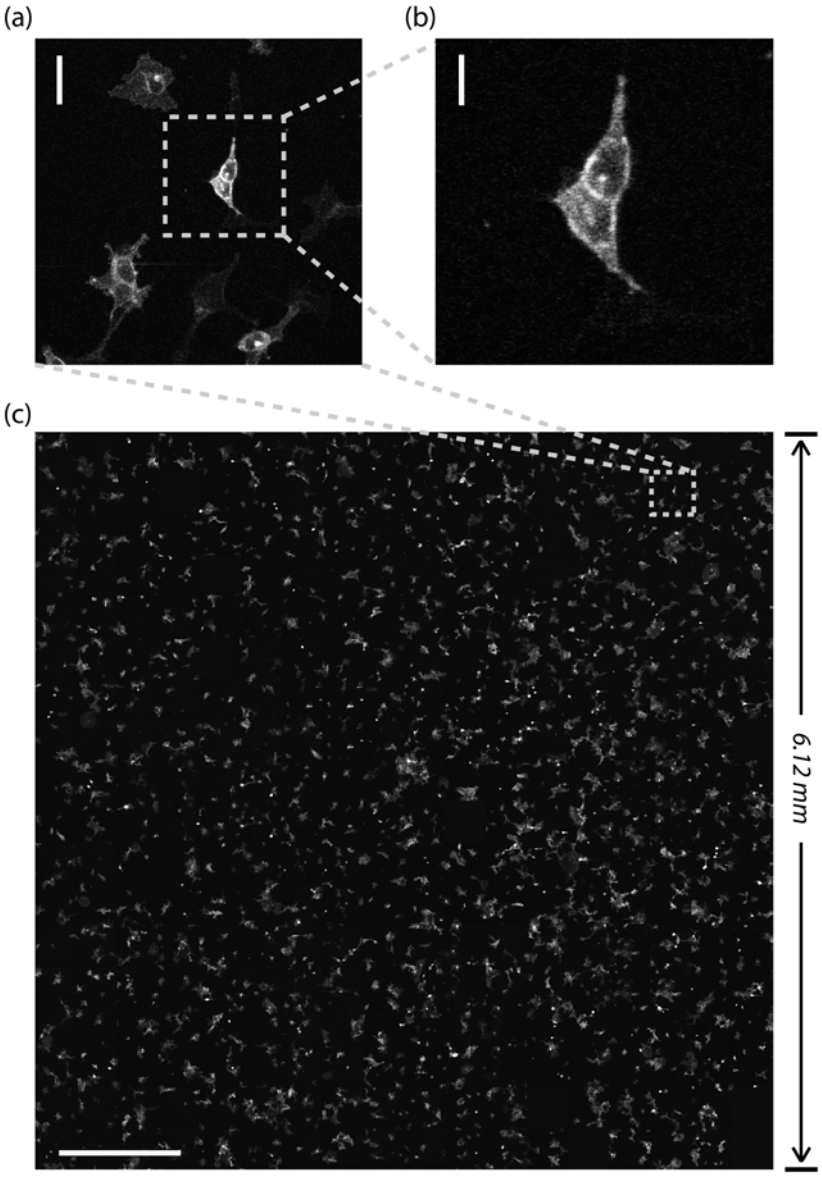

Figure 2.4: Large scale screening 2P imaging under 1200 nm **excitation.** (a) single FOV image of a cell culture of HEK293T cells expressing Archon1. Scale bar: 50 µm. (b) Digital zoom only shows sufficient resolution to mark the cell membrane. Scale bar: 20 µm. (c) large scale image of the same sample with an 8.45 mm diagonal. Scale bar: 1 mm. All images were taken on the Octoscope.

2.3.5. PATTERNED ILLUMINATION

Shaping the illumination reduces background fluorescence and improves the signal-to-noise ratio tremendously, especially for in vivo imaging. The Octoscope is able to pattern both 1P and 2P excitation light onto selected regions with sufficient accuracy to not only tag the cell body (Figure 2.5(a), left), but also the cell membrane (Figure 2.5(a), right). This is useful for voltage imaging as the voltage-sensitive fluorescence is collected from GEVIs located in the cell membrane, and therefore only the outer edge of the cell provides a useful signal, as opposed to, for instance, calcium imaging, where the useful signal can be recorded from the entire cytosol. The cells marked with white dotted lines were selected for projection. The bottom left figure shows whole cell patterning, while the bottom right figure only has the cells' membrane projected. This patterning is also possible *in vivo*. Figure 2.5(b) top left displays a widefield image of a zebrafish larva expressing GCaMP6s, flood illuminated with 488 nm. Fluorescence from different depths contributes to background fluorescence and noise. Patterned illumination was applied to the cell membrane (in the dashed square) using the DMD and 1P excitation (Figure 2.5(b), top right) and using the galvo scanners and 2P excitation (Figure 2.5(c), top right). Cross-section profiles of the cell fluorescence (dashed horizontal lines in Figure 2.5(b) and Figure 2.5(c) bottom), show accurate patterning of the cell membrane in both modalities and a marked increase in SNR and decrease in background fluorescence for both 1P and 2P patterned illumination.

2.4. CONCLUSION

We demonstrate a compact, versatile, multimodal microscope with patterned illumination capabilities and the temporal and spatial resolution necessary for voltage imaging in 1P and 2P excitation schemes, in inverted and upright configurations. The compact design and hardware automation make advanced physical and biological imaging experiments in physical and biological samples possible on the same setup without the need for elaborate hardware reconfigurations or realignment. Patterned illumination capabilities at high spatial and temporal resolution allow a spectrum of voltage imaging, optogenetic, and all-optical electrophysiological experiments, of which we have shown a few proof-of-principle examples.

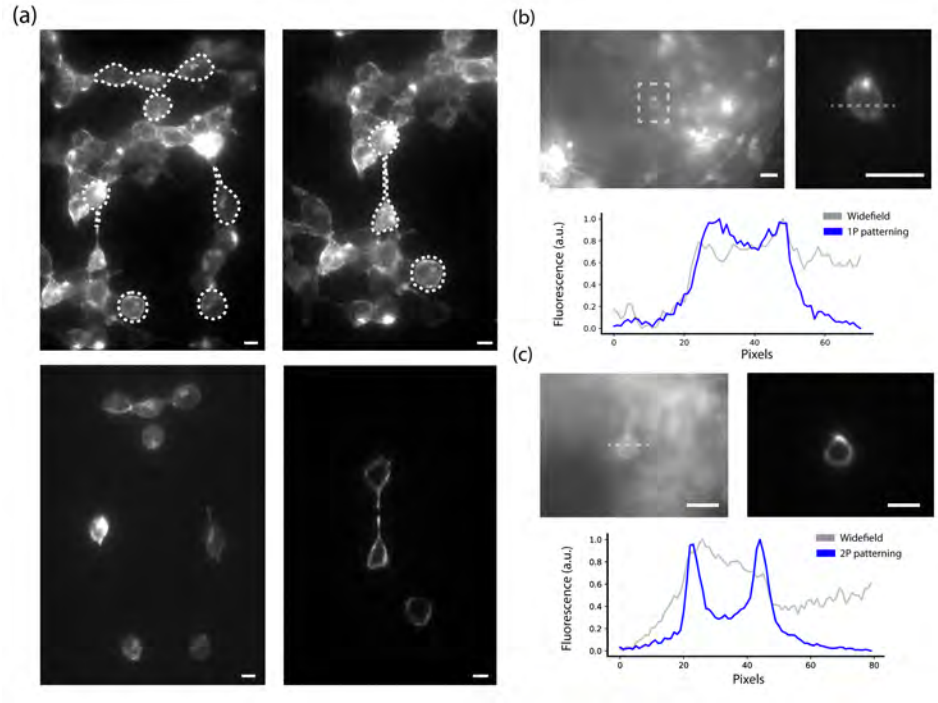

Figure 2.5: Patterned illumination on the Octoscope can mark cell bodies and cell membranes in vitro and in vivo. (a) HEK293T cell cultures (top) imaged with 488 nm excitation. DMD patterning of cell bodies (bottom left) and cell membranes (bottom right) is possible. (b) Top left: Widefield image of cells expressing GCaMP6s in zebrafish larva, excited at 488 nm. Top right: 1P patterning of 488 nm illumination on the cell membrane. Bottom: cross-section along the dotted line in widefield and patterned illumination mode. (c) Top left: the widefield image of cells in zebrafish larva under 488 nm excitation. Top right: 2P patterning of 900 nm illumination on the chosen cell membrane. bottom: cross-section along the dotted line in 1P widefield and 2P patterned illumination mode. Scale bars: 10 µm.

REFERENCES

[1] E. W. Miller. “Small molecule fluorescent voltage indicators for studying membrane potential”. In: *Current Opinion in Chemical Biology* 33 (2016), pp. 74–80.

[2] H. H. Yang and F. St-Pierre. “Genetically encoded voltage indicators: opportunities and challenges”. In: *Journal of Neuroscience* 36.39 (2016), pp. 9977–9989.

[3] Y. Xu, P. Zou, and A. E. Cohen. “Voltage imaging with genetically encoded indicators”. In: *Current opinion in chemical biology* 39 (2017), pp. 1–10.

[4] G. Nagel, T. Szellas, W. Huhn, S. Kateriya, N. Adeishvili, P. Berthold, D. Ollig, P. Hegemann, and E. Bamberg. “Channelrhodopsin-2, a directly light-gated cation-selective membrane channel”. In: *Proceedings of the National Academy of Sciences* 100.24 (2003), pp. 13940–13945.

[5] F. Zhang, L.-P. Wang, E. S. Boyden, and K. Deisseroth. “Channelrhodopsin-2 and optical control of excitable cells”. In: *Nature methods* 3.10 (2006), pp. 785–792.

[6] D. Gradmann, A. Berndt, F. Schneider, and P. Hegemann. “Rectification of the channelrhodopsin early conductance”. In: *Biophysical journal* 101.5 (2011), pp. 1057–1068.

[7] D. R. Hochbaum, Y. Zhao, S. L. Farhi, N. Klapoetke, C. A. Werley, V. Kapoor, P. Zou, J. M. Kralj, D. Maclaurin, N. Smedemark-Margulies, *et al.* “All-optical electrophysiology in mammalian neurons using engineered microbial rhodopsins”. In: *Nature methods* 11.8 (2014), pp. 825–833.

[8] H. H. Yang, F. St-Pierre, X. Sun, X. Ding, M. Z. Lin, and T. R. Clandinin. “Subcellular imaging of voltage and calcium signals reveals neural processing in vivo”. In: *Cell* 166.1 (2016), pp. 245–257.

[9] K. D. Piatkevich, S. Bensussen, H.-a. Tseng, S. N. Shroff, V. G. Lopez-Huerta, D. Park, E. E. Jung, O. A. Shemesh, C. Straub, H. J. Gritton, *et al.* “Population imaging of neural activity in awake behaving mice”. In: *Nature* 574.7778 (2019), pp. 413–417.

[10] K. D. Piatkevich, E. E. Jung, C. Straub, C. Linghu, D. Park, H.-J. Suk, D. R. Hochbaum, D. Goodwin, E. Pnevmatikakis, N. Pak, *et al.* “A robotic multidimensional directed evolution approach applied to fluorescent voltage reporters”. In: *Nature chemical biology* 14.4 (2018), pp. 352–360.

[11] C. A. Werley, M.-P. Chien, and A. E. Cohen. “Ultrawidefield microscope for high-speed fluorescence imaging and targeted optogenetic stimulation”. In: *Biomedical optics express* 8.12 (2017), pp. 5794–5813.

[12] Y. Adam, J. J. Kim, S. Lou, Y. Zhao, M. E. Xie, D. Brinks, H. Wu, M. A. Mostajo-Radji, S. Kheifets, V. Parot, *et al.* "Voltage imaging and optogenetics reveal behaviour-dependent changes in hippocampal dynamics". In: *Nature* 569.7756 (2019), pp. 413–417.

[13] M.-P. Chien, D. Brinks, G. Testa-Silva, H. Tian, F. Phil Brooks III, Y. Adam, B. Bloxham, B. Gmeiner, S. Kheifets, and A. E. Cohen. "Photoactivated voltage imaging in tissue with an archaerhodopsin-derived reporter". In: *Science advances* 7.19 (2021), eabe3216.

[14] V. Venkatachalam, D. Brinks, D. Maclaurin, D. Hochbaum, J. Kralj, and A. E. Cohen. "Flash memory: photochemical imprinting of neuronal action potentials onto a microbial rhodopsin". In: *Journal of the American Chemical Society* 136.6 (2014), pp. 2529–2537.

[15] V. Venkatachalam and A. E. Cohen. "Imaging GFP-based reporters in neurons with multiwavelength optogenetic control". In: *Biophysical journal* 107.7 (2014), pp. 1554–1563.

[16] D. Brinks, A. J. Klein, and A. E. Cohen. "Two-photon lifetime imaging of voltage indicating proteins as a probe of absolute membrane voltage". In: *Biophysical journal* 109.5 (2015), pp. 914–921.

[17] H. Tian, H. C. Davis, J. D. Wong-Campos, L. Z. Fan, B. Gmeiner, S. Begum, C. A. Werley, G. B. Borja, H. Upadhyay, H. Shah, *et al.* "All-optical electrophysiology with improved genetically encoded voltage indicators reveals interneuron network dynamics in vivo". In: *bioRxiv* (2021).

[18] K. Ataka and V. A. Pieribone. "A genetically targetable fluorescent probe of channel gating with rapid kinetics". In: *Biophysical journal* 82.1 (2002), pp. 509–516.

[19] Z. Han, L. Jin, J. Platisa, L. B. Cohen, B. J. Baker, and V. A. Pieribone. "Fluorescent protein voltage probes derived from ArcLight that respond to membrane voltage changes with fast kinetics". In: *PloS one* 8.11 (2013).

[20] F. St-Pierre, J. D. Marshall, Y. Yang, Y. Gong, M. J. Schnitzer, and M. Z. Lin. "High-fidelity optical reporting of neuronal electrical activity with an ultrafast fluorescent voltage sensor". In: *Nature neuroscience* 17.6 (2014), p. 884.

[21] B. Li, M. Chavarha, Y. Kobayashi, S. Yoshinaga, K. Nakajima, M. Z. Lin, and T. Inoue. "Two-photon voltage imaging of spontaneous activity from multiple neurons reveals network activity in brain tissue". In: *Iscience* 23.8 (2020), p. 101363.

[22] E. Neher and B. Sakmann. "The patch clamp technique". In: *Scientific American* 266.3 (1992), pp. 44–51.

[23] H. Ouyang, Y. Deng, W. Knox, and P. Fauchet. "Photochemical etching of silicon by two photon absorption". In: *physica status solidi (a)* 204.5 (2007), pp. 1255–1259.

[24] X. Liang, M. Michael, and G. A. Gomez. "Measurement of mechanical tension at cell-cell junctions using two-photon laser ablation". In: *Bio-protocol* 6.24 (2016), e2068–e2068.

[25] R. Prakash, O. Yizhar, B. Grewe, C. Ramakrishnan, N. Wang, I. Goshen, A. M. Packer, D. S. Peterka, R. Yuste, M. J. Schnitzer, *et al.* “Two-photon optogenetic toolbox for fast inhibition, excitation and bistable modulation”. In: *Nature methods* 9.12 (2012), pp. 1171–1179.

3

AN ADVANCED SOFTWARE FOR VOLTAGE IMAGING: GEVIDAQ

Advanced microscope systems have been applied to facilitate Optogenetics experiments. However, so far, there is no open-source software dedicated to hardware control and data analysis for this type of experiment. Here we developed an advanced and user-friendly software, called "gevidaq", for voltage imaging in Python. This software features a modular widget design, which allows flexible hardware recruiting for different tasks. The software integrates a data analysis module with a machine learning-powered cell segmentation algorithm that provides instant analysis feedback. We demonstrate the software in various applications in our lab.

3.1. INTRODUCTION

OPTOGENETICS has revolutionized our understanding of neural circuitry and dynamics by allowing optical perturbation of the electrical signaling of neurons with high spatial and temporal resolution[1–4]. The complementary tool of voltage imaging, which was recently added to the neuroscientific toolbox and is substantially the topic of this thesis, similarly allows the recording of the electrical dynamics of neurons with high spatial and temporal resolution. The combination of the two techniques creates the possibility of interrogating neural circuits as an optical input-output system in a way that was not possible before[5–7]. The successful implementation of such input-output assays at a microscopic level requires a rethinking of the concept of the microscope, not as a device that makes nice images that are interpreted after the fact, but as an automated, robotic system that permits real-time actuation and manipulation and observation of a live sample. Moreover, it can observe information in a feedback loop both for improved data gathering and novel types of experiments.

In the previous chapter, I have laid out our interpretation of the rethinking of a microscope for this kind of voltage imaging work; this chapter will focus on a rethinking of the software driving such a system.

To achieve the smart voltage imaging above, first, different parts of the microscope, such as laser illumination, patterning devices (Digital Micromirror Device (DMD) and acousto-optic tunable filter (AOTF)), and fluorescence acquisition, need to work in coordination with sub-millisecond-precision synchronization. To sample the signals flowing inside a neuron network, the spatial and temporal patterning must happen at least twice as fast as the frequency of neuron signals, which could go higher than a Kilohertz. Second, during an optogenetics experiment, it is crucial to be able to adapt the patterning and alter the synchronization in a short time with ease, depending on the presented sample or field of view's characteristics. The spatial organization of a biological neural network is highly complicated, and an interrogation process would require trial and error on a range of different sites. The sample neural network displays dynamics on different time scales; thus, constant targeting is never sufficient, especially considering the fluorescence bleaching. Therefore changing imaging targets is necessary. Ideally, the time spent on setup configuration between acquisition sections should be negligible. Third, data analysis in real-time is essential to provide feedback to guide the next round of experiments. For example, when characterizing the optogenetics tool's kinetics, the frequency of the command voltage signal generated via patch clamp across a cell membrane should be adapted according to the kinetics time constant, which can only be calculated by implementing a testing round.

A comprehensive and intelligent software is required to address these requirements. While smart microscopy is a broad topic, the temporal bandwidth, spatial resolution, interfacing with electrophysiological, microfluidic and mechanical components, complex cellular morphologies and cellular dynamics involved in voltage imaging and optoge-

Link to the GitHub page of gevidaq: https://github.com/Brinkslab/gevidaq.git

netics experiments means that current software packages are not sufficiently smart or flexible.

Here we, as the daily users of the all-optical electrophysiology setup (for the setup, see [8]) in a voltage imaging lab, developed the software that meets these requirements, named "gevidaq". The software can set up and coordinate all different parts of the microscope system, with seamless information sharing between them. Catering to a vast range of experiments, the user can customize the investigation pipeline or even the software itself with great flexibility, which is realized based on the widget units for each hardware piece. The data analysis package inside the software provides analytical numbers for each type of experiment with minimum configuration needed. Powered by a machine-learning-based cell detection neural network, the cell segmentation ability is robust and accurate and can share detection results within all microscope widgets for potential applications. The graphical user interface is user-friendly and flattens the learning curve. The software powers the home-built microscope in our lab and performs multiple voltage imaging experiments[8]. In this chapter, we will introduce the design principles (section 3.2), implementation of these principles (section 3.3), different software tools inside (section 3.4.1), and applications (section 3.4.2) using gevidaq. With the open-source gevidaq, we would like to contribute a free programming tool to the neuroscience committee to accelerate the research progress.

Figure 3.1: The logo of gevidaq. This chapter resulted in an open-source software package, gevidaq, that aims to provide a free framework for neuroscientists to program their own experimental software. Link to the GitHub page: https://github.com/Brinkslab/gevidaq.git

3.2. DESIGN PRINCIPLES

Voltage imaging experiments typically involve coordination between different sets of devices for different types of experiments. Taking that into account, the primary design principle is modular programming, in which each piece of hardware control or a function unit is a module. The corresponding control modules can easily be assembled when recruiting a different set of functional units. The communication between modules can be channeled through the main panel so that the information generated from the in-

dividual pieces can be shared with the whole assembly. This is a crucial feature of this intelligent microscope. The analysis module can pass the results to all parts of the software through this inter-module communication and then guide the decision-making for the next experiment.

Here the incarnation of the module is a widget. A widget for each function unit is composed of a front-end graphical interface and a back-end actuator. Commanding the hardware can be done via human interaction through the widget user interface or by calling the functions in the application programming interface (API) from the backend. A widget can call functions from its backend(s) from other widgets. Each widget can stand alone and run itself. For applications that involve a selection of widgets, the main panel can be created as a deck to contain the useful widgets and pass information between them, as illustrated in Figure 3.2.

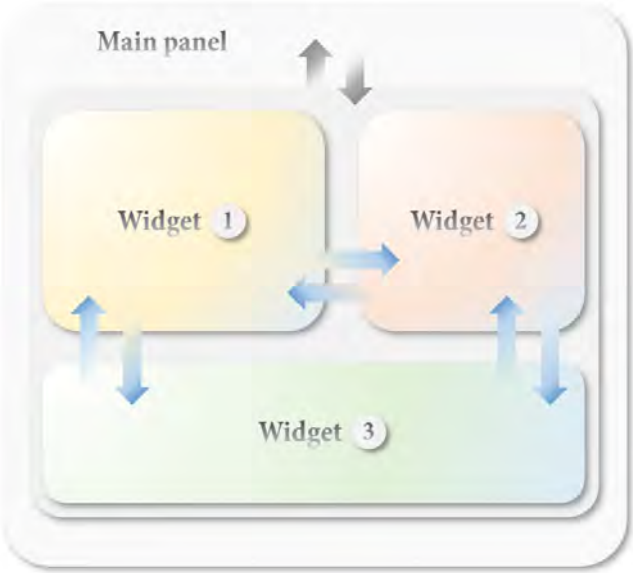

Figure 3.2: Software design principle. The software is modularised into widgets, where each widget is in charge of one specific function. Each widget has a graphical user interface (GUI) and a backend that provides a mutual interface. Individual widgets can be assembled on a motherboard.

3.3. IMPLEMENTATION

3.3.1. DEPENDENCIES

PROGRAMMING LANGUAGE

Being able to run every piece of the setup programmatically in one language is vital for improving efficiency and allowing future development. In most cases, devices come with software provided by the manufacturer, and commercial software like LabVIEW and Matlab can take care of most of the hardware control and data analysis. However, integrating various programming languages limits the accessibility of the code. Using separate executables controlling individual pieces of hardware blocks synchronization, as it is not straightforward to pass variables, parameters, or data from one device to another.

The open-source language Python is chosen as the programming language[9]. It has a short learning curve, good readability, and vast library support. It is also the most widely used programming language for machine learning, which eases the integration of machine learning networks into the system. With its excellent portability, deploying it on different PCs is straightforward. The same software has been deployed on multiple PCs for different setups (Figure 3.3).

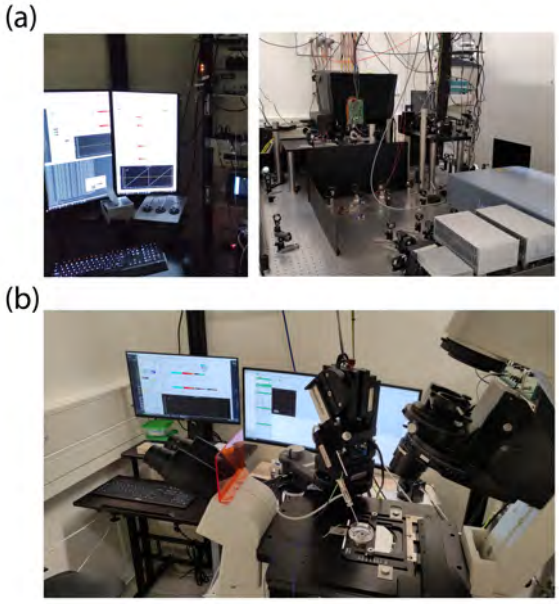

Figure 3.3: Setups that run gevidaq software. (a) The multimodal fluorescence microscope which is introduced in Chapter 2 uses gevidaq as the only operation software. (b) A fluorescence-lifetime imaging microscope uses gevidaq to run the electrophysiology experiments.

GRAPHICAL USER INTERFACE

Without a graphical user interface (GUI), the software operation learning curve becomes extremely steep, and the flexibility while running the software dramatically decreases. We developed a user-friendly GUI that should allow novice users to operate the software.

We chose the Python package PyQt5 as the building library for the GUI because it offers fast plots for embedded graphs. The PyQt5 library features a great variety of support for building widgets. In PyQt5, each user's action will emit a 'signal', which is received by a 'slot' that can be a function inside or outside the widget. The communication between widgets can be established by connecting output PyQt's signals to other widgets' slots. It is also possible to gather output variables to the main panel to make it global or import global data.

The graphical data display gives informative feedback and is an important part of a GUI. We chose PyQtGraph as the graphics library for the software. Compared to other Python graphics libraries like Matplotlib, it features rich interactions and fast display. These are important to our applications, as in a lot of cases, we need user input to define spatial information, and fast display to monitor dynamics.

CELL SEGMENTATION NETWORK

The cell segmentation accuracy determines the precision level of the feedback from the smart microscope system. To account for the complex spatial distribution of cells, we trained a machine learning network to take over the cell segmentation task. The algorithm, called Mask R-CNN, is based on a regional-based convolutional neural network[10]. It provides accurate segmentation masks with category information even when the cells are clustered together. The details are introduced in section 6.3.3.

3.3.2. HARDWARE CONTROL WIDGETS

The hardware control widgets library includes a variety of devices from different manufacturers; each has its software logic and control protocols. In general, there are three levels of interaction with the hardware: via direct construction and sending of serial commands; via calls to and use of the application programming interface (API), or via direct input/output (IO) of analog (0 to 5 V) or digital (0 or 5 V) voltage signals via a data acquisition and control/multifunctional IO platform (see Chapter 2). Both front-end user interface widgets and backend hardware control interfaces are built for each device.

SERIAL COMMUNICATION

Serial communication, in which data is transferred sequentially one bit at a time, is widely used in computer communication, such as Universal Serial Bus (USB) port, Ethernet port, or High-Definition Multimedia Interface (HDMI) port. In Gevidaq, widgets use the RS-232 standard for control of, for example, a motorized sample stage (MAC5000, Ludl), a motorized filter slider (ELL9, Thorlabs), a femtosecond pulsed laser (Spectra-Physic Insight X3), and a micro-manipulator (Patchstar, Scientifica).

The Python library used here is PySerial, which encapsulates the communication through serial ports. An example is shown in the Appendix 3.6.

Sample stage control With the sample stage widget, the sample stage carrying a petri dish can move to an absolute target coordinate; parameters such as movement speed can be set in advance. Relative movement can be performed using the four arrow buttons or keyboard shortcut (Figure 3.4).

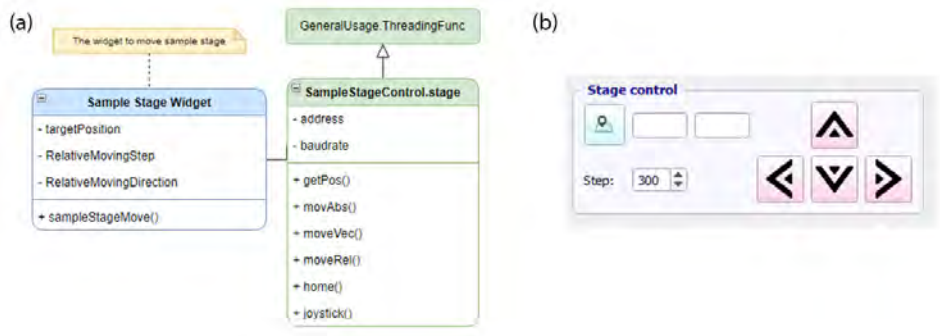

Figure 3.4: Class diagram and GUI of the sample stage control widget. By inputting the coordinates, the sample stage can move to an absolute position. Relative movement can be achieved by clicking the arrows with four directions marked.

Filter widget Two groups of filters are crucial in a microscope system: excitation filters that regulate the wavelength and amplitude of excitation laser and emission filters that block unwanted wavelength. These filters are mounted on sliders whose positions can be controlled through serial communication. The filter widget has two control containers, where buttons specify the filters that are placed (Figure 3.5).

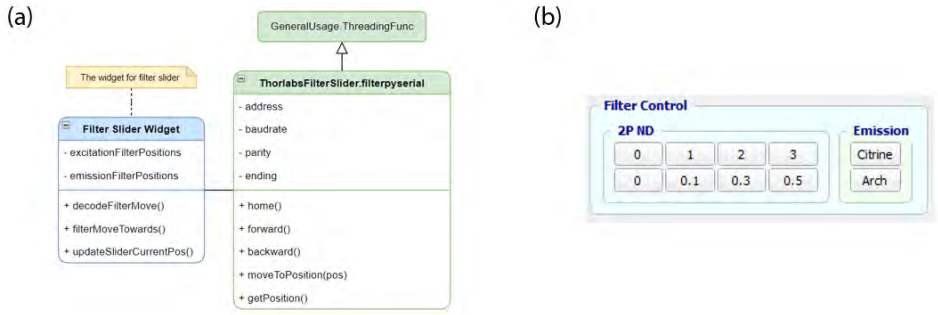

Figure 3.5: Class diagram and GUI of the filters widget. Clicking the button will switch the corresponding excitation or emission filter into the optical pathway.

Laser control Through the laser widget (Figure 3.6), the tunable femtosecond pulsed laser (Insight X3, Spectra Physics) can be controlled through interaction with UI or calling its backend functions. The laser can switch between running and alignment modes, which regulates the output power. Switches of the pump laser diode and shutter are placed below, along with spin-boxes that set the wavelength and the status watchdog timeout. A laser status watchdog thread will run continuously in the back end and update the current status in the UI. When closing the widget, the user can choose from "Standby" which does not shut off the laser diode, and "Hibernate" which does shut it off.

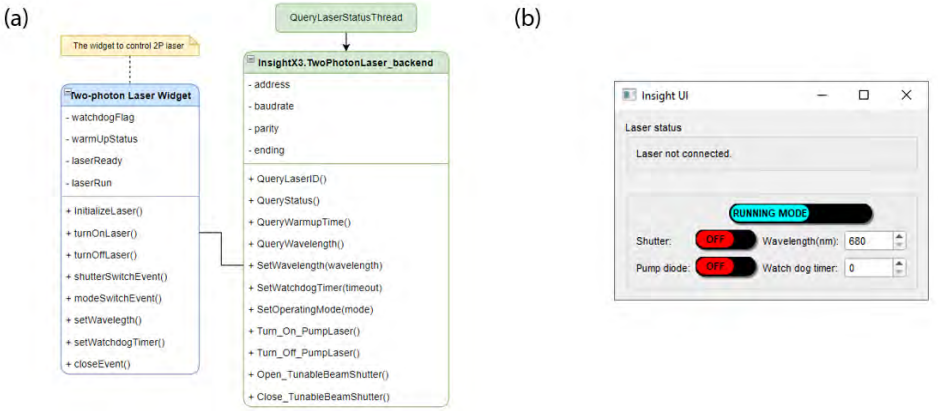

Figure 3.6: Class diagram and GUI of the laser control widget. The laser status is monitored and shown on the top part. The backend uses serial commands to control the laser and monitor the laser status continuously in a thread.

APPLICATION PROGRAMMING INTERFACE

An application programming interface (API) is a function and protocol assembly to interface or integrate with other application programs. In Windows systems, it usually manifests as dynamic-link library files. A dynamic-link library (DLL) is a highly modularized function library developed by Microsoft. It realizes the flexible and efficient reuse of encapsulated functions and data for other applications. As most executable software assembles all the core functions in its DLL files, it is possible to utilize provided DLL files to perform the same operations as the original software from manufacturers. Some manufacturers such as Thorlabs and Hamamatsu provide API and software development kits (SDK) for researchers to facilitate their software customization, and some such as Physik Instrumente and National Instruments, directly provide a completed Python wrapper library for customers with detailed documentation.

We built several backend interfaces based on manufacturer-provided DLL files. As most DLLs are coded in C or C++, to call them in Python, a foreign function library called ctypes is used to wrap the shared library with C compatibility.

Camera control The camera is the most important and complicated part of the microscope. To communicate with the Hamamatsu ORCA-Flash 4, we built a widget with a backend actuator to realize most of its functions, with improvements in operating logistics compared to the commercial software. The backend actuator also provides the interface to many other widgets, supplying captured images to for instance the coordinates widget and the screening widget.

The Hamamatsu camera UI is shown in Figure 3.7. It mainly contains three parts: camera general settings, acquisition setup, and live viewing display. In general settings containers, parameters for instance exposure time, region of interest settings, and timing clock settings, can be configured. In the acquisition part, a spec container updates readout camera properties such as internal frame rate and exposure time; in the "live" tab, a user can start and end the camera live streaming, snap the image, and save the snapped image; in the recording configuration tab, recording parameters, video length and buffer size for example can be set. The live view is updated in the right viewing window when the camera is live streaming. Through mouse interaction, the live view can pan and zoom in and out. The auto contrast adjustment of the live view can be switched on and off. An ROI item can be placed in the image for magnified viewing. It is also the field of view indicator for sub-frame recording. An indicator above the ROI selector displays the maximum frame rate achievable in the region.

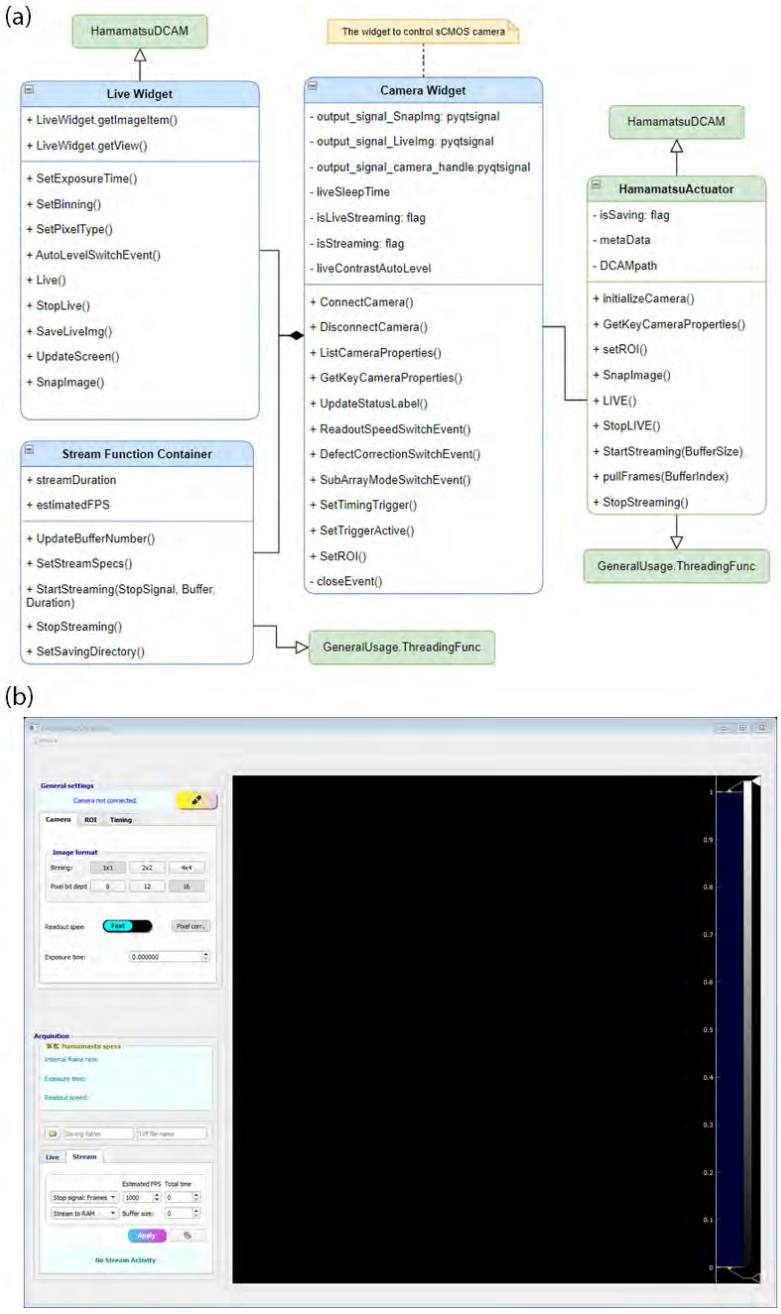

Figure 3.7: Class diagram and GUI of the Hamamatsu camera widget. The camera widget can realize the same functions as the commercial software, with a GUI improved in user-friendliness. The backend provides an interface for other widgets to recruit the camera.

To build the Hamamatsu camera backend, a DCAM-API (Digital CAMera Application Programming Interface) is provided. Through this API, one can call standard camera functions from other programming languages such as Python. A basic interface to the Hamamatsu camera was provided on Github (https://github.com/ZhuangLab/storm-control.git), and our backend actuator was further developed based on it. To use the interface, a simplified example is shown in the Appendix 3.6.

Objective motor control The motor control widget is in charge of the communication between the lab PC and the carrier motor. After connecting the motor through the function provided by the API, a user can call commands, for example, move to an absolute target position or a relative one. The widget keeps track of the motor's current position and shows it in the spin-box. A sliding bar, which also indicates the current position, is placed to facilitate quick adjustment. This is quite convenient when finding the focus.

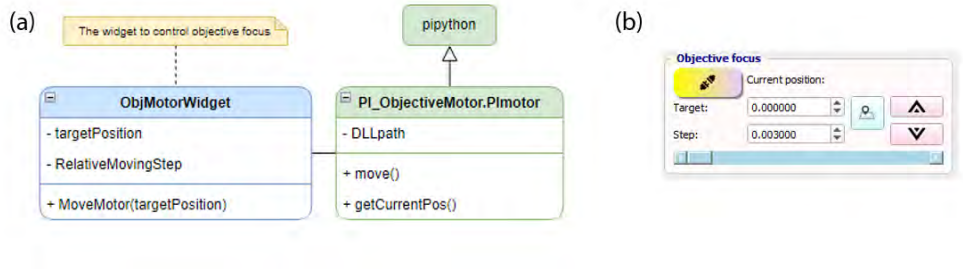

Figure 3.8: Class diagram and GUI of the motor control widget. The motor's manufacturer PI (Physik Instrumente) provides an API to interface with the motor. Calling its function through ctypes can drive the objective to a precise focus.

Coordinates widget To make a spatial patterning through a DMD or galvo scanning mirrors, there are three main processes that need to happen in sequence: a user's input route, translation to the projector's coordinates, and execution. We integrate all these functions into one coordinates widget.

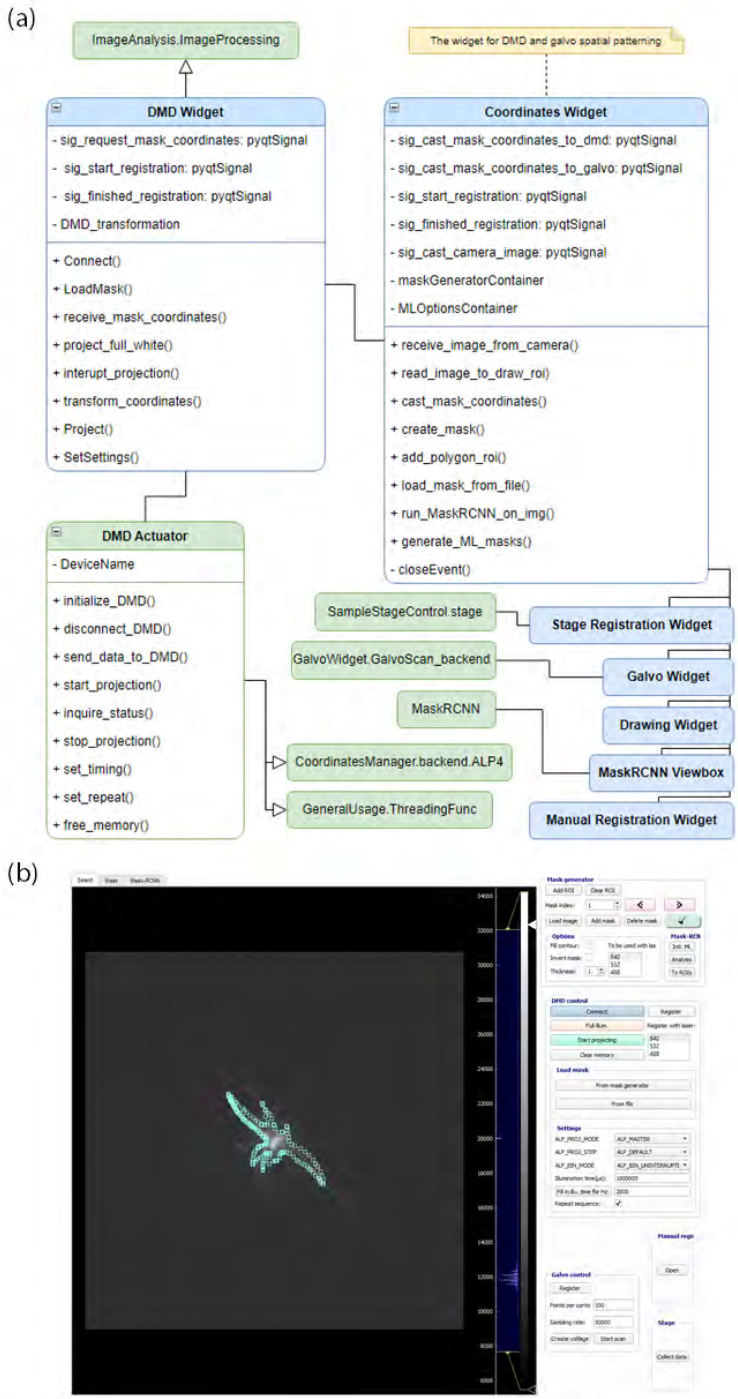

Figure 3.9: Class diagram and GUI of the Coordinates widget. The coordinates widget realizes the excitation laser's spatial patterning. The user's input masks, either from free-hand drawing or selecting machine learning generated ROIs, will be transformed into the projector's coordinates for projection.

For user input, a drawing widget is developed. The canvas can be a live camera image or an image file loaded by browsing file explorer. Defining the mask can be done through freehand drawing, polygon selection, or by selecting machine learning segmented ROIs. The masks can be adjusted by dragging the ROI handles. Multiple masks can be added in sequence for projection. The drawing widget is placed on the left side of the coordinates widget.

The second part, translation to the projector's coordinates, is done by the coordinates widget itself. The registration procedure contains two parts. The first part is obtaining the corresponding coordinates in the camera image, which is done by projecting grids of circle masks onto fluorescence markers and locating them on the camera. Then, these coordinates are used in a first-order polynomial transformation to calculate the transformation matrix. The DMD registration involves AOTF, camera, and DMD backend. A similar concept is used for registration of the galvo mirrors registration.

For the actual projection, a DMD widget is developed for DMD control. It can load the masks from the drawing widget or from existing binary images or videos. Detailed settings, for instance, the projecting mode and illumination time, can be defined in the settings container. The DMD can be set to controller projection mode, in which it runs on its own clock, or worker mode, in which it waits for trigger input from other devices.

Translation stage widget In order to select the emission pathway, we placed a reflection mirror on a motorized translation stage, which moves the mirror in or out of the pathway. The manufacturer provides an API for the control, which is relatively straightforward. With the "Move" function, the stage moves the reflection mirror into the pathway to direct the emission toward the PMT. With the "Home" function, the mirror is carried outside the pathway so that the emission goes into the camera instead. In the widget, the switching is realized through a toggle button that writes "camera position" and "PMT position" (3.10).

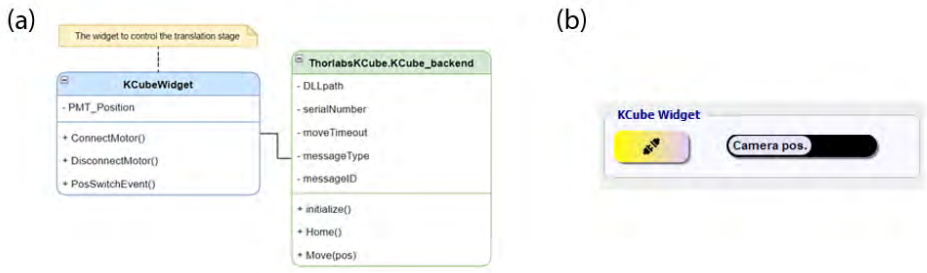

Figure 3.10: Translation stage widget. The widget to control the Thorlabs' KBD101 K-Cube brushless DC motor. In the Octoscope it is used to switch the image acquisition device, and it is controlled by the toggle button.

DATA ACQUISITION PLATFORM

Many devices in the setup, for instance, galvanometer scanner, patch clamp amplifier, perfusion system, and AOTF, directly require analog or digital control signals. In contrast, others such as PMT send out current signals that need to be measured. A central data acquisition platform is needed to issue all these tasks in synchronization. The National Instruments data acquisition (DAQ) card is employed as the electronic signals interface solution between the end device and computer.

NI-DAQmx is the latest data acquisition driver of National Instruments for the DAQ board hardware. The manufacturer provides an API (Application Programming Interface) implemented in Python, named nidaqmax, for interacting with it. As the original NI-DAQmx driver is implemented in C, the package is essentially a ctypes Python wrapper around it. A simple example of writing and reading signals is shown in the Appendix 3.6.

To provide easy access to the DAQ functions through Python, a comprehensive backend, DAQ operator, was developed based on the nidaqmx package. It only requires desired outboard signals and recording channels as input and will take care of organizing waveforms, configuring hardware, and DAQ execution (Figure 3.11). All DAQ-related applications can use the DAQ operator backend as the interface to control the DAQ.

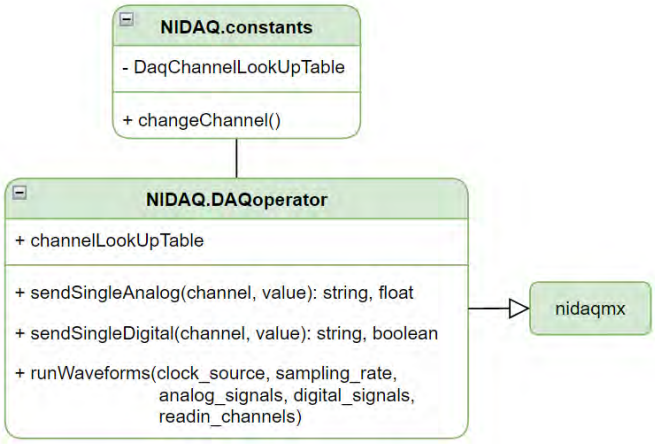

Figure 3.11: Class diagram of the NI-DAQ backend: DAQ operator. It inherits the manufacturer-provided nidaqmx package and reprograms the execution process into a single function that takes only essential inputs.

AOTF widget An acousto optic tunable filter (AOTFnC-VI S from AA Optoelectronics) allows parallel fast intensity modulation on specific wavelengths. The amplitude of the RF wave passing through the birefringent crystal can be modulated through the input analog and digital signals. The AOTF widget has sliders and textboxes as input to set the

laser amplitudes and a toggle button to set the laser on and off (Figure 3.12). The input will be converted into voltage signals and fed into the DAQ for execution.

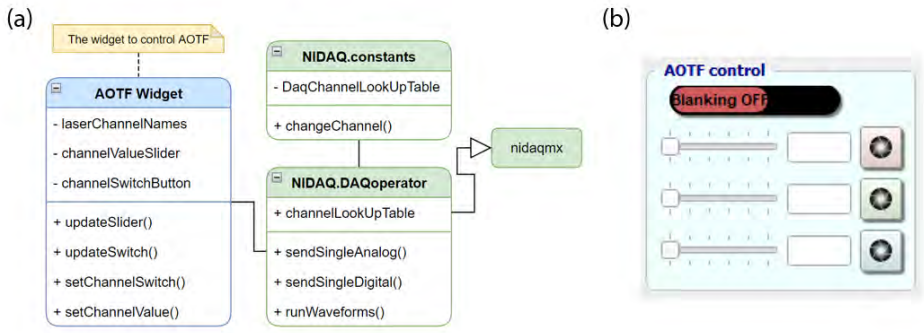

Figure 3.12: Class diagram and GUI of the AOTF widget. The widget turns the input sliding bar's positions into analog signals sent from the NI-DAQ. The blanking all button controls the digital input to the AOTF which governs the binary on and off.

Seal test widget The seal test is essential for setting up the patch clamp experiments, as it provides continuous electric feedback to the user to help infer the probe status. A seal test widget is built to configure the parameters and translate the DAQ signals into data that reflects the patch status in real-time (Figure 3.13).

In a seal test, a continuous voltage signal is supplied to the probe, and the patch circuit's current is monitored. For the testing wave setup, the "Gain" and "Wave settings" containers in the widget determine the probe's gain and the waveform's amplitude. The actual sending and receiving of the voltage and current signals are done through the DAQ backend. A Sliding Window widget is built and embedded inside the main window to display the received signal from the patch amplifier. The current is displayed as a single period corresponding to a voltage probing cycle. The resistance and capacitance are extracted from the current and displayed in real-time under the current display window. This information gives a measure of the patch quality. To facilitate the patch clamp break-in process, the "Zap" function is available, which sends short pulses of high-voltage waveform to the patch amplifier.

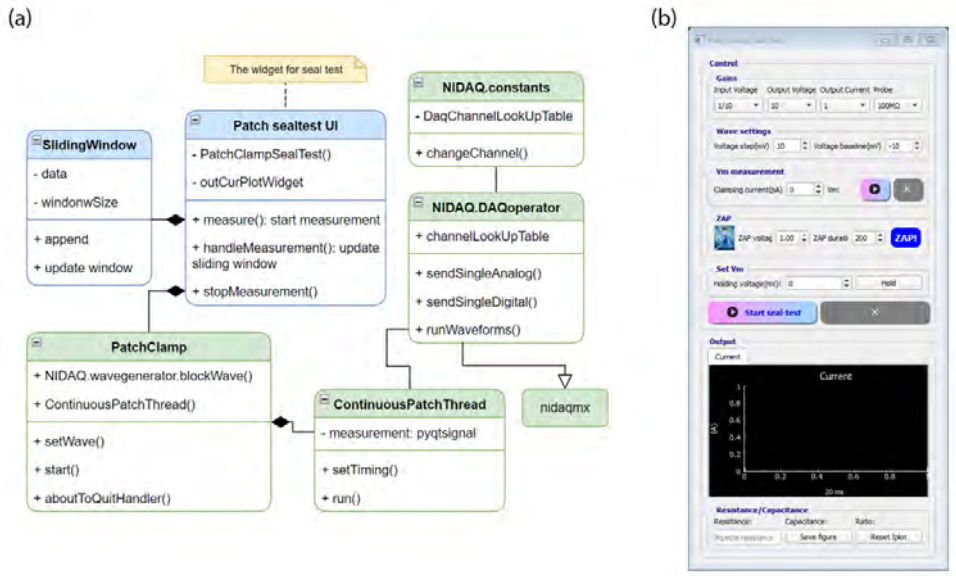

Figure 3.13: Class diagram and GUI of seal test widget. The seal test widget facilitates the patch clamp process by providing real-time feedback, plots, and numbers from the patch amplifier circuit.

Galvo scanning widget The galvanometer scanning mirrors navigate the two-photon laser spot to follow the desired path on the sample. They receive analog voltage signals and translate them into rotating angles determining the laser's landing spot. A galvo scanning backend was written to generate all the scanning routes, including raster scanning, contour scanning, and z-stack scanning. A widget UI was built to interface with the backend, requiring minimal parameter input. When doing the raster scanning, the voltage signals received by DAQ are constructed to form an image, and the image is updated in the live view window continuously. A small viewing window on the right allows real-time monitoring of selected regions of interest from raster scanning images. For contour scanning, a user can place the handles of an ROI item on the raster scanning image to determine the scanning route. The route can be easily adjusted by mouse interaction. When generating the scanning route according to the ROI item and input parameters, the backend checks if this would have the risk of exceeding the maximum acceleration that the scanning mirror can handle. During the scanning, the PMT readings are stored and used to reconstruct the image.

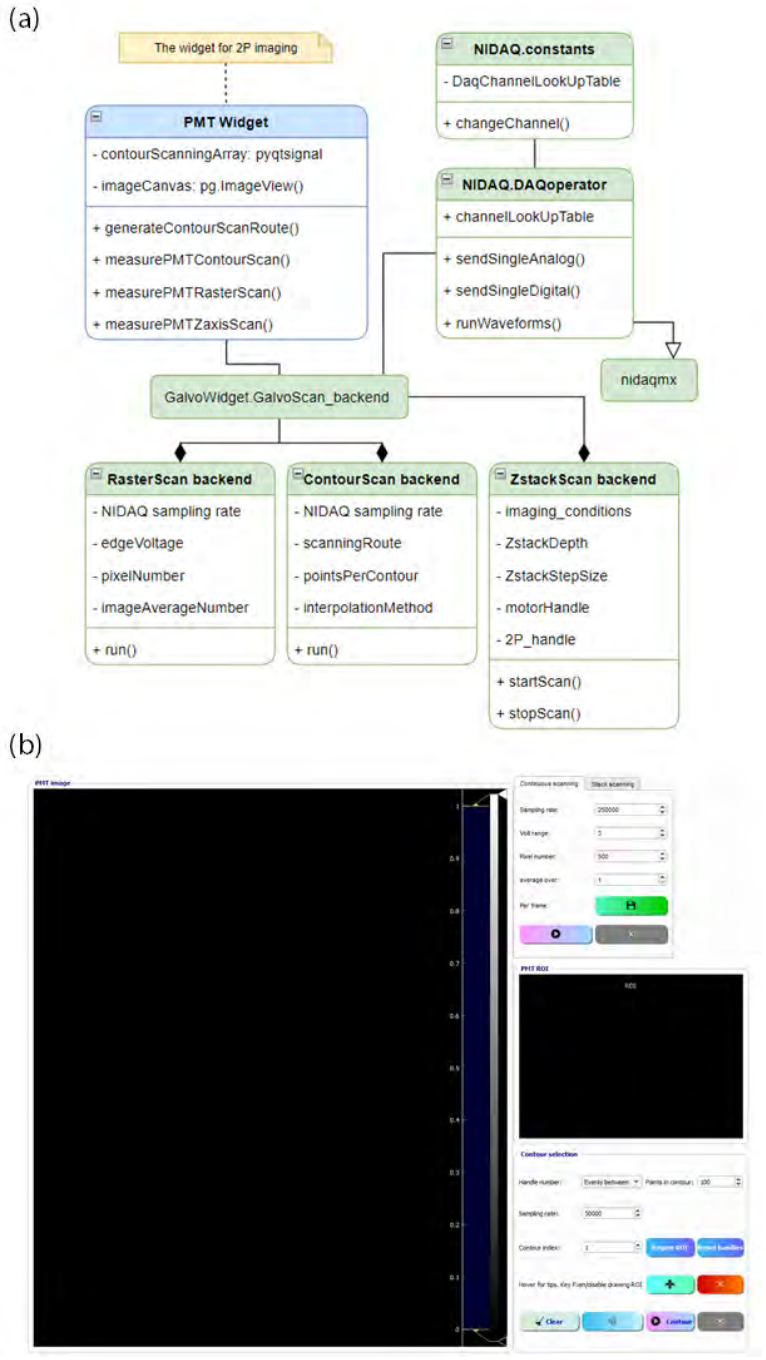

Figure 3.14: Class diagram and GUI of the galvo scanning widget. The widget can provide both the raster scanning live view and the user definited contour scanning. The galvo scanning backend translates the parameter input to corresponding numerical arrays that will be the output from the NI-DAQ.

Waveform widget Figure 3.15 shows the waveform widget through which analog/digital signals can be configured or loaded from a pre-saved file. It is the main widget to interact with the NI-DAQ system (USB-6363, National Instruments), which allows synchronized signaling with high time resolution. High temporal resolution is crucial for the voltage imaging experiment that observes millisecond-scale neuronal events using a complex microscope system. The waveform widget can control the NI-DAQ system to synchronize the devices with trigger signals that can be sampled up to two million times per second.

The widget contains three main parts: a UI, a wave generator, and an operator, which communicats with the DAQ. The UI, which is shown in Figure 3.15(b), contains the input of the required parameters to generate analog and digital waveforms for different devices. A wave generator takes this input and makes the arrays. The shape of the analog waveform ranges from a block, ramp, and defined galvo raster scanning to a contour scanning pattern. The waveform segments can be appended or repeated with the desired delay or offset in between. The corresponding trace will show in the bottom visualization window when generating waveforms. The generated waveforms can be forwarded to DAQ for execution or passed to other widgets depending on requirements. The DAQ operator, as explained in Figure 3.11, takes the waveforms, configures the hardware, and starts the execution. Ahead of running the waveforms, the emission filter slider will move to the position ticked in the "Emission filter" container to ensure correct filtering if fluorescence recording is involved. During the waveform execution, a progress bar will display the progress percentage.

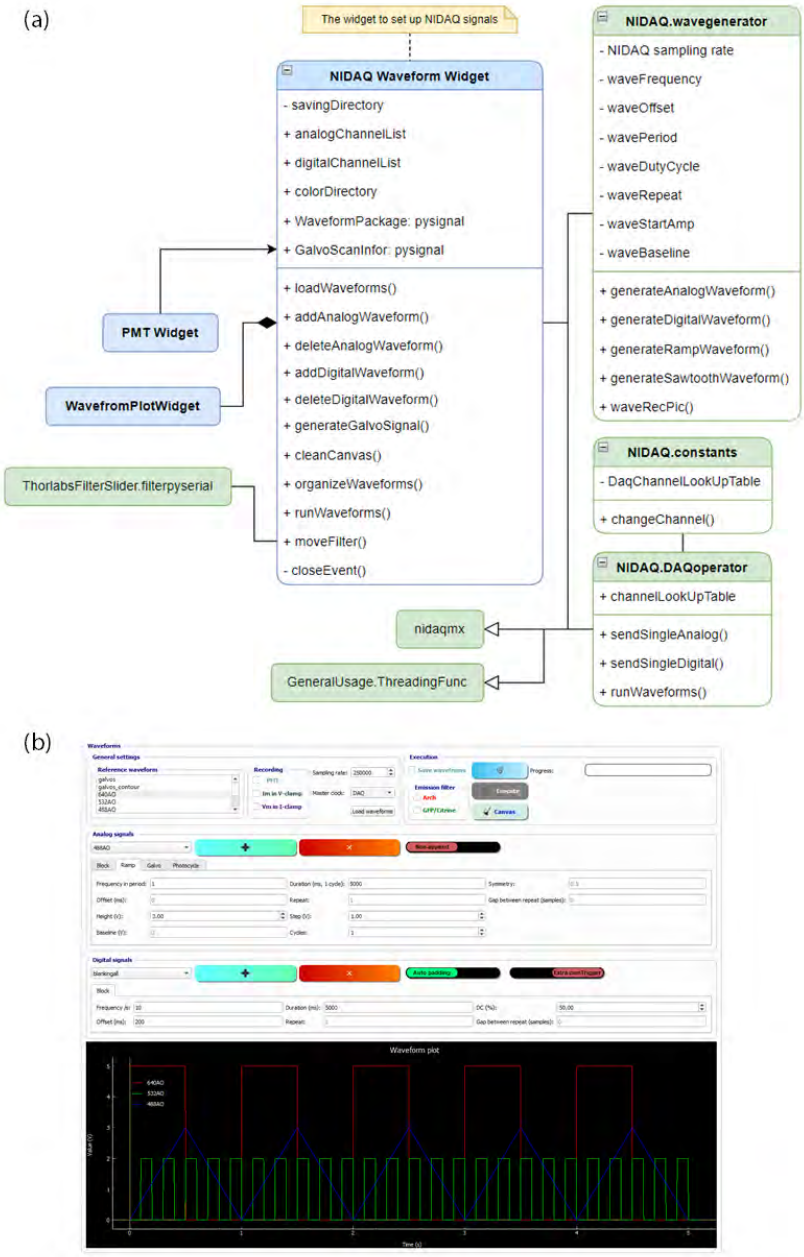

Figure 3.15: Class diagram and GUI of the waveform widget. The waveform widget takes charge of everything related to the DAQ system. Each waveform is received by a device's destination port, and its DAQ channel names are assigned in the lookup table file. The configured waveforms are displayed in different colours at the bottom.

3.3.3. ANALYSIS MODULE

Data analysis transforms experimental recordings into interpretable numbers, which is crucial to explaining current observations and deciding the next experimental steps. Especially when dealing with biological samples, the time spent outside running trials (making decisions, configuring setups, etc.) should be minimized. For example, in our case, when running a patch clamp experiment, the patch quality will deteriorate over time. While the fluorescence response characteristics of the current protein under test are unknown, it is vital to have the analytical results from trials and adjust the clamping voltage frequency accordingly in a short time while the good quality patch still holds. Data analysis is integrated into the widgets to facilitate real-time feedback and cut down time spent outside the trials to provide quick and straightforward analysis visualization on the fly.

IMAGE ANALYSIS LIBRARY

A comprehensive image analysis library was written for all aspects of voltage imaging experiments. It is composed of two main scripts, one with traditional image analysis algorithms and data visualization methods, the other one interfacing with the machine learning network (details in the next section 3.3.3). The traditional image analysis script contains functions such as threshold-based cell masking, cell membrane segmentation, cell contour scanning route generation, mapping different hardware coordinates, cell tracking, 1D and 2D array processing, data visualization, etc. It is the base for all data analysis taking place in the software, and the results are delivered to different widgets and presented to the user.

MACHINE LEARNING ASSISTED CELL SEGMENTATION

In voltage imaging, spatial patterning offers advantages such as cell-specific targeting and improved image quality. As introduced in the coordinates widget (paragraph 3.3.2), this requires the input of mask (i.e. area of the sample to illuminate) by the user. This input can be freehand drawing or configuring polygons on a recorded image. Manual masking works well when dealing with a small number of samples. However, it would become laborious as the target's number increases and the mask's fidelity varies depending on the user's skill.

We looked into machine learning (ML) networks to facilitate and standardize cell segmentation. The Mask R-CNN algorithm, a regional-based convolutional neural network, was proposed by Facebook AI Research (FAIR) and showed promising results on object detection and segmentation[10]. We trained the network with manually annotated cell data and optimized the network's original weights file for HEK cell detection and segmentation. The network's segmentation accuracy is evaluated by calculating the widely used metrics such as the intersection over union (IoU) scores and the F-score. The IoU

scores for mask and BBox are above 0.75, and The average F-score is 0.92 for average precision 50, which proves excellent detection and segmentation ability (refer to chapter 6 for more details). A segmentation on 6.12 × 6.12 mm field of view of cells is shown in Figure 3.16. The whole segmentation takes around 4 minutes and 30 seconds (on Nvidia Quadro P4000 GPU), and in total 2991 cells are segmented.

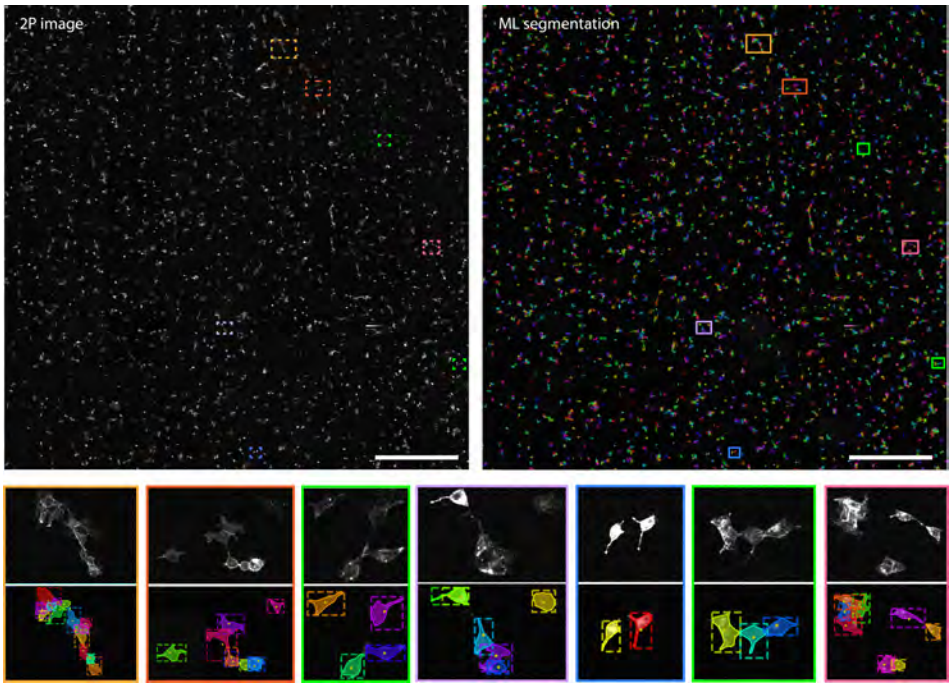

Figure 3.16: An example of the ML cell segmentation. On the left the original 2P image is shown, and on the right the segmentation provided by the machine learning network is shown. The scale bars are 1 mm.

We built a high-level interface for the HEK cell detection and segmentation so that it can be easily integrated into widgets. As an example, we present how this interface integrates into the coordinates widget. Instead of hand-drawing cell masks, the machine learning module will display all detected cell masks as ROIs on the canvas with one button click. The user can click on the mask population to recruit them and fine-adjust each cell's mask by moving the ROI handles (More details are introduced in section 3.4.2). The network is also employed to analyze the cell screening data. Cell membrane brightness statistics are drawn from the masks provided by the algorithm (The application is introduced in section 3.4.2). The ML cell segmentation network offers much more efficient and consistent cell segmentation compared to manual labeling.

WHOLE-CELL PATCH ANALYSIS WIDGET

To characterize the voltage response of a GEVI, a voltage clamp experiment is usually carried out in which the membrane potential of a cell is manipulated to go through step functions while the fluorescence of a protein is recorded at the same time. A patch clamp analysis widget was built to present the results of the currently running experiment, with minimal input needed (Figure 3.17).

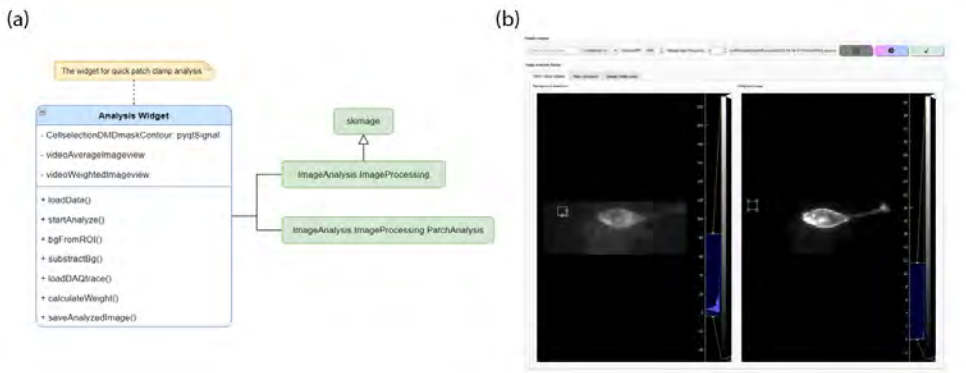

Figure 3.17: Class diagram and GUI of the patch analysis widget. The main feature of the program is the simple input needed to provide a straightforward analysis summary. An image analysis library is created to provide a vast range of data processing functions.

To analyze voltage clamp experiments, the only input parameters needed from a user are a manually selected background region and the voltage frequency. The location of the file to be analyzed is, by default, the last saving directory. In the widget, a background ROI item with handles can be resized and placed onto the window displaying the averaged video image (Figure 3.18(a)). The program will do the analysis and generate figures and tables for data visualization after the start button is clicked (Figure 3.18(b)).

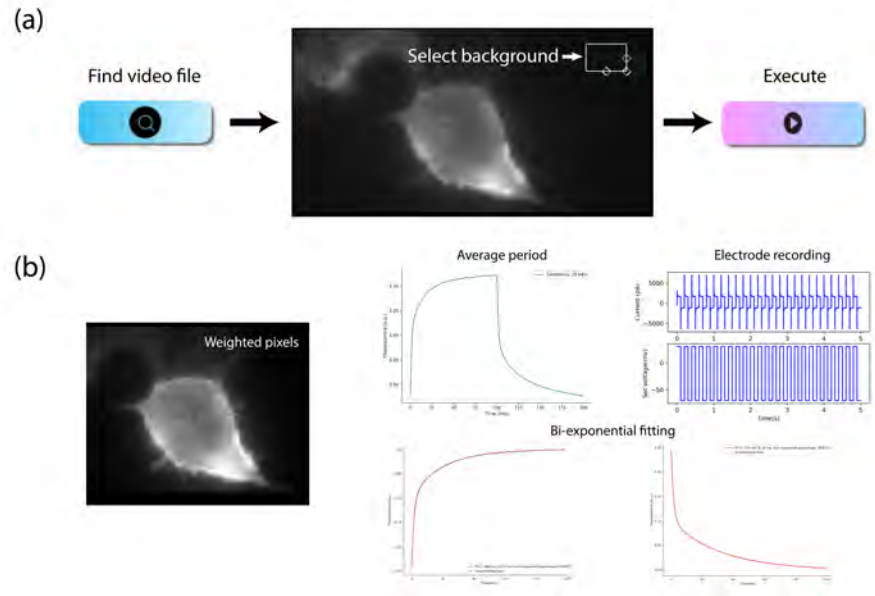

Figure 3.18: Illustration of the process and product of the patch analysis. (a) In total, three steps are needed for the voltage clamp data analysis: direct the recorded data folder, check the background region, and start the analysis. The data location is, by default, the same as the last recording's directory. (b) Showcase of the analysis product. It includes a weighted image after the maximum-likelihood pixel weighting algorithm[11], plots of the patch amplifier's voltage and current recordings, and averaged single period with numbers indicating the sensitivity and time response of the recorded protein.

For the voltage clamp analysis, the averaged background trace from the ROI region is calculated and smoothed. The background is then subtracted at each frame. A maximum-likelihood pixel weighting algorithm[11] is used to further de-emphasize background pixels and generate an image with weighted pixels. F_{bl} (baseline fluorescence) and F_{ss} (steady-state fluorescence) values are calculated from weighted fluorescence at resting potential and during the voltage step after reaching steady state, then, the sensitivity $\Delta F / F_0$ is presented as $(F_{\mathrm{ss}} - F_{\mathrm{bl}}) / F_{\mathrm{bl}}$. The up-swing and down-swing phases are fitted to bi-exponential functions, and the fast and slow constants are summarized to represent the kinetics. All data and figures from the analysis will be saved in a folder inside the main directory.

The whole computing process takes about 15 seconds on our lab PC, which equips an Intel Xeon W-2145 CPU. For the current clamp experiment, the recorded voltage signal can be displayed by selecting the file in the DAQ trace display tab. It provides stand-alone and interactive data plotting windows and is very convenient and straightforward

to visualize the measured data.

3.4. RESULTS

3.4.1. ASSEMBLED SOFTWARE

COMPREHENSIVE MICROSCOPE SOFTWARE

A comprehensive microscope software, as well as the main interface of gevidaq, is built as a collection of all widgets for daily use in our lab[8]. The software's structure is shown in Figure 3.19. The main widget, which is the initial user interface, serves as a motherboard into which all individually developed widgets are plugged. It is the information center that is able to access or set variables in each widget, as well as pass variables from one to another. All frequently used microscope functions are easily accessible in the GUI, and it is easy to modify in future development. The software covers most day-to-day experiments in a voltage imaging lab, and the applications are shown in section 3.4.2.

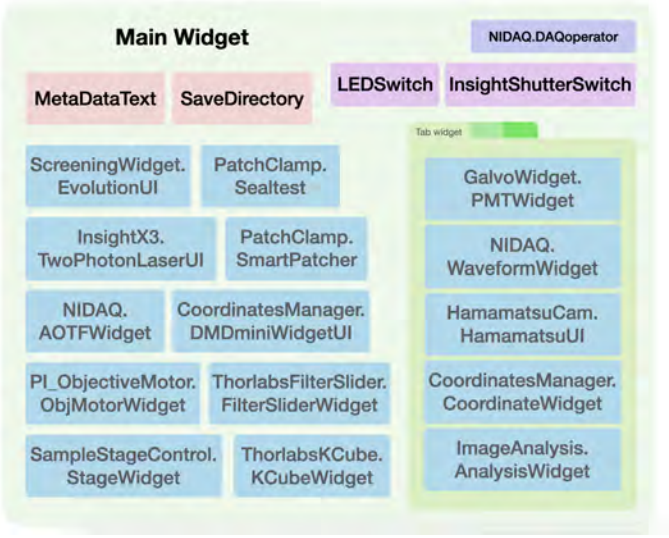

Figure 3.19: The components of the comprehensive microscope software. Each of the blue blocks represents a modular widget which is introduced in the previous section. A main widget accommodates the widgets and serves as a central data hub and provides communication channels. Extra functions are added to facilitate data management, for example, the directory and metadata storage settings.

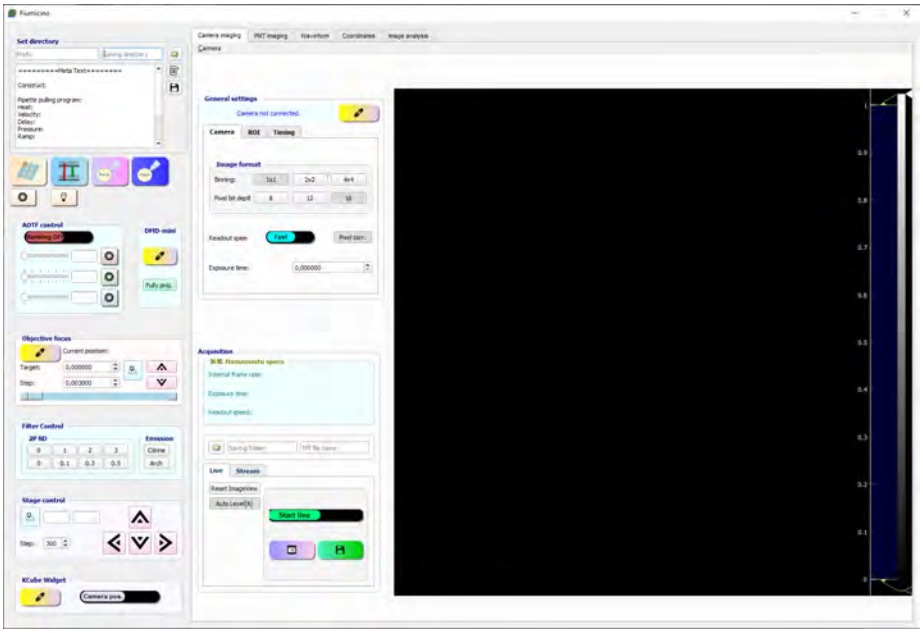

Figure 3.20: The main GUI of the microscope software.

AUTOMATED SCREENING SOFTWARE

Using the waveform widget and several hardware backends, we built an automated screening software to support large-scale cell screening and analysis under either 1P or 2P excitation (Figure 3.21 (a)). It is used to run the directed evolution under 2P excitation (see Chapter 6) and measure protein brightness in cells (see Chapter 4 and 5).

To set up a screening section, there are three configuration levels from bottom to top. The lowest level is the commands at each dwell time. It is assembled from the waveform widget and the Hamamatsu camera backend. In the waveforms configuration part, it is possible to set up triggers not only for galvo scanners and PMT, but also for any other devices in the microscope system, including triggers to the camera. The camera can be set to acquire images with desired parameters according to the triggers. Multiple waveform packages can be added in sequence, giving the possibility to add another level of complexity to the screening pipeline. This gives great flexibility to the screening, which allows all possible imaging modalities from the multi-modal microscope to be added to the assay. The screening round settings container comes after the waveforms settings and constitutes the second configuration level. Here, one can input the parameters for the sample stage movement, settings for the auto-focus during the screening, excitation, emission filter execution, and two-photon laser wavelength used for the current screening round. Multiple rounds can be added in sequence. At the very top level, lies the input for the number of repeats of the round screening compartment over different fields of

view. There are also configurations for the saving path and buttons for execution.

We built a GUI with ML facilitated image analysis backend for the data analysis (Figure 3.21 (b)). The analysis will start automatically after the screening and will rank the cells based on their multi-parameter metrics. Each cell has its profile stating its coordinates, original image, segmentation mask, brightness, area, and location in the multi-parameter metrics plot. All the information is saved in a sheet at the end. Each cell can be revisited for follow-ups such as picking up and gene sequencing.

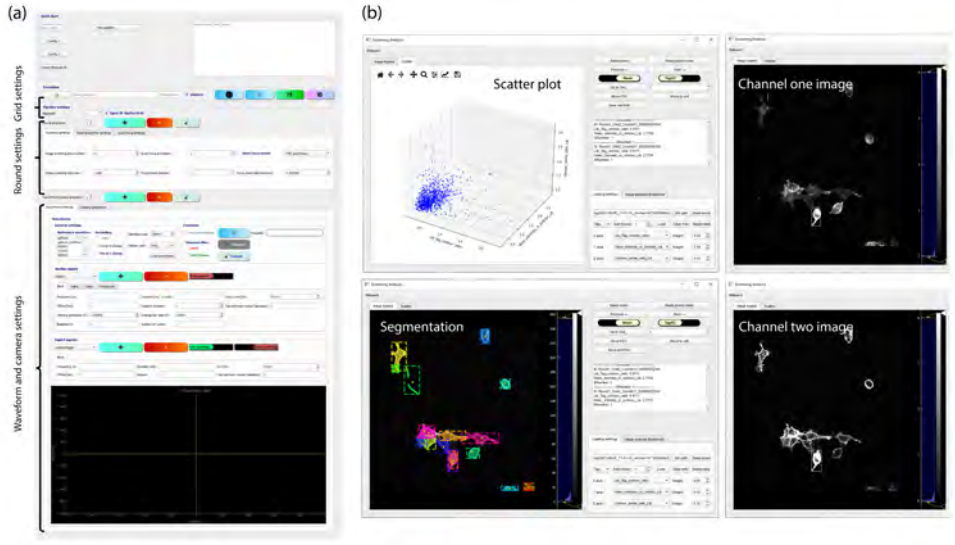

Figure 3.21: The screening and analysis software. (a) A new screening pipeline can be configured from bottom to top and will be saved as a pipeline file. To repeat the same pipeline, only loading the pipeline file is needed. A summary of the configuration will be displayed at the top. (b) The screening analysis software provides a detailed analysis of the data. Cells in each frame are segmented and categorized by the ML network. An interactive scatter plot with customized axes is shown after the analysis is done. Each cell has its index, and all the related information can be examined, such as its fluoresce at different screening rounds and its segmentation mask.

SMART PATCHER SOFTWARE

Single-cell electrophysiological experiments are delicate and difficult tasks that require experienced hands. Here, we demonstrate an automated whole-cell patch system with a minimum intervention needed, which we call the Smart Patcher. The system software is built based on the existing backend interface from the camera, objective motor, micromanipulator, sample stage, and NI-DAQ. This further develops algorithms and pipelines

to perform pipette autofocus, tip localization, Gigaseal, and break-in (Figure 3.22). A custom-built pressure control system is also added to the microscope system to replace manual pressure delivery. The smart patch clamp application is introduced in detail in section 3.4.2.

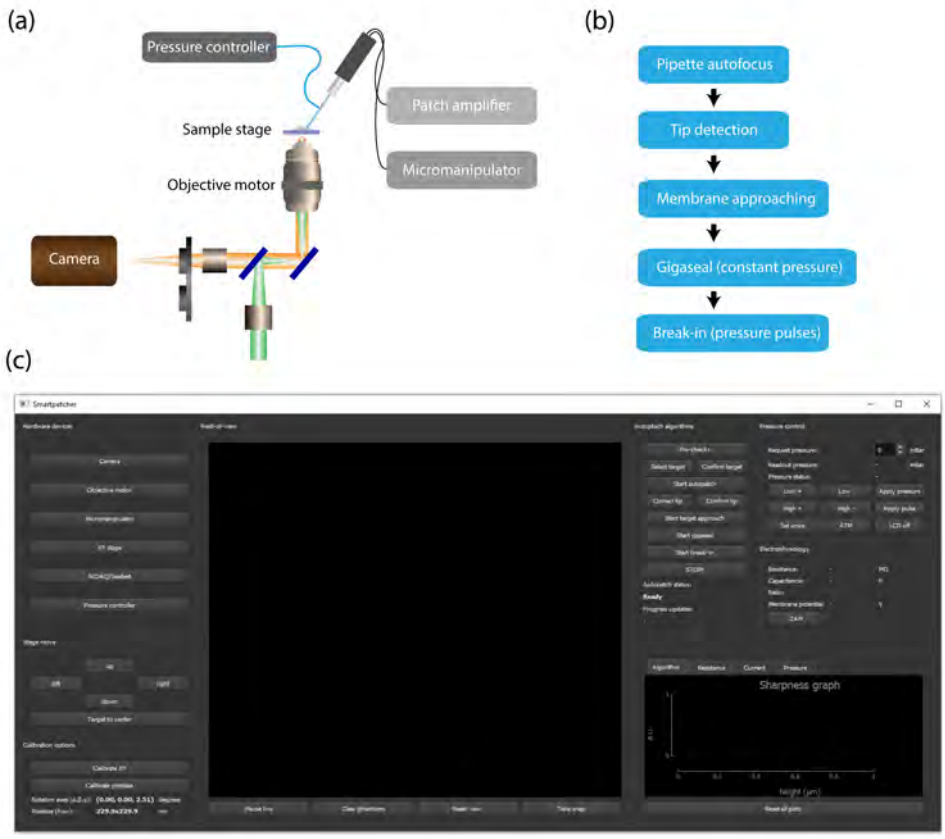

Figure 3.22: Components and GUI of the Smart Patcher software. (a) The hardware back-ends involved include the camera, the objective motor, the micromanipulator, the sample stage, and NI-DAQ for the patch amplifier. Together they perform a series of actions during a whole-cell patch, as shown in (b). (c) In the GUI, there are control panels for all the peripheral hardware involved in the patch clamp experiments on the left side, a live camera window in the middle, operation buttons and monitoring plots for the whole-cell patch clamp, and a pressure controller on the right side.

3.4.2. APPLICATIONS

We demonstrated the applications of gevidaq in different experiments, ranging from *in vitro* electrophysiological experiments on HEK cells and cultured neurons to imaging tasks including patterned projections, large-scale screening, and volumetric 2P imaging in zebrafish. These applications prove the versatility and efficiency of gevidaq.

STREAMLINED CHARACTERIZATION OF PROTEIN PROPERTIES WITH REAL-TIME FEEDBACK

Measuring the response of proteins such as genetically encoded voltage indicators (GEVI) to changes in membrane potential is one common task among all laboratories studying optogenetics. The software we developed here enables streamlined characterization with real-time feedback for adjusting the trial conditions, thus greatly improving the efficiency of finding the optimal trial conditions.

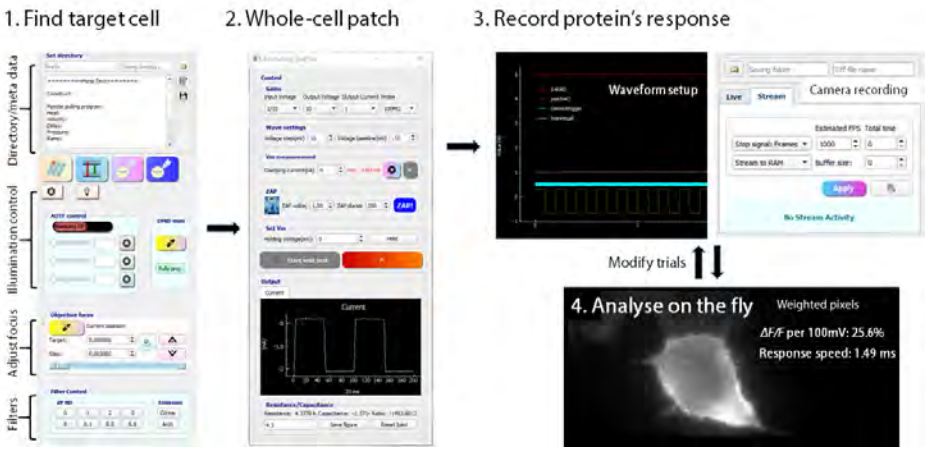

Figure 3.23: Illustration of the streamlined protein characterization pipeline. The main GUI is arranged to make all microscope functions directly accessible. The widgets related to the cell-finding stage are listed on the left panel. For the second stage, the patch clamp seal test widget shows in a pop-up window as an individual process in parallel. To perform the recording, the waveform widget and the camera widget work closely together. The generated data is analyzed in real-time, providing all the statics and plots regarding the protein's properties. The next round of investigation can be adjusted accordingly immediately after.

The first step of a characterization experiment is to find a target cell expressing the fluorescent protein of interest. In this process, the illumination is set up through the AOTF widget, the DMD quick start widget, and the LED toggle button, which are grouped

together in the GUI with the emission filter and objective control widgets, allowing for straightforward creation of required imaging settings.

The second step is to establish a whole-cell patch connection with the target cell. The camera widget provides a live view, while the seal test widget (introduced in paragraph 3.3.2) helps to configure the seal test waveform settings and monitor the current feedback in the patch clamp amplifier circuit. Assuming an ideal cell, cell capacitance scales with the cell membrane area, and cell resistance scales inversely with the cell area. Patch quality can therefore be qualitatively assessed by computing cell area from capacitance and resistance measurements and checking how well they match. The closer the ratio of both computed areas is to one, the better the patch quality. This ratio is displayed in the GUI.

In the actual experiment, we alter the current in the patch circuit and record the fluorescence response of the patched cell. The command voltage governing the current through the amplifier circuit is controlled by the waveform widget. The voltage signals can be configured in the widget or loaded through a file browser. The camera recording is prepared through the camera widget; this includes narrowing down the recording field of view and switching the camera trigger mode. All aspects of the experiment are synchronized by trigger signals sent from the waveform widget. All the recording data and metadata will be saved in a folder that is automatically named prior to the experiment.

Since the properties of the protein are unknown, it is vital to analyze recorded data and obtain statistics on the fly so that the next trial parameters can be adjusted before the patch connection or cell health deteriorates. As introduced in section 3.3.3, the analysis can be done directly after the data acquisition. From graphical summaries of the statistics, the user can evaluate whether the patch voltage frequency is suitable. For example, if the sensor's response is too slow to be fully captured under the current frequency, then the patch voltage frequency can be lowered by changing the waveforms during the next trial.

During electrophysiology experiments, it is also straightforward to display electrical signals from the patch amplifier. The only user input is to select the recorded file. This real-time feedback is useful, for example, when characterizing the threshold potential of a patched neuron. With the help of the interactive signal display, the amplitude and duration of the current injection can be optimized instantly, as shown in Figure 3.24.

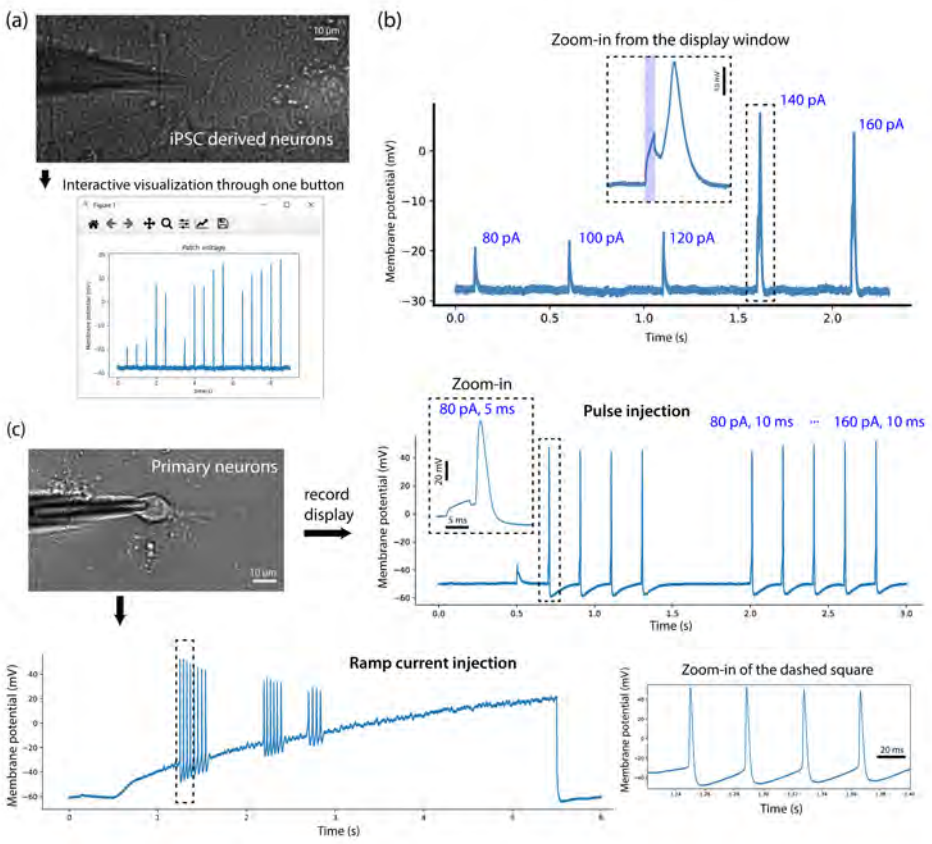

Figure 3.24: Analysis during the electrophysiology experiment can be provided instantly. The recorded electric signals from the patch amplifier can be plotted on the fly in an interactive manner. (a) In this current injection showcase performed on an iPSC-derived neuron, the membrane potential response to different current amplitudes was plotted immediately after the experiment. The threshold value to evoke an action potential can be found in the plot. (b) Zoom-in from the interactive display of the trace in A. (c) Data display during a primary neuron patch clamp session. Each spike can be examined in detail by selecting the zoom-in area through computer mouse interaction.

SMART PATCH CLAMP

We automated the whole cell patch clamping routine. This routine can be run in a standalone program ("Smart patcher") or as part of the overall software.

The autopatch process can be divided into six parts: pre-checks, pipette autofocus, tip

detection, target approach, gigaseal formation, and break-in. The process is illustrated and further explained in Figure 3.25. In the current version of the software, manual input is still needed to progress between different steps of the processes, and to confirm registration between the coordinate systems of the micromanipulator positioning the Pipette and the camera imaging the cell. During the experiment, a live camera view is provided, and parameters like the patch probe's current, the patch circuit's resistance, and the pressure in the pipette are monitored and plotted on the right panel.

The performance of the automated patch clamp system is evaluated by the success rate at each step and summarized in Table 3.1. The success is evaluated by the estimation of the patch quality as outlined before. Here, indirect success means the re-activation of an autopatch algorithm after failure results in success. The system shows comparable performance to literature[12], and in our lab, improved the success rate of inexperienced users.

Table 3.1: Timings and success ratios of the autopatch algorithm over nine whole-cell patch attempts.

	Time	Direct success ratio	Indirect success ratio
Reset + Pre-checks	5:17 min	n.a.	n.a.
Autofocus	2:06 min	78%	100%
Soft-calibration	42 sec	n.a.	n.a.
Manual correction, approach	2:07 min	100%	no data
Gigaseal	1:38 min	56%	33%
Break-in	3:30 min	83%	0%

SPATIAL LIGHT PATTERNING BASED ON MACHINE LEARNING SEGMENTATION

DMD projection provides the setup with the ability to spatially patterned light, which can be used to record or activate a selected population of cells. The coordinates widget is designed to make the projection process straightforward, as demonstrated in Figure 3.26.

Given a fluorescence image of cells (Figure 3.26(a) left), which can be automatically provided from the camera widget's emitted signal, the widget can run our trained machine learning network on the image and provide segmentation and classification results within 2 seconds (Figure 3.26(a) right). All detected cells of interest can be selected by clicking on them in the widget. ROIs with handles will be created so that fine-tuning can be done if necessary. ROIs can also be created manually if the machine-learning algorithm does not detect cells of interest. These ROIs are then converted into DMD masks for projection by the backend, with tunable contour thickness, and for different lasers. A sequence of masks can also be created for sequential projection. Figure 3.26(b) shows the projection results of different contour thicknesses on selected HEK293T cells.

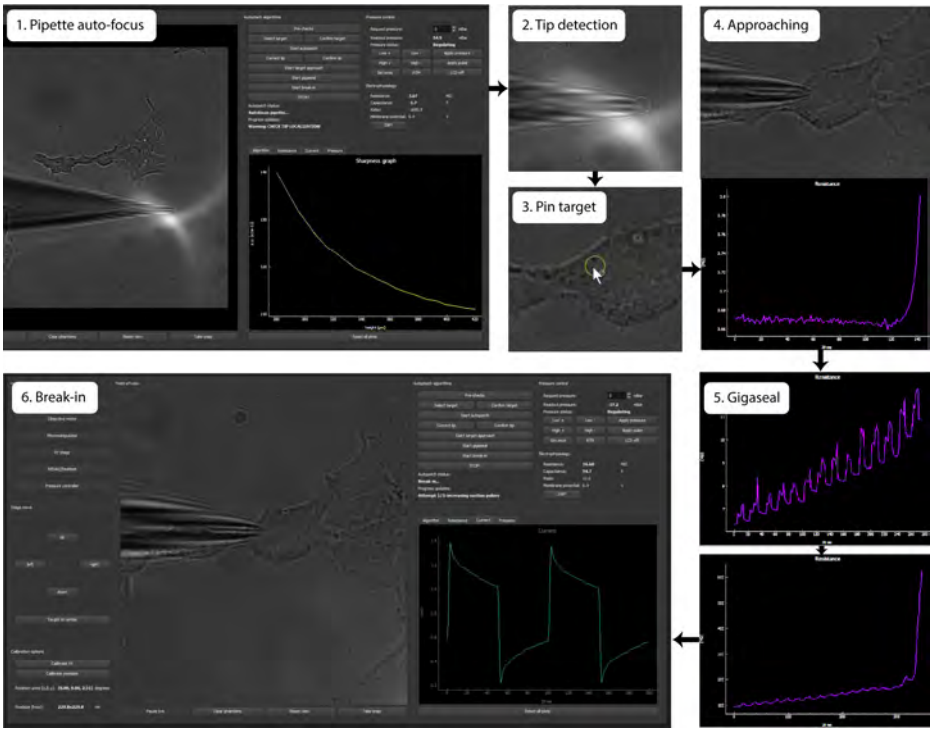

Figure 3.25: The software views during the autopatch process. During the first step, pipette autofocus, the pipette focus degree is evaluated by the image's variance-of-Laplacian. The sharpness score, which keeps decreasing, updates on the right panel. In the second step, the algorithm detects the pipette tip's location, and the user can correct the results if necessary by placing an ROI item on the tip. A user places another ROI item during the third step, which provides the algorithm with the landing spot for the pipette. This is normally inside the cell, but not in the cell nucleus. Afterward, the micromanipulator drives the pipette to approach the cell. During this process, the algorithm monitors the resistance of the circuit. It stops descending the pipette when the resistance increases by 2 MΩ, indicating that the pipette touches the cell membrane. In the 5th step, the pressure controller supplies a negative pressure to draw the cell membrane into the pipette to form a gigaseal. This step assures that there's no current leak from the pipette-membrane contact. After the circuit resistance goes over 1000 MΩ, the 6th part, break-in, starts. The pressure controller supplies negative pressure pulses to rupture the cell membrane inside the pipette. The current in the circuit will then show an RC curve on the display.

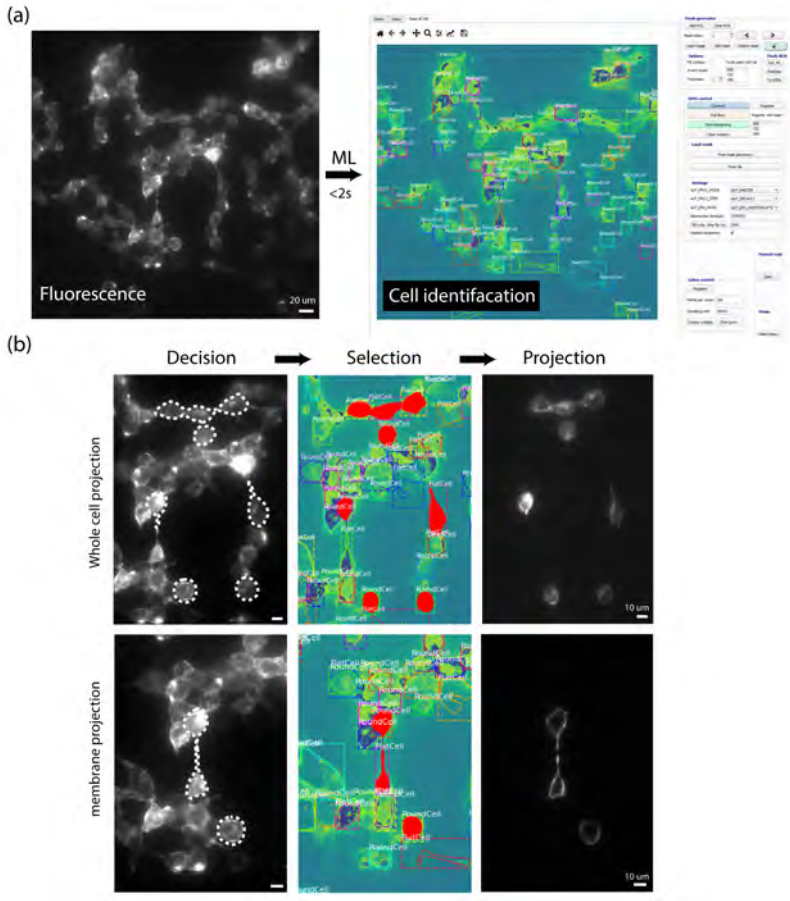

Figure 3.26: Cells in a complex network can be segmented and precisely projected with minimal user input. The segmented cell masks from the machine learning network can be presented in the coordinates widget immediately after the image acquisition. The user can click to recruit the cells for targeted illumination, and the projection can be limited to the cell membrane area.

AUTOMATED CELL SCREENING

Using the software introduced in section 3.4.1, we are able to carry out large-scale cell screening and use that to perform directed evolution on proteins. Example applications are shown in Figure 3.27. The reconstructed screening images across the entire petri dish are shown in Figure (a). Both the 1P and 2P brightness of specific proteins can be compared using this software, as shown in Figure 3.27(b) and (c).

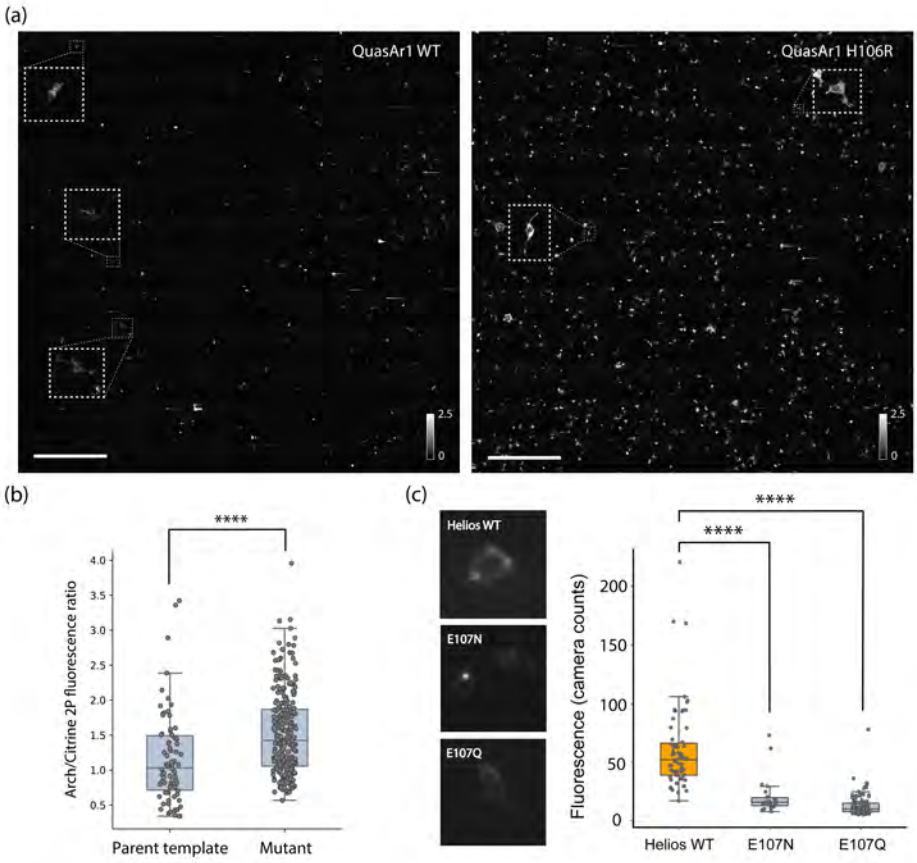

Figure 3.27: Cell screening applications, demonstrated through brightness measurements of proteins under both 2P and 1P imaging. (a) Reconstructed large-scale 2P screening images of the voltage sensor QuasAr and its single mutant H106R. The screening pipeline was executed through the screening software. The images were acquired by PMT under 1200 nm excitation using the galvo scanning backend. The contrast is adjusted to the same level. The scale bar is 1 mm. (b) The normalized brightness comparison between the parent template and its mutant. The cells were screened for two rounds, one for the tag protein fluorescence and the other for the recording fluorescence. The ratio between the two represents the expression-normalized brightness. The mutant shows improved brightness. (c) 1P brightness comparison between Heliorhodopsins and its single mutants. The screening involves coordination between the AOFT and the camera. The result shows that the rhodopsin's counterion mutations show diminished fluorescence.

ZEBRAFISH VOLUMETRIC 2P IMAGING

Volumetric imaging is an important way to help understand biological tissues network in three dimensions (3D). In our lab, the two-photon excitation laser scanning microscopy (TPLSM) enables deep tissue sectioning imaging with single-cell resolution, which is used to perform volumetric imaging. We developed the z-stack volumetric scanning function inside the galvo scanning widget (paragraph 3.3.2). This functional unit utilizes the backend developed for the 2P laser scanning and the objective motor. After setting up the laser using the laser control widget and the filters using the filter widget, the user can input some parameters such as scanning depth and step size, then start the fully automated scanning.

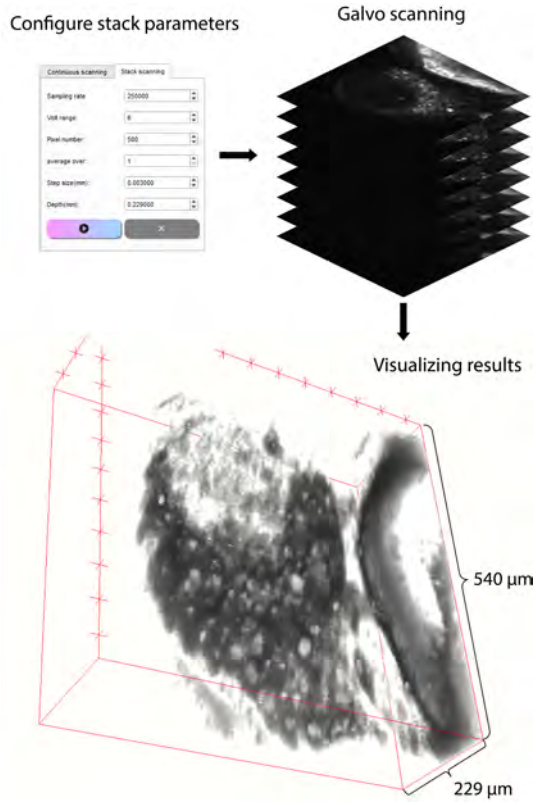

Figure 3.28: Volumetric 2P imaging of zebrafish. The zebrafish embryo was injected with Ubiquitin_mNeonAce plasmid. The images were taken using the galvo stack imaging module at 900 nm excitation wavelength. A volume of 540 × 540 × 229 µm was imaged.

An example is shown in Figure 3.28, in which a dechorionated zebrafish embryo's head is imaged. Microinjection of the fluorescent protein plasmid with ubiquitin vector was

carried out into a zebrafish embryo at the one-cell stage. Because of the ubiquitin vector, there is an expression of the fluorophore throughout most of the tissues of the zebrafish[13]. The reconstructed data shows the cell organization of the zebrafish head at an early development stage.

3.5. DISCUSSION

gevidaq has achieved the first step in building a truly smart microscope for voltage imaging: constructing a back-end to drive all hardware, building widgets with easy control, and providing analysis feedback in real-time to assist close-loop experiments. It brings advanced assistance covering the current scope of research in electrophysiology and protein engineering.

A comparison to all other microscope software will show the uniqueness of gevidaq. Compared to the most popular open-source software such as Micromanager and ImageJ, gevidaq aims to combine the functions of this two software in one software and in one programming language. Using only Python means that it is much easier to program and maintain than micromanager and ImageJ. The low-entry threshold aims to encourage more people to contribute, resulting in the support of more hardware. Another unique feature of gevidaq is its focus on optogenetics experiments. The software layout and user logic favours the smoothest experience during optogenetics experiments. Compared to commercial microscope software, the flexibility and independence of gevidaq make it special. Customizing the software can be done at any time, as opposed to long waiting times and high costs when making a request to the supplier. Compared to homemade software in Matlab/Labview, gevidaq achieves both analyzing and hardware control in, one software and one programming language. Another feature is its huge machine learning potential, as Python is currently the most widely used language in machine learning.

The future direction of voltage imaging in our lab involves more complex samples and research questions in tissue and *in vivo*. Adapting to those investigations in the network is the development goal in the next stage of the software.

One key feature to be added is the network analysis ability in typical all-optical neuronal network interrogation experiments. The data acquisition and first-stage image analysis can be done in the current version to turn the variance at each cell data into a network model with nodes, and the ability to simulate or even predict is the goal of the next iteration. The advancing machine learning field will provide an algorithm suitable for reconstructing the network, and the acquired data can be fed as training data in real-time. It will be ideal for generating a probability map on neurons and guiding the next round of interrogation, and through this iterative process, we will gradually learn the role of certain populations in behavioral tasks. Hopefully, these analytical tools will provide decent statics to guide the sampling space and decrease the amount of time and photons needed during the experiment.

Another potential feature is to adapt the illumination according to the sample and minimize the photobleaching and heating. By analyzing the dynamics of live video, the algorithm will be able to determine the cell of interest and shape the illumination accordingly to minimize the number of photons pumped into the sample. This would take place in an automated fashion and thus be much faster than human decision and operation.

Currently, the supported hardware is limited. After this software is published as open source, we hope that researchers with different hardware will adapt the backends and share their interface adaptions.

3.6. APPENDIX

3.6.1. PYSERIAL EXAMPLE

Pyserial package is used for serial communication. In general, the serial port address and the baud rate, which says the maximum communication rate, are specified and passed as arguments. Usually, a statement that cleans up resources at the end is used to initialize the serial connection. Then one can read or write encoded information from or to the port.

```
import serial        #Import the pyserial library

address = "COM7"     #Specify the port
baudrate = 9600      #Specify the baudrate

with serial.Serial(address, baudrate) as Insight: # Open serial port
    command = 'ON'                    #Turn on the Insight laser
    command = command.encode("ascii") #Convert the string into ASCII
    standard
    Insight.write(command)            #Send the command
```

Listing 3.1: PySerial example. In this example, serial communication is established through USB port 7, and an encoded command is sent.

3.6.2. HAMAMATSU CAMERA CONTROL EXAMPLE

Here is an example of controlling the camera through an application programming interface (API). The workflow starts with loading the DLL file by WinDLL function from ctypes. To initialize the camera, the DCAM-API library needs to be initialized by the host application, and for that, the dcamapi_init function inside the DLL needs to be called first. Since in C language, there are many distinguishing features different from Python, some translation work is necessary. One major adjustment is that the memory address pointer needs to be specified in C, which can be paired by ctypes built-in functions. The larger grouped C++ variables structure can be assembled similarly, as shown

in the example DCAMAPI_INIT ctypes structure. After the creation of the variable instance above, it is then ready to be passed to DLL function through ctypes by reference. In the example, DCAMAPI is initialized and returns the number of Hamamatsu cameras found. Once opened, all communication and data acquisition described in documents can be done through the API.


```
import ctypes

# The dcam initialization structure
class DCAMAPI_INIT(ctypes.Structure):
    _fields_ = [("size", ctypes.c_int32),
                ("iDeviceCount", ctypes.c_int32),
                ("reserved", ctypes.c_int32),
                ("initoptionbytes", ctypes.c_int32),
                ("initoption", ctypes.POINTER(ctypes.c_int32)),
                ("guid", ctypes.POINTER(ctypes.c_int32))]

# Initialization
# Load dcamapi.dll
dcam = ctypes. WinDLL(r'M:\HamamatsuCam\19_12\dcamapi.dll')

paraminit = DCAMAPI_INIT(0, 0, 0, 0, None, None)
paraminit.size = ctypes.sizeof(paraminit)

#Call dcamapi_init function from dll to initialize camera.
dcam.dcamapi_init(ctypes.byref(paraminit))

#Return number of Hamamatsu camera found
n_cameras = paraminit.iDeviceCount

print("found:", n_cameras, "cameras")
```

Listing 3.2: DCAMP API example

3.6.3. NI-DAQ CONTROL EXAMPLE

Several variables need to be specified before configuring DAQ tasks: the sampling rate for all signals, the data array needs to be sent, and the storage place for recorded data. After that, using the "with" statement, the NI-DAQmx task object can be created, and Python will take care of cleaning up resources afterward. Depending on the specific tasks one aims at, analog/digital input/output channels need to be added to the tasks with designated ports. Other parameters like sampling rate, clock source, and samples per channel need to be filled in afterward. Finally, the channel writer or reader object needs to be created with the associated task. The execution of the write or read behavior can be started with the "start" command. After the tasks are done, the connection will be closed.

```
import nidaqmx
import numpy as np

sampling_rate = 5   #Sampling rate of DAQ
data = np.array([1.1, 2.2, 3.3, 4.4, 5.5])  #Data to send
```

```
data_holder = np.zeros(5)  #Storage room for recorded data.

with nidaqmx.Task() as Task_1, nidaqmx.Task() as Task_2:
    #Add the channel to the task
    Task_1.ao_channels.add_ao_voltage_chan("Dev0/ao0")
    Task_2.ai_channels.add_ai_voltage_chan("Dev1/ai22")

    #Configure the clock timing of tasks
    Task_1.timing.cfg_samp_clk_timing(sampling_rate, source='ai/
    SampleClock', sample_mode= AcquisitionType.FINITE, samps_per_chan
    =5)
    Task_2.timing.cfg_samp_clk_timing(sampling_rate, sample_mode=
    AcquisitionType.FINITE, samps_per_chan=5)

    #Start the tasks
    writer = AnalogSingleChannelWriter(Task_1.out_stream)
    reader = AnalogSingleChannelReader(Task_2.in_stream)

    writer.write_many_sample(data)
    writer.start()
    reader.read_many_sample(data = data_holder,
    number_of_samples_per_channel = 5)
    reader.start()

    writer.wait_until_done()
    reader.wait_until_done()
```

Listing 3.3: NI-DAQmx example

REFERENCES

[1] M. Scanziani and M. Häusser. “Electrophysiology in the age of light”. In: *Nature* 461.7266 (2009), pp. 930–939.

[2] E. Papagiakoumou, F. Anselmi, A. Bègue, V. De Sars, J. Glückstad, E. Y. Isacoff, and V. Emiliani. “Scanless two-photon excitation of channelrhodopsin-2”. In: *Nature methods* 7.10 (2010), p. 848.

[3] Z. Zhang, L. E. Russell, A. M. Packer, O. M. Gauld, and M. Häusser. “Closed-loop all-optical interrogation of neural circuits in vivo”. In: *Nature methods* 15.12 (2018), pp. 1037–1040.

[4] L. E. Russell, H. W. Dalgleish, R. Nutbrown, O. M. Gauld, D. Herrmann, M. Fişek, A. M. Packer, and M. Häusser. “All-optical interrogation of neural circuits in behaving mice”. In: *Nature Protocols* (2022), pp. 1–42.

[5] E. Ronzitti, R. Conti, V. Zampini, D. Tanese, A. J. Foust, N. Klapoetke, E. S. Boyden, E. Papagiakoumou, and V. Emiliani. “Submillisecond optogenetic control of neuronal firing with two-photon holographic photoactivation of chronos”. In: *Journal of Neuroscience* 37.44 (2017), pp. 10679–10689.

[6] Y. Adam, J. J. Kim, S. Lou, Y. Zhao, M. E. Xie, D. Brinks, H. Wu, M. A. Mostajo-Radji, S. Kheifets, V. Parot, *et al.* “Voltage imaging and optogenetics reveal behaviour-dependent changes in hippocampal dynamics”. In: *Nature* 569.7756 (2019), pp. 413–417.

[7] L. Z. Fan, S. Kheifets, U. L. Böhm, H. Wu, K. D. Piatkevich, M. E. Xie, V. Parot, Y. Ha, K. E. Evans, E. S. Boyden, *et al.* “All-optical electrophysiology reveals the role of lateral inhibition in sensory processing in cortical layer 1”. In: *Cell* 180.3 (2020), pp. 521–535.

[8] X. Meng, L. Huismans, T. Huijben, G. Szabo, R. Van Tol, I. De Heer, S. Ganapathy, and D. Brinks. “A compact microscope for voltage imaging”. In: *Journal of Optics* 24.5 (2022), p. 054004.

[9] G. Van Rossum and F. L. Drake. *Python 3 Reference Manual*. Scotts Valley, CA: CreateSpace, 2009. ISBN: 1441412697.

[10] K. He, G. Gkioxari, P. Dollár, and R. Girshick. “Mask r-cnn”. In: *Proceedings of the IEEE international conference on computer vision*. 2017, pp. 2961–2969.

[11] J. M. Kralj, A. D. Douglass, D. R. Hochbaum, D. Maclaurin, and A. E. Cohen. “Optical recording of action potentials in mammalian neurons using a microbial rhodopsin”. In: *Nature methods* 9.1 (2012), pp. 90–95.

[12] Q. Wu, I. Kolb, B. M. Callahan, Z. Su, W. Stoy, S. B. Kodandaramaiah, R. Neve, H. Zeng, E. S. Boyden, C. R. Forest, *et al.* “Integration of autopatching with automated pipette and cell detection in vitro”. In: *Journal of Neurophysiology* 116.4 (2016), pp. 1564–1578.

[13] C. Mosimann, C. K. Kaufman, P. Li, E. K. Pugach, O. J. Tamplin, and L. I. Zon. “Ubiquitous transgene expression and Cre-based recombination driven by the ubiquitin promoter in zebrafish”. In: *Development* 138.1 (2011), pp. 169–177.

4

Expanding the Family of Genetically Encoded Voltage Indicators with a Candidate Heliorhodopsin Exhibiting Near-infrared Fluorescence

Genetically encoded voltage indicators (GEVIs), particularly those based on microbial rhodopsins, are gaining traction in neuroscience as fluorescent sensors for imaging voltage dynamics with high-spatiotemporal precision. Here we establish a novel GEVI candidate based on the recently discovered subfamily of the microbial rhodopsin clade, termed heliorhodopsins. We discovered that upon excitation at 530-560 nm, wild-type heliorhodopsin exhibits near-infrared fluorescence, which is sensitive to membrane voltage. We characterized the fluorescence brightness, photostability, voltage sensitivity, and kinetics of wild-type heliorhodopsin in HEK293T cells and further examined the impact of mutating key residues near the retinal chromophore. The S237A mutation significantly improved the fluorescence response of heliorhodopsin by 76%, providing a highly promising starting point for further protein evolution.

4.1. INTRODUCTION

DETAILED studies of neural circuitry and computation are contingent upon resolving the electrical dynamics of several neurons in parallel with high spatiotemporal precision. Direct visualization of changes in neural membrane potential has been facilitated by engineering bright and sensitive probes of which the fluorescence is modulated by changes in membrane voltage. These engineered transmembrane proteins are termed genetically encoded voltage indicators (GEVIs)[1]. Various GEVI families have been optimized over the past years, and particularly GEVIs based on microbial rhodopsin proton-pumps have enabled the recording of activity in an ensemble of neurons with sub-millisecond response time[2].

The first rhodopsin-based GEVI was derived from the bacterial Proteorhodopsin, discovered due to the success of metagenomic sequencing efforts in Monterey Bay[3]. Another proton pump, Archaerhodopsin-3 (Arch) from the archaea Halorubrum sodomense, was found to be a better GEVI candidate for expression in mammalian cells[4]. The first Arch versions were very dim and required several iterations of molecular evolution[4–8]. Many flavors of Arch-based GEVIs have since been developed with improved brightness, sensitivity, and membrane targeting, the most recent ones being Archon1 and Quasar6[4, 9, 10]. Quasar6a has a reported voltage sensitivity of 73 ± 8% per 100 mV in HEK293T cells and a significant improvement in SNR in neurons over earlier versions[10]. The evolved brightness of Archon1 and Quasar6a have enabled in vivo imaging in mice and zebrafish, in combination with a spectrally orthogonal Channelrhodopsin for *in vivo* all-optical electrophysiology[9–11].

Arch-based GEVIs exhibit complex photophysics, and various models have been proposed over time to shed light on its voltage sensitivity[12, 13]. Wild-type Arch and some other rhodopsins typically display weak fluorescence arising from the retinal chromoph ore[14]. Retinal is covalently bound to the protein via a Schiff-base linkage with a Lysine, which is normally protonated. The near-infrared fluorescence of this retinal protonated Schiff-base (RPSB) is modulated by the charge distribution of nearby residues lining the binding pocket. Light absorption initiates the photocycle of the protein via a sequence of conformational changes, which in turn can impact RPSB fluorescence due to changes in electrostatic interactions. Canonically, photon absorption in the ground state leads to isomerization of the RPSB from all-*trans* to 13-*cis* and relocation of its proton to a negatively charged counterion acceptor (M-state). Photophysical characterization of Arch suggests that the reprotonation of the Schiff-base (M to N) is influenced by membrane voltage and populates the N-state, where an increased likelihood of photon-absorption leads to a fluorescent Q-intermediate[12].

The complex photophysics of Arch and the high tunability of its fluorescent brightness, voltage sensitivity, and kinetics by targeted mutations have made it an exciting candidate to investigate and evolve further as a GEVI[4, 7, 9, 15, 16]. However, besides Arch,

This Chapter has been published as: Ganapathy, Srividya*, Xin Meng*, Delizzia Mossel, Mels Jagt, and Daan Brinks. "Expanding the family of genetically encoded voltage indicators with a candidate heliorhodopsin exhibiting near-infrared fluorescence." *Journal of Biological Chemistry*, 299, no.6 (2023).

only a handful of rhodopsin proton-pumps have been engineered as GEVIs, despite the expansive diversity of the microbial rhodopsin family. Other rhodopsins with different ionic transport or sensory functions remain vastly unexplored as potential GEVIs, despite all having the same tunable retinal chromophore in common. In addition, novel rhodopsins with unique properties are continuously being added to the family, which deserve further exploration of their bioengineering potential. Recently, metagenomic sequencing in Lake Kinneret led to the discovery of a new family of rhodopsins termed heliorhodopsins[17]. They were found to be abundant in the photic zone occurring in diverse host species ranging from bacteria to viruses[17].

Heliorhodopsins are also heptahelical retinal binding proteins but are remarkably different from other microbial rhodopsins due to an inverted insertion in the membrane with a cytoplasmic N-terminal[17]. Their precise physiological functions are thought to be diverse and are unknown as of yet. No clear ion translocation has been found, with the exception of a viral heliorhodopsin which functions as a light-gated proton channel[18]. They display a relatively long photocycle (~1-5 seconds)[17, 19] indicating that they may have some kind of sensory or signaling role. Recent studies suggest that heliorhodopsins may be involved in membrane signaling via light-induced lipid remodelling[20] or the transport of membrane-impermeable molecules[21]. The crystal structures of two heliorhodopsin variants have recently been resolved, shedding some light on their unusual properties[19, 22]. Bacterial HeR-48C12 contains a large cytoplasmic RPSB cavity with several polar residues and water molecules. This arrangement enables transient proton transfer from the RPSB and back via a proton-accepting group (involving H23 and H80). This polar H-bonded environment is highly amenable for tuning the spectral properties of retinal[23], making Helios an interesting candidate for bioengineering.

In this study, we demonstrate the potential of heliorhodopsin (bacterial HeR-48C12, Figure 4.1(a) to function as a fluorescent indicator of membrane voltage. We show that wild-type heliorhodopsin displays voltage-dependent fluorescence, which can be improved with targeted mutations in the retinal binding pocket. This research paves the way for further evolution of heliorhodopsin-based GEVIs and opens the door for engineering other members of the microbial rhodopsin clade.

4.2. MATERIALS AND METHODS

4.2.1. PLASMIDS AND MATERIALS

The pBAD vector for recombinant expression of heliorhodopsin HeR-48C12 containing an N-terminal 6xHis tag (pBAD-Helios-NT-6xHis) was a kind gift from Alina Pushkarev and Oded Béjà. The sequences for targeting and endoplasmic reticulum export motifs (TSX3ER2) and Citrine were derived from MPC020: CamKII CMV_NovArch_citrine, which was a gift from Adam Cohen (Addgene plasmid #153193)[8]. The pCAG backbone was derived from pCAG-Archon1-KGC-EGFP-ER2-WPRE, which was a gift from Edward Boyden (Addgene plasmid #108423)[9].

4.2.2. *E.coli* CULTURING AND PURIFICATION

pBAD-Helios-NT-6xHis was transformed into chemically competent *E. coli* cells (NEB® 5-alpha, NEB) as per the manufacturer's protocol. Overnight cultures were grown in LB medium under ampicillin selection (100 μg/mL) in a shaking incubator at 37°C, 150 rpm. The following day, the culture was diluted 1:50 times to a volume of 400 mL. Opsin expression was induced an OD_{600} of 0.4-0.6 by adding a final concentration of 0.2% arabinose. 20 µM all-*trans* retinal dissolved in ethanol was added to the culture, and it was left shaking for another 14-18 hours. The cells were pelleted by centrifugation at RT, 4000g, 20 min, and washed twice with an equal culture volume of 150 mM NaCl. The cell pellet was resuspended in 4 mL lysis buffer containing 50 mM Tris, 300 mM NaCl, 0.1% DDM, and lysed using a French press. Membrane vesicles were pelleted by ultracentrifugation at 100,000g, 45 min, 4°C. The pellet was resuspended in 50 mM Tris, 20 mM imidazole, 300 mM NaCl, 2% DDM, pH 6.5, and was left to mix for 1 hour, RT. Insoluble debris was spun down at 100,000g, 45 min, 4°C, and the supernatant was loaded onto a column containing Ni^{2+}NTA resin for purification of the His-tagged protein using affinity chromatography. The resin was washed with 10 bed volumes of 50 mM Tris, 50 mM imidazole, 300 mM NaCl, 0.1% DDM, pH 6. The purified protein was eluted in 50 mM Tris, 500 mM imidazole, 300 mM NaCl, 0.1% DDM, pH 6, and concentrated using a 10 kDa spin column (Millipore). The absorption and emission spectra of the purified protein were recorded at RT (Lambda365, Perkin Elmer and FLS980, Edinburgh Instruments)

4.2.3. CONFOCAL IMAGING

E.coli cells expressing pBAD-Helios-NT-6xHis were grown as described above. The cell was spun down, and the cell pellet was washed thrice and resuspended in an equal culture volume of PBS. The cell suspension was plated onto 35 mm imaging dishes with a 10 mm glass coverslip (Cellvis) coated with poly-L-lysine (Thermo-Fisher). Fluorescence images were captured using laser-scanning confocal microscopy (Nikon Eclipse Ti inverted) at excitation wavelengths of 561 and 640 nm and emission at 595/50 nm and spinning disk (IX81, Olympus) confocal microscopy

4.2.4. CLONING

HeR-48C12 was amplified from pBAD-Helios-NT-6xHis and combined with TSX3ER2 and Citrine using overlap-extension PCR with Phusion high fidelity master mix (NEB). The primers used for cloning are listed in the Supporting Information (SI, Table 4.1). TX3ER2 and Citrine were inserted at the C-terminal end of the protein due to the inverted orientation of heliorhodopsin in the membrane. The pCAG backbone was amplified using a high-fidelity polymerase KODextreme hot start (Merck Sigma). TSX3ER2-Citrine-Helios was inserted into pCAG using Gibson assembly (Gibson assembly mastermix, NEB) to generate pCAG-Helios. Point mutations were generated by PCR using end-to-end primers with the mutation site encoded in the forward primer. KODextreme

polymerase was used for amplification, and the product was ligated (KLD enzyme mix, NEB) and transformed into NEB® 5-alpha Competent cells. The primer sequences used for mutagenesis are provided in the supplementary information (SI, Table 4.1).

4.2.5. HEK CELL CULTURING

HEK293T cells were grown at 37°C, 5-10% CO_2 in Dulbecco's modified Eagle medium supplemented with 10% fetal bovine serum and Penicillin/Streptomycin. The cells were transfected at a confluency of 80% with 600-1000 ng of plasmid and 6 µL of TransIT293T (Mirus) transfection reagent. 24 hours after transfection, the cells were plated onto 35 mm imaging dishes containing a 10 mm glass coverslip (Cellvis) coated with fibronectin (Merck).

4.2.6. PATCH CLAMP ELECTROPHYSIOLOGY

Whole-cell voltage clamp recordings were performed at room temperature (25°C) 48-72 hours after transfection. The cells were rinsed with extracellular buffer containing 125 mM NaCl, 2.5 mM KCl, 15 mM HEPES, 1 mM $CaCl_2$, 1 mM $MgCl_2$ and 30 mM Glucose; pH 7.3; osmolarity adjusted to 310 mOsm. Micropipettes were pulled from borosilicate glass capillaries (World Precision Instruments, 1.5 mm OD, 0.84 mm ID) using Next Generation Micropipette Puller (Sutter Instrument, P-1000) to obtain a pipette resistance of 5-10 MΩ. The pipettes were filled with intracellular buffer containing 125 mM potassium gluconate, 8 mM NaCl, 0.1 mM $CaCl_2$, 0.6 mM $MgCl_2$, 1 mM EGTA, 10 mM HEPES, 4 mM Mg-ATP and 0.4 Na-GTP; pH 7.3; osmolarity adjusted to 295 mOsm. The micropipettes were positioned using the Patchstar micromanipulator (Scientifica). All patch clamp data were acquired in voltage-clamp mode using AM Systems Model 2400 Patch Clamp Amplifier, using voltage steps ranging from -100 to 100 mV. Simultaneous fluorescence measurements were performed as described below.

4.2.7. FLUORESCENCE IMAGING

These experiments were performed using a home-built multimodal microscope with a patch-clamp add-on, the design of which has been described recently[24]. Epi-fluorescence imaging was performed using two laser beams at 488 nm (OBIS 488 LX, Coherent) and 532nm (MLL-III-532, CNI) focussed onto the back aperture of a 25X objective (XLPLN25-XWMP2, Olympus). An illumination power of 11.2 $mW\,mm^{-2}$ and 37.23 $mW\,mm^{-2}$ were used for brightness screening for 488 nm and 532 nm respectively. For patch clamp characterization, the 532 nm intensity was 87.6 $mW\,mm^{-2}$. The emission light was filtered using a multi-band dichroic mirror (Di03-R405/488/532/635-t3-32x44, Semrock) and a 552-779.5 bandpass filter (FF01-731/137-25, SemRock). The images were acquired at a frame rate of 100 or 500 Hz using an sCMOS camera (ORCA Flash4.0 V3, Hamamatsu; 2048 x 2048 pixels, 6.5 μm pixel size). The voltage pulses, illumination, and camera

recording were synchronized using the National Instruments DAQ (USB-6363). All software for controlling the hardware, image acquisition, and analysis were custom written in Python[24].

4.2.8. DATA ANALYSIS

From the recorded camera video, a background region was manually selected. The averaged background trace from this region was calculated and then smoothed. At each frame, the time-corresponding background value was subtracted. A maximum-likelihood pixel weighting algorithm was utilized to extract the fluorescence trace. The trace was then corrected for photo-bleaching by normalization against the bi-exponential fitting of itself. An average period was calculated from it. To measure the change of fluorescence in response to membrane voltage, F_{bl} (baseline fluorescence) and F_{ss} (steady-state fluorescence) values were computed from fluorescence at resting potential and during the voltage step after reaching steady state, then the sensitivity ΔF / F_0 was presented as (F_{ss} - F_{bl})/F_{bl}. To show the protein dynamics, the up-swing (inverted to use the same equation for both up-swing and down-swing) and down-swing phases were segmented, then fitted to a bi-exponential function: $F(t) = A \times (C \times \exp((-t)/t_1) + (1 - C) \times \exp((-t)/t_2))$, in which A is a constant, C is the magnitude percentage between two single exponential functions, t_1 is a fast time constant and t_2 is a slow time constant.

4.3. RESULTS AND DISCUSSION

4.3.1. EXPRESSION AND FLUORESCENCE IMAGING OF HELIOS IN E. COLI

In order to assess the fluorescence properties of wild-type heliorhodopsin (hereby called Helios), we did a preliminary characterization in *Escherichia coli*. Recombinant N-terminal 6XHis tagged Helios was overexpressed in *E. coli* and purified using Ni^{2+}NTA affinity chromatography. The absorption spectrum of purified Helios displayed a λ_{max} at 549 ± 1 nm, in good agreement with reported values[17]. Upon excitation at 550 nm, we obtained a distinct emission band extending from 600 nm into the near infra-red region, peaking at ~700 nm (Figure 4.1(b)) We estimated a fluorescence quantum yield of 6×10^{-4}, which is in agreement with the typical range reported for other microbial rhodopsins[4, 5, 25].

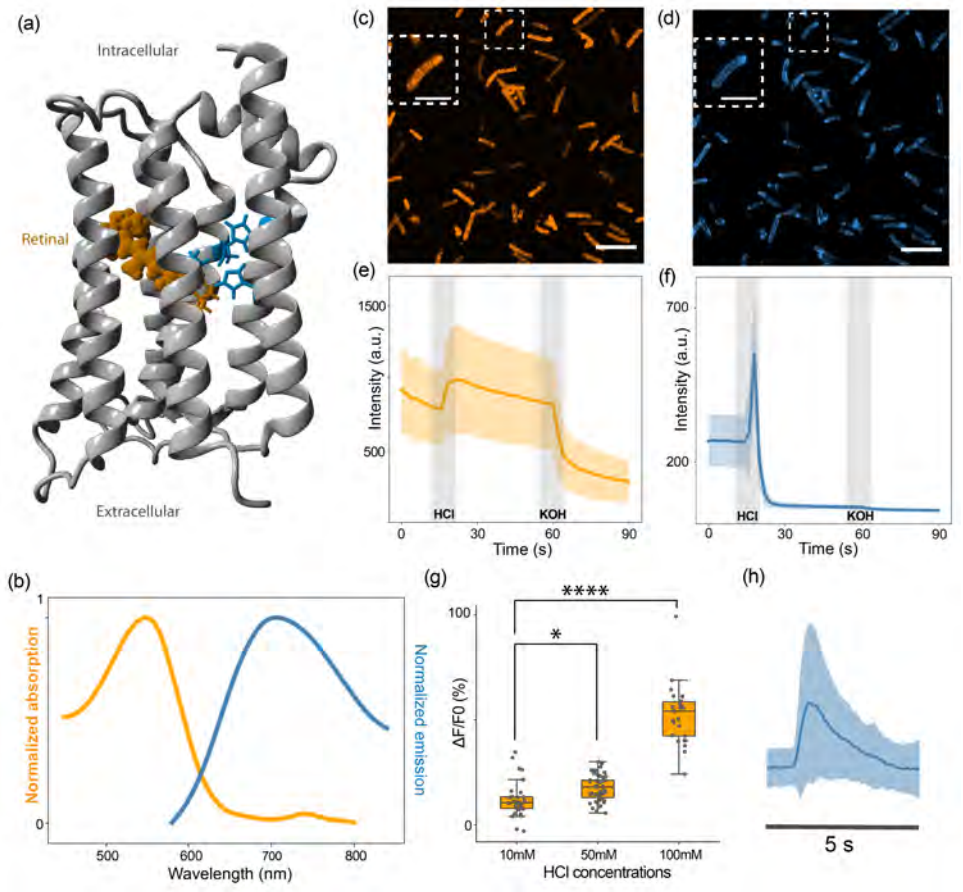

Figure 4.1: Preliminary characterization of Helios fluorescence (a) Crystal structure of Helios48C12 (PDB 6su3) displaying the retinal Schiff-base in orange and residues involved in color tuning in blue (b) Normalized absorption and emission spectra of purified WT Helios (c-d) Representative confocal fluorescence images of *E.coli* expressing Helios under 561 nm (c) and 640 nm (d) illumination, with the inset representing a zoom-in of an individual cell (e-f) Fluorescence response of *E.coli* expressing Helios to 25 mM HCl and 25 mM KOH addition under 561 nm (e) and 640 nm (f) illumination (n=45 cells). Videos were recorded at 1fps. The thick line is the mean response, with the lighter region representing the SD; the grey blocks indicate the time point of HCl or KOH addition. (g) Quantification of *E.coli* fluorescence response under 561 nm illumination to increasing concentrations of extracellular HCl addition (10 mM: 12.23 ± 8.52; n=35; 50 mM: 17.55 ± 6.13; n=50; 100 mM: 52.28 ± 14.08; n=39. All statistics are mean ± SD; in the boxplots, the boundaries of the whiskers are based on an interquartile range of 1.5, and each grey dot in the boxplot represents a cell. The p-value of the one-way ANOVA test is 1.16×10^{-30}. The p-values of 50 mM and 100 mM against 10 mM are 0.045 and 1.90×10^{-14}, Tukey's post hoc test (h) Spinning-disk confocal fluorescence response of Helios at 640 nm illumination recorded at 10 fps. All statistics are mean ± SD.

Next, we directly imaged Helios in intact *E. coli* cells using confocal microscopy. Bright fluorescence was seen localized to the cell membrane when imaged under 561 and 640 nm illumination (Figure 4.1(c) and (d)), though with some moderate photobleaching (SI, Figure 4.5). Biexponential fitting of the photobleaching response yielded time constants of 20 and 120 s for the 561 and 640 nm fluorescence respectively (SI, Figure 4.5). We tested the sensitivity of this fluorescence to changes in extracellular pH, as a preliminary indicator of voltage sensitivity. Upon addition of 25 mM HCl to the cells, an increase in fluorescence was seen in the 561 nm channel well above the photobleaching background (Figure 4.1(e)). This step response in fluorescence was roughly linear with increasing concentrations of HCl (Figure 4.1(f)) and could be reversed upon the addition of 25 mM KOH (Figure 4.1(e)). However, in the 640 nm channel, we observed an initial large rise in fluorescence followed by rapid quenching of the signal within 3-4 seconds (Figure 4.1(g), (h)). This fluorescence could not be recovered with dark incubation or KOH addition (Figure 4.1(g)). Furthermore, it was not impacted by the presence of the 561 nm illumination pulse. This quenching reaction possibly involves a complex photocycle pathway characterized by the pH-dependent inactivation of a near infra-red photointermediate. Since our interest is in the use of heliorhodopsin as GEVI which requires a linear and reversible response to membrane voltage, we focused on the ~561 nm fluorescence of Helios.

4.3.2. CHARACTERIZATION OF HELIOS WT IN HEK293T

Helios was cloned into an expression vector for human embryonic kidney (HEK293T) cells driven by the strong pCAG promoter. Based on prior efforts to optimize the membrane trafficking of Arch[4], we added a tri-repeat of targeting sequences and endoplasmic reticulum motif (TSX3ER2) with Citrine as a fusion protein for localization (Figure 4.2(a)), based on the design of Quasar3[26]. HEK293T expressing pCAG-Helios was imaged using a home-built epi-fluorescence microscope with a patch-clamp add-on for electrophysiology (Figure 4.2(b)). Strong near infra-red fluorescence (660–800 nm) could be seen when imaged at 488 and 532 nm in agreement with the measurements in *E. coli* (Figure 4.2(c)). Interestingly, no fluorescence was seen upon 639 nm excitation, possibly due to differences in binding-pocket conformation in the mammalian expression system versus *E. coli*. While Helios expression was mostly localized to the plasma membrane (Figure 4.2(c)), intracellular aggregates and overexpression leading to cell death were also seen, likely due to the strong pCAG promoter. The ratios of membrane fluorescence to soma fluorescence, as measured by quantifying the image intensity at the cell contour and soma, respectively, show similar values around 1 for WT and mutants, indicating that expression is distributed within the cell (SI, Figure 4.7). Helios exhibited moderate photobleaching at 532 nm (SI, Figure 4.6), with a fast constant of 11.16 ± 3.39 ms (54.9% ± 0.14%) and a slow constant of 158.39 ± 3.39 ms (n = 6 cells; all statistics are mean ± standard deviation (SD)).

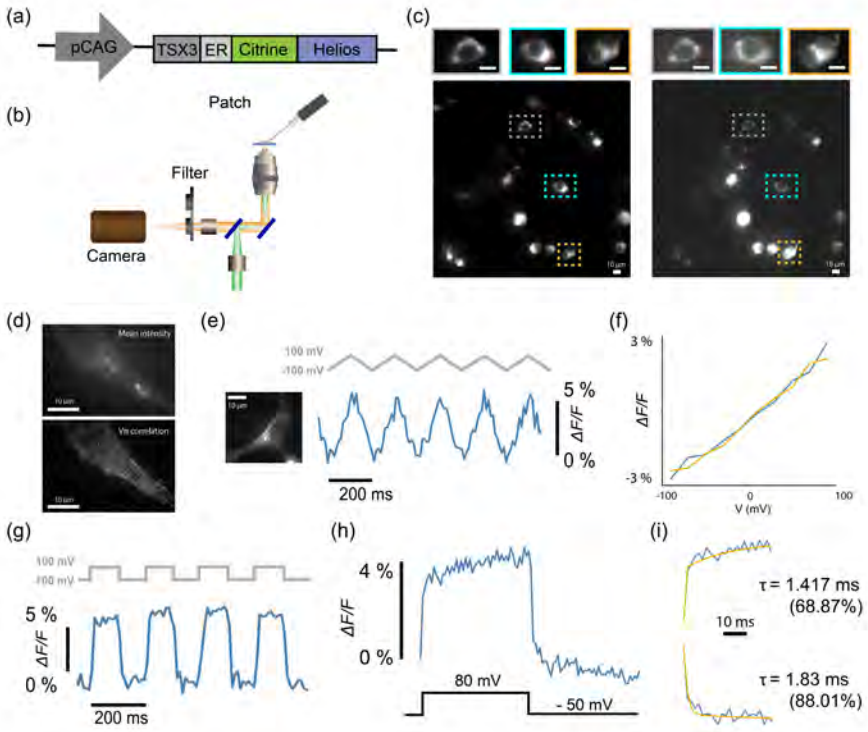

Figure 4.2: Characterization of voltage sensitivity of WT Helios in HEK293T cells (a) Schematic of the plasmid for expression of Helios under the pCAG promoter with the targeting motifs (TSX3, ER) and Citrine as a fusion protein (b) An illustration of the setup used for simultaneous fluorescence imaging with voltage-clamp electrophysiology (c) Full field of view fluorescence images of HEK293T cells expressing Helios WT under 488 nm (left) and 532 nm excitation (right). The zoom-in view on the top displays representative individual cells. (d) Top: mean intensity image from a video of a voltage-clamped cell expressing Helios. Bottom: The correlation map between the video and the membrane voltage. (e) Characterization of the fluorescence response of Helios to whole-cell voltage-clamp. Left: Fluorescence image of the patched HEK293T cell. Right: Helios fluorescence response to 200 mV voltage ramps recorded at 100 fps. The illumination intensity was 87.6 $\mathrm{mW\,mm^{-2}}$. (f) Averaged upswing and downswing traces from 25 trials. (g) Helios fluorescence response to 200 mV voltage steps recorded at 100 fps. (h) Averaged fluorescence response to 130 mV voltage steps recorded at 500 fps. (e) Biexponential fitting analysis and kinetics of voltage-sensitive fluorescence.

We assessed the voltage sensitivity of Helios at room temperature by modulating the

membrane potential of HEK293T cells expressing Helios using whole-cell patch-clamp electrophysiology and measuring the changes in fluorescence. Correlation of per-pixel fluorescence change with the change in membrane voltage showed characteristic localization of the voltage-sensitive fluorescence at the cell membrane (Figure 4.2(d)). In combination with mean intensity images displaying significant somatic fluorescence (Figures 4.2(c), (d)), this indicates Helios displays proper membrane trafficking but is overexpressed in most cells. 200mV voltage ramps were used at a frequency of 5 Hz (Figure 4.2(e)). The concurrent fluorescence response was recorded at 532 nm on a sCMOS camera at a frame rate of 100 Hz. Helios displayed a linear response to membrane voltage over a -100 to +100 mV range (Figures 4.2(f)). Subsequently, 200 mV voltage pulses were delivered at a frequency of 5 Hz, for a total duration of 5 seconds. Here, the 532 nm fluorescence response was recorded at a frame rate of 100 Hz (Figure 4.2(g)) or 500-1000 Hz for high-speed characterization of the time constants (Figure 4.2(h), (i)). The signal was temporally averaged after subtracting the background signal and correcting for photobleaching. The fractional change in fluorescence was extracted and normalized to a 200 mV step (from -100 mV to +100 mV) yielding a $\Delta F / F_0$ of 6.14% ± 1.35% per 200 mV for Helios WT (n = 7 cells; mean ± SD) Biexponential fitting of the fluorescence trace measured at 500 Hz yielded a fast time constant for the upswing of 2.06 ± 0.47 ms (62%) and of 2.40 ± 0.40 for the downswing (n = 3 cells). (Figure 4.2(i)).

4.3.3. COMPARISON BETWEEN HELIOS MUTANTS

The voltage response of Helios appeared to be substantially dominated by the recording speed in our measurements. We were intrigued by the step-like fluorescence response to the 200 mV voltage block recorded at 500 Hz since this is a compatible speed at which *in vivo* voltage imaging is typically performed, where Arch-based sensors tend to have comparable or slower responses. Therefore, we attempted to improve the fluorescence and voltage sensitivity of Helios by targeting mutations in the retinal binding pocket.

Arch and other rhodopsin proton pumps typically have two negatively charged counterion resides functioning as a complex. In contrast, Helios contains a single E107 as the counterion, which is hydrogen bonded to the RPSB along with an uncharged S237 (Figure 4.3(a))[17, 22]. E107 has a pK_a at 3.7 and is, therefore, likely to be unprotonated under physiological conditions[17]. The counterion influences the charge distribution of the RPSB, and mutations to neutral residues often cause spectral red-shifts in many rhodopsins[27]. In the case of Arch, the red-shifting D95N and D95Q mutations eliminated the photocurrent and improved the voltage sensitivity[7, 15]. Thus, we tested the analogous E107N and E107Q mutations in Helios as the first target. However, the E107N and E107Q mutants showed diminished fluorescence (Figure 4.3(b), (c)) with the WT brightness being 3 times higher than E107N and 5 times higher than E107Q (23 E107N and 107 E107Q cells contribute to the mean brightness calculation; 532 nm, 87.6 mW mm^{-2}). No clear voltage response could be measured for these mutants.

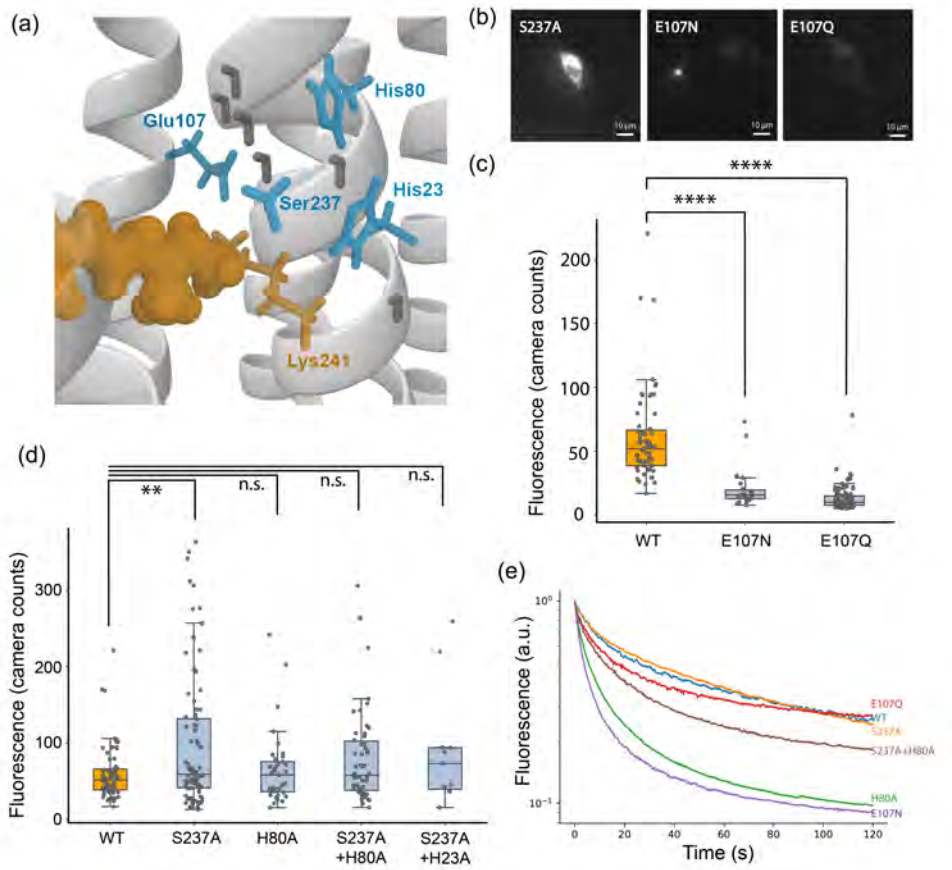

Figure 4.3: Brightness and photobleaching of Helios mutants (a) Binding pocket view of the crystal structure of Helios displaying the retinal Schiff base (orange) and key color tuning residues (blue). (b) Representative fluorescence images of HEK293T cells expressing the Helios mutants S237A, E107N, and E107Q. The contrast across the images is adjusted to the same level. (c) Comparison of brightness values of HEK293T cells expressing Helios WT (60.6 ± 36.1, n = 63 cells), E107N (20.4 ± 15.9, n = 23 cells) and E107Q (12.7 ± 9.0, n = 107 cells). All statistics are mean ± SD. The p-value of the one-way analysis of variance (ANOVA) test is 7.7×10^{-29}. The p-values of E107N and E107Q against WT Helios were both smaller than 1×10^{-8}, Tukey's post hoc test. In the boxplots in subfigures (c) and (d), the boundaries of the whiskers are based on an interquartile range of 1.5, and each grey point in the plot represents one measurement. (d) Comparison of brightness values of HEK293T cells expressing WT Helios (60.6 ± 36.1, n = 63 cells), S237A (97.8 ± 88.3, n = 92 cells), H80A (65.3 ± 47.4, n = 37 cells), S237A+H80A (= 81.7 ± 63.9, n = 54 cells) and S237A+H23A (91.4 ± 78.2, n = 11 cells). The p-value of the one-way ANOVA test is 9.51×10^{-3}. The p-values of S237A, H80A, S237A+H80A, and S237A+H23A against WT Helios are: 7.68×10^{-3}, 0.997, 0.446 and 0.632, Tukey's post hoc test. The illumination intensity was $37.23\,\mathrm{mW\,mm^{-2}}$. (e) Normalized photobleaching traces of Helios WT and mutants. All statistics are mean ± SD.

This may be attributed to the stronger interaction of the Helios RPSB with the surrounding water-dense Schiff base cavity[22].In most microbial rhodopsins, the counterion usually functions as the primary acceptor for proton transfer from the RPSB upon isomerization[28]. However, in heliorhodopsins, the Schiff base cavity collectively functions as the primary proton acceptor[17, 19, 22]. The hydrogen-bonded network involving the charged binding pocket residues and water molecules participates in the transient transfer of the Schiff base proton from and back to the RPSB[17]. A recent study identified color-tuning mutations in several of these conserved binding pocket residues, including H23, H80, and S237, which interact directly with the RPSB[23]. We, therefore, turned our attention to these sites, focusing on the mutations which were reported to cause spectral red-shifts i.e. H23A, H80A, and S237A[23] (Figure 4.3(a)).

We screened HEK293T cells expressing the above mutants for their fluorescence brightness (532 nm, 37.23 $mW\,mm^{-2}$). The averaged brightness of S237A is 23% higher than the WT (the mean fluorescence is calculated from 63 WT cells and 92 S237A cells, p-value = 0.00186), while there was no significant change for the other tested mutations (Figure 4.3(d)). However, prolonged illumination of the cells revealed differences in photobleaching behavior among the Helios mutants. While S237A and E107Q had comparable photobleaching rates to the WT, H80A, and E107N photobleached significantly faster. Bioexponential fitting of the photobleaching curves revealed that the photobleaching is of a different nature in WT compared to the mutants: where WT bleaching is characterized by a relatively strong, high and fast time constant that of S237A is dominated by a relatively strong, but less high and slow time constant. (SI, Figure 4.6). In a combination mutant, S237A saved some of the long-term fluorescence loss of H80A (Figure 4.3(e)).

4.3.4. VOLTAGE SENSITIVITY OF HELIOS S237A MUTANTS

Because of the increased fluorescence brightness of the S237A mutant and its positive effect on photobleaching, we focused our investigations of voltage sensitivity on S237A and mutant combinations with it (Figure 4.4). We assessed the voltage sensitivity of S237A, S237A+H80A and S237A+H23A (Figure 4.4(a)). Sensitivities were (as ΔF / F_0 per 200 mV): 6.14% ± 1.35% for Helios WT (n = 7 cells; all statistics are mean ± SD), 6.49% ± 1.4% for S237A (n = 4 cells), 5.11% ± 1.23% for S237A+H80A (n = 5 cells) and 5.86% ± 0.17% for S237A+H23A (n = 4 cells) (Figure 4.4(b)). No statistically significant difference in voltage sensitivity was measured between any of the mutants. We compared the response speed of the S237A mutant to a 200 mV voltage step to that of Helios WT (Figure 4.4(c)). We found that S237A had a response time of 1.69± 0.04 ms (82%) (n = 2 cells) and 1.95± 0.11 (86%) for the up- and downswing respectively (Figure 4.4(d)). We found no significant difference in the speed of voltage response between S237A and WT (Figure 4.4(e)).

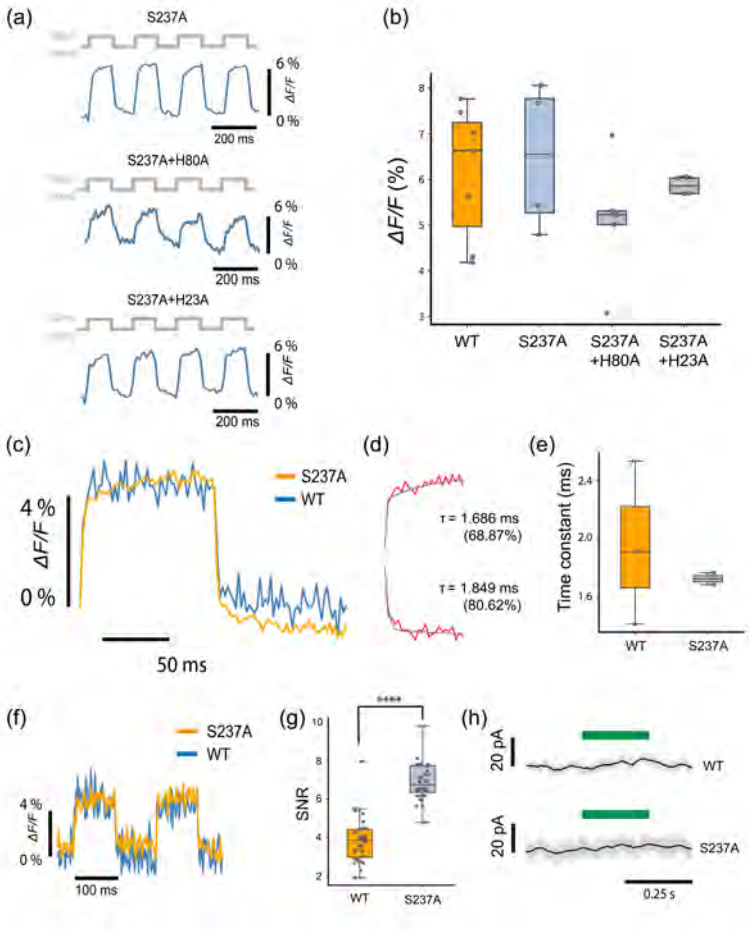

Figure 4.4: Characterization of voltage sensitivity of Helios mutants (a) Fluorescence traces of Helios mutants in response to 200 mV voltage clamp square waves. From top to bottom: S237A, S237A+H80A and S237A+H23A. (b) Comparison of voltage sensitivity between Helios WT and mutants. The voltage sensitivities per 200 mV are: WT: 6.14 ± 1.35%; S237A: 6.48 ± 1.40%; S237A + H80A: 5.11 ± 1.23%; S237A + H23A: 5.86 ± 0.18%. The p-value of the ANOVA test is 0.45. In subfigures (b), (e) and (g), the boundaries of the whiskers are based on an interquartile range of 1.5, and each grey point in the plot represents one measurement. (c) Overlay of averaged fluorescence response (25 periods) to 200 mV voltage steps from Helios WT and S237A, at 500 fps. (d) S237A has fast kinetics as the upswing tau = 1.68 ms (component percentage 68.87%) and downswing tau = 1.84 ms (component percentage 80.62%) (e) Comparison between WT and S237A rising fast time constants. WT: 1.95± 0.45 ms (62%) (n = 3 cells); S237A: 1.72± 0.04 ms (82%) (n = 2 cells). (f) Overlay of raw fluorescence response to a 200 mV voltage step from WT and S237A, at 500 fps. (g) SNR bar graphs of the WT (3.93 ± 1.3/500Hz, n = 48 measurements) and S237A (6.93 ± 1.0/500Hz, n = 48 measurements). The p-value of the independent t-test is 4.1×10^{-22}. The SNR from S237A is significantly higher (76.3%) than that from the WT. (h) Both the WT and S237A show no photocurrent upon 532 nm laser illumination. All the data were acquired under an intensity of 87.6 mW mm^{-2}. All statistics are mean ± SD.

Given the relatively minor increase in brightness of S237A compared to WT and the similar voltage sensitivity and response speed, we were intrigued by the fact that the S237A fluorescence traces were substantially less noisy than the WT traces (Figure 4.4(f). We quantified the signal to noise (SNR) with which we could detect a voltage step with Helios WT and S237A. We calculated the noise as the standard deviation of the fluorescence for the 100 ms where the voltage was +100 mV. We found that the voltage detection SNR for S237A (6.93 ± 1.0/500Hz, n = 48 measurements) is 76.3% higher than that of WT Helios (3.93 ± 1.3/500Hz, n = 48 measurements). We wondered whether the increased noise in the WT recordings was due to photocurrent effects but measured no discernible photocurrent at -30 mV upon illumination with green light (532 nm, 87.6 mW mm^{-2}.) in either WT or S237A (Figure 4.4(h)).

4.3.5. COMPARISON OF VOLTAGE-SENSITIVE FLUORESCENCE BETWEEN ARCH AND HELIOS

Voltage-sensitive fluorescence in Arch was shown to arise from photoexcitation of a pre-fluorescent 13-*cis* N-like state to a highly fluorescent Q-intermediate, either directly during the normal photocycle as in Arch WT[12] or due to photoexcitation of an accumulated all-*trans* O-intermediate as in Arch (D95N)[6]. Early work on Bacteriorhodopsin also showed pH-sensitive fluorescence arising from excitation of the all-*trans* O-interme diate[29]. The seconds-long photocycle[17] and short excited state lifetime (sub picoseconds)[30] of Helios suggests that we also measure photo intermediate fluorescence under our imaging conditions. This could involve an accumulated O-intermediate, but probably via a different route due to its distinct photocycle. Contrary to Arch, Helios displays a long-lived 13-*cis* O-intermediate, which reisomerizes to the ground state in seconds[17, 31]. The preceding transition from the M to O state involves proton back-transfer from the PAG and reprotonation of the Schiff base, which could be influenced by membrane voltage. Further biophysical characterization of Helios will shed light on the photointermmediates and transitions involved in its voltage-sensitive fluorescence.

Prior work on Arch variants indicates that the increase in fluorescence quantum yield arises from the protonated Schiff base and a neutral counterion, where voltage regulates the equilibrium between protonated and deprotonated SB[4, 32]. This is influenced by the electrostatics of the RPSB environment and accessibility to proton transfer via the hydrogen-bonded network, which is quite different between Helios and Arch. The Arch binding pocket contains three water molecules[33], while for Helios at least seven internal water molecules have been reported in the retinal cavity[34]. Furthermore, the primary proton transfer event from the RPSB occurs in the cytoplasmic direction in Helios, as opposed to the extracellular transfer in Arch. The back-transfer from the PAG in Helios could reduce the fidelity of Schiff base deprotonation under negative voltage, thereby limiting the voltage-sensitive response. These differences complicate a direct comparison between Arch and Helios. Nonetheless, we attempt to shed light on the discrepancy between their voltage sensitivities and the influence of the counterion using insights from their crystal structures and mutation studies.

Mutation of the Arch counterion D95X leads to protonation and an increase in fluorescence under positive membrane voltage, which is not the case for the Helios counterion E107. In Helios, E107 does not stabilize the protonated SB as effectively as D95 in Arch. The weaker counterion interaction is compensated for by surrogate counterions involving other residues in combination with the water cavity and possibly anions. In addition, Arch has a second negatively charged counterion at D222, which is occupied by S237 in Helios. The large red-shift of the S237A mutant indicates that this residue (in combination with the surrounding water network) is probably crucial in stabilizing the charge on the protonated SB[23]. In the E107Q mutant, reorganization of the binding pocket stabilizes the RPSB due to interactions with S237[35] or even anions, as E107Q can bind anions even at physiological pH values[36, 37]. Thus neutralizing the counterion in Helios (as in the E107Q mutant) is not analogous to the Arch D95X mutation. However, our results with S237A demonstrate that this may be a useful fluorescence and/or sensitivity tuning site instead of E107, also due to evidence of its reorientation during proton transfer[22]. A combination of mutations at S237 and other binding pocket residues, which can stabilize the retinal protonated Schiff base, will likely improve the voltage-sensitive fluorescence of Helios.

4.4. CONCLUSION

We investigated the potential of heliorhodopsin as a GEVI and the effect of several mutations on its brightness, voltage sensitivity, photobleaching statistics, response speed, and photocurrent characteristics. The S237A mutant had a beneficial effect on fluorescence brightness without compromising photobleaching, voltage sensitivity, or response speed and can be used as a template for further protein evolution. Since S237A is directly hydrogen bonded to the RPSB near H80 and is an important color-tuning residue, saturation mutagenesis of S237 or further mutant combinations in the binding pocket will likely yield improved variants. Additionally, membrane-targeted expression of Helios variants can be improved by modifying the design of the expression construct, for instance, by rearranging trafficking motifs, using a different fusion protein, or inserting spacer elements.

We expect that future electrophysiological investigations into heliorhodopsins might increase our understanding of their native function and exact photodynamics, which will aid further bioengineering efforts.

4.5. AUTHOR CONTRIBUTIONS

S. G. and D. B. conceptualization; S. G. and X. M. methodology; X. M. software; S. G., X. M., D. M., M. J., and D. B. formal analysis; S. G., X. M., D. M., and M. J. investigation; S. G., X. M., and D. B. data curation; S. G., X. M., and D. B. original draft; S. G., X. M., and D. B. visualization; D. B. supervision; D. B. project administration; D. B. funding acquisition.

4.6. SUPPORTING INFORMATION

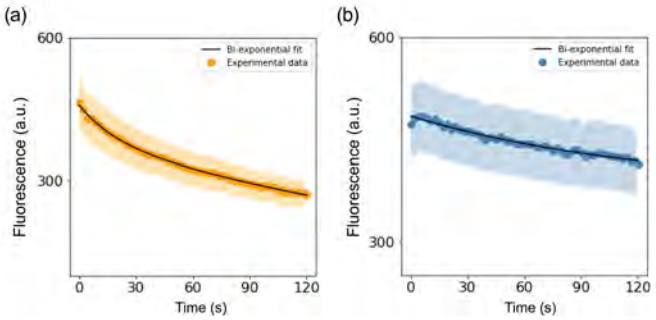

Figure 4.5: Photobleaching of Helios expressed in *E. coli*. Photobleaching curves of Helios under 561 nm and 640 nm (b) laser-scanning confocal illumination acquired at a scan speed of 1 fps.

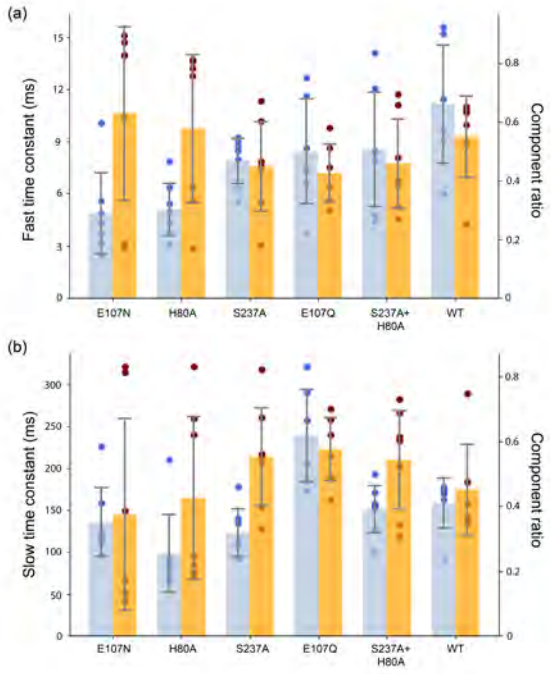

Figure 4.6: Photobleaching time constants and component percentages for 6 Helios mutants. Result of bioexponential fits to the photobleaching curves recorded under 87.6 mW mm^{-2}. illumination under 532 nm.

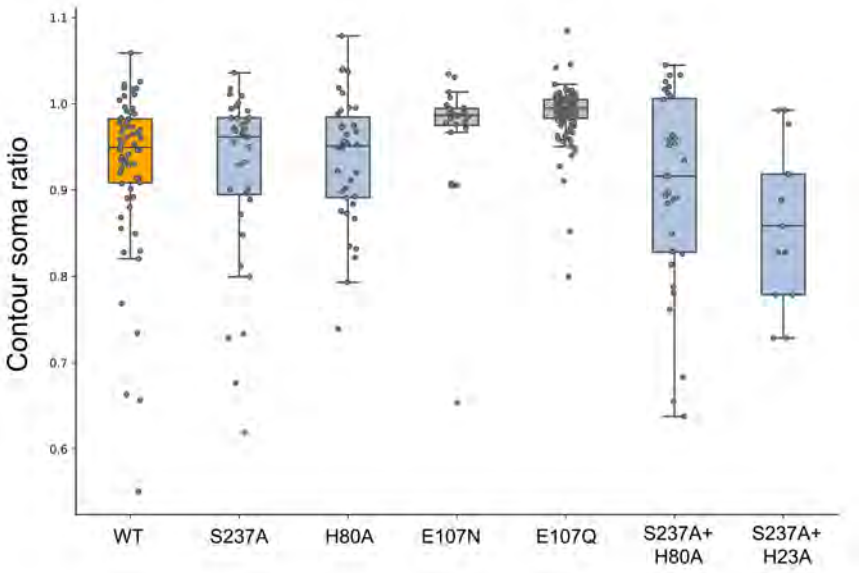

Figure 4.7: The fluorescence ratios between the cell contour membrane and soma expression from Helios WT and its mutants. The boundaries of the whiskers are based on an interquartile range of 1.5, and each grey point in the plot represents one measurement.

Table 4.1: Primer sequences used in this study. Primers used for Gibson assembly cloning of Helios into the expression construct used in this study and for further generating the various site-directed mutants described here.

Primer name	Sequence
Helios-fwd	ctgtacaaaAAGGAGATATACATACCCATGG
Helios-rev	aagcttgatatcgaattcGTTTAAACTTAAGCAGGAATTAAC
TSX3ER2-fwd	ttctgggggcagcgggggatccaccATGTCAAGGATCACCTCTG
TSX3ER2-rev	cgcccttgctcacTTCATTCTCATAACAAAAGCC
Citrine-fwd	tatctccttTTTGTACAGCTCGTCCATG
Citrine-rev	tatctccttTTTGTACAGCTCGTCCATG
FCK-fwd	GAATTCGATATCAAGCTTATC
FCK-rev	GGTGGATCCCCCGCTGCC
pCAG-fwd	TGTACAAGTAAAGCGGCCC
pCAG-rev	AACCATGGTGGCGGTACC
TSX3ER2-Citrine-Helios-fwd	accgccaccatggttTCAAGGATCACCTCTGAGG
TSX3ER2-Citrine-Helios-rev	ggccgctttacttgtacaTTAAGCAGGAATTAACGTTCC
Helios-E107N-fwd	tcgttgggttAACtattcactttcttc
Helios-E107Q-fwd	tcgttgggttCAGtattcactttcttc
Helios-E107-rev	AAGATGTTTTGATTCTTCATAAG
Helios-H80A-fwd	tctgctcttttGCCtttattgtttc
Helios-H80-rev	caacccaagaaatagcgcaactg
Helios-S237A-fwd	tacattgtgttgGCCttagttgcaaaatc
Helios-S237-rev	agcacgttctcctctgaggtaatta
Helios-H23A-fwd	gctggagtttttGCCcttttgcaaatg
Helios-H23-rev	aattctgttgaagttttgtaagga

REFERENCES

[1] I. Mollinedo-Gajate, C. Song, and T. Knöpfel. “Genetically Encoded Voltage Indicators”. In: *Optogenetics* (2021), pp. 209–224.

[2] Y. Gong. “The evolving capabilities of rhodopsin-based genetically encoded voltage indicators”. In: *Current opinion in chemical biology* 27 (2015), pp. 84–89.

[3] J. M. Kralj, D. R. Hochbaum, A. D. Douglass, and A. E. Cohen. “Electrical spiking in Escherichia coli probed with a fluorescent voltage-indicating protein”. In: *Science* 333.6040 (2011), pp. 345–348.

[4] D. R. Hochbaum, Y. Zhao, S. L. Farhi, N. Klapoetke, C. A. Werley, V. Kapoor, P. Zou, J. M. Kralj, D. Maclaurin, N. Smedemark-Margulies, *et al.* “All-optical electrophysiology in mammalian neurons using engineered microbial rhodopsins”. In: *Nature methods* 11.8 (2014), pp. 825–833.

[5] R. S. McIsaac, M. K. Engqvist, T. Wannier, A. Z. Rosenthal, L. Herwig, N. C. Flytzanis, E. S. Imasheva, J. K. Lanyi, S. P. Balashov, V. Gradinaru, *et al.* “Directed evolution of a far-red fluorescent rhodopsin”. In: *Proceedings of the National Academy of Sciences* 111.36 (2014), pp. 13034–13039.

[6] E. C. Saint Clair, J. I. Ogren, S. Mamaev, D. Russano, J. M. Kralj, and K. J. Rothschild. “Near-IR resonance Raman spectroscopy of archaerhodopsin 3: effects of transmembrane potential”. In: *The Journal of Physical Chemistry B* 116.50 (2012), pp. 14592–14601.

[7] Y. Gong, J. Z. Li, and M. J. Schnitzer. “Enhanced archaerhodopsin fluorescent protein voltage indicators”. In: *PLoS One* 8.6 (2013), e66959.

[8] M.-P. Chien, D. Brinks, G. Testa-Silva, H. Tian, F. Phil Brooks III, Y. Adam, B. Bloxham, B. Gmeiner, S. Kheifets, and A. E. Cohen. “Photoactivated voltage imaging in tissue with an archaerhodopsin-derived reporter”. In: *Science advances* 7.19 (2021), eabe3216.

[9] K. D. Piatkevich, E. E. Jung, C. Straub, C. Linghu, D. Park, H.-J. Suk, D. R. Hochbaum, D. Goodwin, E. Pnevmatikakis, N. Pak, *et al.* “A robotic multidimensional directed evolution approach applied to fluorescent voltage reporters”. In: *Nature chemical biology* 14.4 (2018), pp. 352–360.

[10] H. Tian, H. C. Davis, J. D. Wong-Campos, L. Z. Fan, B. Gmeiner, S. Begum, C. A. Werley, G. B. Borja, H. Upadhyay, H. Shah, *et al.* “All-optical electrophysiology with improved genetically encoded voltage indicators reveals interneuron network dynamics in vivo”. In: *bioRxiv* (2021).

[11] L. Z. Fan, S. Kheifets, U. L. Böhm, H. Wu, K. D. Piatkevich, M. E. Xie, V. Parot, Y. Ha, K. E. Evans, E. S. Boyden, *et al.* "All-optical electrophysiology reveals the role of lateral inhibition in sensory processing in cortical layer 1". In: *Cell* 180.3 (2020), pp. 521–535.

[12] D. Maclaurin, V. Venkatachalam, H. Lee, and A. E. Cohen. "Mechanism of voltage-sensitive fluorescence in a microbial rhodopsin". In: *Proceedings of the National Academy of Sciences* 110.15 (2013), pp. 5939–5944.

[13] D. Brinks, A. J. Klein, and A. E. Cohen. "Two-photon lifetime imaging of voltage indicating proteins as a probe of absolute membrane voltage". In: *Biophysical journal* 109.5 (2015), pp. 914–921.

[14] A. Andreeva, V. Kolev, and T. Lazarova. "Fluorescence spectroscopy of bacteriorhodopsin at room temperature". In: *OPTIKA'98: 5th Congress on Modern Optics*. Vol. 3573. SPIE. 1998, pp. 359–362.

[15] J. M. Kralj, A. D. Douglass, D. R. Hochbaum, D. Maclaurin, and A. E. Cohen. "Optical recording of action potentials in mammalian neurons using a microbial rhodopsin". In: *Nature methods* 9.1 (2012), pp. 90–95.

[16] N. C. Flytzanis, C. N. Bedbrook, H. Chiu, M. K. Engqvist, C. Xiao, K. Y. Chan, P. W. Sternberg, F. H. Arnold, and V. Gradinaru. "Archaerhodopsin variants with enhanced voltage-sensitive fluorescence in mammalian and Caenorhabditis elegans neurons". In: *Nature communications* 5.1 (2014), p. 4894.

[17] A. Pushkarev, K. Inoue, S. Larom, J. Flores-Uribe, M. Singh, M. Konno, S. Tomida, S. Ito, R. Nakamura, S. P. Tsunoda, *et al.* "A distinct abundant group of microbial rhodopsins discovered using functional metagenomics". In: *Nature* 558.7711 (2018), pp. 595–599.

[18] S. Hososhima, R. Mizutori, R. Abe-Yoshizumi, A. Rozenberg, S. Shigemura, A. Pushkarev, M. Konno, K. Katayama, K. Inoue, S. P. Tsunoda, *et al.* "Proton-transporting heliorhodopsins from marine giant viruses". In: *bioRxiv* (2022).

[19] W. Shihoya, K. Inoue, M. Singh, M. Konno, S. Hososhima, K. Yamashita, K. Ikeda, A. Higuchi, T. Izume, S. Okazaki, *et al.* "Crystal structure of heliorhodopsin". In: *Nature* 574.7776 (2019), pp. 132–136.

[20] A. Chazan, A. Rozenberg, K. Mannen, T. Nagata, R. Tahan, S. Yaish, S. Larom, K. Inoue, O. Béjà, and A. Pushkarev. "Diverse heliorhodopsins detected via functional metagenomics in freshwater Actinobacteria, Chloroflexi and Archaea". In: *Environmental Microbiology* 24.1 (2022), pp. 110–121.

[21] J. Flores-Uribe, G. Hevroni, R. Ghai, A. Pushkarev, K. Inoue, H. Kandori, and O. Béjà. "Heliorhodopsins are absent in diderm (Gram-negative) bacteria: Some thoughts and possible implications for activity". In: *Environmental microbiology reports* 11.3 (2019), pp. 419–424.

[22] K. Kovalev, D. Volkov, R. Astashkin, A. Alekseev, I. Gushchin, J. M. Haro-Moreno, I. Chizhov, S. Siletsky, M. Mamedov, A. Rogachev, *et al.* "High-resolution structural insights into the heliorhodopsin family". In: *Proceedings of the National Academy of Sciences* 117.8 (2020), pp. 4131–4141.

[23] M. Singh, K. Inoue, A. Pushkarev, O. Béjà, and H. Kandori. “Mutation study of heliorhodopsin 48C12”. In: *Biochemistry* 57.33 (2018), pp. 5041–5049.

[24] X. Meng, L. Huismans, T. Huijben, G. Szabo, R. Van Tol, I. De Heer, S. Ganapathy, and D. Brinks. “A compact microscope for voltage imaging”. In: *Journal of Optics* 24.5 (2022), p. 054004.

[25] L. Barneschi, E. Marsili, L. Pedraza-González, D. Padula, L. De Vico, D. Kaliakin, A. Blanco-González, N. Ferré, M. Huix-Rotllant, M. Filatov, *et al.* “On the fluorescence enhancement of arch neuronal optogenetic reporters”. In: *Nature Communications* 13.1 (2022), p. 6432.

[26] Y. Adam, J. J. Kim, S. Lou, Y. Zhao, M. E. Xie, D. Brinks, H. Wu, M. A. Mostajo-Radji, S. Kheifets, V. Parot, *et al.* “Voltage imaging and optogenetics reveal behaviour-dependent changes in hippocampal dynamics”. In: *Nature* 569.7756 (2019), pp. 413–417.

[27] M. Hoffmann, M. Wanko, P. Strodel, P. H. König, T. Frauenheim, K. Schulten, W. Thiel, E. Tajkhorshid, and M. Elstner. “Color tuning in rhodopsins: the mechanism for the spectral shift between bacteriorhodopsin and sensory rhodopsin II”. In: *Journal of the American Chemical Society* 128.33 (2006), pp. 10808–10818.

[28] O. P. Ernst, D. T. Lodowski, M. Elstner, P. Hegemann, L. S. Brown, and H. Kandori. “Microbial and animal rhodopsins: structures, functions, and molecular mechanisms”. In: *Chemical reviews* 114.1 (2014), pp. 126–163.

[29] H. Ohtani, Y. Tsukamoto, Y. Sakoda, and H.-o. Hamaguchi. “Fluorescence spectra of bacteriorhodopsin and the intermediates O and Q at room temperature”. In: *FEBS letters* 359.1 (1995), pp. 65–68.

[30] S. Tahara, M. Singh, H. Kuramochi, W. Shihoya, K. Inoue, O. Nureki, O. Béjà, Y. Mizutani, H. Kandori, and T. Tahara. “Ultrafast dynamics of heliorhodopsins”. In: *The Journal of Physical Chemistry B* 123.11 (2019), pp. 2507–2512.

[31] T. Urui, M. Mizuno, A. Otomo, H. Kandori, and Y. Mizutani. “Resonance Raman determination of chromophore structures of heliorhodopsin photointermediates”. In: *The Journal of Physical Chemistry B* 125.26 (2021), pp. 7155–7162.

[32] A. Silapetere, S. Hwang, Y. Hontani, R. G. Fernandez Lahore, J. Balke, F. V. Escobar, M. Tros, P. E. Konold, R. Matis, R. Croce, *et al.* “QuasAr Odyssey: the origin of fluorescence and its voltage sensitivity in microbial rhodopsins”. In: *Nature communications* 13.1 (2022), p. 5501.

[33] J. F. Bada Juarez, P. J. Judge, S. Adam, D. Axford, J. Vinals, J. Birch, T. O. Kwan, K. K. Hoi, H.-Y. Yen, A. Vial, *et al.* “Structures of the archaerhodopsin-3 transporter reveal that disordering of internal water networks underpins receptor sensitization”. In: *Nature Communications* 12.1 (2021), p. 629.

[34] S. Tomida, S. Kitagawa, H. Kandori, and Y. Furutani. “Inverse hydrogen-bonding change between the protonated retinal Schiff base and water molecules upon photoisomerization in heliorhodopsin 48C12”. In: *The Journal of Physical Chemistry B* 125.30 (2021), pp. 8331–8341.

[35] K. Wijesiri and J. A. Gascón. “Microsolvation Effects in the Spectral Tuning of Heliorhodopsin”. In: *The Journal of Physical Chemistry B* 126.31 (2022), pp. 5803–5809.

[36] M. Singh, K. Katayama, O. Béjà, and H. Kandori. “Anion binding to mutants of the Schiff base counterion in heliorhodopsin 48C12”. In: *Physical Chemistry Chemical Physics* 21.42 (2019), pp. 23663–23671.

[37] J. E. Besaw, J. Reichenwallner, P. De Guzman, A. Tucs, A. Kuo, T. Morizumi, K. Tsuda, A. Sljoka, R. Miller, and O. P. Ernst. “Low pH structure of heliorhodopsin reveals chloride binding site and intramolecular signaling pathway”. In: *Scientific reports* 12.1 (2022), pp. 1–16.

5

Developing Novel Optogenetics Tools From a Promising Microbial Rhodopsin Platform: Gloeobacter Rhodopsin

Despite the huge bio-engineering potentials for optogenetics, only a handful of microbial rhodopsins have been explored. To broaden the characteristics of microbial rhodopsins for voltage imaging applications and expand the optogenetics toolbox, we chose a proton pump rhodopsin named Gloeobacter violaceus rhodopsin (GR) based on previously reported features such as strong near infra-red fluorescence. The characterization of wild-type GR shows that it is a promising platform for further development towards Optogenetic applications. By targeting 40 mutation sites spread along the proton transfer pathway, we found mutants with distinguishing features that have never been reported before. We propose some candidates as genetically engineered voltage indicators (GEVIs) with different application specialties: generic sensors, sensors with high dynamic range (sensitivity), and ultra-bright sensors. We also propose one candidate to be used as a silencer of neuronal activity because of its exceptionally high photocurrent.

5.1. INTRODUCTION

OPTOGENETICS has revolutionized neuroscience in the last 15 years. Compared to the traditional electrode-based methods, it has multiple advantages: genetic targeting allows investigation of specific neuronal subtypes; the optical methods make it almost noninvasive; the throughput and multiplexing potential are orders of magnitude higher than that of electrode-based methods. Optogenetics has allowed the exploration of neural circuits across different scales, from synapses to brain regions, both *in vitro* and *in vivo*.

The development of novel optogenetic tools is advancing at a fast pace, and the contribution from the microbial rhodopsin family is prominent. In the first demonstration of optogenetics, a rhodopsin-based actuator was developed to sensitize neurons that only respond to light[1]. The discovery of the light-sensitive rhodopsin, Channelrhodopsin-2 (ChR2) from algae, greatly accelerated the application of optogenetics tools to control neuronal spiking[2]. It was broadly used as a spike-evoking actuator across model organisms and demonstrated clinical application potential, such as partial restoration of vision in patients[3]. Apart from functioning as an actuator or silencer, rhodopsin-based tools are also developed as indicators to report membrane potential. One major family is derived from Archaerhodopsin (Arch), and its latest version has been used in combination with optogenetic activation and silencing to study hippocampal plasticity in behaving mice[4]. These rhodopsin-based genetically engineered voltage indicators (GEVIs) have unique advantages compared to indicators of other designs, such as sub-millisecond time response. However, only several rhodopsins have been characterized regarding their GEVI potentials out of their diverse family tree.

To expand the optogenetics toolbox, we explored the potential of *Gloeobacter violaceus* rhodopsin (GR), an outward proton pump isolated from unicellular cyanobacterium which has never been tested as GEVI before[5, 6]. GR is closely related to xanthorhodopsin (XR) and thermophilic rhodopsin (TR) and structurally has a root-mean-square deviation (RMSD) of 1.69 Å when superimposed to XR from the X-ray crystallographic study[7]. It is involved in ATP synthesis and could complement the energy production from chlorophyll-based photosynthesis[8]. (Modulation of spectral properties and pump activity [9]) GR is able to bind an antenna carotenoid which further improves its proton pumping capability[10, 11].

GR is an excellent template for developing optogenetics tools. Its relatively fast photocycle time makes it a good candidate for optogenetic silencer[12], and it shows the brightest fluorescence as compared to other microbial rhodopsins in mouse hippocampal neurons, which is a precious property as an indicator[13].

In this chapter, we explore the potential of GR as an optogenetic sensor and actuator. First, we characterized the Optogenetic properties of wild-type (WT) GR using fluorescent microscopy with concomitant patch-clamp recordings, as described in Chapter 4. The characteristics of wild-type GR, such as brightness, photocurrent, voltage sensitivity, and kinetics, already prove that GR is an excellent and versatile template for the further

development of optogenetics tools. Following that, we performed site-directed mutagenesis based on rational design and characterized those mutants. In total, 40 mutants from 3 main protein regions (the retinal binding pocket, the proton donor, and the proton release site) and the combinations of mutations were characterized. Based on these data, we compared and proposed several GEVI candidates with distinguishing features that have never been reported before: generic, high voltage sensitivity, and high brightness. We also proposed one mutant from the proton release complex as an optogenetics silencer, because of its stronger photocurrent than the latest Arch-based silencer.

5.2. CHARACTERIZATION OF GR WILD-TYPE

5.2.1. OPTOGENGTIC PROPERTIES

We expressed GR in the HEK cells and measured its fluorescence. Compared to other wild-type rhodopsins, such as Arch, GR fluorescence was relatively easy to measure under our illumination conditions (Figure 5.1(a)). We performed a brightness screening under red and blue illumination (639 nm: 80 $mW\,mm^{-2}$; 488 nm: 3.8 $mW\,mm^{-2}$;) and compared its brightness directly to the latest Arch-based GEVI QuasAr6a (Figure 5.1(c)). The fluorescence is normalized to cell expression (see methods). Based on the average cell membrane fluorescence, the brightness of wild-type GR under red illumination is about 42% of QuasAr6a.

We recorded the photocurrent of GR under 639 nm illumination (625 $mW\,mm^{-2}$) in whole-cell patch clamp experiments (Figure 5.1(b)). The photocurrent becomes stationary (118.13 ± 28.38 pA, mean ± SEM) after a transient peak at the beginning of the recording. The positive value means that the protons are pumped out of the cell. This photocurrent is more than an order of magnitude higher than that of Arch3, showing that the GR proton transfer efficiency is much higher[14].

To characterize the voltage response of GR, we performed voltage clamps on the HEK cells expressing GR. A typical single-trial trace in response to the 100 mV step voltage is shown in Figure Figure 5.1(d). GR shows decent voltage sensitivity (61.03% ± 11.16%, mean ± SEM, n= 4 cells) from -70 to 30 mV, which is higher than Arch (15% without background subtraction) and comparable to the reported value of QuasAr6a (73% over 100 mV, 43% in neurons)[14, 15]. The kinetics of the voltage response (Fast upswing time constant (ms): 3.31 at 67.9%, Fast downswing time constant (ms): 3.62 at 74.8%) is fast at room temperature ($20^{\circ}C$) (Figure 5.1(f)). This is comparable to the kinetics of QuasAr6a (3.42 ms) measured in our lab. We calculated the linearity of the GR voltage response, and it shows an R-square value of higher than 0.99 for both upswing and downswing fittings (Figure 5.1(h)).

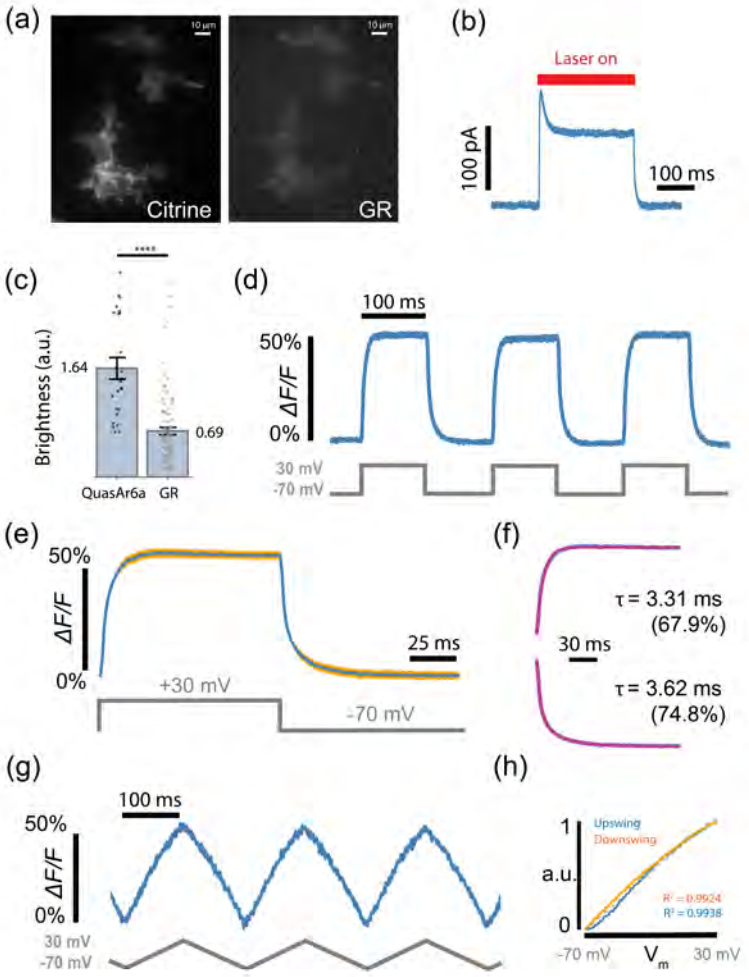

Figure 5.1: Characterization of GR wild-type. (a) Fluorescence of HEK cells expressing the Citrine and GR construct under excitation at 488 nm and 639 nm respectively. Scale bar: 10 µm. (b) An averaged photocurrent recording from a HEK cell expressing GR. The red bar indicates red laser illumination (illumination power: 625 mW mm^{-2}). (c) Expression normalized brightness of GR, compared to QuasAr6a. The mean and SEM values for QuasAr6a and GR are 1.64 ± 0.015 and 0.69 ± 0.0057. The error bar shows SEM. The independent t-test has a p-value of 4.38×10^{-10}. (d) Fluorescence response from a voltage-clamp measurement (from −70 mV to 30 mV). A maximum-likelihood pixel weighting algorithm was applied to generate the trace. (e) Averaged response to 30 mV to -70 mV voltage steps. The orange region shows SEM. (f) The kinetics of the upswing and downswing response to the 100 mV step. From the bi-exponential fitting, the fast time constant of the uprise is 3.31 ms with a percentage of 67.9%; The fast constant of the downswing is 3.62 ms with a percentage of 74.8%. (g) Fluorescence response under voltage clamp with a ramp from −70 mV to 30 mV. (h) Averaged ramp response from 15 trials. R-squares of the linear regression on the upswings and downswings are 0.9924 and 0.9938.

5.2.2. MECHANISM OF THE OPTOGENETICS PROPERTIES

The strong photocurrent is a consequence of the relatively fast photocycle of less than 100 ms[12]. Its photocycle is similar to proteorhodopsin (PR), which has most of the typical photointermediates seen in BR, as described in Chapter 1[12]. One of the unique features of GR is the strong presence of L/K-like and the N/O intermediates[8, 12]. Its M intermediate has sub-millisecond fast decay and is possibly in equilibrium with the L intermediate[12]. The proton is uptaken between the N and O intermediates, which is followed by proton release. The proton donor, Glu132, is deprotonated in the N-like intermediate, which is not strongly red-shifted and is reprotonated during the uptake event towards the O intermediate[12].

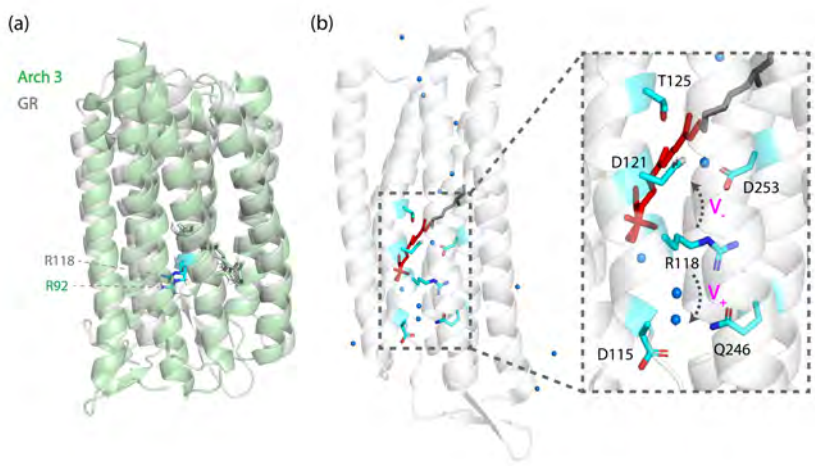

Figure 5.2: Potential voltage-sensing mechanism of GR, adapted from Arch described in Chapter 1. (a) Overlay of GR (light grey) and Arch3 (light green). Residue R92 from Arch3 and R118 from GR are highlighted in cyan (Arch3 PDB: 6GUZ; GR PDB: 6NWD). (b) The reorientation of Arg118 might happen under different membrane potentials. At negative voltage, it interacts with Asp121 and Asp253; at positive voltage, it faces towards the proton release group, and the counterion Asp121 might form a hydrogen bond with Thr125. The resulting rearrangement of the hydrogen bond network at positive voltage might decrease the interaction between RSBH+ and Asp121.

The voltage-sensing mechanism of Arch3 may provide a template to better understand the voltage-sensitive fluorescence of GR (Figure 5.2). The voltage-dependent reorientation of the residue Arg92 was identified as a critical event leading to the voltage-modulated fluorescence of Arch3[16]. This reorientation at higher voltage rearranges the hydrogen bond network and causes the prohibition of water intrusion and decreased interaction between the counterion and RSBH+. In BR, movement of the analogous Arg82

towards the extracellular half was identified in the early M intermediate, and this leads to the perturbation of the proton release group[17]. This site is highly conserved across rhodopsins. Structurally overlaying Arch3 and GR, Arg118 is the analogous residue in GR. Arg118 was found to be one of the three residues surrounding the proton release cavity[7]. The free energy barrier of Arg118 movement is likely small such as Arg82 in BR[17]. It is possible that, such as in Arch3, the voltage sensitivity of GR comes from the reorientation of Arg118. At negative membrane potential, it is likely that Arg118 faces towards the counterion and interacts with Asp121 and Asp253; while at positive membrane potential, Arg118 faces the extracellular side and interacts with Asp115 and Gln246. The deprotonation of RSBH+ to the counterion Asp121 is less probable at positive voltage due to the possible new hydrogen bond between Asp121 and T125, as discussed in Arch3[16].

5.3. CHARACTERIZATION OF GR MUTANTS THROUGH SITE-DIRECTED MUTAGENESIS

The above characteristics of GR wild-type demonstrate its potential to be used as a tool in optogenetics upon further engineering: it exhibits large voltage sensitivity, larger than the latest Arch-based GEVI[15]; this voltage-sensing response has fast kinetics, which is comparable to the Arch-based sensors; the brightness of wild-type GR is already higher than that of Arch, which was used as a template for engineering the latest sensors[13]; in addition, the efficient proton transfer and high photocurrent make it a candidate to function as an optogenetic silencer.

To further engineer GR towards an optimized optogenetics tool, we carried out mutagenesis on various sites and collected data to reflect its relevant properties. In this section, the data of the mutants from three main regions in the protein (retinal binding pocket at section 5.3.2, proton donor at section 5.3.3 and proton release complex at section 5.3.4) and the combinations across regions (section 5.3.5) is presented. The section concludes with a discussion of a potential mechanism.

5.3.1. MUTATIONS AT ARG118

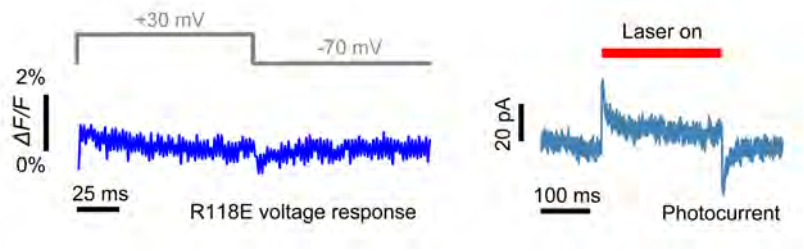

Figure 5.3: Characterization of the GR R118E mutants. Left: The voltage response measured using patch clamp, averaged from 3 cells. Right: The photocurrent response under red laser illumination. For both subfigures, the illumination power at 639 nm is 625 mW mm^{-2}

.

Before diving into the three regions, we will first take a closer look at the Arg118 mutant. In section 5.2.2, it is hypothesized that Arg118 plays an important role in voltage sensing. We mutated this site and measured the voltage response of GR R118E. The fluorescence trace shows no obvious voltage sensitivity, which is in line with the hypothesis (Figure 5.3 right). A small amount of photocurrent was measured during red laser illumination (Figure 5.3 left).

5.3.2. MUTATIONS AT THE RETINAL BINDING POCKET

The retinal binding pocket of GR shares conserved general features with BR while also having notable differences. The retinal is bonded to helix G via Lys257, a homolog of Lys216 of BR[7, 8]. In GR, the primary proton acceptor and counterion are Asp121 in helix C adjacent to the RSB, analogous to Asp85 in BR[8]. The hydrogen-bonded network between the aspartic acid pair (Asp85 and Asp212) and RSB in BR is conserved in GR, which involves Asp121, Asp253, and RSB[7].

However, the pK_a of the counterion in GR (5.9) is much higher than that of BR (2.5), similar to proteorhodopsin (GPR), possibly to adapt to the alkaline environment in the ocean[8, 18]. Another major difference from BR is the connection between the counterion Asp121 and His87 in helix B, which is conserved in GPR[19]. Apart from those, only one water molecule is found inside the hydrogen-bonded network formed by the aspartic acid pair (Asp121 and Asp253) and RSB[7]. While in BR, three water molecules were found to ensure the efficiency of the proton transfer between the RSB and the counterion[20].

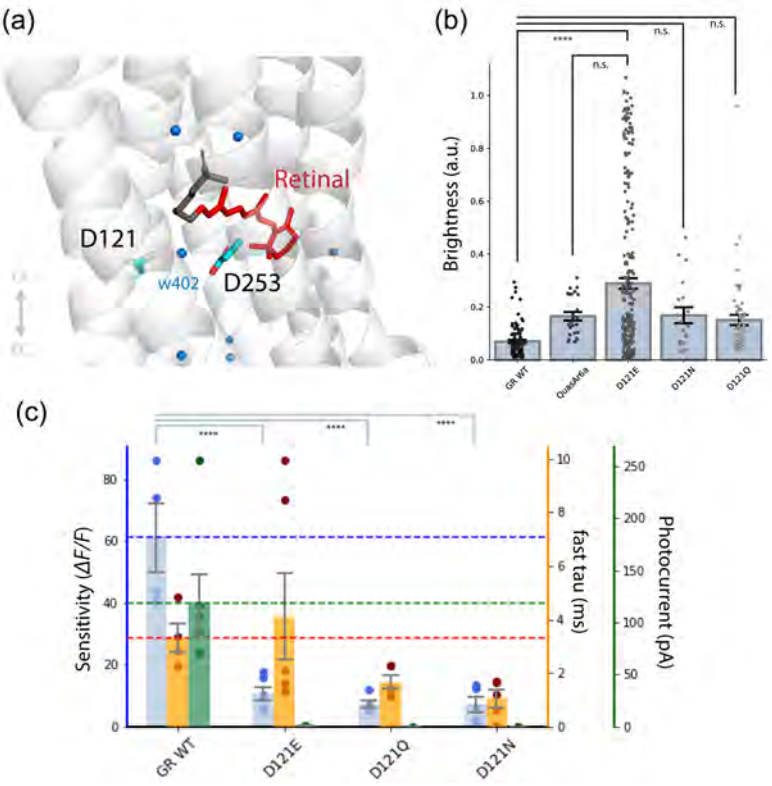

Figure 5.4: Characterization of the GR counterion mutants. (a) The crystal structure in the counterion vicinity in GR. The primary counterion, D121, sits next to the retinal binding site. The water molecules are shown in blue spheres, with the water-402 marked between D121 and D253. PDB: 6NWD. (b) Comparison of brightness values of HEK293T cells expressing GR WT (0.070 ± 0.0057, n = 100), QuasAr6a (0.164 ± 0.016, n = 24), D121E (0.289 ± 0.020, n = 294), D121N (0.168 ± 0.029, n = 19), D121Q (0.150 ± 0.019, n = 56). All statistics are mean ± SEM. The p-value of the one-way analysis of variance (ANOVA) test is 3.24×10^{-12}. The p-values of D121E, D121N, and D121Q against WT are 1.9×10^{-12}, 0.485, and 0.273, Tukey's post hoc test. (c) Comparison of voltage sensitivity, kinetics, and photocurrent of GR WT (4 cells), D121E (6 cells), D121Q (5 cells), and D121N (5 cells). Voltage sensitivity per 100 mV: 61.03% ± 11.16%, 10.64% ± 2.09%, 7.27% ± 1.20%, 7.10% ± 2.52%; fast time constant (ms): 3.31 ± 0.55, 4.13 ± 1.61, 1.66 ± 0.25, 1.04 ± 0.31; photocurrent (pA): 118.13 ± 28.38, 0.32 ± 0.03, 0.02 ± 0.002, -0.03 ± 0.016. The p-value of ANOVA test is 1.87×10^{-6}. The p-values of D121E, D121Q and D121N against WT are 8.25×10^{-6}, 5.93×10^{-6} and 5.69×10^{-6}.

For GR to serve as GEVI, the mechanism of proton transfer under illumination would need to be eliminated. RSB is key to the proton transfer; hence, the retinal binding pocket and its interacting residues are vital[12]. During the engineering of first-generation GEVIs based on GPR and Archaerhodopsin, the counterion is the first mutation site target to break the photocurrent[14, 21]. In several previous studies, mutations at Asp121 in GR demolished the photocurrent[8, 22, 23]. Therefore we first characterized a number of mutants targeted at the counterion Asp121 (Figure 5.4).

COUNTERION MUTANTS

The measurements of the D121N and D121Q mutants show no detectable photocurrent under red illumination (laser intensity: 625 $\mathrm{mW\,mm^{-2}}$; membrane potential: −30 mV; pH: 7.4). Neutralizing charge at the counterion position alone completely cripples proton transfer. Upon substitution of Asp with Glu in D121E, the photocurrent exists only at a very minimal level. The proton transfer efficiency is sensitive to the protonation capacity of the counterion.

In terms of voltage sensitivity, both the charged counterion mutant (D121E) and neutral ones (D121Q and D121N) are still voltage-sensitive but display a decrease compared to the wild-type. It is generally assumed that the voltage sensitivity of GEVIs comes from the membrane potential modulated equilibrium between protonated and deprotonated RSB[16]. In the D121E mutant, proton transfer from the RSB to the Glu can still occur, resulting in a slightly higher photocurrent (0.32 ± 0.03 pA, mean and SEM), which is in line with the higher voltage sensitivity of D121E compared to D121N/Q. In the D121E mutant, it is possible that the hydrogen bonds involving the counterion E121 (for example, the potential hydrogen bond between E121 and T125 whose analogue in Arch3, T99, was identified to form the bond with the counterion at positive voltage[16]) are strengthened, and the hydrogen bond network rearrangement due to membrane potential change is less prominent, which means a smaller difference in the RSB protonation status as a function of the voltage across the protein barrel than in wildtype GR.

It is worth noting that the asparagine substitution in the counterion results in a decrease in the pK_a of RSB in BR and PR, while the pK_a of GR D121N mutant was measured to be similar to the wild-type[8, 24]. In the more distant Arch3 family from archaea, the counterion mutant D95N shows a lower RSB pK_a and 50% greater sensitivity, which is opposite to the D121N mutant in GR[14]. The hydrogen network in the counterion vicinity is different as fewer water molecules are involved in the RSB binding pocket in GR than Arch; the proton transfer from RSBH+ to the alternative proton accepter Asp253 might be more difficult in GR once the counterion is neutralized.

The kinetics of the counterion mutants are comparable to the wild-type, and all display a fast response to the membrane potential changes (Figure 5.4(c)). The proton transfer speed of these mutants to reach equilibrium is on par with the wild-type.

In the characterization of the fluorescence brightness, the counterion mutants all show

a significant improvement (Figure 5.4(b)). Compared to the most evolved QuasAr sensors QuasAr6a, the brightness of D121N/Q is at the same level, while D121E shows a 75.6% increase[15]. It could be because deprotonation is in general more difficult in these mutants and a bigger protonated RSB population brings higher fluorescence. It was characterized that all mutations at the counterion introduce a red-shift in the absorption spectrum maxima (λ_{max}) except the D121E mutant, which shows an around 8 nm blue-shift[23]. In BR, disabling or disrupting the counterion extends the excited state lifetime when the counterion is neutralized, leading to a higher fluorescence[25, 26]. This is very likely the same in GR.

RETINAL BINDING POCKET MUTANTS

A set of mutations spread along the retinal binding pocket was characterized (Figure 5.5). Mutation sites T125, A256, and W122 are located near the RSB; mutation site F260 is near the proton donor E132.

The mutation site W122 is positioned right next to the counterion D121. The substitution of Tryptophan for Tyrosine decreases the voltage sensitivity and photocurrent while the time constant is higher, meaning a longer time is required to establish the equilibrium. The mutation site T125 resides on the same helix as the counterion, and it was identified together with the mutations at D121 and A256 to significantly red-shift the λ_{max} of GR[23]. In Arch3 and Archon1, the homology site T99 was identified as responsible for the voltage sensitivity because of its voltage-dependent hydrogen-bond formation with the neutralized counterion[16]. The single mutant, T125C, shows a 2-fold fluorescence compared to the wild-type. Another single mutant at this site, T125L, shows a much-decreased sensitivity while maintaining the same photocurrent and kinetics. This decrease might be due to its importance in voltage-sensing in GR, with a hypothesis that at a positive voltage, it can not form a bond with the counterion anymore. In the A256M mutant, all statistics, including sensitivity, photocurrent, and time constant, show a decrease. It is possible that in this mutant, the proton transfer is impacted, and RSB deprotonation/reprotonation happens on a small scale.

The mutation site F260 is adjacent to the proton donor E132. Replacing it with a positive histidine residue doesn't influence the proton transfer amplitude, as the photocurrent stays at the same level. However, the voltage sensitivity and the speed to reach the equilibrium decrease.

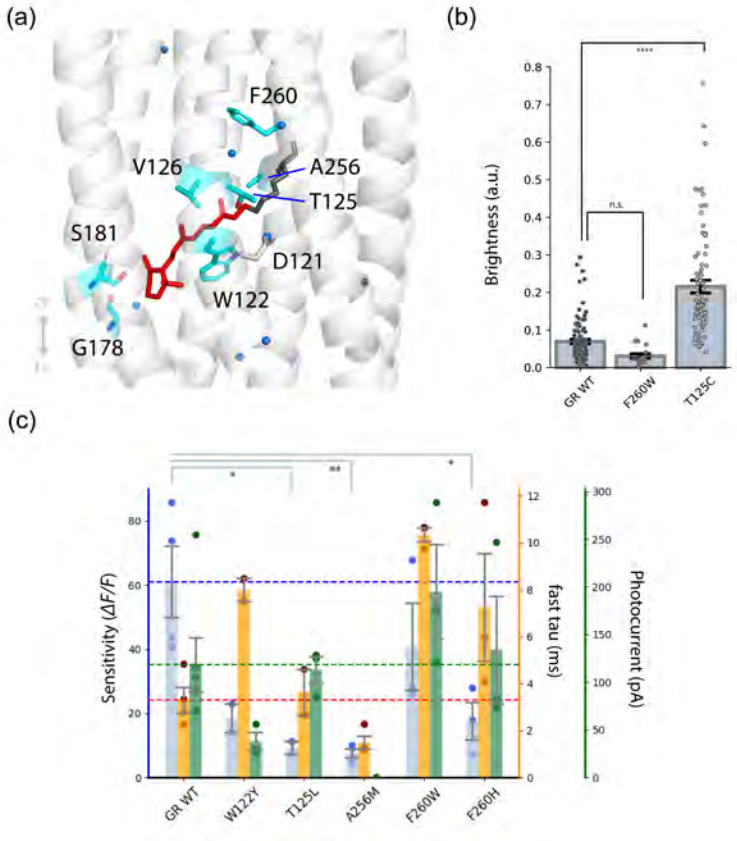

Figure 5.5: Characterization of the GR retinal binding pocket mutants. (a) The structure and important amino acids in the retinal binding pocket. (b) Comparison of brightness values of HEK293T cells expressing GR WT (0.070 ± 0.0057, n = 100), F260W (0.030 ± 0.006, n = 20), T125C (0.215 ± 0.017, n = 96). All statistics are mean ± SEM. The p-value of the one-way analysis of variance (ANOVA) test is 4.15×10^{-17}. The p-values of F260W and T125C against WT are 0.374 and -3.60×10^{-14}, Tukey's post hoc test. (c) Comparison of voltage sensitivity, kinetics, and photocurrent of GR WT (4 cells), W122Y (2 cells), T125L (2 cells), A256M (4 cells), F260W (3 cells), and F260H (3 cells). Voltage sensitivity per 100 mV: 61.03% ± 11.16%, 18.55% ± 4.36%, 9.25% ± 1.96%, 7.54% ± 1.32%, 40.75% ± 13.59%, 17.66% ± 5.91%; fast time constant (ms): 3.31 ± 0.55, 7.99 ± 0.51, 3.65 ± 0.98, 1.49 ± 0.27, 10.35 ± 0.29, 7.25 ± 2.29; photocurrent (pA): 118.13 ± 28.38, 38.1 ± 9.17, 112.86 ± 13.83, 0.0014 ± 0.0034, 195.15 ± 49.22, 133.84 ± 56.49, . The p-value of the ANOVA test is 0.0039. The p-values of W122Y, T125L, A256M, F260W, and F260H against WT are 0.069, 0.021, 0.004, 0.0548, and 0.030.

5.3.3. MUTATIONS AT THE PROTON DONOR

The residues involved in proton-transfer to the RSB in the cytoplasmic side of GR are different from BR in many ways. The proton donor in GR is found to be a Glutamic acid rather than an Aspartic acid in BR[12]. This proton donor, E132, is strongly coupled to the RSB and directly connected to the backbone of the Retinal binding residue K257 through the hydrogen-bridged water together with S77; while in BR, the proton donor D96 does not form a direct hydrogen bond with the RSB or the backbone through water molecule[7]. Because of this long-range interaction, the structural perturbation of E132 was observed upon retinal photoisomerization at the start of the photocycle[27].

Substitution of the glutamate residue with an aspartate residue results in a decreased photocurrent (Figure 5.6(c)). Previous studies observed that the photocycle turnover time for E132D is multiple times slower[12]. This explains the overall lower photocurrent amplitude.

The voltage sensitivity of E132D is several times smaller than that of the wild-type. Through visible-light spectroscopy, E132D was found to exhibit an order of magnitude delayed M intermediate decay[12]. As D132 may have a higher pK_a than E132, the proton-transfer from D132 to RSB is much less probable than from E132 in wild-type. Applying the assumption that the voltage sensitivity comes from the equilibrium between RSB protonation states, the E132D mutant would lead to a minor population difference in the protonation equilibrium, which would explain the decreased voltage sensitivity[16]. Probably due to the accumulated blue-shifted M states, the overall brightness is lower than the wild-type(only three cells measurement).

The E132D mutant has a very similar fluorescence rise time to the wild-type in response to a voltage step. Despite the slowed-down photocycle, it takes a short time to establish the new RSB protonation equilibrium (relatively smaller change reflected by decreased sensitivity) driven by membrane potential change.

Neutralization of the proton donor site, E132Q, shows a reversed (less bright at higher membrane potential) voltage sensitivity (Figure 5.6(c)). Reversing the voltage sensitivity was also demonstrated in Ace with the proton donor mutant D92N[28]. It was reasoned that the protonation equilibrium is between RSB and the extracellular half of the protein in the mutant instead of RSB and the cytoplasmic half.

In the photocurrent measurement, a transient outward current is observed when the light is turned on (except the first pulse), and a transient inward current when the light is turned off (Figure 5.6(b)). This shows that at the very first moment that the illumination is turned on, the proton transfers towards the extracellular side, and no proton can be supplied to RSB for active pumping. The cross-membrane potential influences the likelihood of RSB protonation. If the equilibrium is indeed between RSB and the extracellular side now, then at a higher voltage, there would be more deprotonated RSB and, thus, lower fluorescence.

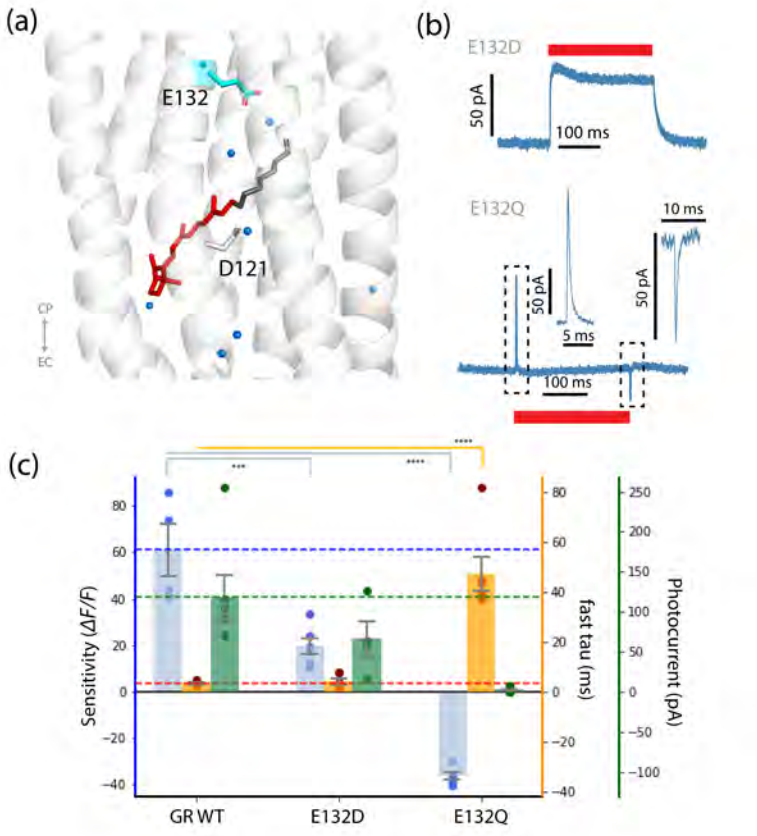

Figure 5.6: Characterizations of the GR proton donor mutants. (a) The proton donor Glu132 is located at the cytoplasmic side of the protein. D121 is the counterion in GR. The water molecules are represented in blue spheres. (b) The photocurrent measurements of E132D and E132Q. The traces are averaged from 8 responses. The red bars indicate the laser illumination periods. Laser power: 625 mW mm^{-2}. (c) Comparison of voltage sensitivity, kinetics, and photocurrent of GR WT (4 cells), E132D (6 cells), and E132Q (6 cells). Voltage sensitivity per 100 mV: 61.03% ± 11.16%, 19.73% ± 3.39%, -36.12% ± 1.50%; fast time constant (ms): 3.31 ± 0.55, 4.27 ± 1.17, 47.36 ± 7.03; photocurrent (pA): 118.13 ± 28.38, 66.09 ± 22.50, 2.39 ± 1.21. For sensitivity: the p-value of the ANOVA test is 4.64×10^{-8}; the p-values of E132D and E132Q against WT are 4.08×10^{-4} and 3.92×10^{-8}.

The voltage response kinetics of E132Q are very slow, with a time constant of up to 50 ms. The photocycle study shows that the E132Q mutant has extremely slow M decay (up to several seconds), and the M intermediate coexists with a red-shifted N/O inter-

mediate[12]. The disruption at the proton donor site may be coupled to the RSB through the direct hydrogen bond; the proton transfer pathway is very inefficient, affecting the establishment speed of the protonation equilibrium.

5.3.4. MUTATIONS AT THE PROTON RELEASE COMPLEX

The proton release site of GR has a tighter structure compared to BR and XR[7] (Figure 5.7(a)). The glutamate pair responsible for the early/fast proton release in BR photocycle is missing in GR, and one of the glutamate is replaced by uncharged glutamine side chain Gln246[7]. The proton release in GR happens at the end of the photocycle after the proton uptake between the N and O intermediates[12]. A hydrogen-bonded network responsible for proton release is formed between Arg118, Gln246, and Asp115 instead in GR, and it accommodates two water molecules (rather than three in BR) in this region[7]. Near Asp115 at the extracellular opening, a glutamate E166 forms a salt bridge with R174, and this pair can modulate the relative position of helices E and G[7].

The residue responsible for the proton release is Asp115 which is located at the end of the helix. Four mutants were characterized on this site, three of them with a neutral charge. The D115E mutant retains the negative charge and shows a higher photocurrent than the wild-type (Figure 5.7(d)). This shows that the proton transfer pathway is intact, and the photocycle turnover time is even faster. Probably the proton release is more efficient in this mutant.

The voltage sensitivity, however, is around 22% per 100 mV, much smaller than the wild-type. In this case, the faster proton transfer efficiency correlates with a smaller difference in the RSB protonation population. The fluorescence response speed to voltage remains the same as the wild-type. Since the negative charge remains on this site, it is still possible for Arg118 to interact with E115.

Two polar uncharged amino acid substitutions, Q and N, were characterized at the D115 site. The D115Q mutant displays a decreased photocurrent, which is reasonable as the proton-releasing site is disabled; while still more than half of the photocurrent remaining says that D115 is not the only site involved in proton release. The voltage sensitivity decreases to the same level (19%) as the D115E mutant, and the kinetics is also similar to D115E. The interaction probability between Arg118 and D115Q could be similar to the case of D115E.

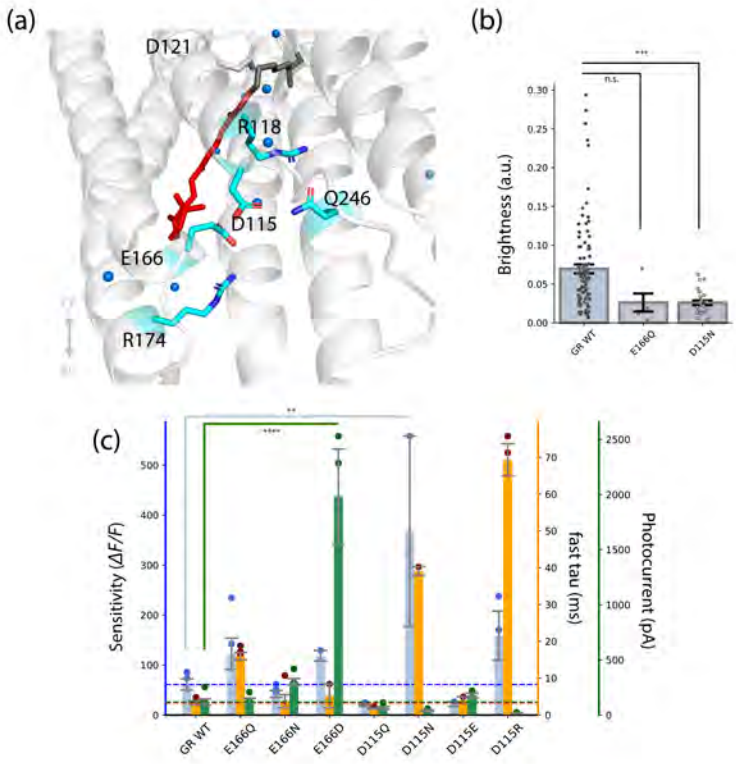

Figure 5.7: Characterizations of the GR mutants at proton release complex.. (a) The structure of GR proton release complex. (b) Comparison of brightness values of HEK293T cells expressing GR WT (0.070 ± 0.0057, n = 100), E166Q (0.026 ± 0.010, n = 5) and D115N (0.026 ± 0.003, n = 25). All statistics are mean ± SEM. The p-value of the one-way analysis of variance (ANOVA) test is 3.7×10^{-4}. The p-values of E166D and D115N against WT are 0.156 and 6.01×10^{-4}, Tukey's post hoc test. (c) Comparison of voltage sensitivity, kinetics, and photocurrent of GR WT (4 cells), E166Q (5 cells), E166N (5 cells), E166D(2 cells), D115Q (6 cells), D115N (2 cells), D115E (2 cells) and D115R (3 cells). Voltage sensitivity per 100 mV: 61.03% ± 11.16%, 122.59% ± 31.32%, 42.17% ± 6.92%, 118.70% ± 10.55%, 19.20% ± 1.56%, 367.87% ± 190.32%, 22.03% ± 4.50%, 158.64% ± 49.50%; fast time constant (ms): 3.31 ± 0.55, 16.00 ± 0.96, 3.76 ± 1.78, 5.19 ± 3.22, 1.71 ± 0.16, 39.11 ± 1.12, 4.06 ± 0.89, 69.32 ± 4.35; photocurrent (pA): 118.13 ± 28.38, 131.40 ± 22.51, 301.64 ± 29.88, 1981.77 ± 430.81, 63.68 ± 12.41, 41.19 ± 7.41, 177.62 ± 21.44, 16.34 ± 4.35. For sensitivity: the p-value of the ANOVA test is 4.65×10^{-4}; the p-values of D115N against WT is 0.002. For photocurrent: the p-values of E166D against WT is 2.87×10^{-12}.

The D115N mutant behaves very differently from D115Q, although both amino acids are uncharged. It has a slightly lower photocurrent than D115Q. However, it displays a huge voltage sensitivity, a $\Delta F / F_0$ up to 367% across 100 mV. The time it takes for the fluorescence to reach the new equilibrium increases the same amount as the sensitivity compared to D115Q (22 times increase from 1.7 ms to 39.1 ms, and the sensitivity increases 18.3 times). The D115N mutant can change the population of protonated RSB more dramatically under the influence of membrane potential. If the turning of Arg118 towards Asp115 is the reason for the sensitivity, it is then possible that Arg118 can form stronger interaction with either N115 or other sites under a slow time scale (It could be that the RSB equilibrium is established beyond the counterion and shifts until the release pocket.) The resting potential fluorescence of D115N is low compared to the wild-type.

The D115R mutant turns the negative charge at the proton release site into a positive charge. As the positive Arginine introduces more disturbance than Asparagine, the photocurrent is persistent but decreases compared to the D115N mutant (16.3 pA). It is in line with the previous hypothesis that D115 is not the only necessary site for proton release. The voltage sensitivity is more than two times larger than the wild-type, reaching a $\Delta F / F_0$ of up to 158.6%. It can form a large difference in protonated/deprotonated RSB populations like the D115N mutant. The kinetics of this is very slow, even much slower than D115N. It could be that Arg118, in this case, interacts with other sites (like Gln246) at positive membrane potential. The formation of this interaction between Arg118 and the other site might happen very inefficiently, causing an extremely slow response time. D115R likely has an extremely slow photocycle turnover, and the very inefficient proton transfer influences the speed of proton transfer to/from the RSB. In D115N and D115R mutants, the accumulation of protons at the releasing half could influence the hydrogen bond organization in the RSB region so that it is more favourable to a deprotonated RSB, while the reprotonation from the donor still happens at a similar scale with the wild-type.

Another mutation site we targeted in the proton release region is Glu166, which is near Asp115 and forms a salt bridge with Arg174 on the neighbouring helix (Figure 5.7(a)). Among the three mutants characterized, one (E166D) retains the negative charge, and the other two (E166Q and E166N) neutralize the charge.

The E166D mutant triggers a huge outwards photocurrent under red illumination (639 nm, 625 $\mathrm{mW\,mm^{-2}}$, with an average of 1981 pA, almost 20 times of the wild-type (Figure 5.7(c)). The difference of the pK_a in this site influences the proton release. In this mutant, the difference in the side chain will influence the salt bridge and the distance between the helix E and D. This rearrangement in the extracellular opening structure is likely to greatly improve the proton transfer efficiency.

The voltage sensitivity of E166D is 60% higher than the wild-type (118.7% $\Delta F / F_0$). The time to reach the voltage-induced equilibrium is proportionally longer. It might allow Arg118 to form a stronger connection with the proton release group and lead to the sensitivity increase. The more efficient proton transfer pathway accompanies a more differentiated RSB protonation population.

The E166Q mutant neutralizes the negative charge at this site; thus, the salt bridge with Arg174 is possibly abolished/rearranged. The voltage sensitivity is higher than the wild-type and similar to the E166D. The time constant is, however, quite large. The E166N mutant displays a higher photocurrent than the wild-type and E166Q. The voltage sensitivity has decreased while the time constant remains the same.

5.3.5. COMBINATION OF MUTATION SITES

INVOLVING THE COUNTERION

One feature of the counterion mutants is the eliminated photocurrent. This is an important attribute for a GEVI, and we combined these counterion mutants with other mutants in the proton-transfer pathway. The goal here is to increase the voltage sensitivity of the couterion mutants, to improve their performance as GEVIs.

Combining the D121E with any other binding pocket mutation sites shows a moderate, sometimes smaller, voltage sensitivity similar to D121E (D121E/T125C, D121E/A256M, D121E/T125C/A256M). The photocurrent remains zero. The kinetics is also similar to D121E. In the case of D121E/T125C and D121E/T125C/A256M, the voltage sensitivity is slightly lower than D121E. However, the D121E/T125C/A256M mutant displays a much-improved brightness (0.755 against 0.070 of WT, Figure 5.8(b)), which coincides with previous research[23].

Combining the D121E with mutations at the proton release region yields mutants with distinct features (Figure 5.8(c)). Adding the D115N mutation to D121E increases the voltage sensitivity to more than three times that of the D121E mutant, although it is still lower than the wild-type (32.7% $\Delta F / F_0$). The kinetics are slightly faster than D121E (1.94 ms versus 4.14 m), meaning that the RSB protonation equilibrium is a quick process. The photocurrent is the same as D115N, which is less than half of the wild-type (39.7 pA). It seems that compared to D115N, the influence of the counterion mutation D121E on the proton transfer is negligible. Under the influence of extracellular changes, the proton could go to D121E or the alternative counterion and transfer down the line. The triple mutant, D121E/A256M/D115N, shows similar characteristics to D121E/D115N, except for a decreased sensitivity (still higher than D121E). The A256M mutant alone has a low sensitivity such as D121E, and it seems that combining binding pocket mutations, in this case, narrows the difference in RSB protonation population under different voltages. On top of the triple mutant, the D121E/A256M/T125C/D115N mutant shows higher voltage sensitivity than the triple mutant (D121E/A256M/T125C), but with a photocurrent and slower kinetics probably due to the N115.

The combination of D121E and D115R results in a mutant that exhibits averaged characteristics from the individual ones (Figure 5.8(c)). The voltage sensitivity is around 56.79%, which is in the middle of 10.64% from D121E and 158.64% from D115R. The fast time constant, 14.71 ms, is also slower than D121E but faster than D115R. The photocurrent is around 20.35 pA, similar to that of D115R.

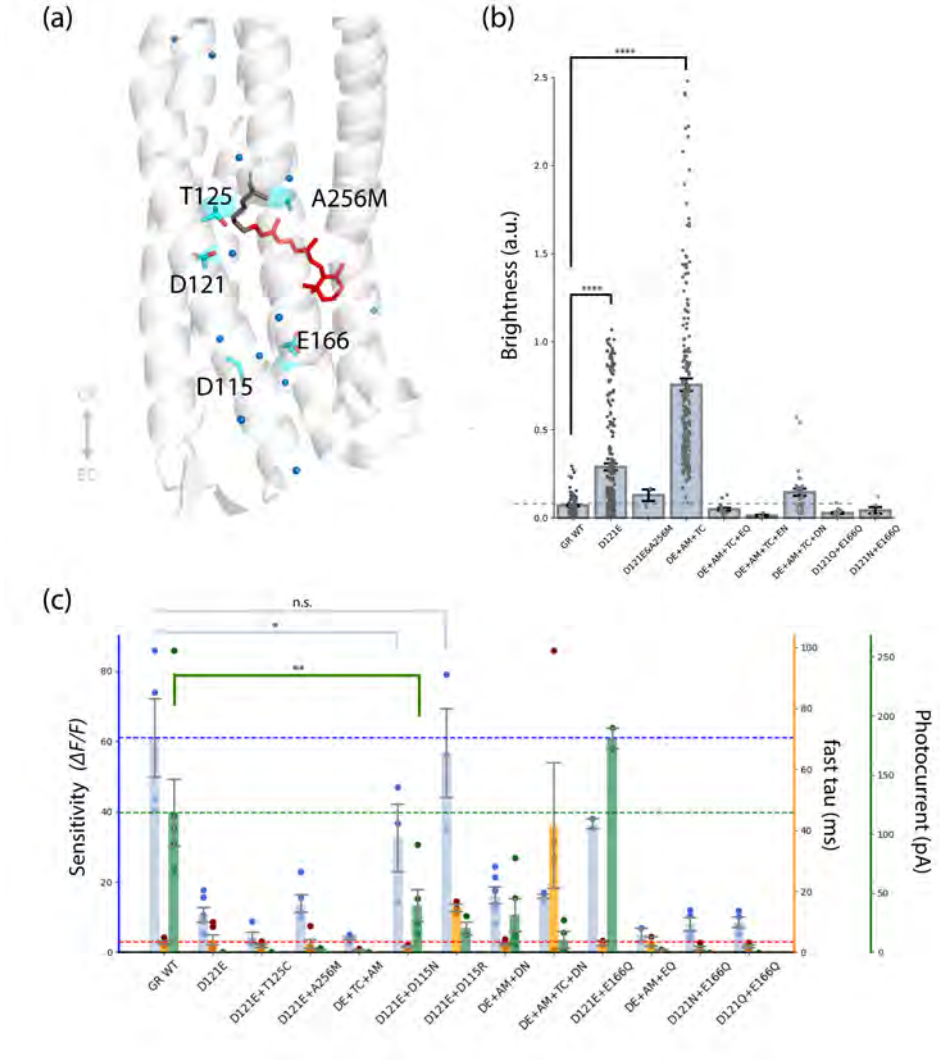

Figure 5.8: Characterizations of the mutants combinations involving the counterion. (a) The crystal structure of the counterion D121 and other sites involved in the characterizations. The water molecules are shown in blue spheres. PDB: 6NWD. (b) Comparison of brightness values of HEK293T cells expressing GR WT (0.070 ± 0.0057, n = 100), D121E (0.289 ± 0.020, n = 249), D121E+A256M (0.128 ± 0.027, n = 3), D121E+A256M+T125C (0.755 ± 0.036, n = 237), D121E+A256M+T125C+E166Q (0.049 ± 0.008, n = 16), D121E+A256M+T125C+E166N (0.012 ± 0.004, n =4), D121E+A256M+T125C+D115N (0.145 ± 0.019, n = 35), D121Q+E166Q (0.027 ± 0.004, n = 19), D121N+E166Q (0.043 ± 0.017, n = 6). All statistics are mean ± SEM. The p-value of the one-way analysis of variance (ANOVA) test is 3.73×10^{-57}. The p-values of D121E and D121E+A256M+T125C against WT are 5.97×10^{-5} and -3.30×10^{-13}, Tukey's post hoc test.

Figure 5.8: (c) Comparison of voltage sensitivity per 100 mV, kinetics and photocurrent of GR WT (61.03% ± 11.16%, 3.31 ± 0.55 ms, 118.13 ± 28.38 pA, 4 cells), D121E (10.64% ± 2.09%, 4.13 ± 1.61 ms, 0.32 ± 0.03 pA, 6 cells), D121E+T125C (4.26% ± 1.52%, 2.14 ± 0.53 ms, -0.02 ± 0.01 pA, 4 cells), D121E+A256M (13.89% ± 2.48%, 2.83 ± 1.45 ms, 1.22 ± 1.2 pA, 5 cells), D121E+T125C+A256M (4.05% ± 0.44%, 0.89 ± 0.19 ms, -0.03 ± 0.02 pA, 5 cells), D121E+D115N (32.68% ± 9.63%, 1.94 ± 0.40 ms, 39.68 ± 13.72 pA, 3 cells), D121E+D115R (56.79% ± 12.65%, 14.71 ± 1.17 ms, 20.35 ± 5.17 pA, 3 cells), D121E+A256M+D115N (16.28% ± 2.42%, 2.87 ± 0.38 ms, 31.74 ± 13.92 pA, 6 cells), D121E+T125C+A256M+D115N (16.03% ± 0.55%, 41.72 ± 20.6 ms, 10.63 ± 6.83 pA, 4 cells), D121E+E166Q (36.61% ± 1.37%, 3.05 ± 0.84 ms, 181.21 ± 8.78 pA, 2 cells), D121E+A256M+E166Q (5.04% ± 1.97%, 3.64 ± 1.52 ms, 2.01 ± 0.36 pA, 2 cells), D121N+E166Q (8.03% ± 1.89%, 1.45 ± 0.59 ms, 1.09 ± 0.49 pA, 4 cells) and D121Q+E166Q (8.63% ± 1.48%, 2.0 ± 0.46 ms, -1.12 ± 0.36 pA, 4 cells). For sensitivity: the p-value of ANOVA test is 4.47×10^{-11}; the p-values of D121E+D115N and D121E+D115R against WT are 0.02, and 1. For photocurrent, the p-value of D121E+D115N against WT is 0.006.

Another combination we characterized is D121E/E166Q (Figure 5.8(c)). The photocurrent of the double mutant (181.2 pA) is even higher than the E166Q mutant (131 pA). In this case, compared to E166Q, the counterion mutation D121E does not impair the proton transfer; however, the transfer is facilitated. The voltage sensitivity is more than three times that of D121E; the fluorescence kinetics is as fast as D121E. In both the double mutants involving the combination of D121E and the proton release site mutation, the voltage sensitivity is a compromise between the two, and dynamics are fast, comparable to existing Arch-based sensors. Adding the A256M mutation to the double mutant brings down the sensitivity to lower than D121E and eliminates the photocurrent. The proton transfer seems to be crippled, as well as the ability for protons to go in and out of RSB.

D121N and D121Q are also combined with E166Q for characterization. Different from D121E/E166Q, both of them showed voltage sensitivity no different from D121Q and D121N, at around 7% $\Delta F / F_0$. The photocurrent is also demolished, showing that the negative charge on the counterion is a necessity for the proton transfer. With the photocurrent completely gone, it seems that the RSB protonation/deprotonation scale is limited by the neutralized counterion, and the influence from the proton release site is cut off. In other words, the negative counterion is necessary to engineer GR towards high voltage sensitivity.

INVOLVING PROTON RELEASE SITES

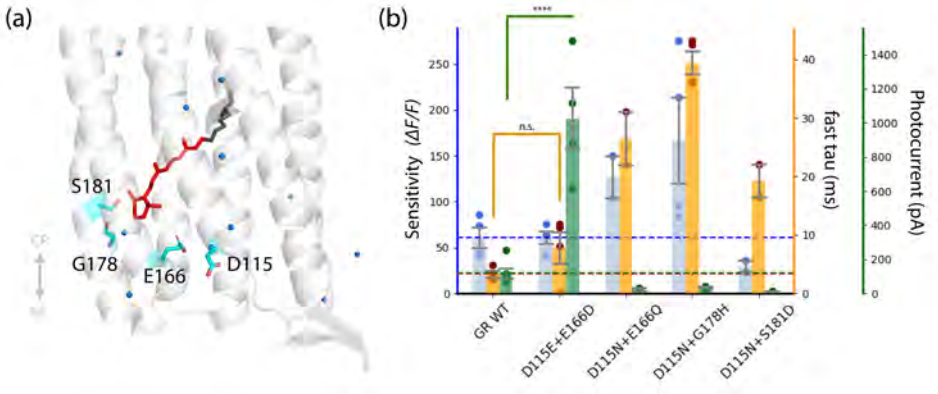

Figure 5.9: Characterizations of the mutants combinations at the proton release complex.. (a) The locations of measured sites. (b) Comparison of voltage sensitivity, kinetics, and photocurrent of GR WT (4 cells), D115E+E166D (4 cells), D115N+E166Q (2 cells), D115N+G178H (4 cells) and D115N+S181D (2 cells). Voltage sensitivity per 100 mV: 61.03% ± 11.16%, 60.98% ± 6.82%, 126.76% ± 23.03%, 167.01% ± 46.65%, 29.57% ± 6.14; fast time constant (ms): 3.31 ± 0.55, 7.8 ± 2.7, 26.52 ± 4.58, 39.5 ± 1.96, 19.22 ± 2.86; photocurrent (pA): 118.13 ± 28.38, 1025.67 ± 182.43, 23.2 ± 11.21, 35.42 ± 5.07, 10.34 ± 4.01. For sensitivity: the p-value of the ANOVA test is 0.035, and all the p-values are not significant; for photocurrent: the p-value of the ANOVA test is 1.03×10^{-5}, and the p-value of D115E+E166D against WT is 2.5×10^{-5}.

The D115 mutation site was combined with several single mutants and characterized (Figure 5.9). The combination of D115E and E166D results in a mutant that shows an average effect on the voltage sensitivity and photocurrent (60.9% ΔF / F_0 and 1025.6 pA sit perfectly in the middle of the two single mutants statics). Their impact on each other seems linear.

The D115N/E166Q mutant displays a decreased photocurrent compared to either single mutant. The disruption in the proton transfer builds up in the proton release pocket, and the proton transfer efficiency is relatively low (23.2 pA). The sensitivity is the same as E166Q, which is much smaller than D115N. It seems that E166Q imposes a limit on the sensitivity. The voltage response dynamics are in between the two single mutants.

5.4. DISCUSSION

5.4.1. KEY SITES

The GR protein is a concise and delicate piece of machinery, and any changes in the protein would influence the hydrogen-bonding network and lead to functional differences. Though, some sites have more substantial influence than others as seen from the results in section 5.3.

In terms of voltage sensitivity, several sites along the protein play a crucial role in changing the voltage-sensing behaviour. The first one is R118, which is analogous to R92 in Arch3 (Figure 5.10). In Arch3, the flipping of Arg92 at different membrane potentials initiates the tuning of the hydrogen bonding network and leads to the modulation of RSB protonation[16]. While in GR, mutating R118 causes the loss of voltage sensitivity. This suggests that, like in Arch3, the voltage-modulated reorientation of R118 rearranges the hydrogen bonding network and changes the proton transfer efficiency between RSB and the counterion D121 and D253. As a result, at a more positive voltage, the deprotonation from RSBH+ to the counterion is less probable, which means a larger fluorescent population of GR molecules.

The counterion, D121, is another crucial site that is directly involved in voltage sensing. Mutating this residue would directly influence the RSB deprotonation and, thus, the voltage sensitivity. All three counterion mutants that we characterized display a largely decreased voltage sensitivity. For D121N and D121Q, which abolish the negative counterion, the RSB deprotonation becomes more difficult as demonstrated previously by a lack of the M intermediate in the photocycle[12]. This would result in a smaller gap in the protonated/deprotonated RSB population under different membrane potentials. For the negatively charged counterion mutant D121E, the slightly longer Glutamic acid would alter/reorganize the hydrogen bonding network involving the counterion. For example, the interaction between T125 and E121 might be stronger. This could lead to a higher barrier to deprotonate the RSBH+, which limits the room for voltage modulation.

The proton donor, E132, is an important engineering site, as some mutants can change the polarity of voltage sensitivity. It is a crucial site involved in the proton transfer: the proton on RSB is replenished from the proton donor in the photocycle. Changing from the negative Glutamic acid to polar uncharged Glutamine reverses the voltage sensitivity: at a positive voltage, the fluorescence emission becomes less with slow kinetics. As demonstrated by a previous study[12], the M decay is prolonged, which means diminished proton supply from the inside of the cell. It is likely that at a higher voltage, the RSBH+ is even more likely to be deprotonated; since the extracellular half is unchanged in the proton donor mutant, the cytoplasmic side might be involved in the new equilibrium.

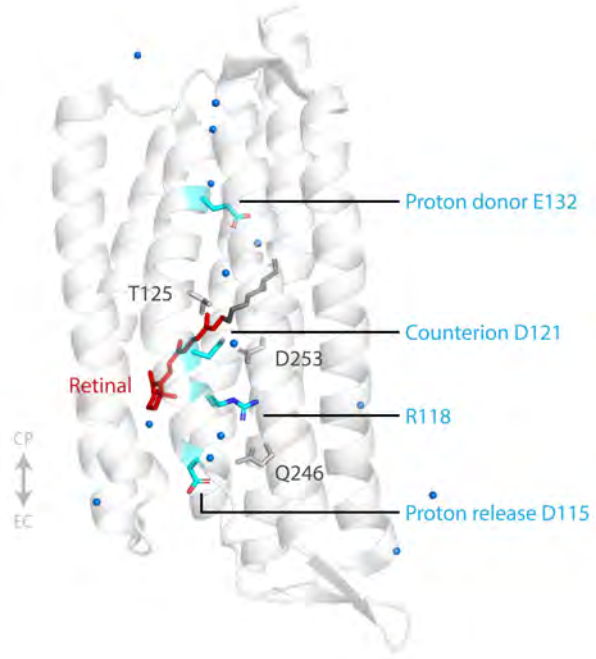

Figure 5.10: The locations of key sites in GR. The four identified sites that are crucial to voltage sensing are located along the proton transfer pathway. Other potential important sites in voltage-sensing, such as T125, D253, and Q246, are marked in the figure as well.

Mutations at the negatively charged proton release site, D115, also have an impact on voltage sensitivity. Neutralizing D115 to Q and N leads to a huge increase in sensitivity, while remaining part of the photocurrent, as seen in section 5.3.4. The positively charged arginine makes 115 very unlikely to be protonated. It is possible that at a positive voltage, R118 can form a stronger interaction with the proton release complex, and that the counterion is more probable to form a hydrogen bond with T125, which means less probable proton transfer from RSBH+ to the counterion D121.

In terms of photocurrent, mutations at E166 cause a dramatic change in the photocurrent amplitude. The E166N and E166D mutants both have a highly improved photocurrent compared to the WT, while E166D shows about 20-fold increase. It is likely that the original salt bridge between E166 and R174 has a crucial effect on the extracellular structure of the protein, and the disturbance in this structure will increase the proton transfer efficiency.

In terms of fluorescence emission, D121 mutants and T125C, greatly improve the brightness. These two sites were identified in previous studies to cause a red-shift in the ab-

sorption maxima[23]. The cause was reasoned to be the disruption of the interaction between the RSBH+ and the counterion, and the energy barrier to enter the photocycles is higher in these mutants. T125 in GR was aligned with T99 in Arch3, which was a key site responsible for voltage sensing; it forms a hydrogen bond with the counterion at a positive voltage. Mutants involving T125 show a decreased voltage sensitivity.

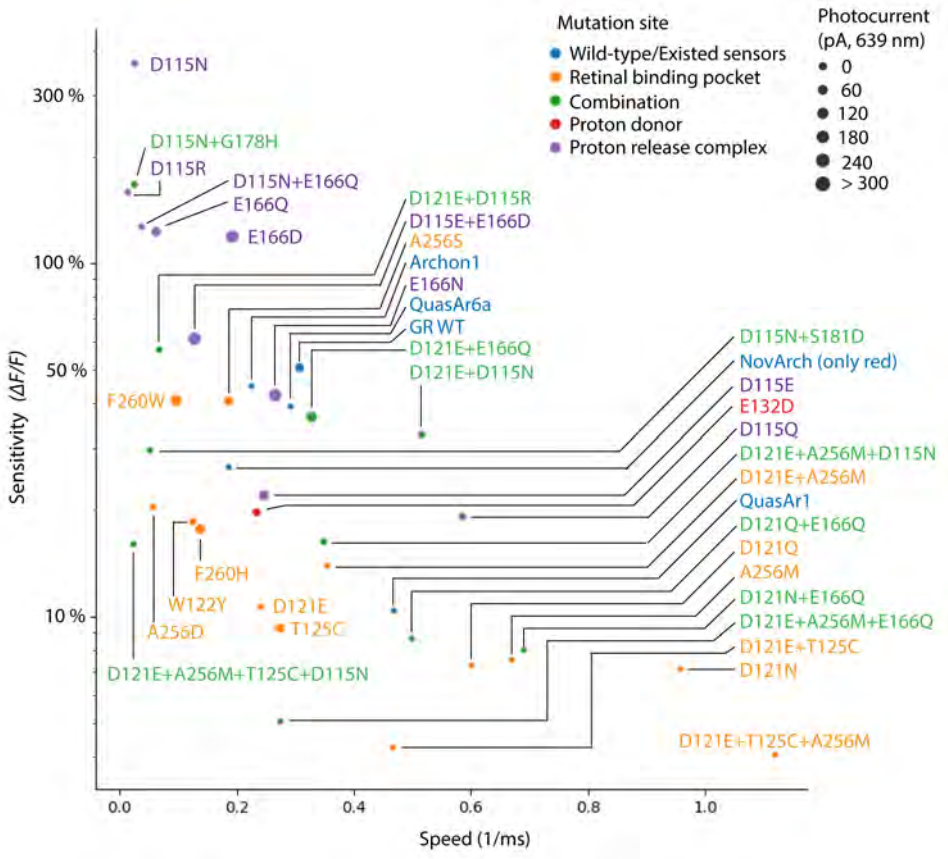

Figure 5.11: Visualization of GR mutants characterizations with existing GEVIs. The y-axis represents the voltage sensitivity change from −70 mV to 30 mV. Three parameters, voltage sensitivity, speed, and photocurrent, are represented in the figure. The location of the mutation is represented in colors.

5.4.2. TOWARDS AN INDICATOR

The wild-type GR already has all the good parameters of a GEVI except the photocurrent (Figure 5.1). We examined data from nearly 40 mutants and discussed the potential in-

fluence of these mutations in section 5.3. The performance of all characterized mutants discussed in previous sections is displayed in the scatter plot in Figure 5.11 along with other optimized GEVIs.

In the pool of mutants that are discussed above, we selected the ones that have very limited photocurrent and examined their performance in terms of voltage reporting SNR in Figure 5.12.

GENERIC VOLTAGE INDICATOR

GEVIs with balanced parameters between voltage sensitivity, brightness, and kinetics are considered generic voltage indicators. The counterion mutants themselves have promising features to be generic GEVIs: under red illumination, they have brighter fluorescence than the most evolved rhodopsin-based GEVI QuasAr6a, as well as fast kinetics at the same level. The mutant D121E exhibits a brightness that is 75.6% higher than QuasAr6a and comparable kinetics. The drawback is the moderate voltage sensitivity at around 12%. In terms of the SNR over 100 mV steps in HEK cells, D121E is about 43% of QuasAr6a, 67% of Archon1, and 170% of QuasAr1.

In the follow-up mutants that we tried to improve upon the voltage sensitivity of D121E, the double mutant D121E/D115R, exhibits a much-improved voltage sensitivity (56.79%, 14.71 ms and 20.35 pA, Figure 5.8) compared to D121E (10.26%, 2.09 ms and 0.32 pA, Figure 5.8), and is 42% more sensitive than QuasAr6a (39.2% in our measurements). In the SNR comparison, D121E/D115R is 74% higher than D121E, 20% higher than Archon1, and reaches 76% of QuasAr6a (Figure 5.12). D121E/D115R has the potential to be a generic GEVI with a high voltage sensitivity.

BRIGHT VOLTAGE INDICATOR

The D121E/T125C/A256M mutant exhibits phenomenally high brightness, about 4.75 times the brightness of QuasAr6a (Figure 5.12). The 639 nm Arch fluorescence of this mutant is 0.76 that of the citrine one, nearly 1. Considering laser power difference (the power of the 488 nm laser is about 4.75% of the 639 nm laser), the quantum yield of the triple mutant D121E/T125C/A256M is roughly 3.64% of citrine, reaching 0.027. The major bottleneck of most currently used rhodopsin-based GEVIs is their relatively dim fluorescence, which results in poor SNR and forbids many *in vivo* applications. The triple mutant D121E/T125C/A256M with its exceptional brightness offers a solution for experimental cases where a bright and millisecond-response voltage indicator is needed.

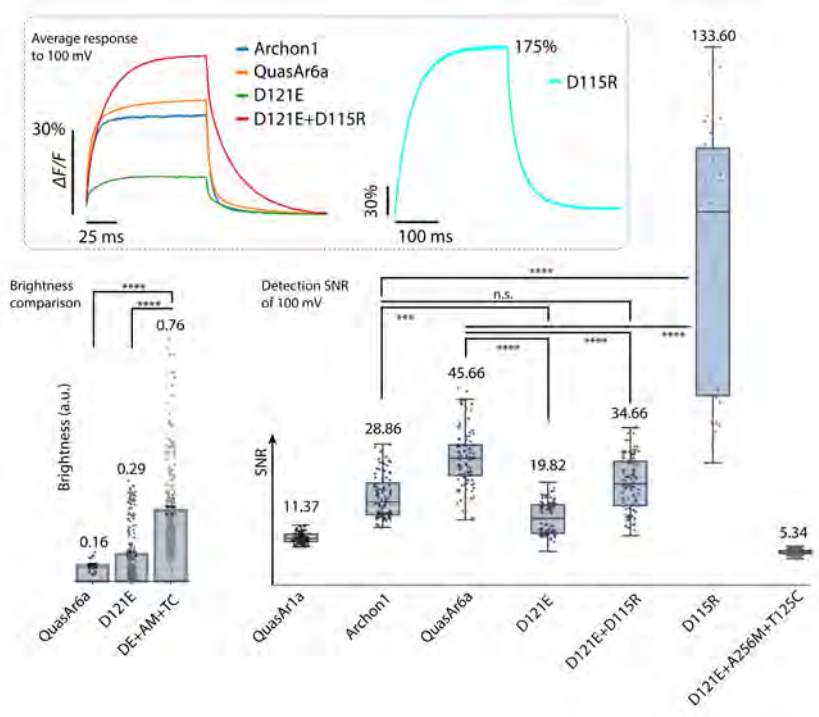

Figure 5.12: Comparison of potential GEVI candidates. Top: Averaged responses to 100 mV steps from Archon1, QuasAr6a, D121E, D115R, and D121E+D115R. Left: Brightness comparison between QuasAr6a, D121E, and D121E+A256M+T125C. Right: Comparison of SNR calculated from averaged response to 100 mV steps. The mean SNR values are marked on top of each boxplot. In the boxplots, the boundaries of the whiskers are based on an interquartile range of 1.5; each grey dot in the boxplot represents a 100 mV step measurement. Significance is calculated using Tukey's post hoc test.

HIGH-SENSITIVITY VOLTAGE INDICATOR

The Asp115 mutants D115R and D115N exhibit the highest voltage sensitivities of any reported GEVIs, rhodopsin-based or otherwise. The D115N mutant has a $\Delta F / F_0$ of 367% across 100 mV, and the D115R mutant has a $\Delta F / F_0$ of 158.6%. Both have slow kinetics (fast time constant: 39.11 ± 1.12 and 69.32 ± 4.35, mean ± SEM) and some photocurrent (41.19 ± 7.41 and 16.34 ± 4.35 pA, mean ± SEM. See section 5.3.4). In the SNR comparison, the SNR of D115R is exceptionally higher than QuasAr6a, reaching almost three times of QuasAr6a (Figure 5.12). The high sensitivity and low baseline fluorescence characteristics mean that in *in vivo* applications, neurons at resting potential in the background will produce much less fluorescence. This might be critical in applications where

the excitation is not strictly confined and background fluorescence contributes greatly to the noise, such as in standard 1P wide-field fluorescence imaging.

5.4.3. TOWARDS A SILENCER

Proton transfer from the cytoplasmic to the extracellular side will repolarize the cells. Outwards proton pumps such as Arch have been applied and developed further to serve as a silencer[29, 30]. As compared in Figure 5.13, under the same red illumination, E166D shows a nearly 2.8 times photocurrent than that of eArch3.0.

It can potentially be used as a red-shifted silencer with better performance than the Arch-based ones. If the photocurrent under blue is negligible, the combination of E166D and another blue laser excited indicator, like ASAP, can form an all-optical electrophysiology pair. With the spatial patterning tool and linear/nonlinear excitation laser, the inhibition on neurons can be delivered deep in tissue.

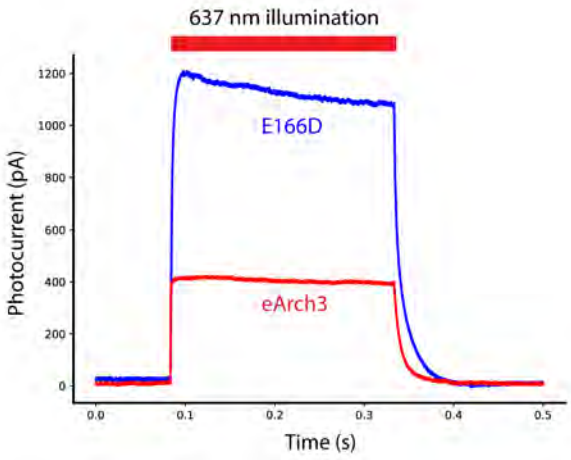

Figure 5.13: Photocurrent comparison between the E166D mutant and eArch3.0. Under the same 637 nm laser illumination (power: 300 mW mm^{-2}; Coherent OBIS laser), E166D shows an average photocurrent of 1125 pA (3 cells), higher than 400 pA of eArch3 (4 cells).

5.4.4. TWO-PHOTON USAGE

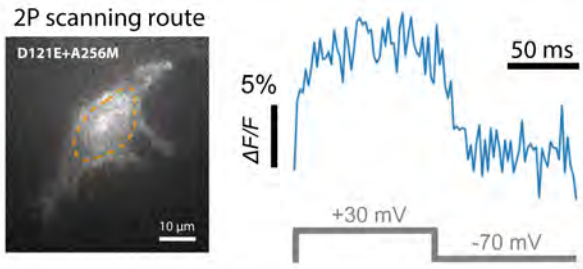

Figure 5.14: The D121E/A256M mutant shows sensitivity under 2P excitation. Left: the image of the cell under the patch clamp and the 2P contour scanning route. Right: the averaged response to the 100 mV steps.

The D121E/A256M mutant shows a ΔF / F_0 of around 8% to 100 mV under the 1200 nm excitation. It shows that GR has the potential to become a bright GEVI for 2P usage under further engineering. A possible way would be using the directed evolution approach introduced in Chapter 6.

5.5. OUTLOOK

In the work described above, we established a good understanding of identifying key functional residues and how they would likely shape the performance of the GR mutants. However, it is still difficult to pinpoint the exact amino acid substitution which will result in a desired property. A broad sampling of the amino acid substitutions through site-saturation mutagenesis is one way to ensure the coverage of all possible substituents[23, 31]. To further exploit the potential of GR, it is crucial to increase the throughput of the methodology for mutant characterization. The patch clamp technique provides accurate control and readout; however, it is quite time-consuming and laborious.

The potential strategy to greatly improve efficiency in sampling various mutants is to use the video-based screening method. Using the HEK293 cells expressing the inward-rectifying channel Kir2.1, it is possible to introduce reproducible spikes under electric field stimulation (EFS) pulses[31, 32]. Through our 1P screening system, we can record high-frame-rate videos of the fluorescence response. Key parameters like brightness, voltage sensitivity, and kinetics can be extracted from the videos.

One potential issue would be that the GR mutants with substantial photocurrent would disturb the field-evoked spiking, probably in an inhibitory way. In terms of screening for

voltage indicators, the photocurrent mutants will have decreased measured numbers in voltage sensitivity. Although the desired indicators would not be influenced, we could infer the photocurrent existence in mutants through the previous data set to exclude them from subsequent screening. The combined mutants are less likely to have photocurrent. Through the screening, the outstanding mutants functioning as voltage indicators can be further characterized in detail through patch clamp, including measuring the photocurrent. To evolve/engineer only the photocurrent properties of GR mutants, screening in *E.coli*[32] in combination with pH measurements in libraries[8] can be done in a relatively straightforward way.

5.6. METHOD

5.6.1. GLOEOBACTER RHODOPSIN PLASMID

The GR gene is encoded in a plasmid with a CMV promoter and enhancer to facilitate its production in mammalian cells[33]. The GR gene is linked to the Citrine gene, which encodes for a fluorescent protein Citrine[34], resulting in a fusion protein of the two. The linker between the two proteins is the trafficking sequence (TS) from Kir2.1[35]. At the end of the fusion protein, there are three different sequences attached for optimal production and localization: the first part is the same Kir2.1 TS inserted three times, called TSx3, which increases the membrane localization[35]; the second part is called ER2 which is the endoplasmic reticulum export signal FCYENEV to again increase membrane localization[36]; and the third part is WPRE, which minimizes the mRNA degradation of the fusion protein[37].

5.6.2. PCR SITE-DIRECTED MUTAGENESIS

The PCR consisted of the KOD Xtreme Hot Start DNA Polymerase (Sigma-Aldrich, St. Louis, MO, USA) using a touchdown PCR protocol. After the PCR, the plasmids are extracted from the PCR mixture with agarose gel extraction using InvitrogenTM SYBRTM Safe DNA Gel Stain (Thermo Fisher Scientific Inc., Waltham, MA, USA) and GeneJET Gel Extraction Kit (Thermo Fisher Scientific Inc., Waltham, MA, USA). After purification, the plasmids are still in a linear form. To convert them back into circular DNA, an additional reaction called the Kinase, Ligase, DpnI (KLD) reaction is performed with a KLD Enzyme Mix (New England Biolabs (NEB), Ipswich, MA, USA). Now the DNA is ready to undergo transformation into bacterial cells.

5.6.3. TRANSFORMATION AND CELL TRANSFECTION

In the transformation process, single plasmids are taken up by bacteria, creating a homogeneous plasmid solution within the individual bacteria and later its subsequent colony.

Chemically made competent bacteria (NEB® 5-alpha Competent E. coli) were used for the transformation and plated on LB-Agar plates with 100 μg/mL ampicillin (Sigma), so only transformed bacteria grew into a colony overnight. After overnight growth on the plate, a few colonies were picked and inoculated in LB with 100 μg/mL ampicillin overnight. The plasmids were extracted using a QIAprep Spin Miniprep Kit (Qiagen) and the sequence of the GR gene including mutation was verified by Sanger sequencing (Marcogen).

One day before transfection, 4.5 × 105 cells were seeded on a 35 mm polystyrene dish (Sarstedt, Nümbrecht, Germany). The cells were transfected using 1.5 or 2.5 μg plasmid DNA with 6 or 7.5 μL TransIT-293 transfection reagent (Mirus Bio LLC, Madison, WI, USA) in 400 µL Opti-MEM (Thermo Fisher Scientific Inc., Waltham, MA, USA). Cells transfected this way, are used in measurements two or three days after transfection.

5.6.4. MICROSCOPE AND DATA ANALYSIS

The microscope used in this study is introduced in Chapter 2. The patch clamp technique is explained in section 4.2.6 in Chapter 4. The data analysis method is introduced in the same chapter in section 4.2.8.

REFERENCES

[1] B. V. Zemelman, G. A. Lee, M. Ng, and G. Miesenböck. “Selective photostimulation of genetically chARGed neurons”. In: *Neuron* 33.1 (2002), pp. 15–22.

[2] E. S. Boyden, F. Zhang, E. Bamberg, G. Nagel, and K. Deisseroth. “Millisecond-timescale, genetically targeted optical control of neural activity”. In: *Nature neuroscience* 8.9 (2005), pp. 1263–1268.

[3] J.-A. Sahel, E. Boulanger-Scemama, C. Pagot, A. Arleo, F. Galluppi, J. N. Martel, S. D. Esposti, A. Delaux, J.-B. de Saint Aubert, C. de Montleau, *et al.* “Partial recovery of visual function in a blind patient after optogenetic therapy”. In: *Nature medicine* 27.7 (2021), pp. 1223–1229.

[4] L. Z. Fan, D. K. Kim, J. H. Jennings, H. Tian, P. Y. Wang, C. Ramakrishnan, S. Randles, Y. Sun, E. Thadhani, Y. S. Kim, *et al.* “All-optical physiology resolves a synaptic basis for behavioral timescale plasticity”. In: *Cell* (2023).

[5] R. Rippka, J. Waterbury, and G. Cohen-Bazire. “A cyanobacterium which lacks thylakoids”. In: *Archives of microbiology* 100 (1974), pp. 419–436.

[6] Y. Nakamura, T. Kaneko, S. Sato, M. Mimuro, H. Miyashita, T. Tsuchiya, S. Sasamoto, A. Watanabe, K. Kawashima, Y. Kishida, *et al.* “Complete genome structure of Gloeobacter violaceus PCC 7421, a cyanobacterium that lacks thylakoids”. In: *DNA research* 10.4 (2003), pp. 137–145.

[7] T. Morizumi, W.-L. Ou, N. Van Eps, K. Inoue, H. Kandori, L. S. Brown, and O. P. Ernst. “X-ray crystallographic structure and oligomerization of Gloeobacter rhodopsin”. In: *Scientific reports* 9.1 (2019), pp. 1–14.

[8] A. R. Choi, L. Shi, L. S. Brown, and K.-H. Jung. “Cyanobacterial light-driven proton pump, Gloeobacter rhodopsin: complementarity between rhodopsin-based energy production and photosynthesis”. In: *PloS one* 9.10 (2014), e110643.

[9] S. Ganapathy, O. Bécheau, H. Venselaar, S. Frölich, J. B. van der Steen, Q. Chen, S. Radwan, J. Lugtenburg, K. J. Hellingwerf, H. J. de Groot, *et al.* “Modulation of spectral properties and pump activity of proteorhodopsins by retinal analogues”. In: *Biochemical Journal* 467.2 (2015), pp. 333–343.

[10] Q. Chen, J. Arents, S. Ganapathy, W. J. de Grip, and K. J. Hellingwerf. “Functional expression of gloeobacter rhodopsin in Synechocystis sp. PCC6803”. In: *Photochemistry and Photobiology* 93.3 (2017), pp. 772–781.

[11] K. Chuon, J.-g. Shim, K.-W. Kang, S.-G. Cho, C. Hour, S. Meas, J.-H. Kim, A. Choi, and K.-H. Jung. “Carotenoid binding in Gloeobacteria rhodopsin provides insights into divergent evolution of xanthorhodopsin types”. In: *Communications Biology* 5.1 (2022), p. 512.

[12] M. R. Miranda, A. R. Choi, L. Shi, A. G. Bezerra Jr, K.-H. Jung, and L. S. Brown. “The photocycle and proton translocation pathway in a cyanobacterial ion-pumping rhodopsin”. In: *Biophysical journal* 96.4 (2009), pp. 1471–1481.

[13] K. Kojima, R. Kurihara, M. Sakamoto, T. Takanashi, H. Kuramochi, X. M. Zhang, H. Bito, T. Tahara, and Y. Sudo. “Comparative studies of the fluorescence properties of microbial rhodopsins: spontaneous emission versus photointermediate fluorescence”. In: *The Journal of Physical Chemistry B* 124.34 (2020), pp. 7361–7367.

[14] J. M. Kralj, A. D. Douglass, D. R. Hochbaum, D. Maclaurin, and A. E. Cohen. “Optical recording of action potentials in mammalian neurons using a microbial rhodopsin”. In: *Nature methods* 9.1 (2012), pp. 90–95.

[15] H. Tian, H. C. Davis, J. D. Wong-Campos, P. Park, L. Z. Fan, B. Gmeiner, S. Begum, C. A. Werley, G. B. Borja, H. Upadhyay, *et al.* “Video-based pooled screening yields improved far-red genetically encoded voltage indicators”. In: *Nature Methods* (2023), pp. 1–13.

[16] A. Silapetere, S. Hwang, Y. Hontani, R. G. Fernandez Lahore, J. Balke, F. V. Escobar, M. Tros, P. E. Konold, R. Matis, R. Croce, *et al.* “QuasAr Odyssey: the origin of fluorescence and its voltage sensitivity in microbial rhodopsins”. In: *Nature communications* 13.1 (2022), p. 5501.

[17] M. Clemens, P. Phatak, Q. Cui, A.-N. Bondar, and M. Elstner. “Role of Arg82 in the early steps of the bacteriorhodopsin proton-pumping cycle”. In: *The Journal of Physical Chemistry B* 115.21 (2011), pp. 7129–7135.

[18] L. S. Brown and K.-H. Jung. “Bacteriorhodopsin-like proteins of eubacteria and fungi: the extent of conservation of the haloarchaeal proton-pumping mechanism”. In: *Photochemical & Photobiological Sciences* 5.6 (2006), pp. 538–546.

[19] T. Tsukamoto, T. Kikukawa, T. Kurata, K.-H. Jung, N. Kamo, and M. Demura. “Salt bridge in the conserved His–Asp cluster in Gloeobacter rhodopsin contributes to trimer formation”. In: *FEBS letters* 587.4 (2013), pp. 322–327.

[20] T. Tanimoto, Y. Furutani, and H. Kandori. “Structural changes of water in the Schiff base region of bacteriorhodopsin: proposal of a hydration switch model”. In: *Biochemistry* 42.8 (2003), pp. 2300–2306.

[21] J. M. Kralj, D. R. Hochbaum, A. D. Douglass, and A. E. Cohen. “Electrical spiking in Escherichia coli probed with a fluorescent voltage-indicating protein”. In: *Science* 333.6040 (2011), pp. 345–348.

[22] A. Vogt, J. Wietek, and P. Hegemann. “Gloeobacter rhodopsin, limitation of proton pumping at high electrochemical load”. In: *Biophysical journal* 105.9 (2013), pp. 2055–2063.

[23] M. K. Engqvist, R. S. McIsaac, P. Dollinger, N. C. Flytzanis, M. Abrams, S. Schor, and F. H. Arnold. “Directed evolution of Gloeobacter violaceus rhodopsin spectral properties”. In: *Journal of molecular biology* 427.1 (2015), pp. 205–220.

[24] A. K. Dioumaev, L. S. Brown, J. Shih, E. N. Spudich, J. L. Spudich, and J. K. Lanyi. “Proton transfers in the photochemical reaction cycle of proteorhodopsin”. In: *Biochemistry* 41.17 (2002), pp. 5348–5358.

[25] L. Song, M. El-Sayed, and J. Lanyi. “Protein catalysis of the retinal subpicosecond photoisomerization in the primary process of bacteriorhodopsin photosynthesis”. In: *Science* 261.5123 (1993), pp. 891–894.

[26] S. Logunov, M. El-Sayed, and J. Lanyi. “Catalysis of the retinal subpicosecond photoisomerization process in acid purple bacteriorhodopsin and some bacteriorhodopsin mutants by chloride ions”. In: *Biophysical journal* 71.3 (1996), pp. 1545–1553.

[27] K. Hashimoto, A. R. Choi, Y. Furutani, K.-H. Jung, and H. Kandori. “Low-temperature FTIR study of Gloeobacter rhodopsin: presence of strongly hydrogen-bonded water and long-range structural protein perturbation upon retinal photoisomerization”. In: *Biochemistry* 49.15 (2010), pp. 3343–3350.

[28] A. S. Abdelfattah, R. Valenti, J. Zheng, A. Wong, K. Podgorski, M. Koyama, D. S. Kim, and E. R. Schreiter. “A general approach to engineer positive-going eFRET voltage indicators”. In: *Nature Communications* 11.1 (2020), p. 3444.

[29] B. Y. Chow, X. Han, A. S. Dobry, X. Qian, A. S. Chuong, M. Li, M. A. Henninger, G. M. Belfort, Y. Lin, P. E. Monahan, *et al.* “High-performance genetically targetable optical neural silencing by light-driven proton pumps”. In: *Nature* 463.7277 (2010), pp. 98–102.

[30] A. Krol, V. G. Lopez-Huerta, T. E. Corey, K. Deisseroth, J. T. Ting, and G. Feng. “Two eARCHT3. 0 lines for optogenetic silencing of dopaminergic and serotonergic neurons”. In: *Frontiers in Neural Circuits* 13 (2019), p. 4.

[31] V. Villette, M. Chavarha, I. K. Dimov, J. Bradley, L. Pradhan, B. Mathieu, S. W. Evans, S. Chamberland, D. Shi, R. Yang, *et al.* “Ultrafast two-photon imaging of a high-gain voltage indicator in awake behaving mice”. In: *Cell* 179.7 (2019), pp. 1590–1608.

[32] H. Tsutsui, Y. Jinno, A. Tomita, and Y. Okamura. “Rapid evaluation of a protein-based voltage probe using a field-induced membrane potential change”. In: *Biochimica et Biophysica Acta (BBA)-Biomembranes* 1838.7 (2014), pp. 1730–1737.

[33] M. F. Stinski and H. Isomura. “Role of the cytomegalovirus major immediate early enhancer in acute infection and reactivation from latency”. In: *Medical microbiology and immunology* 197 (2008), pp. 223–231.

[34] O. Griesbeck, G. S. Baird, R. E. Campbell, D. A. Zacharias, and R. Y. Tsien. “Reducing the environmental sensitivity of yellow fluorescent protein: mechanism and applications”. In: *Journal of biological chemistry* 276.31 (2001), pp. 29188–29194.

[35] V. Gradinaru, F. Zhang, C. Ramakrishnan, J. Mattis, R. Prakash, I. Diester, I. Goshen, K. R. Thompson, and K. Deisseroth. “Molecular and cellular approaches for diversifying and extending optogenetics”. In: *Cell* 141.1 (2010), pp. 154–165.

[36] C. Stockklausner, J. Ludwig, J. Ruppersberg, and N. Klöcker. “A sequence motif responsible for ER export and surface expression of Kir2. 0 inward rectifier K+ channels”. In: *FEBS letters* 493.2-3 (2001), pp. 129–133.

[37] J. E. Donello, J. E. Loeb, and T. J. Hope. “Woodchuck hepatitis virus contains a tripartite posttranscriptional regulatory element”. In: *Journal of virology* 72.6 (1998), pp. 5085–5092.

6

Directed Evolution of the Two-photon Brightness of QuasAr1

A major challenge in optogenetics is the limitation of observation depth due to light scattering in tissue. Two-photon (2P) imaging allows four times deeper observation depth compared to conventional wide-field microscopy and has been widely used in vivo. Voltage imaging using rhodopsin-based voltage indicators has not yet had a successful transition to the 2P regime. Despite the excellent one-photon performance demonstrated in vivo, rhodopsin-based indicators typically suffer from rather poor performance under 2P excitation, as none of them were developed specifically for 2P usage. We aim to improve the 2P brightness of an Archaerhodopsin-based indicator, QuasAr1. With this goal in mind, we developed a protein evolution pipeline, with features such as automation, large-scale screening, and segmentation by machine learning. Two rounds of evolution were carried out, each resulting in a mutant with improved 2P brightness.

6.1. INTRODUCTION

6.1.1. THE ERA OF OPTOGENETICS

To unveil the working mechanisms of the brain, it is vital to decipher neural communication, which is encoded in the modulation of neural membrane potentials. Improving the detection of neural activity has been a constant and central theme in neuroscience.

Electrode-based electrophysiological approaches have been the gold standard since their introduction [1]and have been broadly applied in neuroscience studies for decades. Techniques such as patch clamp can record and manipulate the membrane potential and current of a single neuron with high SNR and temporal resolution in behaving animals[2]. Despite being successfully implemented[3–5], it is very challenging to parallelize the patch clamp approach, which highly limits the application range[6]. Recent developments on extracellular probes have made it possible to record from at most 384 channels per shank, with an excellent temporal resolution, across several brain regions[7–9]. These type of methods such as Neuropixels, however, lacks cell specificity in terms of spatial information and cell types.

The drive to track and control genetically defined neuronal populations with minimal invasion has led to the development and application of optogenetics, which utilizes genetically modified proteins to serve as indicators and actuators or silencers under laser stimulation. Early demonstrations using algal protein to noninvasively control a defined population of neurons with high temporal precision were revolutionary to the neuroscience field[10]. Besides manipulation, there has been a great development in the ability of optogenetics tools to report neuronal activity with various reporting strategies proposed, including monitoring genetically defined populations of neurons by detecting dynamics of calcium[11], vesicular release of neurotransmitter [12], or membrane potential[13].

6.1.2. FROM CALCIUM IMAGING TO VOLTAGE IMAGING

As the most widely used optogenetics investigation tool, calcium imaging uses genetically encoded calcium indicators (GECI) to transduce cellular activities such as action potentials (APs) into fluorescence changes of the protein by sensing calcium influx[11, 14, 15]. It takes advantage of the indispensable role of calcium ions in mediating signaling in nearly every aspect of cellular life, especially in neuron firing[16, 17]. The definitive catalog of GECIs, the GCaMP sensor family, has evolved through decades of iterations[18–21]. For example, the GCaMP6f indicator can detect single APs as well as synaptic responses[19]. In contrast, the following optimization, the jGCaMP7 indicator, provides better single AP detectability, for about 2 to 3 times larger single AP ΔF / F_0 using structure-guided mutagenesis and screening on neurons[20]. The newest generation jGCaMP8 sensor improves kinetics with comparable or even better sensitivity than the

jGCaMP7 sensor (jGCaMP8f fast version has four times faster rise time, 2.5 times faster decay time than jGCaMP7f, which is 24.8 ±6.1 ms to the peak and 67.4 ±11.2 ms half-decay time)[21]. Various studies have applied GECIs to investigate neuron circuits and brain functions in different animal models[22–25].

However, calcium concentration is not a direct translation of membrane potential; thus GECIs can not report sub-threshold depolarizations and hyperpolarizations. The kinetics of calcium imaging is also limited to the range of 10 ms to 100 ms due to the slow calcium ion diffusion and the GECIs sensing mechanism, which makes it challenging to distinguish single spikes in an AP train[15, 26–28]. To follow actual neuron dynamics, it is desired to have an indicator that reports directly the trans-membrane voltage instead of the signaling messengers of cell events. Genetically encoded voltage indicators (GEVIs) were developed as direct transducers from membrane voltage to fluorescence modulations, aiming to report with subcellular spatial resolution, millisecond temporal resolution, and sub-action potential voltage resolution.

GEVIs can be divided into two categories based on their sensing mechanisms: voltage-sensing domain (VSD) based and fluorescent microbial rhodopsins. The first category has a general structure of a fluorescent protein linked to a VSD. With this design, a membrane potential change will lead to a conformational change, which leads to a change in fluorescence brightness of the fluorescent protein via FRET, quenching, or changes in the FP structure[29, 30]. Of the many indicators proposed[31–38], the ASAP family shows the most promising performance[39–42]. The ASAP-type sensors are designed by inserting a circularly permuted GFP (cpGFP) variant into the fourth transmembrane helix VSD of G. gallus voltage-sensing phosphatase. The fluorescence emission of the cpGFP will change when it is perturbed by the membrane potential induced movement of a positively charged VSD transmembrane helix. The newest iteration, JEDI-2P, claims a ΔF / F_0 of around -50%, a kinetics of 0.54 ±0.06 ms fast time constant with a slow time constant of 7.78 ±1.46 ms at 32° to 35° in response to 100 mV voltage steps, and a photobleaching half-life of around 50 s under 55 mW, 920 nm 2P excitation, and its responses under 1P excitation were similar to those under 2P excitation[42]. However, the negative fluorescence response to depolarization means that the resting neurons would produce substantial background noise that contaminates the signals. The blue-shifted excitation wavelength would also be unfavorable to deep tissue imaging, which we will discuss later.

The second GEVI family uses fluorescent microbial rhodopsins, which were originally proton pumps[30]. The first attempt at using these to create a GEVI was based on the hypothesis that the membrane potential would reposition the proton inside the proton transport channel in the rhodopsin and thereby induce a fluorescence spectral shift. This was tested in bacteria using green-absorbing proteorhodopsin (GPR)[43]. Attempts to express and membrane localize these sensors in mammalian cell membranes failed, leading to the search for other microbial rhodopsins that would target the eukaryotic plasma membrane better. Archaerhodopsin 3 (Arch3) from Halorubrum sodomense expressed well in the mouse cortex and showed great performance in silencing neurons[44], making it a good GEVI candidate. Arch shows sub-millisecond response ki-

netics and 35% $\Delta F / F_0$ per 100 mW sensitivity, and the D95N mutant exhibits no photocurrent but a slowed time constant of 41 ms[45]. Arch has gone through several iterations to make it ideal as a voltage indicator; mutations often targeted at improving brightness[46, 47]. Through directed evolution, two archaerhodopsin-based voltage indicators, QuasAr1 and QuasAr2, were found to improve both brightness and voltage sensitivity while retaining millisecond response time and no photocurrent[48]. Coexpressing QuasAr with engineered channelrhodopsin actuator CheRiff, the vector named Optopatch could perform cross-talk–free all-optical electrophysiology *in vivo*. The more sensitive yet dimmer of the two, QuasAr2 (reported as 90% $\Delta F / F_0$ but subsequently typically showing 40% $\Delta F / F_0$ in standard conditions), went through a robotic multidimensional screening evolution and led to a brightness and voltage sensitivity improved sensor, Archon[49]. The soma localized version of Archon was applied to *in vivo* voltage imaging in mice[50] and zebrafish larvae[51]. The most recent iteration, QuasAr6a, and QuasAr6b were evolved through a video-based pooled screening[52]. Compared to Archon, QuasAr6a shows 1.7-fold brightness, while QuasAr6b shows 2-fold brightness and has faster kinetics (1.8 ± 0.5 ms). Furthermore, both can report single spikes and subthreshold events. Recently, an all-optical investigation on hippocampal plasticity was carried out using a construct pair of somQuasAr6a and channelrhodopsin sombC1C2TG[53]. Besides functioning as a single unit, Arch also serves as a VSD in FRET designs. Such sensors include CAESR and mNeon-Ace, which realized single AP detection in drosophila and mice under 1P excitation[29, 54–56]. Another promising iteration is chemgenetic sensors like Voltron, where Ace is fused with a HaolTag that captures e.g. JaneliaFluor(JF) dyes[57, 58]. This combination has led to bright and photostable recordings of electrical dynamics[59], but the addition of the exogenous chromophore still limits its potential use in *in vivo* recordings.

6.1.3. FROM ONE-PHOTON TO TWO-PHOTON EXCITATION

One big challenge in optogenetics is the very shallow recording depth, which is limited to superficial cortical layers under excitation of visible wavelength[60, 61]. Two-photon excitation allows the fluorophore to absorb two photons simultaneously instead of one photon of equivalent energy. This allows the excitation under near-infrared wavelength and brings the advantages of deeper penetration depth, highly confined excitation spot, and less out-of-focus (auto)fluorescence. Despite huge developments in the last decade, there is no red-shifted GEVI optimized for deep tissue two-photon (2P) imaging, a tool greatly desired by the neuroscience community for *in vivo* applications. The ASAP family shows decent *in vivo* two-photon microscopy (2PM) performance[42]. However, the excitation wavelength at 920 nm still means tissue absorption, scattering, and shorter penetration depth[62]. Multiphoton imaging has moved towards longer wavelengths (1200 to 1300 nm for 2P imaging, 1800 to 2000 nm for 3P imaging)[63]; this, combined with the relatively slow response time[64], means that there is significant room for improvement and a need to evolve a GEVI with a fast response to 2P excitation of longer than 1200 nm.

There are, in general, two approaches to evolving proteins: rational protein design and

directed evolution[65, 66]. Rational design is based on the understanding of the functional mechanisms of proteins, and the active site substitutions are verified in a later stage. In the early phase of GEVI engineering, rational design is the main approach. The first engineering effort on Arch3 was to eliminate its photocurrent, which was realized by mutating its counterion that is important for the proton transfer[45]. In the follow-up research, the proton donor site was mutated based on the reasoning that it would alter the RSB protonation kinetics and change the voltage response speed[67]. Since the exact mechanism of the voltage sensitivity and the origin of fluorescence were unknown, directed evolution quickly took over. Directed evolution and rational design differ in the decision-making process of the targeting sites, as it is randomized in directed evolution[66]. This technique has been applied to the engineering of many protein families, including enzymes, fluorescent proteins, and optogenetics tools[66, 68, 69]. Arch3 (D95N) served as the first template for directed evolution, which led to the discovery of QuasAr1 and QuasAr2[48]. Since then, generations of Arch-based GEVIs have been developed through directed evolution, including Arch5, Arch7, NovArch, Archon, and QuasAr6[47, 49, 52, 70].

A recent study has unveiled the key residues and hydrogen bonds responsible for the voltage sensing in Arch3 and Archon; however, how these residues modulate the fluorescence is still unknown[71]. As for the fluorescence origin, it is unsure which state of the Arch protein produces most of the fluorescence, with speculation of an all-*trans* O-like ground state[30]. However, none of these studies covers 2P excitation conditions, which can reach different energy levels and function very differently.

6.1.4. THE MOTIVATION AND CONTENT OF THIS CHAPTER

Current red-shifted GEVIs are evolved under one-photon microscopy (1PM), but their performance under 1PM and 2PM is typically uncorrelated, with 2PM response being poor[42, 64], both in terms of fluorescence brightness and voltage sensitivity. Regarding brightness, the absorption spectra of proteins can be very different between 1P and 2P excitation because their absorptions are governed by different quantum-mechanical rules (for example, 2P absorption spectrum has extra dependence on the change between permanent dipole moments of the states than 1P situation, and owing to the resonant enhancement, 2P absorption can be very strong in a short wavelength window from S_0 to S_n)[72]. Regarding voltage sensitivity, GEVIs like QuasAr1 and QuasAr2 have only a fraction of their sensitivity left under the 2P excitation[64]. The origin of the voltage sensitivity of rhodopsins-based GEVIs is most likely that the membrane potential can modulate the equilibrium between protonated and deprotonated retinal Schiff base in the rhodopsin[71]. It is possible that under 2P excitation, the chromophore is excited to a high-energy, 1P inaccessible, state S_n in which higher-order vibrational and rotational dynamics influence the isomerization dynamics (compared to the normal all-trans to 13-*cis* dynamics) and relaxation pathways. The retinal binding pocket can thus have different hydrogen bonding networks than in normal 1P photocycles. The RSB deprotonation/reprotonation ability, as a result, could be impaired, and this leads to deteriorated

voltage sensitivity. It would therefore be necessary to engineer GEVIs directly under 2P excitation to make them a satisfactory 2P response.

To develop a GEVI optimized for 2PM with improved brightness, we chose the directed evolution method to explore the parameter space. So far, direct evolution on GEVIs has been carried out in two ways regarding library generation: one is based on site-directed saturation mutagenesis with mechanism insight[41, 42]; the other one is based on completely randomized error-prone PCR[49, 52]. Since we know little about the exact mechanism and spots influencing the 2P brightness, the randomized approach was chosen to generate the sample pool.

We developed an automated microscope screening platform and software to evaluate the performance of each mutant. The microscope system provides 2P imaging under the excitation of tunable wavelength with high SNR. The screening pipeline can be set up flexibly using the graphic user interface. An autofocus algorithm was developed to ensure a sharp focus across the whole cover slip. For data analysis, a machine learning network was trained to categorize accurately and segment cells with complex connections and morphology. At the end of the screening, a multi-parameter metric was applied to rank the cell performance. The top outliers were then picked up individually through micro-pipettes, after which the mutation sites were identified through single-cell sequencing. As validation, both the parent constructs and the evolved mutant were cloned and screened to compare the brightness.

We successfully carried out two rounds of directed evolution on the 2P brightness of QuasAr1. This led to the discovery of QuasAr1 H106R/G241S mutant that exhibits a 133% increased per-molecular brightness under 1200 nm pulsed excitation compared to the parent template. It is voltage sensitive under 2P excitation.

6.2. METHODS

6.2.1. RANDOM MUTAGENESIS AND LIBRARY GENERATION

The library generation is carried out by the collaborators in this project. Random mutagenesis was performed using the Random Mutagenesis Kit GeneMorph II (Agilent, Santa Clara, CA, USA). We aimed for a mutation rate of 5-10 mutations/kb. Towards this frequency of mutations, 800 ng of plasmid DNA featuring QuasAr1 was used, equivalent to roughly 80 ng of QuasAr1 amplicon DNA. Additionally, 0.3 µM of primers QuasAr1_fwd and QuasAr1_rev were added (All the primers are listed in Table 6.2). 32 PCR cycles were performed with an annealing temperature of 61°C and other parameters adapted from the manufacturer's protocol.

The backbone of the starting variant of our evolution plasmid was amplified using KOD Xtreme Hot Start DNA Polymerase (Sigma-Aldrich, St. Louis, MO, USA). 2 µg of plasmid DNA, 0.3 µM of primers pLenti_CMV_TSX3_Cit_fwd and pLenti_CMV_

TSX3_Cit_rev and 1 mM of dNTP mix were used for amplification in a 50 µL reaction with 1 unit of polymerase. A touchdown PCR protocol was used with denaturation and extension temperatures of 98°C and 68°C respectively, and annealing temperatures of 66°C in round one, decreasing by 0.5°C every round until round 30, which is the final round. After amplification, 5.7 µL of 10×rCutSmart™Buffer (New England Biolabs, Ipswich, MA, USA) and 1 µL DpnI (NEB) was added, followed by incubation for one hour at 37°*C* to digest the original plasmid DNA to prevent contamination of the library with wild-type plasmid.

Both the backbone of our evolution plasmid and the insert with mutagenized QuasAr1 were purified by agarose gel extraction using Invitrogen™SYBR™Safe DNA Gel Stain (Thermo Fisher Scientific Inc., Waltham, MA, USA) for easy DNA visualization in ambient light and GeneJET Gel Extraction Kit (Thermo) for gel extraction. Backbone and randomly mutagenized QuasAr1 were then assembled with Gibson assembly using the Gibson Assembly Master Mix according to the manufacturer's protocol (NEB), with 100 ng of backbone and a 5 to 1 molar ratio of insert versus backbone.

Gibson assembly product was divided into 8 parts and transformed using 50 µL vials of NEB 5_alpha Competent E. coli using the high-efficiency protocol provided by the manufacturer (NEB), although instead of plating all of the transformed bacteria, 1/200th of the outgrowth culture was plated on LB-Agar plates with 100 ng mL^{-1} ampicillin (Sigma), and the remainder was used to start a 5.7 mL overnight culture. Plasmid libraries were extracted from overnight cultures using two separate QIAprep Spin Miniprep Kit columns (Qiagen, Venlo, Netherlands), after which yield was pooled. Colonies formed by the 1/200th part of the outgrowth culture were counted to estimate library size. Gibson assembly and transformation were repeated until the estimated library size was at least 1×104 clones, which took a total of 50 µL Gibson assembly yield and 32×50 µL of competent cells. When pooling multiple libraries in order to create one library with optimal diversity, the ratio of DNA concentration as measured by nanodrop to estimated library size as determined by colony counting was equal for every library. In order to verify successful random mutagenesis, 6 colonies from the LB-agar plate on which 1/200th of the outgrowth culture was spread were picked and sequenced using Sanger sequencing (Macrogen, Seoul, South Korea).

6.2.2. MICROSCOPE

The microscope used in the screening is a versatile, multimodal imaging system designed for all-optical electrophysiology[73]. Named Octoscope, it combines 1PM, 2PM, and an electrophysiological module into one microscope platform, as introduced in Chapter 2.

For the 2P imaging, the multiphoton imaging module was employed. A wavelength-tunable multiphoton laser (Insight X3, Spectra-Physics) served as the laser source. Neutral Density (ND) filters were placed after the laser source to regulate the intensity. A pair of galvo scanners (6215HR, Cambridge Technology) steered the beam for raster scan-

ning. After being magnified by a scan lens and a tube lens, the laser beam passed through a long-pass dichroic mirror (Di03-R785-t3-32×44, Semrock) and entered the objective (Olympus XLPLN25XWMP2, NA: 1.05, working distance: 2 mm). The laser was focused onto the sample carried by a motorized sample stage (BioPrecision2, Ludl). The sample stage could visit pre-programmed locations in micrometer precision, which allowed the screening of a series of FOVs. On the emission side, a slider with different bandpass filters could choose the emission filter depending on the excitation wavelength. Working in pairs, the system can image both Citrine and Arch protein. For 2P image acquisition, a PMT (H10721-20, peak sensitivity wavelength at 630 nm; Hamamatsu) was mounted to collect all the emission light in a light shielding box. A sCMOS camera (ORCA Flash4.0 V3, Hamamatsu; 2048 × 2048 pixels, 6.5 μm pixel size) was placed at the emission side as well to realize white light and wide field 1P imaging for the cell picking purpose. The switch between the PMT and the camera was made by moving a mirror mounted on a motorized translation stage (DDSM50/M, Thorlabs) to redirect the beam. The output current from the PMT is amplified by a trans-impedance amplifier (DHPCA-100, FEMTO) and lowpass filtered by a programmable electronic filter (USBPGF-S1, Alligator technologies) at half of the sampling rate (125 kHz) to reduce noise.

6.2.3. SOFTWARE

THE SCREENING SOFTWARE

A screening software is developed to facilitate the screening pipeline configuration and execution. It is designed to make the screening process flexible, versatile, and fully automated. The screening execution pipeline can be configured through the three configuration levels, from the waveforms configuration and the screening round settings to the screening grid configurations. The software is written in Python, and the user interface is constructed using Pyqt5. It makes use of the modular control backend introduced in Chapter 3 to communicate with the hardware involved.

A dedicated data analysis software is developed in Python as well. It utilizes a machine learning network trained on our own data for segmentation (implementation introduced in section 6.2.3), and retrieve all the cell metrics based on it for evaluation. Both software are introduced in detail in Chapter 3, section 3.4.1.

MACHINE LEARNING IMPLEMENTATION

The data analysis is done through custom software developed in Python with a user interface. A machine learning network (Github repository: `https://github.com/matterport/Mask_RCNN`) based on Region-based Convolutional Neural Network (R-CNN) was adapted for cell segmentation[74].

We started training our Mask R-CNN network based on an existing weight distribution

which was created by training on the Microsoft Common Objects in Context (COCO) database[75]. The COCO database contains 330 thousand images, of which more than 200 thousand images are annotated, containing a total of 1.5 million annotated objects. Transfer learning based on these weights would significantly save the annotated data set needed, as it already provides the network the ability to detect general objects.

A database with input images and corresponding annotated ground truth was created for the training. The input images were 2P images of HEK293T cells expressing QuasAr1-Citrine. The ground truth for each image includes a binary mask to tell if certain pixels belong to a cell or not, a label for each cell, and the coordinates of every bounding box containing the cell. The database was divided into two groups, one for training and the other one for validation.

In general, the images chosen for the database contain cells of different morphologies and statuses to cover all the cell conditions we would meet in an actual screening. The raw images from the microscope needed some processing before feeding to the database. First, the images were cast from an uint16 to a float32 data type to be compatible with the data type of the kernel feature map, for the same purpose, image scaling and padding were also performed.

The ground truth, which is the output to be used from the network, includes categorical information, which is a category indicating the health condition of the cell, and the binary mask, which tells which pixels in the image belong to the individual cell. In the first part of the annotation, we assigned three different classes to the cells: flat cells, round cells, and dead cells. The flat cells are the typically expressing cells attached to the petri dish bottom. They are the group of cells from which the information is drawn after the screening. The round cells are overexpressing the sensor, which leads to biological artifacts. These cells are unhealthy, quite often digest part of the expressed protein leading to different ratios between the Quasar and Citrine expressed in the cells, and partially detach from the petri dish bottom. The dead cell category includes floating cells, foreign substances in the dish, and saturated pixels in the image. The round cells and the dead cell groups are omitted from the screening results.

In the second part of the annotation, we drew a polygon precisely on the boundary of each cell. To create the annotation in the database, we used the Labelme software(K. Wada, labelme: Image Polygonal Annotation with Python, https://github.com/wkentaro/labelme). For each objective in the image, we placed a polygon following the contour of the cell and assigned it to one of the three classes. This will generate a binary mask with bounding box coordinates for each cell.

In total, 96 images were annotated. We used 72 images, containing 1187 annotated cells, for training. For validation, 24 images, containing 273 annotated cells, were used. We rotated all images (0, 90, 180, and 270 degrees) for database argumentation.

After preparing the database, network training took place. The whole training process can be separated into three stages, as shown in Figure 6.1. In stage one, a residual neural

network, Resnet101, creates the feature maps from the training database[76]. Resnet addresses the difficulty in training deep networks[76] and is successfully applied in a wide range of models[76]. In stage two, a region of interest proposal network is trained to create anchors for regions that contain cells and refine these anchors. In stage three, three networks are getting trained: the bounding box regressor network, the classifier network, and the mask prediction network. As it is possible to train each stage individually or in any desired combination, it gives a lot of room to speed up the training process as well as fine-tune the model accuracy.

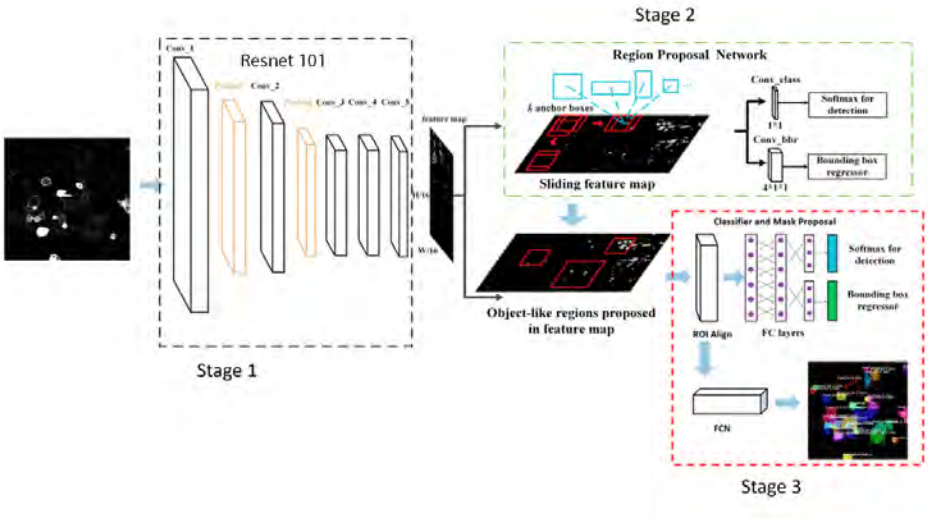

Figure 6.1: Illustration of the three stages in the MaskRCNN algorithm. Stage one uses a convolutional neural network, Resnet101, to extract feature maps. Stage two contains a region proposal network that creates and refines anchor boxes for cells. Stage three mainly refines the bounding boxes, and a classifier and mask prediction network together to produce the final classified binary mask to each cell. Image adapted from Deng, Zhipeng, et al[77].

After the training, we looked at all the logged learned weights and biases from each epoch. We chose the weight files with the lowest validation loss value as our final weight file for the best performance. The performance is introduced in detail in section 6.3.3.

6.2.4. SCREENING PIPELINE EXECUTION

The DMEM in the imaging dish with mutant cells was replaced with extracellular buffer (125 mM NaCl, 2.5 mM KCl, 15 mM HEPES, 1 mM $CaCl_2$, 1 mM $MgCl_2$, and 30 mM Glucose; pH 7.3; osmolarity adjusted to 310 mOsm), and then brought to the microscope after the laser emission was stable. The imaging dish was tightly clamped down onto

the sample stage to prevent relative movement. The field of view of the dish was moved towards the very edge to ensure the sampling of the whole cover slip. All environmental light sources were turned off or blocked to minimize signal contamination. The Citrine channel of the dish was then imaged under 900 nm to bring the dish to an approximate focus. A pre-configured screening pipeline was loaded onto the screening software. After pressing the "start" button, the screening is executed in a fully automated manner. After imaging is finished, data analysis will automatically progress.

6.2.5. CELL PICKING

As opposed to earlier chemical cell selection methods[70, 78], we chose a mechanical selection method because of a putative lower downstream cell loss rate, and aspirated individual cells of the dish using glass micropipettes[49]. The pipette pulling program that yielded pipettes with the right properties is shown in Figure 6.2(a). The produced pipette tip is shown in Figure 6.2(b), which has an open of about 21.7 μm. Figure 6.2(c) shows a pipette image in an actual screening evolution process. The tip opening is about the size of a cell body. The cell to be picked is under the tip, and its 2P image in the Citrine channel is shown in the dashed box on the top right.

The pipette was mounted on a micromanipulator (PatchStar system, Scientifica), and slight overpressure was applied through a syringe connecting to the pipette through the tubing to prevent other cells or residues from entering the pipette. The pipette tip was slowly moved towards the target cell until it was right above. Then the overpressure was released, and suction pulses were applied through the syringe to lift the cell underneath. As soon as this was done, the micromanipulator was commanded to retract the pipette from the petri dish.

6.2.6. SINGLE CELL LYSIS, PCR, AND SEQUENCING

After cell picking, PCR tubes with cells are centrifuged to move the cell to the bottom of the tube, after which all supernatants except for 1 µL are aspirated. The cell is then lysed with 2 µL of Lysis Buffer supplemented with 0.06 µL of proteinase K for two minutes at room temperature, after which Proteinase K is inactivated by heating to 98°C for one minute. After lysis and inactivation, 7 µL of MilliQ containing primers QuasAr1_Lib_scPCR_fwd and QuasAr1_Lib_scPCR_rev and 10 µL of 2X Platinum Direct PCR Universal Master Mix (Invitrogen) are added for a final primer concentration of 0.2 µM each.

(a)

Loop	Heat	Velocity	Delay	Pressure	Ramp
x4	530	21	1	500	530
x1	485	20	1	500	530

(b)

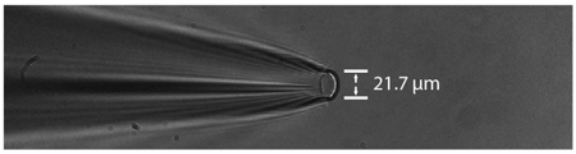

(c)

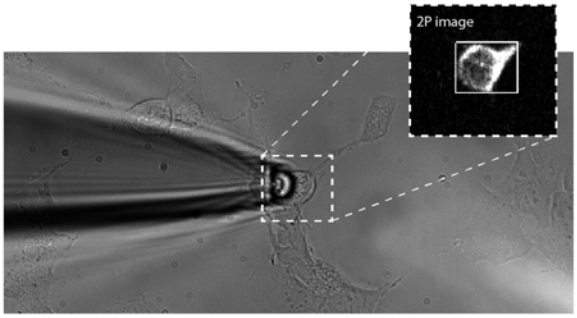

Figure 6.2: Special pipettes were made for the cell picking. (a) The pipette pulling program used for making the pipettes. (b) The white field image of the pipette tip, which has a size of about 21.7 μm. (c) A pipette above a cell during the pickup process in a screening. The 2P image of the picked cell is presented in the top right corner of the image.

After single-cell PCR, the QuasAr1 mutant amplicon is purified by gel extraction and reamplified in another PCR reaction using Q5 polymerase and primers QuasAr1_fwd and QuasAr1_rev. Amplicons are subsequently sequenced by Sanger sequencing (Macrogen) in both directions using HPLC-purified primers QuasAr1_libseq_fwd_HPLC and QuasAr1_libseq_rev_HPLC. Mutations are identified manually after aligning mutant sequences with the QuasAr1(wt) sequence in Benchling.

6.3. RESULTS

The results in the chapter fall into two categories: the engineering results, necessary to perform successful 2P evolution on Quasar1 (section 6.3.1, 6.3.2, 6.3.3, and 6.3.4) and the scientific results (section 6.3.5) showing the successful application of the developed technology.

6.3.1. SCREENING CONFIGURATION

PIPELINE SETUP

The plasmid library that we screened contained mutated QuasAr1s linked to mCitrine. The mCitrine provides an internal calibration. Measured fluorescence brightness of the QuasAr mutant can depend both on the molecular properties of the mutant (increased absorption cross-section or quantum yield) but also on the increased expression of the mutant; measuring the mCitrine fluorescence, which is dependent on the expression level of the fusion protein but not the mutation state of the QuasAr, allows us to distinguish the two effects.

The screening pipeline aims to acquire fluorescence data from all library cells in both the mCitrine and Arch channels. Since the single imaging, FOV is limited to hundreds of micrometers, a proper screening routine is needed to cover the entire petri dish and thus the entire library within a single acquisition. To configure the screening routine flexibly and efficiently, we defined three levels of execution compartments from the top down: grid, round, and waveforms (Figure 6.3).

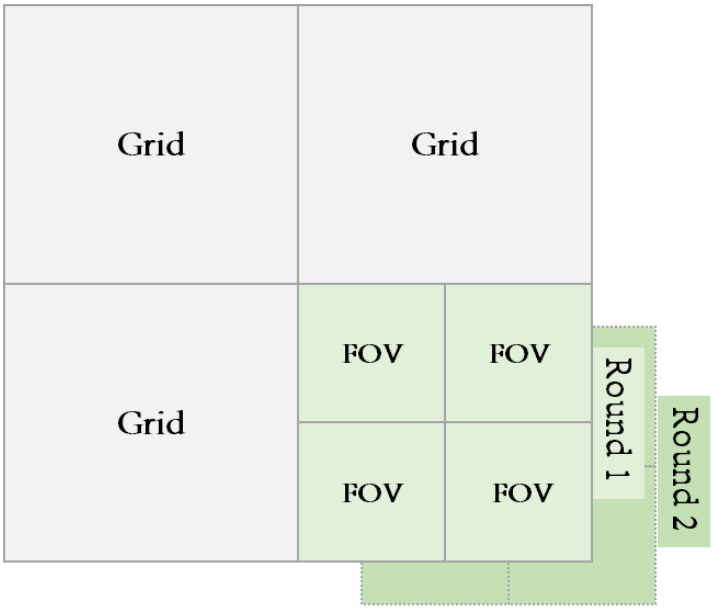

Figure 6.3: Illustration of different screening levels. There are three levels of execution compartments: grid, round, and waveform (at each FOV, waveforms are executed).

The whole screening area is divided into repetitive grids, which contain different rounds of measurements. The cell fluorescence in the Citrine and Arch channels is acquired

separately in these two rounds. The grid size is balanced between two factors: the cell movement and the hardware setup time. With a smaller grid, the time spent covering each round is less, and thus there is less cell movement in between rounds. This would introduce fewer segmentation errors in the analysis. With a larger grid, less switching of imaging configurations between rounds is needed. In a typical screening, we configured 9 grids to cover a 6.12 mm by 6.12 mm area. The time spent between the rounds was around 11 minutes.

Inside each grid, the screening happens in rounds. Measurements of each round cover the whole area inside the grid under the same 2P excitation wavelength, ND filters, and emission filter settings. For each round, there are several parameters that govern the screening process:

• Number of FOVs on each side and the distance between the FOVs: These would decide the screening area of the round. In each grid, we set 36 FOVs and the distance to be the side length of each FOV, which is 340 μm.

• Auto-focus steps and auto-focus methods: The auto-focus step determines how often the auto-focus would happen to correct the focus drifting and how fine the searching steps would be. We set the auto-focus period to be every 2 FOVs. The program allows different focus searching strategies (bi-section and Gaussian fitting, which will be discussed in detail later) and supports both PMT and camera images.

• Z-stack options: Sometimes, it is useful to perform z-max projection to avoid missing optimal focus. It is possible to acquire images at several focus positions in the same FOV in the pipeline. The objective motor would drive the imaging plane to pre-set focuses for each position. We set the z-stack number to 1.

• Laser and filter settings: The excitation laser wavelength can be tuned within a minute at the beginning of each round. The sliders carrying ND filters and emission filters will also move to the predetermined slots, and in this way, we can observe different fluorescent proteins in different rounds. For Citrine fluorescence, we used 900 nm wavelength and ND2 after the laser (14.7mW after objective) at the excitation side and a long-pass filter at the emission side (LP02-514RU-25, SemRock). For Arch fluorescence, we used 1200 nm wavelength and ND 0.5 after the laser (177.5 mW after objective) at the excitation side, and a combination of a long-pass (LP02-664RU-25, Semrock) and a short-pass (FF01-790/SP-25, SemRock) filter at the emission side.

Inside each round, what happens at each FOV is determined through waveforms. The waveforms are signals and triggers from the NI-DAQ system to synchronize all peripheral devices. In a typical 2P evolution experiment, waveforms contain raster scan galvos movement and PMT recording signals under a 250 kHz sampling rate. The waveforms can be adapted for different tasks.

Before the screening, the analysis settings are also configured so that the analysis can start right after the screening and present the cell performance results once finished.

More details about this part will be explained in section 6.3.3.

IMAGING QUALITY CHARACTERIZATION

To minimize the non-biological noise in the screening results, it is important to ensure that the image acquisition is performed with a sufficient signal-to-noise ratio (SNR). Imaging Opsin-based GEVIs under 2P-excitation is always challenging because GEVI fluorescence is two orders of magnitude dimmer than GFP fluorescence under similar excitation conditions. Our setup is designed to offer high-quality 2P imaging, benefitting from a powerful tunable laser source, a sensitive photon detector, a thoroughly shielded light path, and minimal use of optical components for optimized throughput. It is essential to ensure that the SNR from the 2P imaging is sufficient to provide realistic measures of protein brightness.

To characterize the signal level of the 2P imaging, we performed cell membrane contour scanning and analyzed the SNR of the signals. Because of the fast bleaching from 2P raster scanning, only a limited number of images (2~3) can be generated from the same FOV, which hinders the SNR characterization directly from raster scanning. HEK293T cells expressing QuasAr1 wild-type, which is the initial library template, were used as the sample. We set the wavelength of the pulsed laser to 1200 nm, and an ND 1 filter was placed to attenuate the power (93.7 mW after the objective). The target cell was first imaged through raster scanning, and then the contour scanning route was manually drawn onto the cell membrane. The laser focus spot ran over the contour at 500 circles per second in the acquisition. The galvo scanning and PMT signal recording sampling rate was 50 kHz. The PMT signal was low-pass filtered at 25 kHz.

To measure the SNR from the recordings, we first averaged the signal over each contour, which contains 100 samples. This resulted in a 500 Hz recording trace, as shown in Figure 6.4. Then the photobleaching was corrected by fitting the trace to a bi-exponential function. The SNR was calculated as the mean divided by the standard deviation of the trace. An average SNR of 25.39 over 500 Hz was calculated from two trials (20.39 and 30.39).

To back-calculate the SNR of our conventional 2P raster scanning, we first characterize the average number of pixels per cell segmentation. On average, the cell membrane is composed of 520 pixels in an image, which is equivalent to 520 samples recorded. Considering the brightness value is averaged from these recordings (about 5 times more recordings to average from, $20.39 \times \sqrt{5} = 45.47$), 3.16 times more power used in raster scanning ($43.15 \times 3.16 = 143.7$), 5 times shorter sampling rate ($143.7 \div 5 = 28.7$), and the image is averaged over two images ($28.7 \times \sqrt{3} = 40.51$), the estimated SNR of our 2P raster scanning is around 40. This is sufficient to provide measures of brightness. Effectively, it means that purely based on the physical noise, we should be able to distinguish when a mutant is 2.5% brighter than wild-type.

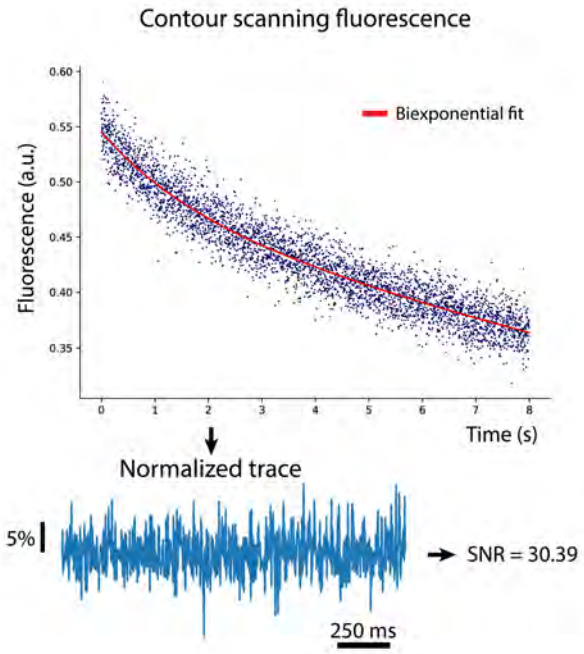

Figure 6.4: Example of contour scan SNR calculation. The raw fluorescence trace is obtained by scanning the 1200 nm laser over the cell membrane for 500 Hz and collecting the emitted fluorescence by PMT. The photobleaching is corrected using a bi-exponential fitting.

6.3.2. SCREENING AUTOMATION

AUTOMATED FOCUS CORRECTION

The theoretical axial resolution of our 2P imaging system is around 2.4 µm ($2 \times \lambda / NA^2$), and the focus drifting beyond that value would produce a wrong representation of the fluorescence. During the screening, it is important to ensure that the program corrects the focus drift induced by the level difference between the sample stage and the objective and the uneven mechanical surface on the sample stage. We characterized the level difference using a petri dish with HEK293T cells expressing Citrine. Across the 6.12 mm × 6.12 mm FOV, a difference of 10.2 µm was measured (Figure 6.5). Because it is important to focus on the cell membrane and use emitted photons to represent protein brightness during the screening, this difference would heavily limit the FOV size that the screening can cover. Automated focus correction was developed and implemented to make sure that the laser focus stays on the cell membrane across the entire FOV.

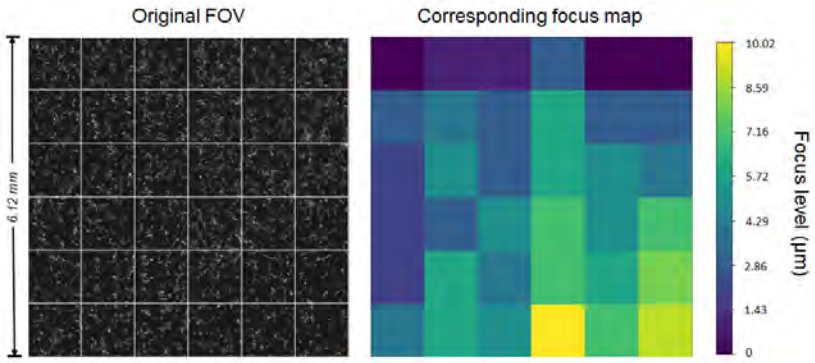

Figure 6.5: Level difference across the whole imaging well. Across the whole 6.12 mm by 6.12 mm imaging area, optimal focus every 1.02 mm was measured. The corresponding focus position map is shown on the right. A maxima difference of 10.2 µm is measured. The sample used here is HEK293T cells expressing QuasAr1-Citrine, which were imaged in the Arch channel.

FOCUS EVALUATION ALGORITHM

To perform autofocusing, an algorithm to properly determine the focus degree in the current FOV is crucial. The cell culture in the petri dish, as much as we want to make it a monolayer, has a 3D structure. Unhealthy cells that express excessive amounts of proteins tend to detach and levitate to a different focus position from the healthy ones, which stick to the dish bottom. A conventional squared-gradient-based sharpness function which evaluates sharpness by computing the gradient of the derivatives would in this case not be able to filter out the signal from the floating cells[79]. When the fluorescence from floating cells dominates the overall signal in the image, previous methods might emphasize these cells instead of the healthy and flat cells, and cloud the judgment on the focus degree.

To find a better-suited algorithm, we looked at the features of these images. The flat cell layer image in general, has more cell structures than the floating cell layer, despite being dimmer. This led us to try local entropy as a measure of sharpness. Adapting Shannon's information entropy to a grayscale image, the entropy of an image can be calculated by:

$$H = -\sum_{n=1}^{K} p_k log_2(p_k) \tag{6.1}$$

where K is the number of gray levels, and p_k is the probability associated with gray level k. It is a simplified translation to 2D space but enough for our purpose[80]. Multiple series of Citrine channel images along different focuses were taken to test its effectiveness, and the local entropy values were computed. One example is shown in Figure 6.6. The image with the highest entropy values is close to the predetermined position that best

represents the membrane-localized protein in cells. The precision is around 2 µm. Given our 2PM axial resolution (2.4 µm), the local entropy algorithm is an excellent method to evaluate the focus degree of the petri dish image.

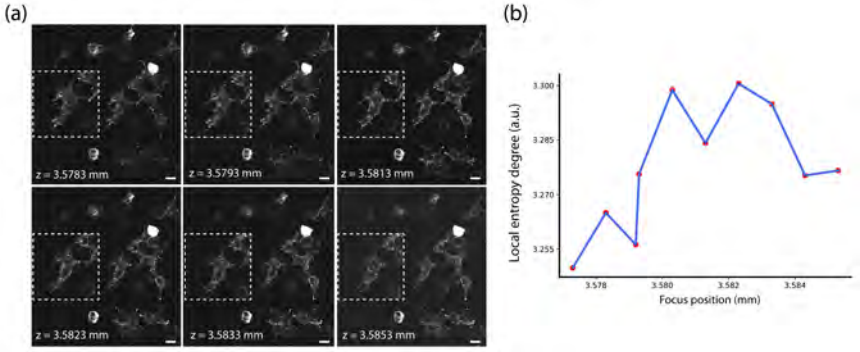

Figure 6.6: Validation of local entropy method as focus evaluation algorithm. (a) Image examples across the z-axis. The scale bar is 10 µm. (b) The measured local entropy values at these positions in (a).

FOCUS-FINDING ROUTE

Having found a method to assess the quality of focus in an image, the next step is optimizing the actual focus finding, i.e. creating a maximally efficient path through the available parameter space tho an optimized focus, using the least amount of time, creating the least sample damage and photobleaching with these extra measurements, and achieving the highest precision. We tested two routes.

First, we used a bi-sectioning search. Given an arbitrary focus, the system will image in the Citrine channel at the current position and two equally spaced positions above and below. In the demonstration in Figure 6.7, we sampled at an arbitrary position and 12 μm apart from both sides. The focus degree of these three locations will be calculated using the local entropy method. The objective focus plane will then move to the half with a higher focus degree, where the next iteration will happen. In this demonstration, we ran three iterations in total, and the theoretical precision is within 3 µm, within the focus resolution of the TPM. Using this strategy, only 6 images are needed, and the total time is around 8.4 seconds. We ran this method in 5 different FOVs from a typical screening dish with cells, and the distance distribution from the optimal focus position judged by the visual sharpness of overall healthy cells shows a mean of 0.499 μm with a standard deviation of 0.54 μm.

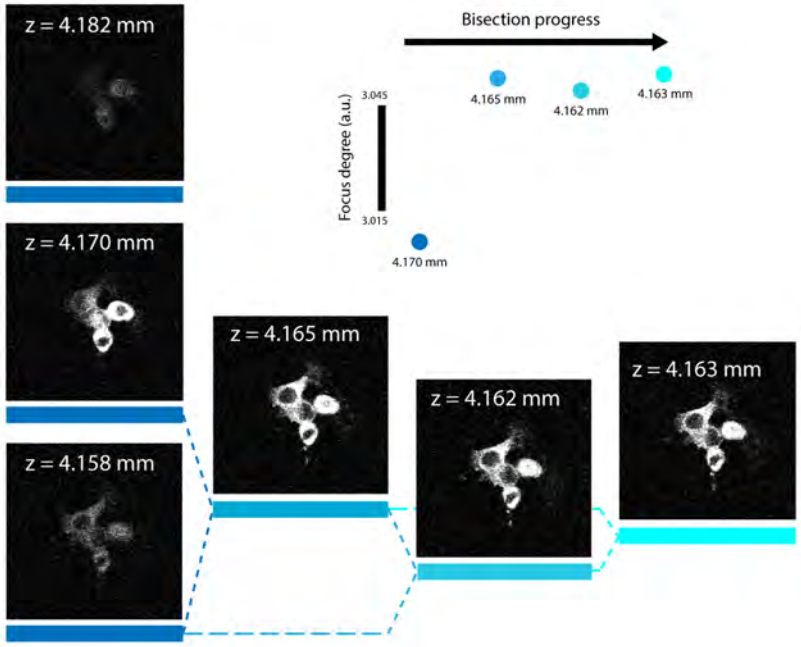

Figure 6.7: Demonstration of the bi-sectioning auto-focus route. The first three evenly spaced focus positions were imaged at the starting focus. The objective motor then drove the focus to the middle of the half with a higher local entropy degree. In this way, the focus degree of the current position will keep increasing, as shown in the top right scatter plot. After three iterations, 6 positions were imaged, and the focus position was within the 3 µm range around the optimal focus location. The sample is HEK293T cells expressing QuasAr1-Citrine and was imaged in the Citrine channel.

Second, we used Gaussian fitting to find the optimal focus. In this case, a series of equally spaced locations along the focus is imaged, and the focus degree of each is calculated. Then we can plot these focus degrees along the z-axis, as shown in Figure 6.8. In principle, we can directly choose the position within the highest focus degree as focus. To increase the precision, a Gaussian fit to the curve is applied, and the highest point of the fit is picked out as the optimal focus position.

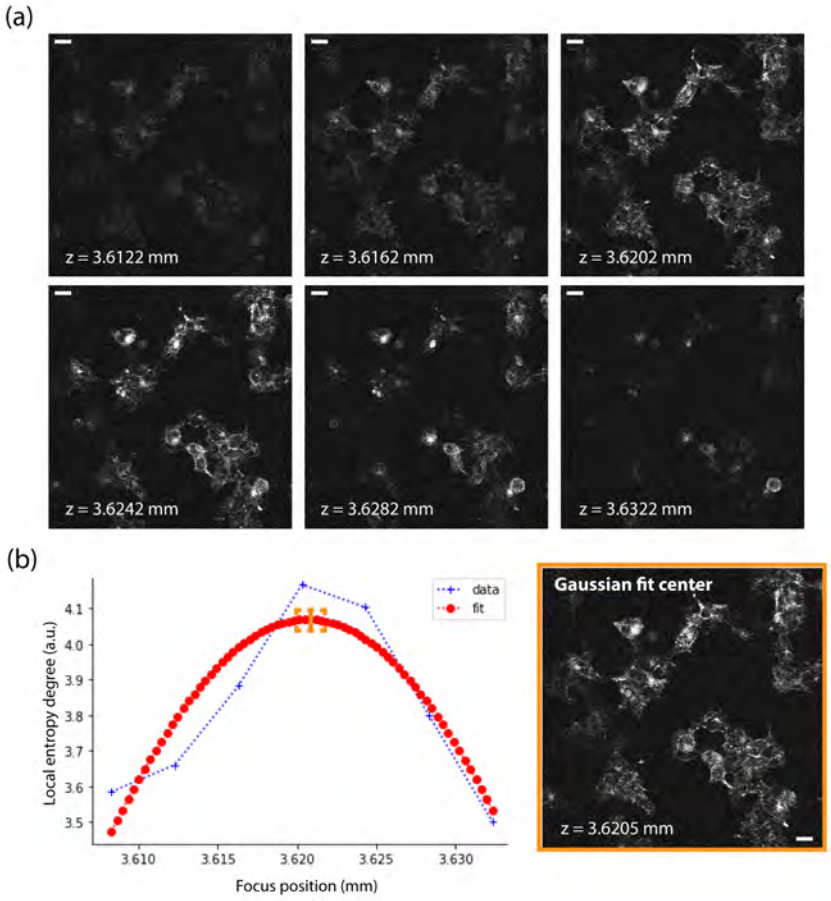

Figure 6.8: Demonstration of the Gaussian fit auto-focus route. A series of equally spaced locations along the focus were sampled, and then a Gaussian fit to the focus degree curve was applied. The highest center point of the fit was chosen as the optimal focus, as marked orange in the bottom left plot. The sample is HEK293T cells expressing QuasAr1-Citrine and was imaged in the Citrine channel. The scale bars are 10 µm.

Comparing the two focus-finding routes, the bi-sectioning method is more robust as the focus degree curve profile is not necessarily a Gaussian shape and the fitting accuracy is more prone to uneven sampling (sampling only one slope for example). Thus we chose the bi-sectioning method as the final focus-finding route. In a typical screening section, an automated focus correction is performed once in every 680 × 680 μm FOV. The only preparation needed is adjusting the first focus to a roughly in-focus position. If there is no cell in the FOV, the algorithm will detect if there is no object and then move to the

neighbouring position. Auto-focus will be performed until there is a cell to keep track of the focus. One screening example is shown in Figure 6.9. As shown in the zoom-in, the focus of these FOV areas stays sharp across the whole 6.12 × 6.12 mm area.

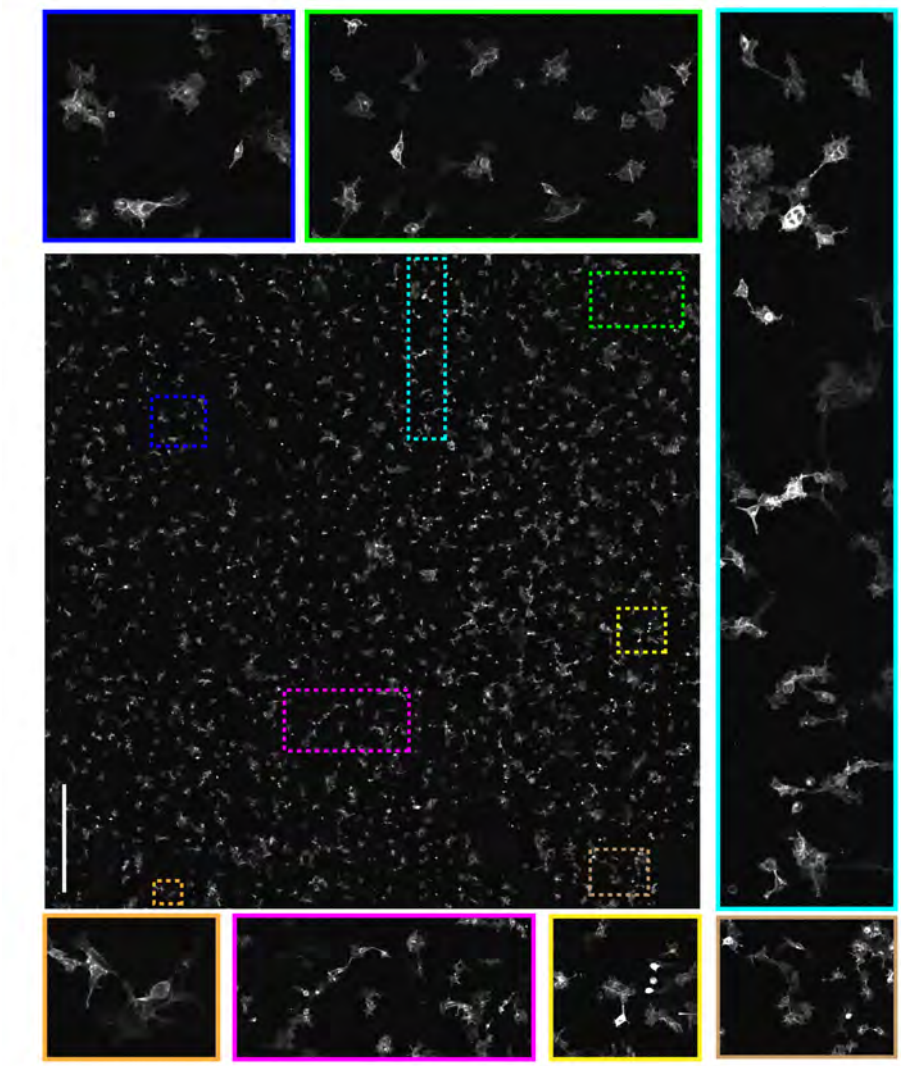

Figure 6.9: Demonstration of focus across the screening area. The zoom-in shows the enlarged area with fluorescent cells. The bounding box color in the showcase corresponds to the color of the dashed box, indicating where the enlarged area is in the original FOV. The sample is HEK293T cells expressing QuasAr1-Citrine and was imaged under 1200 nm excitation. The scale bar is 1 mm.

6.3.3. DATA ANALYSIS

CELL SEGMENTATION USING MACHINE LEARNING

The recorded data consist of large images (6.12 × 6.12 mm, 9000 × 9000 pixels) of cells. Each cell expresses through the above-described optimized expression protocol a single mutated fusion protein consisting of a Quasar1 mutant and Citrine. Each image contains tens of thousands of fluorescent cells: from each cell, the fluorescence originates from one mutated fusion protein. For the successful screen, two more steps are necessary: analyzing the fluorescence of individual cells, and, based on this analysis, extracting the cells containing a mutant showing superior fluorescence characteristics for DNA extraction and sequencing, so we can conclude the fluorescence brightness of individual mutants in the library.

To assess the quality of the mutation and make a selection of cells to pick, several aspects of these fluorescence images need to be assessed: the brightness of Quasar1-mutant fluorescence, normalized for expression by dividing it to the Citrine fluorescence, indicative of a mutation that leads to a higher absorption cross-section or quantum yield; the ratio between quasar fluorescence at the cell membrane and in the rest of the cell body, indicative of the mutation effect on membrane trafficking; and the absolute fluorescence of Quasar at the membrane, together with the normalize fluorescence indicative of the effect of the mutation on expression level.

The most important part of the analysis of the screening data is correct cell segmentation. All the information extracted from individual cells in the screened library is based on these cell masks. Thus the segmentation precision directly influences the screening results. Traditional image processing methods suffer from an inability to distinguish cells when they are in a cluster. While plating and measurement conditions can be adapted to minimize clustering, motile cells will generally form clusters over time[81]. We implemented machine learning to precisely assign masks to cells, even when they are in close contact with each other, and to classify cell groups. We chose the Mask R-CNN algorithm, which is based on a Region-based Convolutional Neural Network (R-CNN)[74]. Manually annotated data was fed to the network, and we performed transfer learning based on the COCO dataset to improve the training efficiency and accuracy[75]. The implementation is explained in section 6.2.3. Next, we quantified the results from the trained network.

The basic metric we selected to quantify the prediction accuracy is the intersection over union (IoU) of a predicted object with ground truth, which in our case is the IoU of a predicted cell bounding box (BBox) and mask with annotated ones. The IoU value ranges between 0 and 1, with 1 meaning the prediction completely overlaps with the ground truth:

$$IoU = \frac{area\ of\ overlap}{area\ of\ union} \tag{6.2}$$

As a reference, the COCO evaluation criteria defines an IoU larger than 0.5 as a good metric and an IoU larger than 0.75 as a strict metric[75]. The IoU metric does quantify

the overlapping; however, it provides no metrics on how well the algorithm can find the object. We looked at other metrics to properly reflect the detection performance of the network, and they are AP50, AP75, Recall, and F-score. These measures give scores on the detecting ability of the algorithm and are introduced in detail in section 6.6.1 in the Appendix.

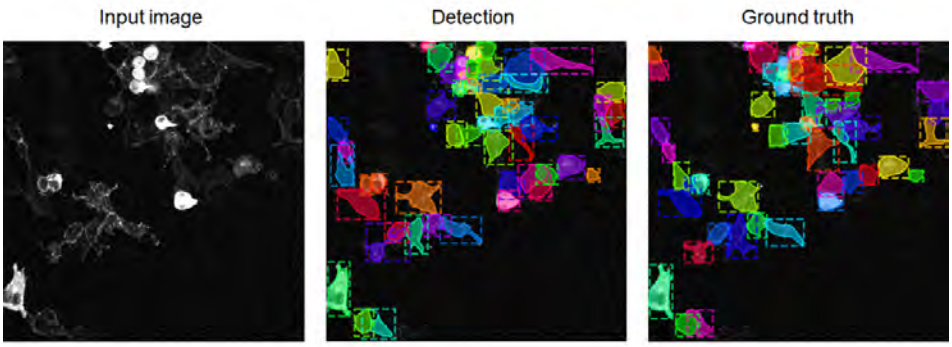

Figure 6.10: Illustration of the intermediate images used for calculating the accuracy. Based on the input image, the ground truth of the image was annotated manually, with each cell masked with a binary boundary and category information. The detection was generated from the trained model weight. The IoU from the cell mask, IoU from BBox, AP scores, Recall scores, and F-scores were calculated from the type of images above.

We calculated the IoU from Mask, IoU from BBox, AP scores, Recall scores, and F-scores for all the training and validation images. The cores are summarized in Table 6.1. The average F-score for validation images is 0.92 for AP50 and 0.63 for AP75. The IoU scores for mask and BBox are above 0.75. The scores suggest that the detection performance is excellent. The detection across the FOV is shown in Figure 6.11.

From the whole cell mask generated from machine learning, it is important to separate the cell membrane from the soma. Because the GEVIs should be expressed in the membrane, any signal from the soma region is considered noise. We generated the cell membrane mask from conventional image processing techniques based on the binary whole-cell mask. First, we found the contour of the whole cell mask and performed closing on it to restore potential breaking points. Next, we performed dilation inwards to thicken the membrane area to the desired thickness. Lastly, we applied morphology opening to smooth the membrane masks.

As a result, after running the cell segmentation algorithm, we obtained detection results from the machine learning network, which tell us which pixels belong to each cell, and category information that tells us the health status of that cell.

Table 6.1: The quantitative scores to evaluate the network performance.

	AP_{50}	$Recall_{50}$	$F_{score50}$	AP_{75}	$Recall_{75}$	$F_{score75}$	IoU_{mask}	IoU_{BBox}
Validation	0.91	0.93	0.92	0.62	0.63	0.63	0.77	0.76
Training	0.94	0.95	0.94	0.71	0.73	0.72	0.79	0.84

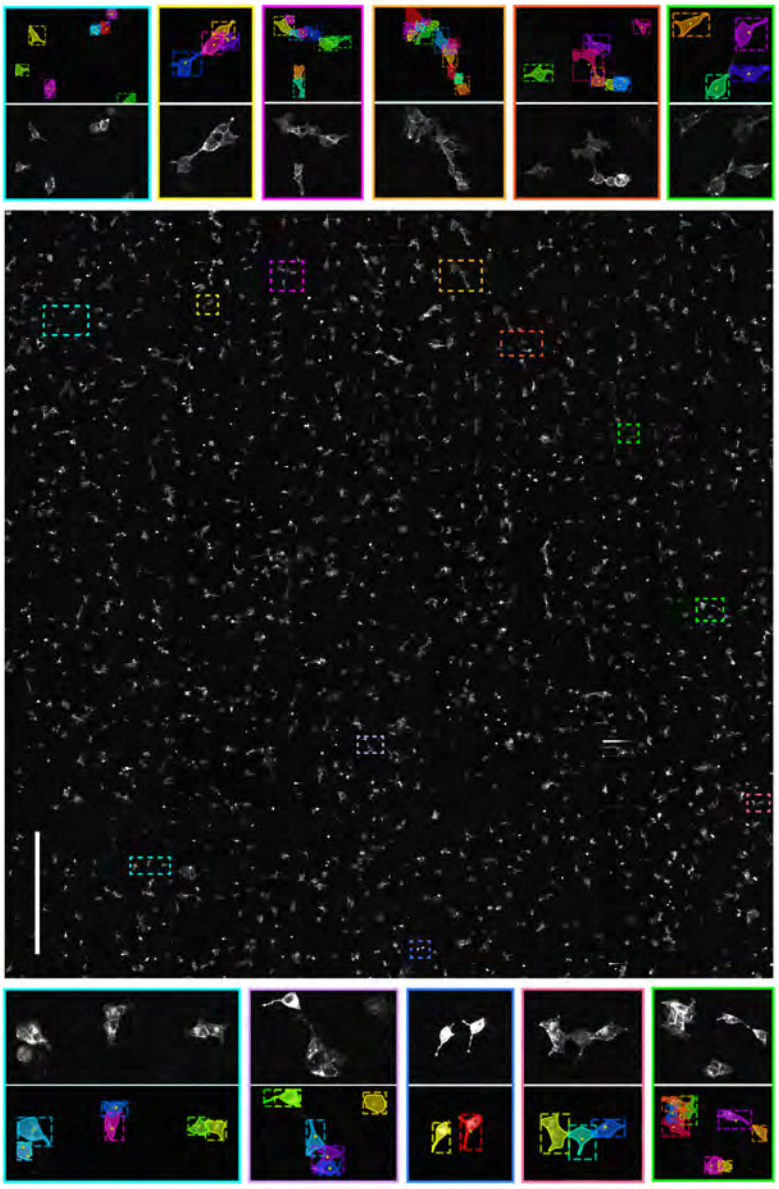

Figure 6.11: Detection results from the MaskRCNN algorithm across the FOV. The detection results from the selected region marked inside the dashed lines are zoomed in for display in corresponding colored squares above and below the whole FOV image. The scale bar is 1 mm.

DETERMINING CELL PERFORMANCE

From the machine learning network, we can select healthy cells and determine their exact pixel locations. From the cell masks, we generated an Excel file containing all the extracted information for each cell, including the file path, the location of the cell bounding box inside the image, the pixel numbers of the cell mask, the average intensity over the whole cell area, the average intensity over the membrane area, and the ratio between the intensities from the two channels in the cell membrane and the cell soma part.

Between the two screening rounds, the cells will migrate in random directions, making it impossible to locate the same cell by looking at the same location. It is important to track individual cells between the screening rounds so that we would have the fluorescence data of the same cell in both Citrine and Arch channels, and we can eventually normalize the Arch channel fluorescence to the expression level which is indicated by the Citrine fluorescence. To do that, we first collected every identified cell bounding box location from both rounds. Then we calculated the IoU of each pair. If the overlapping area of the two is greater than 60% of the cell area, they are identified as from the same cell. After extracting cell membrane fluorescence in both rounds, the ratio between the extracted values from both rounds was calculated and marked as the Arch to Citrine ratio, which is a measure for the cell brightness corrected for expression level.

Filtering based on a contour-to-soma fluorescence ratio threshold and mean intensity threshold was performed during the data collection. The cells with a contour-to-soma ratio of less than one were seen as unhealthy, as another criterion supplementary to the machine learning identification. The cells with Arch channel mean intensity less than 0.25 were also eliminated, as their absolute brightness was too low to provide enough signal-to-noise ratio for accurate cell segmentation.

At last, sorting was performed based on multiple parameters with different weights. The first parameter was the normalized membrane brightness, which was given the highest weight. The second parameter was the absolute intensity in the membrane area, and the third was the contour-to-soma brightness ratio. These parameters were used with relative weights of 0.6, 0.5, and 0.5, based on the rationale that the normalized brightness is the most important metric, while the overall brightness and contour-to-soma ratio serve as sanity checks. This sorting ranked the performance of the mutated fluorescent protein in each cell and allowed us to make a selection for cell picking.

A Python program with a user interface was created to analyze the data, present the cell performance, and facilitate the cell-picking process. The settings for the screening analysis are configured before the screening starts. The analysis automatically starts after the screening is finished and presents the data in interactive plots after it is done. It is shown in Figure 6.12(a) and introduced in detail in section 3.4.1.

6.3.4. CELL SELECTION

The automated analysis generated a scatter plot where the position in space indicated cell performance along several axes, and a sorted list of best-performing cells (i.e. best performing mutated proteins in individual cells). Before picking cells for DNA extraction, we performed a sanity check. We started with the cell with the highest performance score. In the screening analysis software, we checked its scatter position in the plot and its 2P images in both Citrine and Arch channels to ensure the cell had good expression and decent fluorescence. The target cell was marked in a white bounding box to facilitate identification. We also checked the segmentation maps for both channels to avoid false segmentation. As an example in Figure 6.12(b), the third cell was excluded based on those criteria.

After confirming the cell-picking target, the automated sample stage repositioned the region of interest (ROI) of the cell into the center of the microscope FOV by reading the cell location from the data collection sheet. We set up the microscope to provide the 1P Citrine image of the current FOV and correlated it to the 2P Citrine image, which had great similarities. In the camera image, the cell corresponding to the marked target cell in the 2P image was found at approximately the same location (Figure 6.12(c)). Then the cell was picked up using a pipette and sequenced as introduced in the section 6.2.

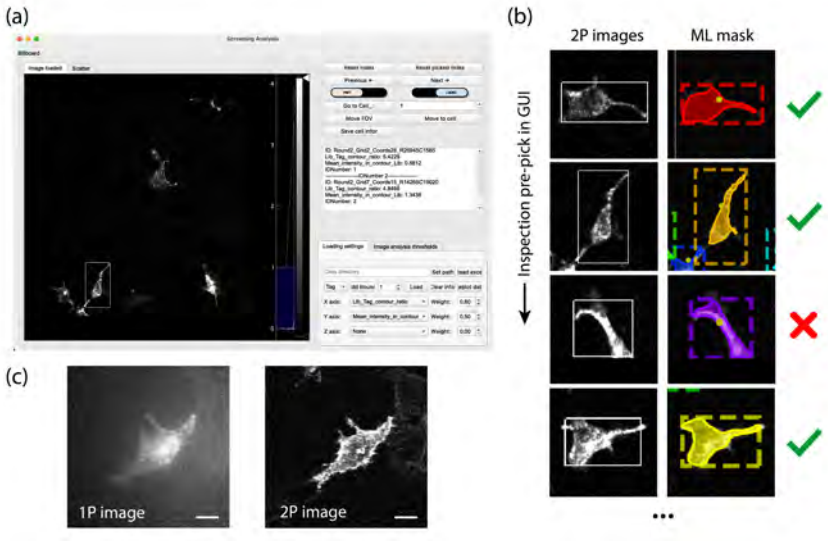

Figure 6.12: The screening analysis GUI and cell inspection illustration. (a) The screening analysis GUI can display all relevant information (fluorescence, location, mask, statics, etc.) of each identified cell in the screening. (b) Illustration of cell inspection as a sanity check before picking. (c) Knowing the coordinates of the target cell, it is straightforward to trace the cell in both 1P and 2P images. Scale bar: 1 µm

6.3.5. EVOLUTION RESULTS

In the first round of evolution, 5 cells were picked, among which one was successfully sequenced and identified not to be wild-type QuasAr1. Its location in the performance scatter plot and original fluorescence images are shown in Figure 6.13(a). The sequencing result reveals a mutation at the H106 site, being an Arginine instead of Histidine.

The mutation site, H106R, serves as the proton donor in the Arch 3 photocycle, and it has been mutated in QuasAr1 (D106H)[48]. The protein structure of Arch 3 with mutation sites labeled is shown in Figure 6.13(b).

To verify its brightness increase, we screened HEK cells expressing QuasAr1 wild-type and QuasAr1 (H106R). Like in the evolution screening, the fluorescence images in the citrine channel were acquired under 900 nm excitation (14.7 mW after objective), and the Arch channel was acquired under 1200 nm excitation (177.5 mW after objective). The fluorescence normalized to the expression level (Arch/Citrine ratio) of QuasAr1 H106R shows a 75% increase compared to the wild-type (Figure 6.13(d) right). Without the expression level normalization, the mean intensity from the membrane of QuasAr1 (H106R) shows a 41% increase compared to the wild-type as well (Figure 6.13(d) left).

To characterize the voltage sensitivity under 2P illumination, we performed a voltage clamp experiment. In a dish with HEK cells expressing QuasAr1 (H106R), We checked the expression levels and found a target cell with good expression. We created a raster-scanned 2P image of the cell to ensure it had decent Arch fluorescence. Then we switched back to 1PM and compared the 1P Citrine image with the LED white light image to find the cell location in the camera under white light illumination, the illumination condition used for patch clamping. After locating the target cell, a whole cell patch clamp was performed using the electrophysiology module on the microscope, which allowed us to manipulate the cell membrane potential. In a recording session, the focus of the pulsed femtosecond laser beam tuned to 1200 nm (93.7 mW after objective) was traced along the manually determined cell membrane contour at 500 Hz circling frequency, and the cell membrane potential was alternated between -70 and +30 mV at 5 Hz. The fluorescence was recorded on a PMT at a 50 kHz sampling rate, resulting in 100 sample points per contour, and low-pass filtered at 25 kHz(Alligator filter).

For the data analysis, every 100 data points collected from one contour scan were summed as one representative value for the cell fluorescence during that time, resulting in a 500 Hz trace. The sensitivity was calculated as around 9% $\Delta F / F_0$ per 100 mV, which is similar to the wild-type QuasAr1 that we measured (shown in the Appendix 6.6).

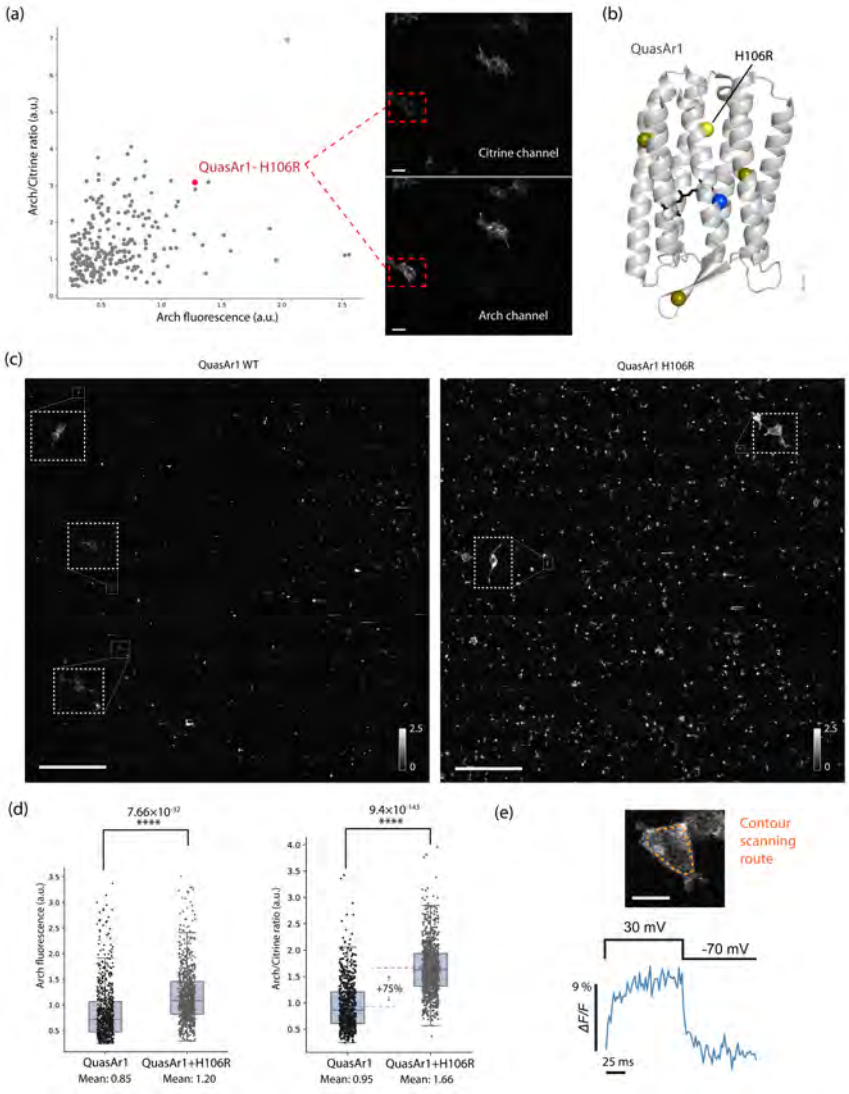

Figure 6.13: Evolution round one. (a) The location of the picked cell in the scatter plot and its fluorescence images. Scale bar: 10 µm. The mutant contains one mutation site, H106R, compared to the parent template QuasAr1. (b) The locations of the mutation sites in QuasAr1. Site 106 is the proton donor in the proton transfer pathway. (c) The whole field 2P images under 1200 nm with the same visualization contrast. Scale bar: 1 mm.(d) The Arch brightness comparison between QuasAr1 (0.85 ± 0.020, n = 674 cells) and QuasAr1 H106R (1.20 ± 0.019, n = 841 cells). The individual t-test shows a p-value of 7.66×10^{-32}. All data are mean ± SEM. In the boxplots, the boundaries of the whiskers are based on an interquartile range of 1.5; each grey dot in the boxplot represents a cell. (d) The normalized brightness comparison between QuasAr1 (0.95 ± 0.018, n = 676 cells) and QuasAr1 H106R (1.66 ± 0.017, n = 841 cells). The individual t-test shows a p-value of 9.4×10^{-143}. QuasAr1 H106R shows an increase of 75%. (e) The 2p voltage sensitivity characterization. Scale bar: 10 µm.

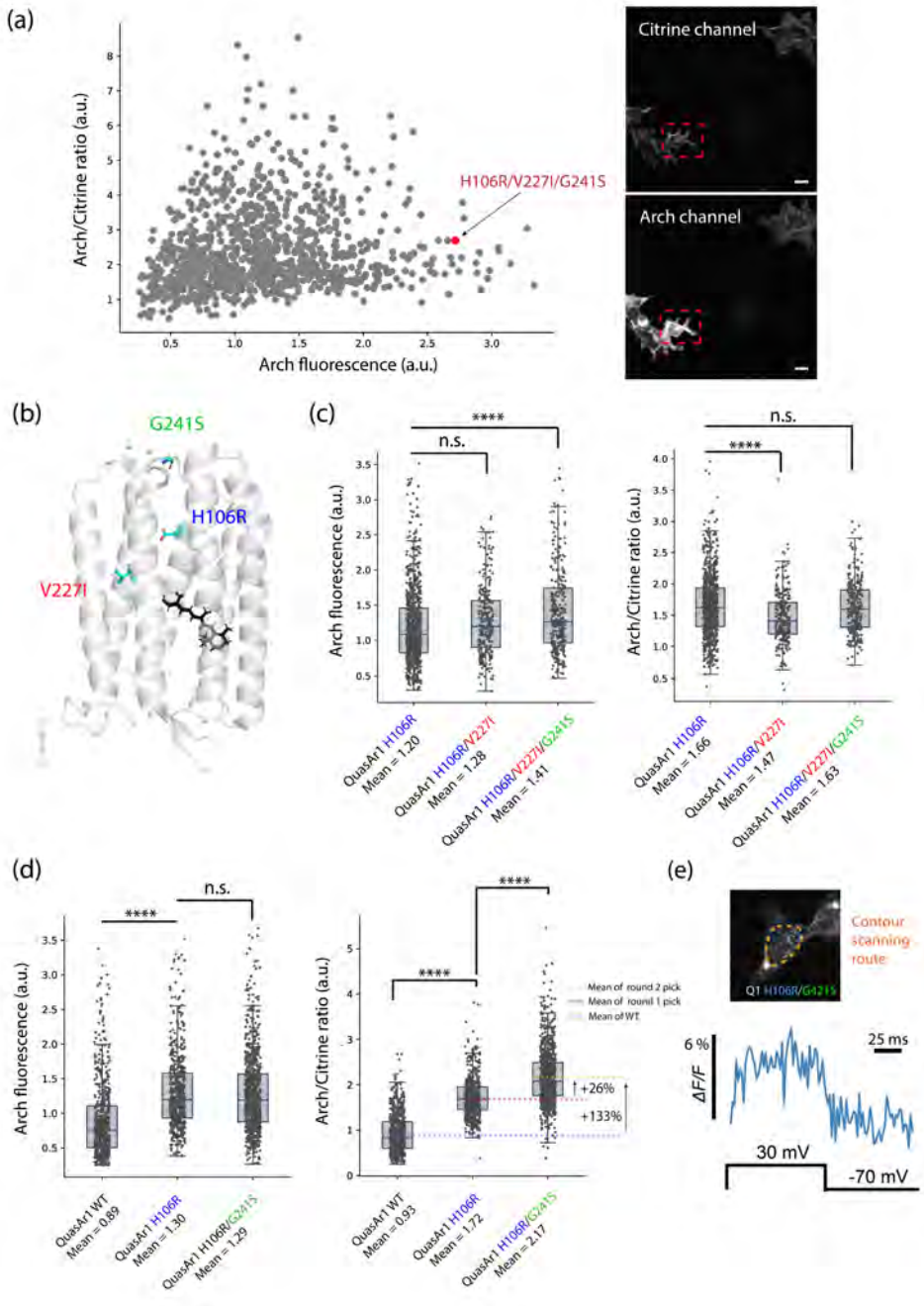
(a)
Arch/Citrine ratio (a.u.)
Arch fluorescence (a.u.)
H106R/V227I/G241S
Citrine channel
Arch channel
(b)
G241S
H106R
V227I
(c)
Arch fluorescence (a.u.)
Arch/Citrine ratio (a.u.)
n.s.
****
QuasAr1 H106R Mean = 1.20
QuasAr1 H106R/V227I Mean = 1.28
QuasAr1 H106R/V227I/G241S Mean = 1.41
QuasAr1 H106R Mean = 1.66
QuasAr1 H106R/V227I Mean = 1.47
QuasAr1 H106R/V227I/G241S Mean = 1.63
(d)
Arch fluorescence (a.u.)
Arch/Citrine ratio (a.u.)
QuasAr1 WT Mean = 0.89
QuasAr1 H106R Mean = 1.30
QuasAr1 H106R/G241S Mean = 1.29
QuasAr1 WT Mean = 0.93
QuasAr1 H106R Mean = 1.72
QuasAr1 H106R/G241S Mean = 2.17
Mean of round 2 pick
Mean of round 1 pick
Mean of WT
+26%
+133%
(e)
Contour scanning route
Q1 H106R/G241S
6 %
ΔF/F
25 ms
30 mV
-70 mV

Figure 6.14: Evolution round two. (a) The location of the picked cell in the scatter plot and its fluorescence images. Scale bar: 10 µm. The mutant contains two extra mutation sites compared to the parent template QuasAr1 H106R: V227I and G241S. (b) The locations of the mutation sites in QuasAr1. (c) The Arch brightness comparison between QuasAr1 H106R (1.20 ± 0.019, n = 841 cells), QuasAr1 H106R/V227I (1.28 ± 0.03, n = 263 cells), and QuasAr1 H106R/V227I/G241S (1.28 ± 0.03, n= 294 cells). The p-value of the one-way analysis of variance (ANOVA) test is 8.35×10^{-8}. The p-values of H106R/V227I and H106R/V227I/G241S against H106R are 7.8×10^{-2} and 4.61×10^{-8}, Tukey's post hoc test. All data are mean ± SEM. In the boxplots, the boundaries of the whiskers are based on an interquartile range of 1.5; each grey dot in the boxplot represents a cell. The normalized Arch brightness comparison between QuasAr1 H106R (1.66 ± 0.017, n = 841 cells), QuasAr1 H106R/V227I (1.47 ± 0.025, n = 263 cells), and QuasAr1 H106R/V227I/G241S (1.63 ± 0.024, n= 294 cells). The p-value of the ANOVA test is 5.2×10^{-8}. The p-values of H106R/V227I and H106R/V227I/G241S against H106R are 2.3×10^{-8} and 5.6×10^{-1}, Tukey's post hoc test.(d) Left: the Arch brightness comparison between QuasAr1 (0.89 ± 0.022, n = 602 cells), QuasAr1 H106R (1.30 ± 0.023, n = 571 cells), and QuasAr1 H106R/G241S (1.29 ± 0.019, n= 878 cells). The p-value of the one-way analysis of variance (ANOVA) test is 8.56×10^{-47}. The p-value of QuasAr1 WT against QuasAr1 H106R is smaller than 1×10^{-5}, and The p-value of QuasAr1 H106R/G241S against QuasAr1 H106R is 0.79, Tukey's post hoc test. Right: the normalized Arch brightness comparison between QuasAr1 (0.93 ± 0.017, n = 602 cells), QuasAr1 H106R (1.72 ± 0.018, n = 571 cells), and QuasAr1 H106R/G241S (2.71 ± 0.020, n= 878 cells). The p-value of the ANOVA test is 2.47×10^{-310}. Tukey's post hoc test shows all p-values are smaller than 1×10^{-5}. The round two pick, QuasAr1 H106R/G241S, shows an increase of 26% compared to the round one pick, and 133% compared to the QuasAr1 WT. (e) The 2P voltage sensitivity characterization of QuasAr1 H106R/G241S.

We then used QuasAr1 H106R as a parent template and carried out another round of evolution. One picked-up mutant shows two extra mutation sites, V227I and G241S (Figure 6.14(a)). Their locations in the protein is shown in Figure 6.14(b). We measured and compared the average absolute Arch fluorescence as well as the normalized brightness from H106R and the triple mutant H106R/V227I/G241S. Although the absolute brightness of the triple mutant is 6.7% higher, its brightness per protein is not significantly different from the template H106R.(Figure 6.14(c)). Along with them, the double mutant H106R/V227I is also compared, which shows even a decrease in normalized brightness (Figure 6.14(c)). Reasoning that V227I might have a negative role in improving the brightness, we further conducted a round of brightness characterization involving QuasAr1, QuasAr1 H106R, and QuasAr1 H106R/G241S mutant without the V227I mutation. The absolute brightness of H106R/G241S does not show an improvement com-

pared to the template H106R (Figure 6.14(d) left). However, it shows a 26% increase in terms of expression-normalized fluorescence compared to QuasAr1 H106R (Figure 6.14(d) right). It is possible that the extra mutation site, G241S, lowers the expression level in the cell as reflected in the lower tag protein amount. Compensated by its higher per-molecule brightness, it reaches the same absolute brightness as the H106R. The potential advantage of this is that QuasAr1 H106R/G241S would lower the required expression level to maintain a certain SNR, and thus introduce less disturbance to the neurons and make them less unhealthy. In one patch clamp session, QuasAr1 H106R/G241S mutant shows a $\Delta F / F_0$ of around 6% from −70 mV to 30 mV under the same 2P excitation.

6.4. DISCUSSION

In this chapter, we introduced a pipeline to evolve the 2P brightness of the Archaerhodopsin-based sensor QuasAr1. The Octoscope platform was able to carry out automated brightness screening over an area of 6.12 mm by 6.12 mm under different 2P wavelengths. We applied a machine learning network to categorize and segment the cells, and the performance of the "healthy" cells was evaluated through three metrics. Cells with the best performance were picked up through micropipettes, and single-cell PCR was performed to reveal the mutation sites. We successfully carried out two rounds of evolution, gaining 85% and 26% increases compared to the previous template. The resulting mutant, QuasAr1 H106R/G241S, shows an increase of 133% in total in the per-molecule brightness compared to QuasAr1 under 1200 nm excitation (Figure 6.14(d)).

The two identified mutation sites, D106 and G241, were also targeted in previous studies. The proton donor site 106 was mutated to D106H in most Arch-based GEVIs since QuasAr1, and G241Q was one of the mutations in Archon1[30]. These mutations play a role in improving the 1P brightness of the Arch sensors. The origin of fluorescence in 1P was considered to have contributions from both the photointermediate fluorescent states and the spontaneous emission[30]. Under high laser illumination power, which is normally the case for Arch-based GEVIs, the ground state is depleted, and a three-photon process (from the ground state to N intermediate and to Q intermediate) is thought to lead to the voltage-sensitive fluorescence[30]. While there are uncertainties about where the 1P fluorescence comes from, less is known about the 2P fluorescence process, and it is challenging to predict 2P performance from 1P data[72]. 2P excitation can excite the molecules to entirely different states and have different isomerizations and photointermediates. At the moment, it is impossible to pinpoint what the H106R and G241S do to the molecules under 2P excitation. It could be that these mutations increase the 2P absorption cross-section by affecting the permanent dipole moments between the fluorescent states[72], which comes from a disturbance in protein structures.

6.5. OUTLOOK

The proposed pipeline is a powerful method to improve the 2P brightness of GEVIs, as demonstrated in QuasAr1. In the future, it can be applied to evolve the 2P brightness of

not only other GEVIs but also other optogenetics tools like GECIs or neurotransmitter sensors to improve their performance.

There are several potential improvements that can be realized in further development of the 2P evolution pipeline. The first is to add the capability to evaluate the voltage response. We have briefly explored the potential of using a perfusion system to bathe the cells in the extracellular buffer of different ion concentrations. We encountered the issue that the buffer-introduced membrane potential change was around 20 mV, which translates to about 1.6% difference in 2P fluorescence, and this signal level was too little to be picked up by the screening system. One potential solution is to use HEK293 cells expressing the inward-rectifying channel Kir2.1 which has a resting potential of around −77 mV[42]. In this case, the buffer-introduced membrane potential change will be ~ 80 mV, and the corresponding fluorescence change can be above the noise and observed by the system.

Another aspect is to improve the throughput of the screening. Ensuring the elimination of wild-type in the library can be helpful[49]. Another approach is to eliminate the non-fluorescent or weakly fluorescent mutants at a prescreening stage. This comes down to making the assumption that very weak 1P fluorescence overwhelmingly originates from mutations that simply break the protein and that the chance that 2P fluorescence would unexpectedly be higher is negligible. While this is a speculative hypothesis that we do not have any direct proof for at the moment, it could be seen as a reasonable way to screen a different, focused part of the protein mutation space. Practically, it can be achieved by introducing a round of fluorescence activated cell sorting (FACS) into the pipeline before the 2P screen. FACS is done through 1P excitation and 1P and 2P fluorescence are not linearly correlated, FACS can eliminate a large population of misfolded non-fluorescent mutants.

A constraint during the screening is the necessity to switch wavelengths which consumes time. With a dual output multi-photon laser, the switching between the fixed wavelength for GFP and tunable wavelength at 1200 nm for Arch would be smooth, and the two channels can be imaged shortly after each other, which eliminates errors induced by morphological changes during the switch.

6.6. APPENDIX

6.6.1. METRICS TO EVALUATE THE MACHINE LEARNING NETWORK PERFORMANCE

Average Precision (AP) is a standard metric to evaluate object detection networks. It is defined as such:

$$AP = \frac{t_p}{t_p + f_p}, \tag{6.3}$$

where t_p is the number of true positive detections, which are objects correctly detected by the model; f_p is the number of false positive detections, which are the wrong system

detections. The threshold we use to tell if it is a correct or incorrect detection according to the ground truth is related to the IoU of each detection. For the AP50 metric, a true positive detection means that the detected object has an IoU larger than 0.5 with ground truth, and for AP75, this threshold is set to 0.75.

The AP50 and AP75 scores provide a measure of strictness and exactness for identifying relevant objects and the percentage of correct detections in all predictions. However, they don't cover the part when objects are not detected. The Recall metric quantifies how well the algorithm finds all the positives with the following equation:

$$Recall = \frac{t_p}{t_p + f_n}, \tag{6.4}$$

where f_n is the number of false negative detections. The number $t_p + f_n$ here represents the number of all ground truths.

To properly evaluate a model, we need to look at both AP and Recall scores, and for that, the F-score is introduced. It is calculated as the harmonic mean of the precision and recall:

$$F_1 = \frac{2}{\frac{1}{recall} + \frac{1}{precision}} = 2 \times \frac{recall \times precision}{recall + precision} \tag{6.5}$$

6.6.2. H106R IN OTHER GEVIS

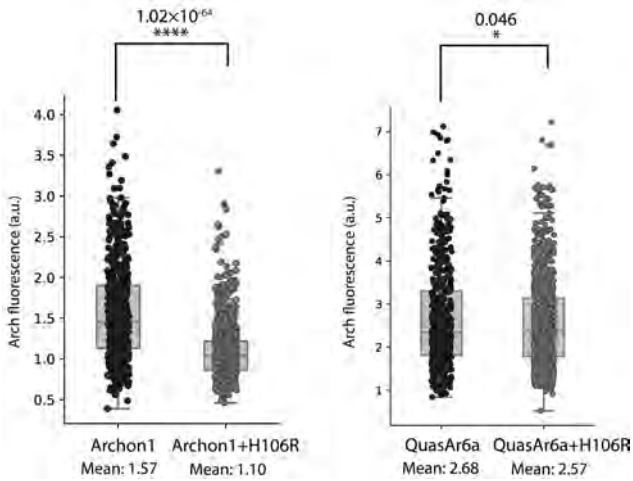

Figure 6.15: Effects of H106R mutation on other Arch-based GEVIs. We put the H106R mutation into Archon1 and QuasAr6a, and compared the brightness change. Archon1 H106R shows a decrease in brightness, while the brightness of QuasAr6a H106R remains similar.

6.6.3. PRIMER SEQUENCES

Table 6.2: Primer sequences used in this study.

Primer name	Sequence
QuasAr1_fwd	ggtcgccaccATGGTAAGTATCGCTCTGCAGG
QuasAr1_rev	tagacttcatCAACGTATCGGCACCGGC
pLenti_CMV_TSX3_Cit_fwd	cgatacgttgATGAAGTCTAGAATCACAAGCGAAGGC
pLenti_CMV_TSX3_Cit_rev	tacttaccatGGTGGCGACCGGTGGATC
QuasAr1_Lib_scPCR_fwd	gacctccatagaagacaccgactccagag
QuasAr1_Lib_scPCR_rev	caggggatgtactcgccttcgcttgtgattc
QuasAr1_libseq_fwd_HPLC	ATGGTAAGTATCGCTCTGCAGG
QuasAr1_libseq_rev_HPL	CAACGTATCGGCACCGGC

REFERENCES

[1] B. Sakmann and E. Neher. “Patch clamp techniques for studying ionic channels in excitable membranes”. In: *Annual review of physiology* 46.1 (1984), pp. 455–472.

[2] D. Lee and A. K. Lee. “In vivo patch-clamp recording in awake head-fixed rodents”. In: *Cold Spring Harbor Protocols* 2017.4 (2017), pdb–prot095802.

[3] I. van Welie, A. Roth, S. S. Ho, S. Komai, and M. Häusser. “Conditional spike transmission mediated by electrical coupling ensures millisecond precision-correlated activity among interneurons in vivo”. In: *Neuron* 90.4 (2016), pp. 810–823.

[4] H.-J. Suk, I. van Welie, S. B. Kodandaramaiah, B. Allen, C. R. Forest, and E. S. Boyden. “Closed-loop real-time imaging enables fully automated cell-targeted patch-clamp neural recording in vivo”. In: *Neuron* 95.5 (2017), pp. 1037–1047.

[5] P. Bazzigaluppi, T. Ruigrok, P. Saisan, C. I. De Zeeuw, and M. De Jeu. “Properties of the nucleo-olivary pathway: an in vivo whole-cell patch clamp study”. In: (2012).

[6] S. B. Kodandaramaiah, F. J. Flores, G. L. Holst, A. C. Singer, X. Han, E. N. Brown, E. S. Boyden, and C. R. Forest. “Multi-neuron intracellular recording in vivo via interacting autopatching robots”. In: *Elife* 7 (2018), e24656.

[7] J. J. Jun, N. A. Steinmetz, J. H. Siegle, D. J. Denman, M. Bauza, B. Barbarits, A. K. Lee, C. A. Anastassiou, A. Andrei, Ç. Aydın, *et al.* “Fully integrated silicon probes for high-density recording of neural activity”. In: *Nature* 551.7679 (2017), pp. 232–236.

[8] C. M. Lopez, S. Mitra, J. Putzeys, B. Raducanu, M. Ballini, A. Andrei, S. Severi, M. Welkenhuysen, C. Van Hoof, S. Musa, and R. F. Yazicioglu. “22.7 A 966-electrode neural probe with 384 configurable channels in 0.13μm SOI CMOS”. In: *2016 IEEE International Solid-State Circuits Conference (ISSCC)*. 2016, pp. 392–393. DOI: 10.1109/ISSCC.2016.7418072.

[9] N. A. Steinmetz, C. Koch, K. D. Harris, and M. Carandini. “Challenges and opportunities for large-scale electrophysiology with Neuropixels probes”. In: *Current opinion in neurobiology* 50 (2018), pp. 92–100.

[10] E. S. Boyden, F. Zhang, E. Bamberg, G. Nagel, and K. Deisseroth. “Millisecond-timescale, genetically targeted optical control of neural activity”. In: *Nature neuroscience* 8.9 (2005), pp. 1263–1268.

[11] C. Grienberger and A. Konnerth. “Imaging calcium in neurons”. In: *Neuron* 73.5 (2012), pp. 862–885.

[12] J. Hefendehl, J. LeDue, R. Ko, J. Mahler, T. Murphy, and B. MacVicar. “Mapping synaptic glutamate transporter dysfunction in vivo to regions surrounding Aβ plaques by iGluSnFR two-photon imaging”. In: *Nature communications* 7.1 (2016), pp. 1–13.

[13] J. J. Mancuso, J. Kim, S. Lee, S. Tsuda, N. B. Chow, and G. J. Augustine. “Optogenetic probing of functional brain circuitry”. In: *Experimental physiology* 96.1 (2011), pp. 26–33.

[14] L. Tian, J. Akerboom, E. R. Schreiter, and L. L. Looger. “Neural activity imaging with genetically encoded calcium indicators”. In: *Progress in brain research* 196 (2012), pp. 79–94.

[15] M. Z. Lin and M. J. Schnitzer. “Genetically encoded indicators of neuronal activity”. In: *Nature neuroscience* 19.9 (2016), pp. 1142–1153.

[16] D. E. Clapham. “Calcium signaling”. In: *Cell* 131.6 (2007), pp. 1047–1058.

[17] M. J. Berridge, P. Lipp, and M. D. Bootman. “The versatility and universality of calcium signalling”. In: *Nature reviews Molecular cell biology* 1.1 (2000), pp. 11–21.

[18] L. Tian, S. A. Hires, T. Mao, D. Huber, M. E. Chiappe, S. H. Chalasani, L. Petreanu, J. Akerboom, S. A. McKinney, E. R. Schreiter, *et al.* “Imaging neural activity in worms, flies and mice with improved GCaMP calcium indicators”. In: *Nature methods* 6.12 (2009), pp. 875–881.

[19] T.-W. Chen, T. J. Wardill, Y. Sun, S. R. Pulver, S. L. Renninger, A. Baohan, E. R. Schreiter, R. A. Kerr, M. B. Orger, V. Jayaraman, *et al.* “Ultrasensitive fluorescent proteins for imaging neuronal activity”. In: *Nature* 499.7458 (2013), pp. 295–300.

[20] H. Dana, Y. Sun, B. Mohar, B. K. Hulse, A. M. Kerlin, J. P. Hasseman, G. Tsegaye, A. Tsang, A. Wong, R. Patel, *et al.* “High-performance calcium sensors for imaging activity in neuronal populations and microcompartments”. In: *Nature methods* 16.7 (2019), pp. 649–657.

[21] Y. Zhang, M. Rózsa, Y. Liang, D. Bushey, Z. Wei, J. Zheng, D. Reep, G. J. Broussard, A. Tsang, G. Tsegaye, *et al.* “Fast and sensitive GCaMP calcium indicators for imaging neural populations”. In: *Biorxiv* (2021).

[22] L. A. Gunaydin, L. Grosenick, J. C. Finkelstein, I. V. Kauvar, L. E. Fenno, A. Adhikari, S. Lammel, J. J. Mirzabekov, R. D. Airan, K. A. Zalocusky, *et al.* “Natural neural projection dynamics underlying social behavior”. In: *Cell* 157.7 (2014), pp. 1535–1551.

[23] Y. Fu, J. M. Tucciarone, J. S. Espinosa, N. Sheng, D. P. Darcy, R. A. Nicoll, Z. J. Huang, and M. P. Stryker. “A cortical circuit for gain control by behavioral state”. In: *Cell* 156.6 (2014), pp. 1139–1152.

[24] A. V. Kalueff, A. M. Stewart, and R. Gerlai. “Zebrafish as an emerging model for studying complex brain disorders”. In: *Trends in pharmacological sciences* 35.2 (2014), pp. 63–75.

[25] N. Vajente, R. Norante, P. Pizzo, and D. Pendin. “Calcium Imaging in Drosophila melanogaster”. In: *Calcium Signaling* (2020), pp. 881–900.

[26] F. Helmchen, K. Imoto, and B. Sakmann. “Ca2+ buffering and action potential-evoked Ca2+ signaling in dendrites of pyramidal neurons”. In: *Biophysical journal* 70.2 (1996), pp. 1069–1081.

[27] H. J. Koester and B. Sakmann. “Calcium dynamics associated with action potentials in single nerve terminals of pyramidal cells in layer 2/3 of the young rat neocortex”. In: *The Journal of physiology* 529.3 (2000), pp. 625–646.

[28] L. Theis, P. Berens, E. Froudarakis, J. Reimer, M. R. Rosón, T. Baden, T. Euler, A. S. Tolias, and M. Bethge. “Benchmarking spike rate inference in population calcium imaging”. In: *Neuron* 90.3 (2016), pp. 471–482.

[29] P. Zou, Y. Zhao, A. D. Douglass, D. R. Hochbaum, D. Brinks, C. A. Werley, D. J. Harrison, R. E. Campbell, and A. E. Cohen. “Bright and fast multicoloured voltage reporters via electrochromic FRET”. In: *Nature communications* 5.1 (2014), p. 4625.

[30] X. Meng, S. Ganapathy, L. van Roemburg, M. Post, and D. Brinks. “Voltage Imaging with Engineered Proton-Pumping Rhodopsins: Insights from the Proton Transfer Pathway”. In: *ACS Physical Chemistry Au* (2023).

[31] M. S. Siegel and E. Y. Isacoff. “A genetically encoded optical probe of membrane voltage”. In: *Neuron* 19.4 (1997), pp. 735–741.

[32] K. Ataka and V. A. Pieribone. “A genetically targetable fluorescent probe of channel gating with rapid kinetics”. In: *Biophysical journal* 82.1 (2002), pp. 509–516.

[33] R. Sakai, V. Repunte-Canonigo, C. D. Raj, and T. Knöpfel. “Design and characterization of a DNA-encoded, voltage-sensitive fluorescent protein”. In: *European Journal of Neuroscience* 13.12 (2001), pp. 2314–2318.

[34] D. Dimitrov, Y. He, H. Mutoh, B. J. Baker, L. Cohen, W. Akemann, and T. Knöpfel. “Engineering and characterization of an enhanced fluorescent protein voltage sensor”. In: *PloS one* 2.5 (2007), e440.

[35] W. Akemann, H. Mutoh, A. Perron, Y. K. Park, Y. Iwamoto, and T. Knöpfel. “Imaging neural circuit dynamics with a voltage-sensitive fluorescent protein”. In: *Journal of neurophysiology* 108.8 (2012), pp. 2323–2337.

[36] L. Jin, Z. Han, J. Platisa, J. R. Wooltorton, L. B. Cohen, and V. A. Pieribone. “Single action potentials and subthreshold electrical events imaged in neurons with a fluorescent protein voltage probe”. In: *Neuron* 75.5 (2012), pp. 779–785.

[37] H. H. Piao, D. Rajakumar, B. E. Kang, E. H. Kim, and B. J. Baker. “Combinatorial mutagenesis of the voltage-sensing domain enables the optical resolution of action potentials firing at 60 Hz by a genetically encoded fluorescent sensor of membrane potential”. In: *Journal of Neuroscience* 35.1 (2015), pp. 372–385.

[38] A. S. Abdelfattah, S. L. Farhi, Y. Zhao, D. Brinks, P. Zou, A. Ruangkittisakul, J. Platisa, V. A. Pieribone, K. Ballanyi, A. E. Cohen, *et al.* “A bright and fast red fluorescent protein voltage indicator that reports neuronal activity in organotypic brain slices”. In: *Journal of Neuroscience* 36.8 (2016), pp. 2458–2472.

[39] F. St-Pierre, J. D. Marshall, Y. Yang, Y. Gong, M. J. Schnitzer, and M. Z. Lin. “High-fidelity optical reporting of neuronal electrical activity with an ultrafast fluorescent voltage sensor”. In: *Nature neuroscience* 17.6 (2014), p. 884.

[40] S. Chamberland, H. H. Yang, M. M. Pan, S. W. Evans, S. Guan, M. Chavarha, Y. Yang, C. Salesse, H. Wu, J. C. Wu, *et al.* “Fast two-photon imaging of subcellular voltage dynamics in neuronal tissue with genetically encoded indicators”. In: *elife* 6 (2017), e25690.

[41] V. Villette, M. Chavarha, I. K. Dimov, J. Bradley, L. Pradhan, B. Mathieu, S. W. Evans, S. Chamberland, D. Shi, R. Yang, *et al.* “Ultrafast two-photon imaging of a high-gain voltage indicator in awake behaving mice”. In: *Cell* 179.7 (2019), pp. 1590–1608.

[42] Z. Liu, X. Lu, V. Villette, Y. Gou, K. L. Colbert, S. Lai, S. Guan, M. A. Land, J. Lee, T. Assefa, *et al.* “Sustained deep-tissue voltage recording using a fast indicator evolved for two-photon microscopy”. In: *Cell* (2022).

[43] J. M. Kralj, D. R. Hochbaum, A. D. Douglass, and A. E. Cohen. “Electrical spiking in Escherichia coli probed with a fluorescent voltage-indicating protein”. In: *Science* 333.6040 (2011), pp. 345–348.

[44] B. Y. Chow, X. Han, A. S. Dobry, X. Qian, A. S. Chuong, M. Li, M. A. Henninger, G. M. Belfort, Y. Lin, P. E. Monahan, *et al.* “High-performance genetically targetable optical neural silencing by light-driven proton pumps”. In: *Nature* 463.7277 (2010), pp. 98–102.

[45] J. M. Kralj, A. D. Douglass, D. R. Hochbaum, D. Maclaurin, and A. E. Cohen. “Optical recording of action potentials in mammalian neurons using a microbial rhodopsin”. In: *Nature methods* 9.1 (2012), pp. 90–95.

[46] N. C. Flytzanis, C. N. Bedbrook, H. Chiu, M. K. Engqvist, C. Xiao, K. Y. Chan, P. W. Sternberg, F. H. Arnold, and V. Gradinaru. “Archaerhodopsin variants with enhanced voltage-sensitive fluorescence in mammalian and Caenorhabditis elegans neurons”. In: *Nature communications* 5.1 (2014), p. 4894.

[47] R. S. McIsaac, M. K. Engqvist, T. Wannier, A. Z. Rosenthal, L. Herwig, N. C. Flytzanis, E. S. Imasheva, J. K. Lanyi, S. P. Balashov, V. Gradinaru, *et al.* “Directed evolution of a far-red fluorescent rhodopsin”. In: *Proceedings of the National Academy of Sciences* 111.36 (2014), pp. 13034–13039.

[48] D. R. Hochbaum, Y. Zhao, S. L. Farhi, N. Klapoetke, C. A. Werley, V. Kapoor, P. Zou, J. M. Kralj, D. Maclaurin, N. Smedemark-Margulies, *et al.* “All-optical electrophysiology in mammalian neurons using engineered microbial rhodopsins”. In: *Nature methods* 11.8 (2014), pp. 825–833.

[49] K. D. Piatkevich, E. E. Jung, C. Straub, C. Linghu, D. Park, H.-J. Suk, D. R. Hochbaum, D. Goodwin, E. Pnevmatikakis, N. Pak, *et al.* “A robotic multidimensional directed evolution approach applied to fluorescent voltage reporters”. In: *Nature chemical biology* 14.4 (2018), pp. 352–360.

[50] L. Z. Fan, S. Kheifets, U. L. Böhm, H. Wu, K. D. Piatkevich, M. E. Xie, V. Parot, Y. Ha, K. E. Evans, E. S. Boyden, *et al.* "All-optical electrophysiology reveals the role of lateral inhibition in sensory processing in cortical layer 1". In: *Cell* 180.3 (2020), pp. 521–535.

[51] U. L. Böhm, Y. Kimura, T. Kawashima, M. B. Ahrens, S.-i. Higashijima, F. Engert, and A. E. Cohen. "Voltage imaging identifies spinal circuits that modulate locomotor adaptation in zebrafish". In: *Neuron* 110.7 (2022), pp. 1211–1222.

[52] H. Tian, H. C. Davis, J. D. Wong-Campos, L. Z. Fan, B. Gmeiner, S. Begum, C. A. Werley, G. B. Borja, H. Upadhyay, H. Shah, *et al.* "All-optical electrophysiology with improved genetically encoded voltage indicators reveals interneuron network dynamics in vivo". In: *bioRxiv* (2021).

[53] L. Z. Fan, D. K. Kim, J. H. Jennings, H. Tian, P. Y. Wang, C. Ramakrishnan, S. Randles, Y. Sun, E. Thadhani, Y. S. Kim, *et al.* "All-optical physiology resolves a synaptic basis for behavioral timescale plasticity". In: *Cell* (2023).

[54] Y. Gong, M. J. Wagner, J. Zhong Li, and M. J. Schnitzer. "Imaging neural spiking in brain tissue using FRET-opsin protein voltage sensors". In: *Nature communications* 5.1 (2014), p. 3674.

[55] Y. Gong, C. Huang, J. Z. Li, B. F. Grewe, Y. Zhang, S. Eismann, and M. J. Schnitzer. "High-speed recording of neural spikes in awake mice and flies with a fluorescent voltage sensor". In: *Science* 350.6266 (2015), pp. 1361–1366.

[56] C. Huang, J. R. Maxey, S. Sinha, J. Savall, Y. Gong, and M. J. Schnitzer. "Long-term optical brain imaging in live adult fruit flies". In: *Nature communications* 9.1 (2018), pp. 1–10.

[57] A. S. Abdelfattah, T. Kawashima, A. Singh, O. Novak, H. Liu, Y. Shuai, Y.-C. Huang, L. Campagnola, S. C. Seeman, J. Yu, *et al.* "Bright and photostable chemigenetic indicators for extended in vivo voltage imaging". In: *Science* 365.6454 (2019), pp. 699–704.

[58] A. S. Abdelfattah, R. Valenti, J. Zheng, A. Wong, K. Podgorski, M. Koyama, D. S. Kim, and E. R. Schreiter. "A general approach to engineer positive-going eFRET voltage indicators". In: *Nature Communications* 11.1 (2020), p. 3444.

[59] A. S. Abdelfattah, J. Zheng, A. Singh, Y.-C. Huang, D. Reep, G. Tsegaye, A. Tsang, B. J. Arthur, M. Rehorova, C. V. Olson, *et al.* "Sensitivity optimization of a rhodopsin-based fluorescent voltage indicator". In: *Neuron* 111.10 (2023), pp. 1547–1563.

[60] C. Stosiek, O. Garaschuk, K. Holthoff, and A. Konnerth. "In vivo two-photon calcium imaging of neuronal networks". In: *Proceedings of the National Academy of Sciences* 100.12 (2003), pp. 7319–7324.

[61] A. Birkner, C. H. Tischbirek, and A. Konnerth. "Improved deep two-photon calcium imaging in vivo". In: *Cell calcium* 64 (2017), pp. 29–35.

[62] N. G. Horton, K. Wang, D. Kobat, C. G. Clark, F. W. Wise, C. B. Schaffer, and C. Xu. "In vivo three-photon microscopy of subcortical structures within an intact mouse brain". In: *Nature photonics* 7.3 (2013), pp. 205–209.

[63] T. Wang and C. Xu. “Three-photon neuronal imaging in deep mouse brain”. In: *Optica* 7.8 (2020), pp. 947–960.

[64] D. Brinks, A. J. Klein, and A. E. Cohen. “Two-photon lifetime imaging of voltage indicating proteins as a probe of absolute membrane voltage”. In: *Biophysical journal* 109.5 (2015), pp. 914–921.

[65] D. Böttcher and U. T. Bornscheuer. “Protein engineering of microbial enzymes”. In: *Current opinion in microbiology* 13.3 (2010), pp. 274–282.

[66] R. J. Kazlauskas and U. T. Bornscheuer. “Finding better protein engineering strategies”. In: *Nature chemical biology* 5.8 (2009), pp. 526–529.

[67] Y. Gong, J. Z. Li, and M. J. Schnitzer. “Enhanced archaerhodopsin fluorescent protein voltage indicators”. In: *PLoS One* 8.6 (2013), e66959.

[68] S. Babakhanova, E. E. Jung, K. Namikawa, H. Zhang, Y. Wang, O. M. Subach, D. A. Korzhenevskiy, T. V. Rakitina, X. Xiao, W. Wang, *et al.* “Rapid directed molecular evolution of fluorescent proteins in mammalian cells”. In: *Protein Science* 31.3 (2022), pp. 728–751.

[69] M. Kannan, G. Vasan, C. Huang, S. Haziza, J. Z. Li, H. Inan, M. J. Schnitzer, and V. A. Pieribone. “Fast, in vivo voltage imaging using a red fluorescent indicator”. In: *Nature methods* 15.12 (2018), pp. 1108–1116.

[70] M.-P. Chien, D. Brinks, G. Testa-Silva, H. Tian, F. Phil Brooks III, Y. Adam, B. Bloxham, B. Gmeiner, S. Kheifets, and A. E. Cohen. “Photoactivated voltage imaging in tissue with an archaerhodopsin-derived reporter”. In: *Science advances* 7.19 (2021), eabe3216.

[71] A. Silapetere, S. Hwang, Y. Hontani, R. G. Fernandez Lahore, J. Balke, F. V. Escobar, M. Tros, P. E. Konold, R. Matis, R. Croce, *et al.* “QuasAr Odyssey: the origin of fluorescence and its voltage sensitivity in microbial rhodopsins”. In: *Nature communications* 13.1 (2022), p. 5501.

[72] M. Drobizhev, N. S. Makarov, S. E. Tillo, T. E. Hughes, and A. Rebane. “Two-photon absorption properties of fluorescent proteins”. In: *Nature methods* 8.5 (2011), pp. 393–399.

[73] X. Meng, L. Huismans, T. Huijben, G. Szabo, R. Van Tol, I. De Heer, S. Ganapathy, and D. Brinks. “A compact microscope for voltage imaging”. In: *Journal of Optics* 24.5 (2022), p. 054004.

[74] K. He, G. Gkioxari, P. Dollár, and R. Girshick. “Mask r-cnn”. In: *Proceedings of the IEEE international conference on computer vision*. 2017, pp. 2961–2969.

[75] T.-Y. Lin, M. Maire, S. Belongie, J. Hays, P. Perona, D. Ramanan, P. Dollár, and C. L. Zitnick. “Microsoft coco: Common objects in context”. In: *Computer Vision–ECCV 2014: 13th European Conference, Zurich, Switzerland, September 6-12, 2014, Proceedings, Part V 13*. Springer. 2014, pp. 740–755.

[76] K. He, X. Zhang, S. Ren, and J. Sun. “Deep residual learning for image recognition”. In: *Proceedings of the IEEE conference on computer vision and pattern recognition*. 2016, pp. 770–778.

[77] Z. Deng, H. Sun, S. Zhou, J. Zhao, L. Lei, and H. Zou. “Multi-scale object detection in remote sensing imagery with convolutional neural networks”. In: *ISPRS journal of photogrammetry and remote sensing* 145 (2018), pp. 3–22.

[78] L. You, P.-R. Su, M. Betjes, R. G. Rad, T.-C. Chou, C. Beerens, E. van Oosten, F. Leufkens, P. Gasecka, M. Muraro, *et al.* “Linking the genotypes and phenotypes of cancer cells in heterogenous populations via real-time optical tagging and image analysis”. In: *Nature Biomedical Engineering* 6.5 (2022), pp. 667–675.

[79] S. Pertuz, D. Puig, and M. A. Garcia. “Analysis of focus measure operators for shape-from-focus”. In: *Pattern Recognition* 46.5 (2013), pp. 1415–1432.

[80] K. G. Larkin. “Reflections on shannon information: In search of a natural information-entropy for images”. In: *arXiv preprint arXiv:1609.01117* (2016).

[81] P. Thomas and T. G. Smart. “HEK293 cell line: a vehicle for the expression of recombinant proteins”. In: *Journal of pharmacological and toxicological methods* 51.3 (2005), pp. 187–200.

7

CONCLUSION AND OUTLOOK

7.1. CONCLUSION

As the name implies, optogenetics requires optics and genetics to work together. My work in this dissertation aims to advance optogenetics from these two directions, more specifically from aspects of microscope platform development and protein engineering.

In optogenetics, we read out neuron activities through fluorescence. Management of photon budget in optogenetics experiments, especially in voltage imaging, is crucial because of issues such as photobleaching and heating ablation *in vivo*. The ability to pattern the excitation light in space, time, and spectrum is required to rationalize the photon influx. Delivering photons with sub-micrometer spatial and sub-millisecond temporal resolution would avoid unwanted excitation in the background or at the wrong time, and significantly improve the signal-to-noise ratio. Another way to benefit the photon budget is to use nonlinear two-photon excitation, which dramatically decreases the out-of-focus autofluorescence and scattering. In Chapter 2, we introduced the development and performance of a multimodal microscope that combines these features. The microscope employs a rotational motor, which can change the direction of the objective. This easy switch between inverted and upright configurations extends the microscope application to both *in vitro* and *in vivo*.

To fully realize the potential of this setup for voltage imaging, my focus shifted from optical engineering to software engineering to develop advanced software, as introduced in Chapter 3. The user-friendly software enables straightforward experiment configuration and provides real-time data analysis to provide feedback. Its modular organization offers great flexibility, editability, and extensibility for future development.

After the hardware and software were set, we started to explore the potential of different rhodopsins. We first investigated a novel rhodopsin family called heliorhodopsin, which differs from the existing type I and type II rhodopsins. This rhodopsin family has many unique features, such as inverted insertion, and is speculated to have a sensory or

signaling role. We carried out the preliminary characterization of Helios in *E.coli* first and discovered that it displayed pH-dependent fluorescence. Then Helios was expressed in HEK293T cells, and we characterized its fluorescence brightness, photostability, voltage sensitivity, and kinetics. Helios in HEK cells showed a mild voltage sensitivity and fast kinetics, which makes it a potential template for future GEVI engineering. We further targeted the retinal binding pocket and tested several mutants along this location. One mutant, S237A, displayed a higher fluorescence and greatly improved voltage detection SNR. This work demonstrated that Helios, different from the other proton pump-based GEVIs, has the potential to report membrane potentials, and its performance can be further improved by bioengineering.

We then looked at comparatively bright proton-pumping rhodopsin, *Gloeobacter violaceus* rhodopsin (GR), which shares a similar structure with the popular template Archaerhodopsin-3 (Arch3). This rhodopsin was engineered to present a red-shifted absorption and showed a higher fluorescence in neurons than Arch3[1, 2]. Through patch clamp characterization, we found that it has outstanding voltage sensitivity, fast kinetics, and a relatively large photocurrent. GR also has bright fluorescence under red illumination, measured by high-throughput screening. All these properties make GR a promising platform for optogenetics. Specifically, we aimed to engineer GR as a GEVI and a light-triggered silencer. We used site-directed mutagenesis to mutate hot spots across the protein and studied the performance of these mutants. The mutation at the counterion increases the brightness but decreases the voltage sensitivity while demolishing the photocurrent, providing a good starting point as a GEVI. Some mutations at the proton release region display a huge voltage sensitivity (ΔF / F_0 up to 367% across 100 mV) that has never been reported before. Even if the response speed is compromised (50 to 70 ms), these mutants provide a novel option for cases when high voltage sensitivity is needed. In the end, we proposed GEVI candidates with distinguishing features: generic usage, high sensitivity, and high brightness. By mutating the proton release region, we also found one mutant that exhibits a 20-times larger photocurrent than the wild-type with fast kinetics. Having a larger photocurrent than the late Arch-based silencer, it is a promising tool to silence neuron activities under red illumination.

For *in vivo* optogenetics, it is more beneficial to use two-photon excitation, while current microbial rhodopsin-based GEVIs are not developed directly under two-photon excitation. We developed a pipeline to evolve the two-photon brightness of QuasAr1 under nonlinear excitation. The screening process is automated through the programmed software, which is also in charge of the analysis employing machine learning for cell segmentation. At the end of the screening, cells with the highest score measuring membrane trafficking, expression-normalized and membrane-localized fluorescence under 1200 nm excitation are picked up and sequenced. In two rounds of evolution, mutants have an increase in two-photon fluorescence of 75% and 30%, respectively, without losing the 2P sensitivity.

7.2. OUTLOOK

Like our Octoscope is designed for both *in vitro* and *in vivo* experiments, the future development of these projects can be divided into these two aspects: *in vitro* protein engineering and advancing *in vivo* optics for optogenetics. These two aspects will work together to improve the SNR of optogenetics readout from both the sample and acquisition sides. In terms of *in vivo* studies, novel actuators will create new possibilities, and the development of microscopes will approach a more gentle way to observe behaviors.

7.2.1. HIGH-THROUGHPUT MICROBIAL RHODOPSIN MINING

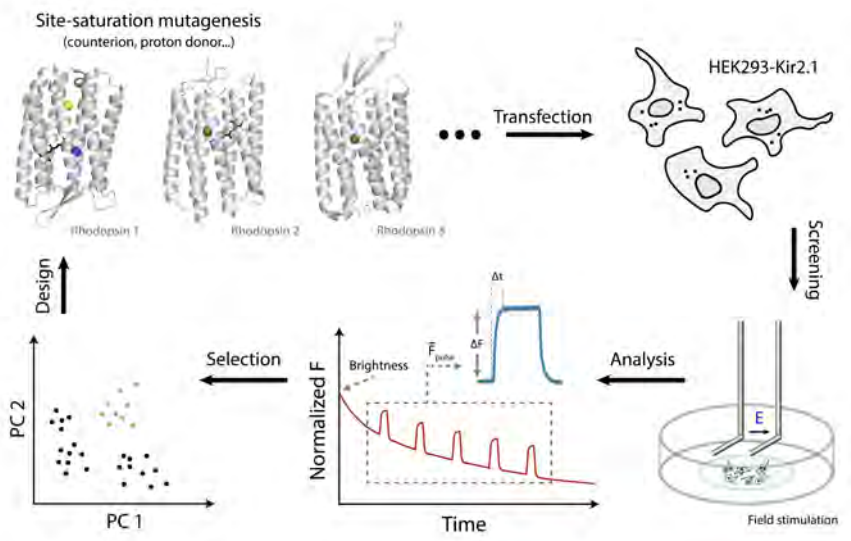

Figure 7.1: Ideal pipeline for high-throughput rhodopsin discovering.

Microbial rhodopsin has an abundant and diverse phylogenetic tree, and it keeps expanding as new members are discovered in lakes and the oceans[3, 4]. On the other hand, only a handful of rhodopsins are characterized in optogenetics scenarios. In Chapter 4 and 5, we explored the potentials of two microbial rhodopsins to function as optogenetics tools, and they displayed decent performance. It is promising to expand our knowledge of the functions of these biochemical machinery in the context of optogenetics.

Based on our accumulating understanding of the functional sites in rhodopsins and hotspots that affect optogenetics performance, the engineering approach combining site-saturation mutagenesis and automated screening will be the most efficient way towards directed evolution. This entails a high-throughput, video-based pipeline to char-

acterize the optical-electrophysiology parameters of rhodopsins.

To realize that, we need to set up biological pipelines, and our screening platform needs minor hardware additions and software upgrades. Novel cloning methods can speed up the sample preparation process, as introduced in previous studies[5]. To be able to extract sensitivity information from a single acquisition, an active biological system is needed, such as HEK293 cells expressing Kir2.1 channels[6]. In these cells, electric field stimulation (EFS) is able to evoke depolarization spikes, and by analyzing the capturing video parameters of the tested mutants, such as brightness, voltage sensitivity, and kinetics can be computed[7, 8]. Regarding the photocurrent, we could predict with good confidence whether the mutations will eliminate the photocurrent (such as mutations involving counterion and its vicinity, combinations at the retinal binding pocket, and drastic changes at functional sites such as proton donor and proton release sites). Patch clamp experiments can always be applied to verify parameters, including the photocurrent.

Further developments in machine learning and MD simulations will likely make it possible to reconstruct a whole time-scale MD simulation model for *in silico* GEVI engineering[9]. Recently, *in silico* simulations have demonstrated their complementary ability to decipher the fluorescent and voltage-sensitive mechanisms of rhodopsins[10, 11]. This would provide insight into the rational design and speed up the screening process.

In an ideal GEVI evolving pipeline, we first select some potential rhodopsin templates based on the polygenic tree and literature studies on functionalities and structures. Then we select crucial targeting sites that might cause a drastic change in its optogenetics performance, such as the counterion, the proton donor, and the proton release site in proton pumps or equivalent in other ion pumps/channels. In the sample preparation stage, site-saturation mutagenesis is performed on these sites and cloned into the HEK cells expressing Kir2.1 channels. The cells are then plated on a 96-well plate or petri dish and put onto the Octoscope. The screening section follows up, which will first take an image in the tag-protein channel and then record a video of the red-channel fluorescence while applying EFS. In the post-processing stage, key parameters of the tested mutants are extracted and compared. These data will help to guide the mutagenesis in the next round.

7.2.2. IMPROVING THE OCTOSCOPE FOR VOLTAGE IMAGING

The Octoscope has the ability to point its objective in any direction and performs 2P contour scanning along a predesigned route as demonstrated in Chapter 2. This permits future *in vivo* 2P GEVI readout applications, such as contour recording jumping between a group of neurons in head-fixed mice on a treadmill.

For future development, different techniques can be applied to improve the SNR, increase the scanning speed, add z-scan ability, and be more efficient in the photon budget. The low-hanging fruit in improving the system SNR is to run a power spectral density

(PSD) analysis over the signals to pinpoint and filter the noise. A bandwidth test over the system also helps to map the frequency response, guiding future sampling rate choice.

The rest can go in two directions: adapting the patterning technique and adapting the laser source. In terms of scanning patterning techniques, mechanical ways such as resonant scanners and non-mechanically constricted ways like acousto-optic deflector (AOD) offer much faster scanning speeds compared to galvanometer scanners. Adding or replacing one or both existing galvo axes will significantly increase the 2D raster scanning throughput, ideally to kilohertz, which matches the time resolution provided by GEVIs. Scanless patterning methods such as temporal focusing is another intriguing technique but would require more reconstruction on the Octoscope[12].

The neurons have a highly complex 3D structure, so it is important to add the rapid z-focus adjusting functionality to the Octoscope for future *in vivo* studies. Compared to moving the objective motor directly to adjust the focus mechanically, it is much faster to do so in scanning techniques such as remote focusing.

Remote focusing is generally realized by altering the wavefront at the conjugated plane to the back focal plane of the objective; or to the sample plane after the objective. Phase change can be introduced at the Fourier plane through an electrically tuneable lens (ETL)[13], a deformable mirror (DM)[14], or a tunable acoustic gradient index of refraction lens (TAG)[15]. A pair of AODs can also realize both lateral and axial scanning[16], and holographic multiplexing of AODs can realize 3D kilohertz random-access volumetric imagin[5, 17]. To induce a change at the conjugated plane of the specimen, a second objective is employed, and a mirror is placed at the focal plane of this objective[18]. By moving this mirror along the optical axis or converting to a faster lateral scanning way, the focus at the imaging objective will change accordingly[19].

During the above-mentioned scanning approaches, the probing laser spot spends most of the time in the background instead of landing on neurons, which costs the imaging speed and generates more heat in the tissue. In our setup, it is possible to first acquire a neuron distribution map and then plan the contour scanning route that passes neurons of interest. The scanning speed can be further improved by accommodating non-mechanical scanning approaches such AOD, as discussed above. As GEVIs require high-power laser excitation, it is desired to "turn off" the excitation outside the cellular region to minimize the heating. With mechanical approaches, spending time moving the focus from spot to spot is inevitable. Adapting the laser excitation to the sample, for example, using a beam blanker, can reduce the average power pumping into the sample; Adapting the laser pulse reputation rate is an even better approach as it requires much less (and thus practical) laser output power[20].

Ideally, the optogenetics observation should have minimal disturbance on the animals during the paradigms. With this goal in mind, approaches such as miniscope are developed, which allow both 1P and 2P optogenetics recording in behaving animals[21–25]. To extend the usability of the Octoscope in freely moving animals, the fiber-based endoscope is an appealing option. In a typical configuration, the scanners and the objective

are placed before the fiber bundle; thus, no miniaturizing scanning system is needed[26, 27]. Recently, a 2P temporal focusing endoscope performed calcium imaging and holographic photostimulation in a freely moving mouse[28]. Extra work on the Octoscope conversion includes beam size adjustment, fiber and gradient-index (GRIN) lens setup.

7.2.3. FURTHER DEVELOPMENT AND APPLICATION OF THE SCREENING ASSAY

The 2P screening pipeline in Chapter 6 successfully carried out rounds of brightness evolution, and the low-hanging improvements are discussed in section 6.4. In this section, further steps will be discussed.

Flow cytometry is a high-throughput measuring method, and FACS has been used at different stages in the 1P evolution process[29, 30]. Since evolution in 2P is novel, direct use of 2P flow cytometry has not been applied in 2P screening yet. 2P flow cytometry is a relatively new topic and has been implemented in ways such as scanning airy beams[31, 32]. For the purpose of 2P brightness screening, a 2P FACS would be very useful to serve as a binary sorter. The threshold can be set to different levels, for example, higher than noise level as a pre-screening measure to exclude non-fluorescent mutants or higher than wild-type to include only mutants with improved brightness. Providing uniform and sufficient 2P illumination and expressing normalization might be a challenge. Temporal focusing might be a candidate to place the laser excitation or holographic cytometry[33], and for expressing normalization, a second wavelength is needed, or it is not a concern at the pre-screening stage. After 2P FACS, the population of investigation should shrink significantly.

Genetically encoded neurotransmitter sensors are gaining more attention as a powerful tool to decipher neuron communication. One potential issue with these glutamate, dopamine, or acetylcholine sensors is that they are not bright or fast enough and that they were not developed under 2P excitation[34]. Even for the more developed calcium indicators, optimization towards 2P performance is limited to spectra tunning[35]. The automated screening platform in our lab is equipped with a perfusion system, which allows the development of a screening pipeline to optimize the performance of genetically encoded neurotransmitter sensors.

REFERENCES

[1] M. K. Engqvist, R. S. McIsaac, P. Dollinger, N. C. Flytzanis, M. Abrams, S. Schor, and F. H. Arnold. "Directed evolution of Gloeobacter violaceus rhodopsin spectral properties". In: *Journal of molecular biology* 427.1 (2015), pp. 205–220.

[2] K. Kojima, R. Kurihara, M. Sakamoto, T. Takanashi, H. Kuramochi, X. M. Zhang, H. Bito, T. Tahara, and Y. Sudo. "Comparative studies of the fluorescence properties of microbial rhodopsins: spontaneous emission versus photointermediate fluorescence". In: *The Journal of Physical Chemistry B* 124.34 (2020), pp. 7361–7367.

[3] K. Inoue, S. Ito, Y. Kato, Y. Nomura, M. Shibata, T. Uchihashi, S. P. Tsunoda, and H. Kandori. "A natural light-driven inward proton pump". In: *Nature Communications* 7.1 (2016), p. 13415.

[4] A. Pushkarev, K. Inoue, S. Larom, J. Flores-Uribe, M. Singh, M. Konno, S. Tomida, S. Ito, R. Nakamura, S. P. Tsunoda, *et al.* "A distinct abundant group of microbial rhodopsins discovered using functional metagenomics". In: *Nature* 558.7711 (2018), pp. 595–599.

[5] V. Villette, M. Chavarha, I. K. Dimov, J. Bradley, L. Pradhan, B. Mathieu, S. W. Evans, S. Chamberland, D. Shi, R. Yang, *et al.* "Ultrafast two-photon imaging of a high-gain voltage indicator in awake behaving mice". In: *Cell* 179.7 (2019), pp. 1590–1608.

[6] Z. Liu, X. Lu, V. Villette, Y. Gou, K. L. Colbert, S. Lai, S. Guan, M. A. Land, J. Lee, T. Assefa, *et al.* "Sustained deep-tissue voltage recording using a fast indicator evolved for two-photon microscopy". In: *Cell* (2022).

[7] H. Tsutsui, Y. Jinno, A. Tomita, and Y. Okamura. "Rapid evaluation of a protein-based voltage probe using a field-induced membrane potential change". In: *Biochimica et Biophysica Acta (BBA)-Biomembranes* 1838.7 (2014), pp. 1730–1737.

[8] Y. Zhang, M. Rózsa, Y. Liang, D. Bushey, Z. Wei, J. Zheng, D. Reep, G. J. Broussard, A. Tsang, G. Tsegaye, *et al.* "Fast and sensitive GCaMP calcium indicators for imaging neural populations". In: *Nature* (2023), pp. 1–8.

[9] I. D. Lutz, S. Wang, C. Norn, A. J. Borst, Y. T. Zhao, A. Dosey, L. Cao, Z. Li, M. Baek, N. P. King, *et al.* "Top-down design of protein nanomaterials with reinforcement learning". In: *bioRxiv* (2022), pp. 2022–09.

[10] A. Silapetere, S. Hwang, Y. Hontani, R. G. Fernandez Lahore, J. Balke, F. V. Escobar, M. Tros, P. E. Konold, R. Matis, R. Croce, *et al.* “QuasAr Odyssey: the origin of fluorescence and its voltage sensitivity in microbial rhodopsins”. In: *Nature communications* 13.1 (2022), p. 5501.

[11] R. Palombo, L. Barneschi, L. Pedraza-González, D. Padula, I. Schapiro, and M. Olivucci. “Retinal chromophore charge delocalization and confinement explain the extreme photophysics of Neorhodopsin”. In: *Nature Communications* 13.1 (2022), p. 6652.

[12] E. Papagiakoumou, E. Ronzitti, and V. Emiliani. “Scanless two-photon excitation with temporal focusing”. In: *Nature Methods* 17.6 (2020), pp. 571–581.

[13] B. Berge and J. Peseux. “Variable focal lens controlled by an external voltage: An application of electrowetting”. In: *The European Physical Journal E* 3 (2000), pp. 159–163.

[14] L. J. Hornbeck. “Deformable-mirror spatial light modulators”. In: *Spatial Light Modulators and Applications III*. Vol. 1150. Spie. 1990, pp. 86–103.

[15] M. Duocastella, B. Sun, and C. B. Arnold. “Simultaneous imaging of multiple focal planes for three-dimensional microscopy using ultra-high-speed adaptive optics”. In: *Journal of Biomedical Optics* 17.5 (2012), pp. 050505–050505.

[16] W. Akemann, S. Wolf, V. Villette, B. Mathieu, A. Tangara, J. Fodor, C. Ventalon, J.-F. Léger, S. Dieudonné, and L. Bourdieu. “Fast optical recording of neuronal activity by three-dimensional custom-access serial holography”. In: *Nature Methods* 19.1 (2022), pp. 100–110.

[17] G. Katona, G. Szalay, P. Maák, A. Kaszás, M. Veress, D. Hillier, B. Chiovini, E. S. Vizi, B. Roska, and B. Rózsa. “Fast two-photon in vivo imaging with three-dimensional random-access scanning in large tissue volumes”. In: *Nature methods* 9.2 (2012), pp. 201–208.

[18] E. J. Botcherby, C. W. Smith, M. M. Kohl, D. Débarre, M. J. Booth, R. Juškaitis, O. Paulsen, and T. Wilson. “Aberration-free three-dimensional multiphoton imaging of neuronal activity at kHz rates”. In: *Proceedings of the National Academy of Sciences* 109.8 (2012), pp. 2919–2924.

[19] T. Chakraborty, B. Chen, S. Daetwyler, B.-J. Chang, O. Vanderpoorten, E. Sapoznik, C. F. Kaminski, T. P. Knowles, K. M. Dean, and R. Fiolka. “Converting lateral scanning into axial focusing to speed up three-dimensional microscopy”. In: *Light: Science & Applications* 9.1 (2020), p. 165.

[20] B. Li, C. Wu, M. Wang, K. Charan, and C. Xu. “An adaptive excitation source for high-speed multiphoton microscopy”. In: *Nature methods* 17.2 (2020), pp. 163–166.

[21] O. Skocek, T. Nöbauer, L. Weilguny, F. Martınez Traub, C. N. Xia, M. I. Molodtsov, A. Grama, M. Yamagata, D. Aharoni, D. D. Cox, *et al.* “High-speed volumetric imaging of neuronal activity in freely moving rodents”. In: *Nature methods* 15.6 (2018), pp. 429–432.

[22] W. Zong, H. A. Obenhaus, E. R. Skytøen, H. Eneqvist, N. L. de Jong, R. Vale, M. R. Jorge, M.-B. Moser, and E. I. Moser. “Large-scale two-photon calcium imaging in freely moving mice”. In: *Cell* 185.7 (2022), pp. 1240–1256.

[23] N. Accanto, F. G. Blot, A. Lorca-Cámara, V. Zampini, F. Bui, C. Tourain, N. Badt, O. Katz, and V. Emiliani. “A flexible two-photon fiberscope for fast activity imaging and precise optogenetic photostimulation of neurons in freely moving mice”. In: *Neuron* 111.2 (2023), pp. 176–189.

[24] J. R. Scherrer, G. F. Lynch, J. J. Zhang, and M. S. Fee. “An optical design enabling lightweight and large field-of-view head-mounted microscopes”. In: *Nature Methods* (2023), pp. 1–4.

[25] J. Zhang, R. N. Hughes, N. Kim, I. P. Fallon, K. Bakhurin, J. Kim, F. P. U. Severino, and H. H. Yin. “A one-photon endoscope for simultaneous patterned optogenetic stimulation and calcium imaging in freely behaving mice”. In: *Nature Biomedical Engineering* (2022), pp. 1–12.

[26] B. N. Ozbay, G. L. Futia, M. Ma, V. M. Bright, J. T. Gopinath, E. G. Hughes, D. Restrepo, and E. A. Gibson. “Three dimensional two-photon brain imaging in freely moving mice using a miniature fiber coupled microscope with active axial-scanning”. In: *Scientific reports* 8.1 (2018), pp. 1–14.

[27] V. Szabo, C. Ventalon, V. De Sars, J. Bradley, and V. Emiliani. “Spatially selective holographic photoactivation and functional fluorescence imaging in freely behaving mice with a fiberscope”. In: *Neuron* 84.6 (2014), pp. 1157–1169.

[28] N. Accanto, F. G. Blot, A. Lorca-Cámara, V. Zampini, F. Bui, C. Tourain, N. Badt, O. Katz, and V. Emiliani. “A flexible two-photon fiberscope for fast activity imaging and precise optogenetic photostimulation of neurons in freely moving mice”. In: *Neuron* (2022).

[29] K. D. Piatkevich, E. E. Jung, C. Straub, C. Linghu, D. Park, H.-J. Suk, D. R. Hochbaum, D. Goodwin, E. Pnevmatikakis, N. Pak, *et al.* “A robotic multidimensional directed evolution approach applied to fluorescent voltage reporters”. In: *Nature chemical biology* 14.4 (2018), pp. 352–360.

[30] H. Tian, H. C. Davis, J. D. Wong-Campos, P. Park, L. Z. Fan, B. Gmeiner, S. Begum, C. A. Werley, G. B. Borja, H. Upadhyay, *et al.* “Video-based pooled screening yields improved far-red genetically encoded voltage indicators”. In: *Nature Methods* (2023), pp. 1–13.

[31] C. F. Zhong, E. R. Tkaczyk, T. Thomas, J. Y. Ye, A. Myc, A. U. Bielinska, Z. Cao, I. Majoros, B. Keszler, J. R. Baker Jr, *et al.* “Quantitative two-photon flow cytometry—in vitro and in vivo”. In: *Journal of biomedical optics* 13.3 (2008), pp. 034008–034008.

[32] A. Paez, E. M. Sundin, G. Navarro, X. Li, T. Boland, and C. Li. “Two-photon flow cytometry with laser scanning two-dimensional airy beams”. In: *Optics Communications* 508 (2022), p. 127804.

[33] Z. Wang, V. Bianco, P. L. Maffettone, and P. Ferraro. “Holographic flow scanning cytometry overcomes depth of focus limits and smartly adapts to microfluidic speed”. In: *Lab on a Chip* (2023).

[34] J. S. Marvin, B. Scholl, D. E. Wilson, K. Podgorski, A. Kazemipour, J. A. Müller, S. Schoch, F. J. U. Quiroz, N. Rebola, H. Bao, *et al.* “Stability, affinity, and chromatic variants of the glutamate sensor iGluSnFR”. In: *Nature methods* 15.11 (2018), pp. 936–939.

[35] M. A. Mohr, D. Bushey, A. Aggarwal, J. S. Marvin, J. J. Kim, E. J. Marquez, Y. Liang, R. Patel, J. J. Macklin, C.-Y. Lee, *et al.* “jYCaMP: an optimized calcium indicator for two-photon imaging at fiber laser wavelengths”. In: *Nature methods* 17.7 (2020), pp. 694–697.

ACKNOWLEDGEMENTS

First of all, I would like to express my gratitude to Daan for giving me this amazing opportunity. It begins with an advertisement online on Optogenetics that caught my eye in late 2017. On the 15th of July 2018, I started in the Brinks lab as the first PhD student. Since then, 5 years have passed, and I surely enjoyed this journey and grew a LOT with the Brinks lab! All the skills, experience, and ideas about science I learnt in the last five years are priceless. Dankjewel Daan! Second, I would like to thank Srividya Ganapathy (Vija), my best colleague in the lab and my sister from another mom. The first question I got from you is whether I need a guided shopping tour in the supermarket, which I rejected. I have paid the price of shopping by figuring out product photos for a couple of years. In these years, our friendship has deepened tremendously, and our scientific research has led to fruitful results. We travelled together, went to events together; and during COVID, we biked from the lab to your place for lunch and spent a significant amount of time at these two places. Shukriyaa Vija, and looking forward to your exciting research achievement at UC San Diego! Next, I would like to thank Marco Locarno, not only the second PhD in the group but also my dearest housemate and bestie. We had so much fun together, especially during the year when we lived in the same house. We cooked for each other, learnt each other's culture, watched TV together, fed the neighbour's cats, took the same course online at the same table, and celebrated Christmas and new year together. We visited your hometown and your parents, and I slept on your bunker bed where you grew up. Thank you, Marco Locarno, for the company during my PhD, and you will shine in your teaching career! Next, I would like to thank the third PhD student in the lab, Zhenzhen Wu, who sometimes is called Zenzen. You always bring me back the good memories of China, especially of food. I was always impressed by the dishes you made when our friends gathered at your place. You always provide me with snacks from your rich snack stock, and those are perfect for the tea break chats. We did a lot of fun activities together, and I can't forget your face captured by the camera on the ride in Efteling, which can be found on our lab website. Thank you again Zhenzhen, and I wish you all the best with the rest of your PhD! Thank you Qiangrui, I enjoyed the chats and talks we had about everything, as well as the time when we were sitting together patching neurons, although sometimes frustrated, giving us spikes of excitement. Thank you, Marco Post, with whom I worked for more than a year, from your master to now a PhD rising star. Thank you for all the help you provided in the projects, and for your tricks and tips on efficient budgeting in the Netherlands. Looking forward to visiting your farm one day! Thank you, Rui Silva, for your insights during the discussions and your amazing bacalhau fish cakes! Thank you Leonie Gouweleeuw, who was the lab technician at the

Lab website: https://www.brinkslab.org/

start, for all the help you provided for us in the lab, and we had great fun in the lab socials. Wish you success in your current position in CCD! Thank you, Huma Safdar, who worked after Leonie to help us in the lab. Huma, you cooked amazing food and always brought them to share with us, I really appreciate it. Best wishes to you, your adorable kids, and your family! Thank you, Apilena Sapioper, for your support in our lab and your great food! Thank you, Mariska Ouwehand and Selina Teurlings, our current biotechnicians in the lab, for keeping everything running smoothly and facilitating our projects! Thank you, Alejandro, Laurens, Lars, it is fun to work and discuss with you in the lab, and hang out in the lab socials, I enjoyed our paintball event! Thank you Ian and Didier, our assistant technicians, for helping out in the lab! Thank you, Gréta, Teun, Lex, Duran, Douwe, Sabine, Hina, Izak, Mels, Delizzia, Martijn, Hilke, Florine, Thieme, Thijs, Polina, Jordan, Robin, and all the other people who spent time in the Brinks lab, you are all a necessary part of the research that we have done, and part of my fun PhD journey.

My last five years won't be the same without everyone in the MINT group. Our closest collaborator in MINT is the Zebrafish Development Lab from Elizabeth Carroll. I am impressed by the work in the Carroll lab and always enjoyed the insightful discussions with Elizabeth. We both learnt for the first time from your PhD and postdoc that you should eat your own whole pizza during the lab dinner. Wish you great success in your new position in the States! Thank you, Nicolò Giovanni Ceffa, our dearest N.G.C. who was the postdoc in Carroll lab. I won't be the same person today without you. We didn't really talk to each other until almost half a year later, but since then, we bonded with each other immediately. Inside the lab, both with an optics background and working with Optogenetics, we shared ideas and helped each other. Outside the lab, you helped me adapt to a very different society, starting from how to properly cook pasta, risotto, etc. We had tons of fun together, playing basketball, playing games, binge-watching together, giving each other creative gifts, and visiting places, including a visit to the Ceffa family in Italy. Wish you success in your postdoc research at MRC Cambridge and lovely pranks on your friends there! Thank you, Laura Maddalena, who was the PhD student in the Carroll lab and one of the interviewers in my PhD application interview. During these years, we exchanged and discussed ideas, and you helped me a lot with zebrafish-related experiments. You organized and contributed a ton (of amazing food) to our social events. You (tried to) taught us how to make ravioli and gnocchi, it's a pity that I only remember the taste. Thank you Laura, and wish you success in your postdoc at IIT! Thank you Arent Kievits for the fun talks and knowledge about the Netherlands, really appreciate your contributions to our socials! Thank you, Bas van der Hoeven and Musa Kalkan, I enjoyed our INT team game nights and junk food dinners, they remind me of my past messy but fun college life. Thank you Nahum, Bregje, Tessa, Bram, and other members of the Carroll lab, I treasure the fun times we spent together.

Thank you Jacob Hoogenboom, my promotor, for the support and valuable discussions in these years. Thank you Kees Hagen, Pieter Kruit, and other PIs in the MINT group for your questions and suggestions during my MINT presentations. Thank you Ryan Lane, your victory on setting the noodle\spaghetti debate shall be passed on. Thank you Aya Maghoub, I will miss the food and snacks you brought us, and I am proud to be your paranymph! Thank you Cristiano Glessi, it is always fun to talk to you, especially

when we are both dressed in Uniqlo. Thank you Yoram Vos and Mathijs Garming, It is fun to learn uncommon technical Dutch words from you. Thank you, Ruud van Tol, Johan van der Cingel, Han van der Linden, Paul Keijzer, and Carel Heerkens, the almighty technicians in the MINT group; without your help, my projects wouldn't be possible. Thank you our secretary Anjella van Vliet for helping and arranging things for me, you made our lives easier. Thank you Mike Simons, Myron Hensgens, Maurice Krielaart, Xiaoli Guo, Serey Loginov, Kerim Arat, Gaudaman Jeevanandam, Aditi Srinivasa, Sangeetha Hari, and the rest of the MINT group, I enjoyed the coffee\cake breaks and pleasant chats in these years.

Lieve Jillian Zwemmer, thank you for your enormous love and support over the past few years! My life wouldn't be the same without your sweetest and kindest influence. Thank you for the great effort in proofreading, correcting this dissertation, translating parts to Dutch, a few strokes in the cover design, as well as suggestions on the propositions!!

Dankjewel Ron and Marjan, you give me a sweet family here in the Netherlands. I could not imagine any better papa and mama-in-law than you. Dankjewel Rob and Shaq, I enjoyed our time together in restaurants, museums, model shops, etc. Your house has always been my favorite place to visit.

Finally, my sincere gratitude to my parents, Jing and Xiangjun, who made an unbelievable amount of effort to support and offer me the best. 感謝我的父母，孟祥俊和張靜，多年以來的教導與養育之恩。你們為了我的成長與教育節衣縮食，把最好的都留給了我。正是有了你們的全力支持我才能來到荷蘭攻讀博士。再次衷心感謝！

CURRICULUM VITÆ

Xin MENG

12-10-1992 Born in Anhui, China.

EDUCATION

2011–2015 Bachelor of Physics

Northwest University, Xi'an, China
Optical Information Science And Technology

2015–2018 Master of Engineering

Jiangnan University, Wuxi, China
Optical Engineering and Computational Optics

2018–2023 PhD candidate

Delft University of Technology
Thesis: Novel microbial rhodopsins for optogenetics
Supervisor: Dr. Daan Brinks

WORK EXPERIENCE

2023- Signal & Image Processing Engineer
R&D, Nearfield Instruments, the Netherlands

LIST OF PUBLICATIONS

PUBLICATIONS DURING PHD

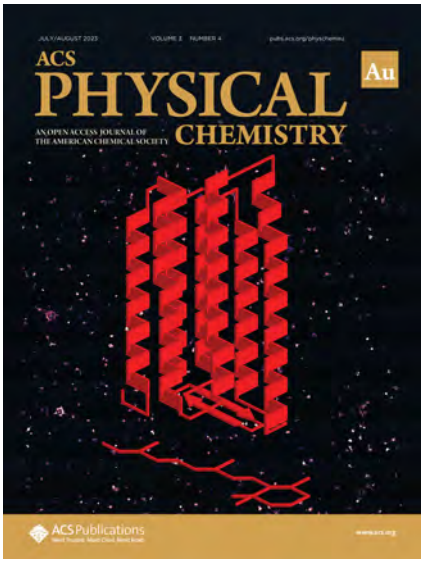

ACS Physical Chemistry Au, Volume 3, Issue 4

.

Meng, Xin, Lex Huismans, Teun Huijben, Greta Szabo, Ruud Van Tol, Izak De Heer, Srividya Ganapathy, and Daan Brinks. "A compact microscope for voltage imaging." *Journal of Optics* 24, no. 5 (2022): 054004. (Chapter 2 of this thesis.)

Meng, Xin*, Srividya Ganapathy*, Lars van Roemburg, Marco Post, and Daan Brinks. "Voltage Imaging with Engineered Proton-Pumping Rhodopsins: Insights from the Proton Transfer Pathway." *ACS Physical Chemistry Au* (2023). (Introduction of this thesis. Author contributions see footnote.)

Ganapathy, Srividya*, Xin Meng*, Delizzia Mossel, Mels Jagt, and Daan Brinks. "Expanding the family of genetically encoded voltage indicators with a candidate Heliorhodopsin exhibiting near-infrared fluorescence." *Journal of Biological Chemistry* 299, no.6 (2023). (Chapter 4 of this thesis. Author contributions see section 4.5.)

* These authors contributed equally to this work. CRediT: **Xin Meng** conceptualization (lead), data curation (lead), formal analysis (lead), investigation (lead), methodology (equal), software (lead), writing-original draft (lead), writing-review & editing (lead); **Srividya Ganapathy** conceptualization (lead), data curation (lead), formal analysis (lead), funding acquisition (supporting), investigation (lead), methodology (lead), writing-original draft (lead), writing-review & editing (lead); **Lars van Roemburg** formal analysis (supporting), investigation (equal), methodology (equal), visualization (equal), writing-review & editing (supporting); **Marco Post** formal analysis (supporting), investigation (equal), methodology (equal), writing-review & editing (supporting); **Daan Brinks** conceptualization (lead), funding acquisition (lead), investigation (supporting), methodology (lead), project administration (lead), resources (lead), supervision (lead), writing-original draft (lead), writing-review & editing (lead).

OTHER PUBLICATIONS

Meng, Xin*, Huachuan Huang*, Keding Yan*, Xiaolin Tian, Wei Yu, Haoyang Cui, Yan Kong, Liang Xue, Cheng Liu, and Shouyu Wang. "Smartphone based hand-held quantitative phase microscope using the transport of intensity equation method." *Lab on a Chip* 17, no. 1 (2017): 104-109.

Meng, Xin*, Xiaolin Tian*, Yan Kong, Aihui Sun, Wei Yu, W Qian, X Song et al. "Rapid in-focus corrections on quantitative amplitude and phase imaging using transport of intensity equation method." *Journal of microscopy* 266, no. 3 (2017): 253-262.

Tian, Xiaolin, Xin Meng, Wei Yu, Xiaojun Song, Liang Xue, Cheng Liu, and Shouyu Wang. "In-focus quantitative intensity and phase imaging with the numerical focusing transport of intensity equation method." *Journal of Optics* 18, no. 10 (2016): 105302.

Hu, Junbao, Xin Meng, Qi Wei, Yan Kong, Zhilong Jiang, Liang Xue, Fei Liu, Cheng Liu, and Shouyu Wang. "Numerical tilting compensation in microscopy based on wavefront sensing using transport of intensity equation method." *Journal of Optics* 20, no. 3 (2018): 035301.

Tian, Xiaolin, Wei Yu, Xin Meng, Aihui Sun, Liang Xue, Cheng Liu, and Shouyu Wang. "Real-time quantitative phase imaging based on transport of intensity equation with dual simultaneously recorded field of view." *Optics letters* 41, no. 7 (2016): 1427-1430.

Sun, Aihui, Yan Kong, Xin Meng, Xiaoliang He, Ruijun Du, Zhilong Jiang, Fei Liu, Liang Xue, Shouyu Wang, and Cheng Liu. "Variable aperture-based ptychographical iterative engine method." *Journal of Biomedical Optics* 23, no. 2 (2018): 026007-026007.

Xu, Jing, Xiaolin Tian, Xin Meng, Yan Kong, Shumei Gao, Haoyang Cui, Fei Liu, Liang Xue, Cheng Liu, and Shouyu Wang. "Wavefront-sensing-based autofocusing in microscopy." *Journal of Biomedical Optics* 22, no. 8 (2017): 086012-086012.

Jian, Dan*, Bin Wang*, Huachuan Huang, Xin Meng, Cheng Liu, Liang Xue, Fei Liu, and Shouyu Wang. "Sunlight based handheld smartphone spectrometer." *Biosensors and Bioelectronics* 143 (2019): 111632.